Modelling the Evolution, Rheology, and Buttressing of Antarctic Pinning Points

Dissertation

der Mathematisch-Naturwissenschaftlichen Fakultät

der Eberhard Karls Universität Tübingen

zur Erlangung des Grades eines

Doktors der Naturwissenschaften

(Dr. rer. nat.)

vorgelegt von

Auguste Clara Jones Henry

aus Sligo, Irland

Tübingen

2023

Gedruckt mit Genehmigung der Mathematisch-Naturwissenschaftlichen Fakultät der Eberhard Karls Universität Tübingen.

Tag der mündlichen Qualifikation:	18.01.2024
Dekan:	Prof. Dr. Thilo Stehle
1. Berichterstatter/-in:	Prof. Dr. Reinhard Drews
2. Berichterstatter/-in:	Prof. Dr. Elisa Mantelli

ABSTRACT

The Antarctic Ice Sheet (AIS) has the potential to substantially influence global sea level under a warming climate. Precise projections of ice loss from the AIS rely on an understanding of physical mechanisms and an accurate model representations of coastal ice flow dynamics. Regulation of ice flow towards the open ocean occurs due to the drag caused by ice rises and ice rumples, areas of grounded ice which form in ice shelves and are surrounded by otherwise floating ice. Due to their complicated flow regimes and small sizes, isle-type ice rises and ice rumples, more generally known as pinning points, are often under-represented in ice flow models. In this thesis, five objectives are outlined which advance our understanding of ice rises and ice rumples; (1) gaining an understanding of the evolution of ice rises and ice rumples in glacial-interglacial cycles, (2) quantifying the buttressing due to pinning points, (3) obtaining the three-dimensional simulation of the stratigraphy of an ice rise with validation against observed stratigraphy, (4) investigating the choice of the Glen's flow law exponent in ice rise dynamics and (5) investigating the relationship between the velocity and anisotropy fields of ice rises.

For the first objective, the evolution of ice rises and ice rumples in response to sea level variation over glacial-interglacial timescales is investigated using the finite element model Elmer/Ice with a full Stokes setup and presented as a publication in Chapter 2. Findings show that the grounded area of ice rises and ice rumples responds with hysteresis to sea level variation. The hysteresis is reflected in the upstream velocity field, meaning that ice shelf buttressing has the potential to be irreversible under a changing climate having significant consequences for the AIS given the large number of pinning points in coastal Antarctica.

The second objective of this thesis is to systematically investigate the influence of model complexity, pinning point geometry and ice shelf flux on ice shelf buttressing forces. Building on previous work highlighting the importance of pinning points in continental grounding line evolution, Chapter 5 presents a manuscript investigating the quantification of pinning points buttressing forces using full Stokes simulations with varying pinning point sizes and upstream ice shelf fluxes. Findings show that variations in upstream ice shelf flux have a more significant influence on changes in pinning point buttressing in comparison with variations in pinning point size. This work shows that when modelling ice shelves with pinning points, it is important to include vertical variations in horizontal velocities to avoid an overestimation of buttressing as seen in the SSA simulations.

For the third and subsequent objectives of this thesis, three-dimensional simulations of Derwael Ice Rise (DIR) are performed. Previous studies of the two-dimensional simulated isochronal stratigraphy of ice rises have been restricted to grounded ice and do not

allow for through-plane flow. Chapter 3 in this thesis presents the results of three-dimensional, partitioned simulations of the stratigraphy of Derwael Ice Rise. Results show a good match between modelled isochrones and observed isochrones obtained from airborne data in grounded ice and across the grounding zone. This work provides a tool for comparison with ice cores and radargrams, allowing co-validation and extrapolation of the age field beyond observed data points, as well as for choosing sites for ice core drilling.

The fourth objective is to investigate the influence of the choice of Glen's flow law exponent on the age field of the DIR, building on a study which found that the often-used Glen's flow law of $n = 3$ is an under-estimation in ice shelves. The results are presented in Chapter 3 and show that differences between using a Glen's flow law exponent of $n = 3$ and $n = 4$ result in age differences of $<$ 5% at 95% depth. The largest differences between simulations with Glen's flow law exponents of $n = 3$ and $n = 4$ are seen in the shear zones between DIR and the ice shelf, where shear strain rates are significantly higher in the $n = 4$ simulation. This has consequences, for example, in fracture modelling where the choice of Glen's flow law exponent may result in differing fracture initialisation.

The fifth and final objective of this thesis is to investigate the anisotropy field of DIR using a semi-Lagrangian crystal orientation tensor evolution equation. With the further development of geophysical methods using radar to infer crystal orientation, it has become much more feasible to make comparisons between models and observations of ice anisotropy. In Chapter 4, the results of simulations of the three-dimensional anisotropy field of DIR are presented. In these simulations, the influence of the strain-rate and deviatoric stress tensors on the crystal orientation evolution is varied, based on previous studies. Results vary across the ice rise, but most significantly at the tail ends of the flow divide where horizontal divergence of flow occurs. A framework for comparing modelled anisotropy with observations is developed and estimates are presented for the error resulting from an assumption in radar data acquisition that one crystal orientation tensor eigenvector is vertical.

The work presented in this thesis provides an improvement in the understanding of the role of ice rises and ice rumples in ice sheet dynamics, and an investigation of the model representation of ice flow processes. In terms of the significance for future work, this thesis provides a number of tools for comparison with observations allowing for co-validation and model development.

ZUSAMMENFASSUNG

Der antarktische Eisschild hat das Potenzial, den globalen Meeresspiegel bei weiterer Klimaerwärmung erheblich zu erhöhen. Genaue Vorhersagen verlangen ein umfassendes Verständnis der physikalischen Prozesse und eine genaue Modelldarstellung der Eisdynamik in Küstennähe. Der Eisfluss in den Ozean wird durch den Gegendruck von Eisrücken und Eishöckern bestimmt, Gebiete in welchen schwimmendes Schelfeis mit dem Ozeanboden in Kontakt sind. Aufgrund ihres komplizierten Strömungsregimes und ihrer geringen Größe sind inselförmige Eisrücken und Eishöcker, die allgemein als 'Pinning Points' bezeichnet werden, in Eisflussmodellen oft vernachlässigt. In dieser Arbeit werden fünf Ziele ausgeführt, die zu einem verbesserten Verständnis von Eisrücken und Eishöcker beitragen; (1) Verständnis der Entwicklung von Eisrücken und Eishöcker in Glazial-Interglazial-Zyklen, (2) Quantifizierung des Gegendrucks durch Pinning-Points, (3) drei-dimensionale Simulation der internen Stratigraphie eines Eisrücken mit Validierung anhand gemessener interner Schichtung, (4) Bestimmung des Exponenten im Glen'schen Fließgesetz und (5) Untersuchung des Zusammenhangs zwischen Geschwindigkeits- und Anisotropie-Feldern von Eisrücken.

Das zweite Ziel dieser Arbeit ist die Abhängigkeit des Gegendrucks von Modellvereinfachungen, der räumlichen Ausdehnung der Pinning-Points und der Schelfeisströmung des Schelfeises. Aufbauend auf früheren Arbeiten, in denen die Bedeutung von Pinning-Points für die zukünftige Entwicklung der kontinentalen Gründungslinie hervorgehoben wurde, quantifiziert Kapitel 5 den Gegendruck von Pinning-Points anhand vollständiger Stokes-Simulationen mit unterschiedlich grossen Pinning-Points und Schelfeisströmungen stromaufwärts. Die Ergebnisse zeigen, dass Variationen in der Schelfeisströmung einen größeren Einfluss auf die Veränderung des Gegendrucks von Pinning Points haben als Variationen in ihrer räumliche Ausdehnung. Die vertikalen Variationen der horizontalen Flussgeschwindigkeiten sollten insbesondere bei der Modellierung von Schelfeis mit Pinning-Points berücksichtigt werden, wie es in den SSA-Simulationen beobachtet wurde, um eine mögliche Überschätzung des Gegendrucks zu verhindern.

Für das dritte Ziel dieser Arbeit werden dreidimensionale Simulationen des Derwael Ice Rise, einem Eisrücken in der Ostantarktis, und dem Schelfeis in seiner Umgebung, durchgeführt. Bisherige Simulationen der zweidimensionalen Stratigraphie von Eisrücken beschränkten sich nur auf das gegründete Eis und vernachlässigten den waagrechten Eiszufluss. In Kapitel 3 dieser Arbeit werden die Ergebnisse von dreidimensionalen, numerisch-partitionierten Simulationen der internen Stratigraphie des Derwael Ice Rise vorgestellt. Die Ergebnisse zeigen eine gute Übereinstimmung zwischen den modellierten und den gemessenen Isochronen, welche aus luftgestützten

Radardaten über der Gründungslinie aufgenommen wurden. Diese Übereinstimmung ermöglicht nun den Abgleich mit Eisbohrkernen und Radargrammen, um das Altersfeld zu validieren und Standorte für zukünftige Eiskernbohrungen auszuwählen.

Das vierte Ziel ist die Untersuchung des Einflusses des Exponenten im Glen'schen Fließgesetzes auf das Altersfeld, aufbauend auf einer Studie, die ergab, dass der häufig verwendete Exponent von $n = 3$ eine Unterschätzung für Schelfeis darstellt. Unterschiede zwischen der Verwendung eines Exponenten von $n = 3$ und $n = 4$ führen zu Altersunterschieden von < 5 % in 95 % in der Tiefe. Die größten Unterschiede zwischen Simulationen mit einem Exponenten von $n = 3$ und $n = 4$ sind in den Scherungszonen zwischen Derwael Ice Rise und dem Schelfeis, wo die Scherungsraten in der $n = 4$-Simulation deutlich höher sind. Dies hat Konsequenzen, z.B. bei der Spaltenmodellierung, wo die Wahl des Exponenten ausschlaggebend bei der Spaltenbildung ist.

Das fünfte Ziel dieser Arbeit besteht in der Untersuchung der Anisotropie der Kristallstruktur im Derwael Ice Rise anhand eines semi-Lagrange'schen Ansatzes. Mit der Weiterentwicklung geophysikalischer Methoden, bei denen Radar zur Bestimmung der Kristallorientierung eingesetzt wird, sind Vergleiche zwischen Modellen und Beobachtungen der Eisanisotropie wesentlich einfacher geworden. Letztens werden verschiedene Einflüsse der Dehnungsraten und der deviatorischen Spannungstensoren auf die Entwicklung der Kristallstruktur untersucht. Die Einflüsse variieren über den gesamten Eisrücken, insbesondere wo eine horizontale Divergenz der Strömung auftritt. Es wird eine Methode für den Vergleich der modellierten Anisotropie mit Radarmessungen entwickelt. Mit dieser Methode kann der Fehler, der sich aus der Annahme über die vertikale Ausrichtung der Kristallstruktur bei der Radardatenerfassung ergibt, bestimmt werden.

Die dargelegten Resultate tragen zu einer verbesserten Modelldarstellung von Eisrücken und Eishöcker in der Eisschilddynamik bei. Was die Bedeutung für künftige Arbeiten angeht, so bietet diese Arbeit eine Reihe von Methoden für den Vergleich mit Beobachtungen, die einen Abgleich und Modellentwicklung ermöglichen.

ACKNOWLEDGMENTS

First and foremost, I would like to thank Reinhard Drews and Clemens Schannwell for giving me the opportunity to pursue my PhD studies in two fantastic research environments in a topic which I never lost interest in. Your patience and understanding has been invaluable as I tried to find my feet during the times of corona at the beginning of my PhD, to celebrating with me after successes. Thanks also to Paul Bons, my second supervisor at the University of Tübingen. Thank you for the discussions about ice micro-structure and for your help in navigating the administrative side of thesis submission.

I would like to thank all those at the Max Planck Institute for Meteorology for sharing your wide areas of expertise and for challenging me to become a scientist I am truly proud to be. I would like to thank all those in the Ocean Physics group for allowing me to dip my toes into understanding the workings of global climate models. I would like to thank all those in IMPRS for the many interesting conversations, adventures and fun times together. Many thanks go to the organisers of IMPRS and especially to Antje, who has been an incredible help, providing invaluable advice at each stage of my PhD.

I will forever be thankful for the time spent in the Geophysics group at the University of Tübingen. With kindness and understanding as a baseline, the group has allowed me to develop as a self-confident scientist. Vjeran, many thanks for answering my questions about the inner workings of the Elmer/Ice model — you played a pivotal role during the last few years. Your kind words and constant support have been invaluable during my PhD. Reza, thank you for your support while we were both finishing up our theses. Falk, I'm grateful to have had you as a travel partner for several research trips, most memorably Ötztal. Many thanks to Leah, Guy, Alexandra, Falk, Anne and Christian who read over parts of my thesis before submission. Thank you to the rest of the Geophysics group (present and past): Inka, Rebecca, Michael, Akash, Greta, Valentina and Leonie. I will always remember the Stocherkahn adventures, the uncountable coffee breaks, the lunches, the dinners, the visit to Shooters, the hiking adventures, the list goes on.

I would like to thank my Master's thesis supervisor at the University of St. Andrews, David Dritschel, whose support has been instrumental to my development towards being an independent scientist. You have been a very important mentor to me both during and after my time in St. Andrews.

I am incredibly grateful to all those I have met along the way at conferences, summer schools, research visits, workshops and courses. Special thanks go to the fellow students and lecturers at the Karthaus Summer School who I am happy to meet around every corner at EGU. Thanks go to Olaf for allowing me to join the glaciology course

at Vernagtferner, Austria. An insight into icy science beyond idealised mathematical models was much needed.

Thanks go to all those I had the pleasure to meet during my research visit in the UK. Special thanks go to Jakub Stoček, Ian Hewitt, David Dritschel and Jacques Vanneste for hosting me at the British Antarctic Survey in Cambridge and the Universities of Oxford, St. Andrews and Edinburgh. Special thanks also go to Carlos, Oli, Alex, Alvaro and Ronan for the many ice rise conversations.

Thanks go to my friends from Sligo, St. Andrews, Hamburg and Tübingen: Jenny, Pinhsin, Ed, Logan, Paul, Sophie, Laura, Kate, Eoin, Henry, Daniel and Olga (many of whom I don't see often enough). Thank you to the Tübingen Parkrun gang: Alex, Curtis, Christian, Janina, Ainara and Minilek, and my fellow fiddle players: Thomas and Andrea. Thank you to my flatmates for sharing a truly special WG with me that I have been lucky to call home. Achim, thank you for your endless support and the Spätzle to cheer me up on the more stressful days :)

I thank my family for their support from afar. Thanks Mutti for always believing me and thanks Dad for sharing your fondness of nature with me. Thank you Rob for the adventures together and being a truly supportive brother.

Lastly, I would like to thank the deutsche Forschungsgemeinschaft (DFG) for the funding under the Schwerpunktprogramm "Antarktisforschung mit vergleichenden Untersuchungen in arktischen Eisgebieten" which enabled the opportunity to undertake this work. Furthermore, I would like to thank Jakub Stoček at the British Antarctic Survey for hosting me during a research visit which was funded by the Institute of Mathematics and its Applications.

LIST OF FIGURES

Figure 1 Buttressing due to ice rises and ice rumples 2
Figure 2 Overview of Antarctic ice rises and ice rumples 2
Figure 3 Flow regime types at ice rises 3
Figure 4 Raymond arch migration 5
Figure 5 Relationship between the strain rate and deviatoric stress in an ice shelf 7
Figure 6 The crystal lattice structure of ice 9
Figure 7 Deformation of ice from divide to ice shelf 10
Figure 8 Schmidt diagrams of c-axes 11
Figure 9 Fabric types derived from crystal orientation tensor 12

Contents

Page No.

ABSTRACT **iv**

ZUSAMMENFASSUNG **vi**

ACKNOWLEDGEMENTS **viii**

LIST OF FIGURES **x**

1 Introduction **1**
1.1 The role of pinning points in Antarctic Ice Sheet evolution 1
1.1.1 Ice rises and ice rumples 1
1.1.2 Formation and evolution of ice rises and ice rumples . . . 3
1.1.3 Ice shelf buttressing 4
1.1.4 Ice rises as an archive 4
1.2 Ice flow modelling 6
1.2.1 Full Stokes 6
1.2.2 Shallow ice approximation (SIA) 8
1.2.3 Shallow shelf approximation (SSA) 8
1.2.4 Blatter-Pattyn approximation 8
1.2.5 Ice as an anisotropic material 9
1.2.6 Finite element modelling 12
1.2.7 Data integration and comparison 13
1.3 Research objectives 15
1.4 Author contributions 16
1.4.1 First-author contributions 16
1.4.2 Co-author contributions 17

2 Hysteretic evolution of ice rises and ice rumples in response to variations in sea level **18**
1 Introduction 19
2 Methods 20
2.1 Governing equations 20
2.2 Idealised model domain set-up 23
2.3 Shallow ice approximation (SIA) comparison 24
2.4 Comparison with the Vialov approximation 24
2.5 Design of transient simulations 25
3 Results 26
3.1 Steady-state analysis before sea level perturbation 26
3.2 Ice-rise-to-ice-rumple transitions triggered by sea level variation 29
4 Discussion 32
4.1 The influence of basal sliding on the geometry and transient behaviour of ice rises 32

4.2 The hysteretic behaviour of ice rises over glacial cycles . . 34
5 Conclusions 35

3 Predicting the three-dimensional age-depth field of an ice rise 43
1 Introduction 45
2 Derwael Ice Rise 46
3 Methods 46
3.1 Governing equations 48
3.2 Observational data, initial conditions and boundary conditions 49
3.3 Model spin-up procedure 50
4 Results 52
4.1 Model parameter choice and applied surface mass balance 52
4.2 Comparisons between modelled and observed stratigraphy 52
4.3 Velocities and strain rates 54
5 Discussion 57
5.1 Progress and challenges for three-dimensional ice rise modelling 57
5.2 Comparison between modelled and observed stratigraphy 59
5.3 Glen's flow law exponent 60
5.4 Model limitations and future research direcitons 61
6 Conslusions 62

4 Modelling the three-dimensional, diagnostic anisotropy field of an ice rise 67
1 Introduction 68
1.1 Motivation 69
1.2 Derwael Ice Rise (DIR) 70
2 Methods 71
2.1 Governing equations 71
3 Results 73
3.1 Analysis of simulated anisotropy field 73
3.2 Comparison of simulations with differing parameter choice 75
3.3 Metrics for comparison with radar data 77
4 Discussion 80
4.1 Dependence of the anisotropy field on the velocity and stress fields 80
4.2 Implications for viscosity coupling 82
4.3 Model representation of anisotropy 83
4.4 Framework for comparison with observations 84
5 Conclusions 84

5 Ice-shelf dynamics due to pinning point buttressing 90
1 Introduction . . . 91
2 Methods . . . 92
2.1 Stokes equations . . . 93
2.2 Shallow shelf approximation (SSA) . . . 94
2.3 Blatter-Pattyn approximation (BPA . . . 95
2.4 Analytical ice shelf solution . . . 95
2.5 Calculation of stress . . . 95
2.6 Ice shelf forces . . . 96
3 Results . . . 97
3.1 Benchmark simulations . . . 97
3.2 Full Stokes simulations . . . 99
3.3 Comparison with lower-order models . . . 101
4 Discussion . . . 103
4.1 Implications for ice shelves . . . 103
4.2 Limitations and outlook . . . 104
4.3 Model representation of pinning points . . . 104
5 Conclusions . . . 105

6 Summary, conclusions and implications 108
6.1 Major findings . . . 108
O1: Advances in the understanding of ice rise evolution . . . 108
O2: Advances in our understanding of pinning point buttressing 109
O3: Modelling the stratigraphy of an ice rise . . . 109
O4: Understanding the role of the Glen's flow law exponent . . . 110
O5: Advances in anisotropy modelling . . . 110
6.2 Implications and outlook . . . 110

Appendix 112

"At the heart of the ridiculous, the sublime."
- Derek Mahon

1 INTRODUCTION

1.1 THE ROLE OF PINNING POINTS IN ANTARCTIC ICE SHEET EVOLUTION

The Antarctic Ice Sheet contributes the greatest source of uncertainty in future sea level projections, holding roughly 58 m of sea level equivalent as ice (Morlighem et al., 2020). It is known that the Antarctic Ice Sheet had fluctuated in volume and extent over previous glacial-interglacial cycles (Albrecht, Winkelmann, and Levermann, 2020; Deschamps et al., 2012), and in combination with other glaciated regions across the Earth, has resulted in sea level variations of roughly 120 m (Grant et al., 2014). These sea level variations have substantial consequences for ice sheet evolution.

It has been shown that if the transition point from grounded to floating ice is positioned on a retrograde slope, unstable retreat of the grounding line will occur (Schoof, 2007), although exceptions do exist (Greenwood et al., 2021; Gudmundsson et al., 2012). Conversely, if the grounding line is positioned on a prograde slope, advance of the grounding line will occur. The dependence of current state of a system on its past evolution is referred to as *hysteresis*. The induced hysteresis during glacial-interglacial cycles (Durand et al., 2009; Garbe et al., 2020; Schoof, 2007) highlights the intricate dependence of continental ice sheet dynamics on processes occurring at and in the vicinity of the continental grounding line such as ice shelf buttressing forces (Callens et al., 2014; Gudmundsson, 2013; Haseloff and Sergienko, 2018) and gives an indication as to possible future tipping point scenarios (Lenton et al., 2019; Rosier et al., 2021). Due to the complex evolution of the Antarctic Ice Sheet, particularly in coastal areas, it is important to understand the dynamics of pinning points, in the form of ice rises and ice rumples.

1.1.1 *Ice rise and ice rumples*

Ice rises are found within the ice shelves surrounding the Antarctic continent and are defined as areas of ice grounded on anomalies in the underlying bed surrounded by otherwise floating ice. Ice rises contain what is called a *flow divide*, from where ice flows towards the surrounding ice shelves. In contrast to ice rises, ice rumples are generally smaller and are distinguishable by a mere slowing down of the ice due to the underlying bed anomaly, with the velocity direction aligning with that of the surrounding ice shelf (Smith, 1986). Ice rises and ice rumples are found in every major ice shelf, with a total of 170 ice rises and more than 500 ice rumples observed around the coast of Antarctica (Fig. 2, Matsuoka et al., 2015).

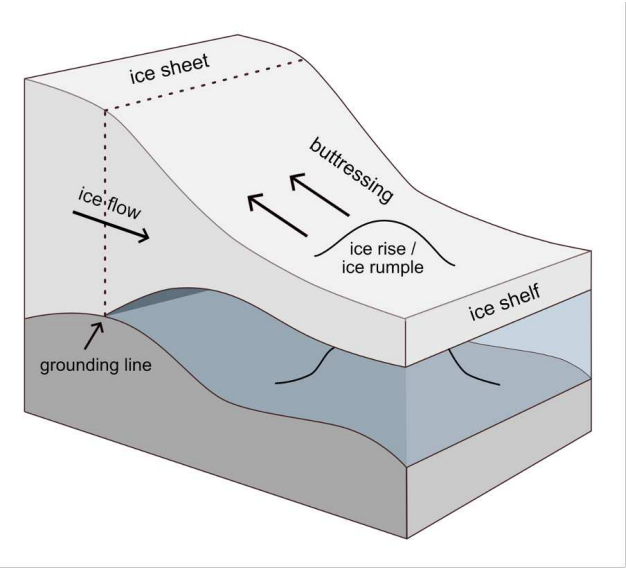

Figure 1: Ice rises and ice rumples are locally grounded areas within an ice shelves which act to buttress the upstream ice flow. The buttressing force within the ice shelf influences the continental grounding line position. The resulting influence on grounding line evolution has consequences for the amount of grounded ice in the Antarctic Ice Sheet and sea level projections.

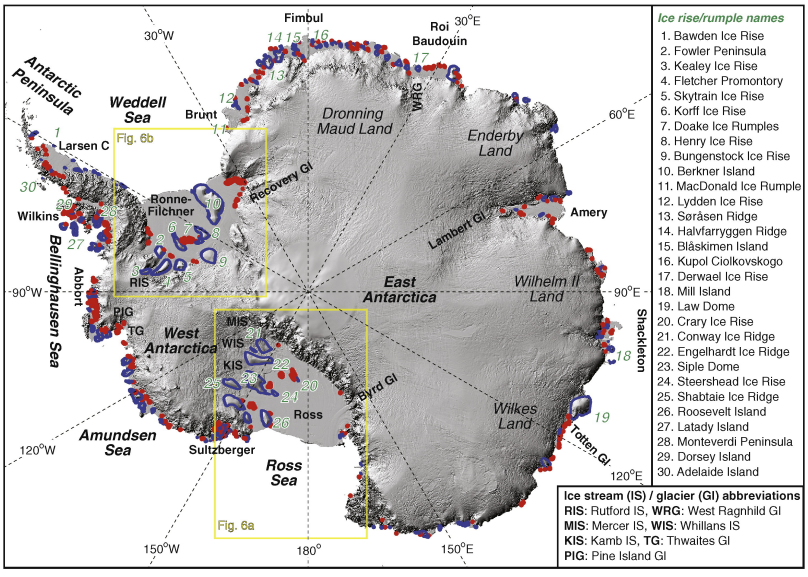

Figure 2: Outlines of ice rises in blue and ice rumples in red around the coast of Antarctica, with major ice rises named on the right hand side (Matsuoka et al., 2015). The two largest Antarctic ice shelves are shown in the boxes 6a and 6b.

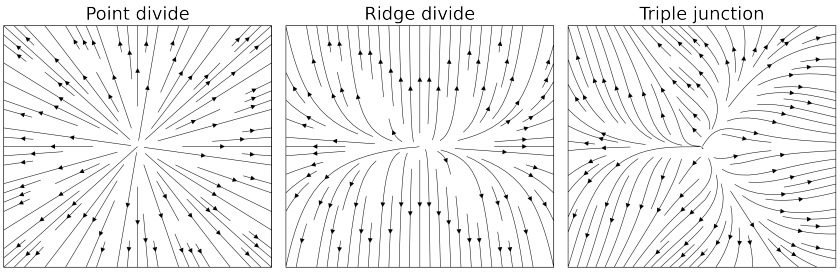

Figure 3: Types of horizontal flow regime present at ice rises. A point divide has a horizontal velocity field originating at a point divide, a ridge divide has a flow regime which originates at a line, and a triple junction flow regime contains three lines which meet at a central point from which streamlines originate. The type of flow regime has an influence on the isochronal stratigraphy of an ice rise, with anticlines (Raymond arches) forming in areas where horizontal velocity vectors are divergent or opposing.

Ice rises can be categorised into a number of different types, with varying flow regimes, referred to as having a point divide, ridge divide or triple junction (Fig. 3). Isle-type ice rises refer to ice rises which are completely surrounded by floating ice shelves, whereas promontory ice rises remain connected to the continental ice sheet via an area of grounded ice. The side of an isle-type ice rise facing the flow of the ice shelf, referred to as the *stoss side*, tends to be much thicker than the much less restricted *lee side*. Ice rises differ by the type of flow divide present with the most trivial, albeit rarest, type of flow divide being a point source (Fig. 3). The other types of flow regime are a ridge divide, with a line acting as the horizontal velocity field source and a triple junction, made up of three ridges divides meeting at a central point (Gillet-Chaulet and Hindmarsh, 2011; Hindmarsh et al., 2011).

1.1.2 *Formation and evolution of ice rises and ice rumples*

Fluctuations in the extent of the Antarctic Ice Sheet allow ice rises and ice rumples to form, evolve, and transition from one flow regime to another. Ice rises and ice rumples can disappear into the continental ice sheet or when an ice shelf ungrounds from the bed anomaly below (Drews et al., 2015). As highlighted in Matsuoka et al. (2015), ice rises can form due to a number of mechanisms. During deglaciation, an ice rise can emerge as the grounding line retreats around a prominent bed anomaly, leaving behind an isle-type or promontory ice rise. Depending on whether the radial flow regime formed before or after the retreat of the continental grounding line past the bed anomaly, the formation type is referred to as *long-term stable* or *deglacial emergent*, respectively. A further possible formation mechanism during deglaciation is the complete ungrounding of an area followed by regrounding at a bed anomaly due to glacial isostatic rebound and is referred to as *glacial isostatic adjustment (GIA) emergent* (Barletta et al., 2018; Matsuoka et al., 2015). Glacial isostatic rebound occurs during

deglaciation due to lifting of the Earth's surface after the weight of the ice has been removed. The final formation mechanism is due to the grounding of an ice shelf because of thickening induced by a change in the upstream ice flow patterns. Although it has been shown that ice rises and ice rumples change in geometry over time (Kingslake et al., 2018; Kingslake et al., 2016; Wearing and Kingslake, 2019), it is not known which of these formation patterns is most frequent.

1.1.3 *Ice shelf buttressing*

Both ice rises and ice rumples provide buttressing to the upstream ice shelf (Fig. 1), regulating the flow of ice towards the open ocean and having an influence on the continental *grounding line* position (Favier et al., 2012; Favier and Pattyn, 2015; Favier et al., 2016; Fürst et al., 2016; Macayeal et al., 1987; Reese et al., 2018; Still and Hulbe, 2021). This means that although the floating ice of ice shelves has already, in effect, contributed to sea level, there is a backstress on the continental ice sheets that acts to contain the grounded continental ice. Changes in ambient climatic conditions can influence the geometry and stability of an ice shelf (Cook and Vaughan, 2010; Doake et al., 1998; Dupont and Alley, 2005; Gagliardini et al., 2010; Goel et al., 2020; Rott, Skvarca, and Nagler, 1996; Sun et al., 2020; Tinto and Bell, 2011) and thereby cause a change in the buttressing experienced by upstream ice (Pegler, 2016). This is particularly relevant for future projections, as a reduction in the net mass balance of ice shelves will result in a weakening of the buttressing effect due to ice rises and ice rumples. Ice shelves most at risk of destabilisation are those where the ice shelf itself is mainly made up of locally accumulated ice rather than ice accumulated on the Antarctic continent (Višnjević et al., 2023).

1.1.4 *Ice rises as an archive*

Past flow re-organisation and changes in climatic conditions can be inferred from ice rise data using a number of techniques including seismics, radar and ice coring (Bindschadler et al., 2013; Bindschadler, 1993; Bindschadler, Vornberger, and Gray, 2005; Brisbourne et al., 2019; Callens et al., 2014). Ice rises contain flow divides where the flow of ice is significantly slower than in the surrounding ice shelves, meaning relatively old ice can be found here (Drews et al., 2015; Martín and Gudmundsson, 2012; Martín, Gudmundsson, and King, 2014; Martín, Hindmarsh, and Navarro, 2009). Earlier techniques have been developed for inferring the age of ice using the temperature profile (Bindschadler, Roberts, and Iken, 1990). More recently, using ground-penetrating radar to image the sub-surface, the relationship between the isochronal stratigraphy and the velocity field can be derived (Drews et al., 2015; Drews et al., 2013; Martín and Gudmundsson, 2012; Martín, Hindmarsh, and Navarro, 2006, 2009). Features in the isochronal stratigraphy called *Raymond arches* form at flow divides (Fig. 4), with amplitudes giving an indication of the time since the on-

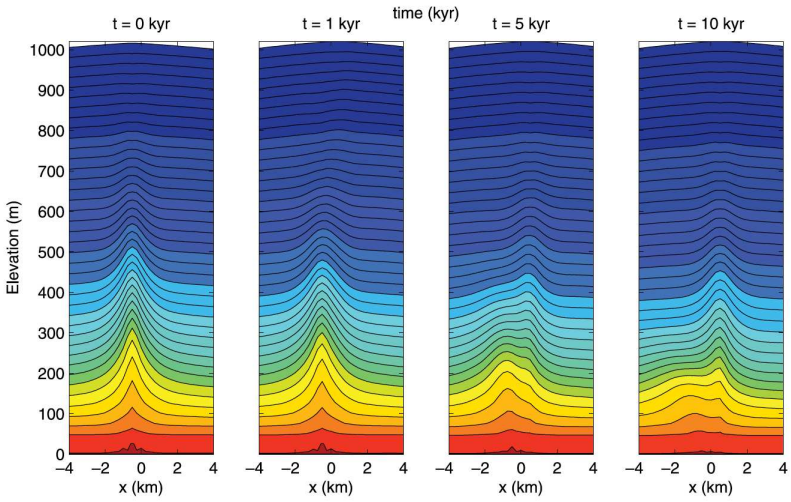

Figure 4: The effect of divide migration on isochronal stratigraphy. The panels show anticlines in the isochronal stratigraphy called Raymond arches which occur at flow divides where there is high horizontal divergence. The isochronal stratigraphy is shown at four points in time in numerical simulations, at times of $t = 0, 1, 5, 10$ kyr. At the time 1 kyr, not much change has occurred except a slight broadening of the Raymond arches. After 5 kyr, the new divide position can be seen in the uppermost isochrones. The previous flow divide position remains evident in the lowermost isochrones, but is no longer evident in the upper half of the ice column. After 10 kyr, Raymond arches at the new divide position are dominant throughout the majority of the ice column, though the previous divide position is evident as broad remnant Raymond arches in the few lowermost isochrones (Martín, Hindmarsh, and Navarro, 2009).

set of stability of the ice rise after changes in external forcing (Drews et al., 2015; Drews et al., 2013; Gillet-Chaulet et al., 2011; Martín and Gudmundsson, 2012; Martín, Hindmarsh, and Navarro, 2006, 2009; Raymond, 1983). A further indicator of ice rise stability is the formation of a double arch beneath a stack of single arches. If a stack of Raymond arches is tilted or a second set of Raymond arches form a distance away from the first set, this indicates that the flow divide has migrated, signalling a local change in external conditions such as a differing ice shelf flow regime, surface mass balance or basal mass balance (Hindmarsh, 1996).

The observed isochronal stratigraphy including Raymond arches (Raymond, 1983) are a useful metric for validation against modelled stratigraphy (Drews et al., 2015; Martín, Hindmarsh, and Navarro, 2009; Rybak and Huybrechts, 2003). As there is a close link between the velocity field and the isochronal stratigraphy, a close match between observed and modelled stratigraphy is an indicator of model performance. Matching the modelled stratigraphy with the observed stratigraphy has previously been used for inferring whether a Glen's flow law exponent of $n = 3$ or $n = 4$ is more appropriate as well as for showing the effect of including anistropic viscosity in simulations

(Martín and Gudmundsson, 2012; Martín, Hindmarsh, and Navarro, 2009). Details of Glen's flow law are outlined in Section 1.2.1.

1.2 ICE FLOW MODELLING

Given the enormity of the Antarctic ice sheet and the complexity of the interaction with the atmosphere (Cavitte et al., 2022; Lenaerts et al., 2014; Schannwell et al., 2019) and ocean (Burgard et al., 2022; De Rydt et al., 2014; Holland and Jenkins, 1999; Jacobs et al., 2011; Jenkins, Nicholls, and Corr, 2010; Naughten et al., 2021), finding a balance between an accurate physical representation of ice flow and realistic computational expense remains a challenge to progression in ice-sheet modelling. To address questions related to ice-flow dynamics, a hierarchy of computational ice-flow models have been developed with varying degrees of accuracy and model intercomparison projects to investigate model performance (Cornford et al., 2020; Gagliardini and Zwinger, 2008; Hindmarsh, 2004; Pattyn et al., 2008, 2012; Pattyn et al., 2013; Seroussi et al., 2019). Continental-scale models are run with simplifications made to the equations describing the motion of ice and at a comparatively low resolution, resulting in the reduced representation of processes such as grounding line (Feldmann et al., 2014; Gladstone, Payne, and Cornford, 2012; Gladstone et al., 2017; Goldberg, Holland, and Schoof, 2009) and pinning point dynamics (Berger et al., 2016; Fürst et al., 2015).

The ice flow dynamics in and around ice rises and ice rumples are complicated in nature, containing areas of (1) grounded and floating ice, (2) divide and flank flow, (3) grounding zones and (4) shear zones. Ice flow equation simplifications (Sections 1.2.2, 1.2.3 and 1.2.4) are not possible at ice rises if accurate modelling of all flow types present at an ice rise are desired. For these reasons, as well as the avoidance of flow approximation coupling and a hydrostatic-equilibrium assumption at the grounding line, it is best to use a full Stokes model set up when modelling an ice rise including its grounding line. However, full Stokes simulations are computationally-expensive and so, in this thesis, results are presented making comparisons with lower-order models.

1.2.1 *Full Stokes*

On the macroscopic scale, ice is modelled as a viscous, non-Newtonian fluid with the effects of inertia and acceleration ignored due to their negligible influence (Greve and Blatter, 2009), so that the equation of motion for ice is

$$\nabla \cdot \sigma + \rho_i \mathbf{g} = 0, \tag{1}$$

where σ is the stress tensor, ρ_i is the ice density and $\mathbf{g} = g\hat{\mathbf{e}}_z$ is the gravitational acceleration. It is furthermore assumed that ice is incompressible so that

$$\nabla \cdot \mathbf{u} = 0, \tag{2}$$

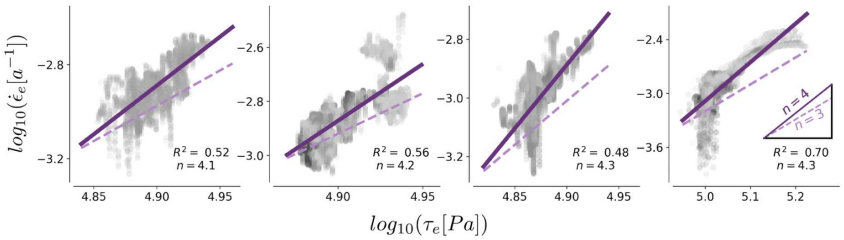

Figure 5: The logarithm of the effective deviatoric stress plotted against the logarithm of the effective strain rate for selected regions in the Ross Ice Shelf. Using regression, the line of best fit is calculated, giving an estimate of the Glen's flow law exponent (solid lines). The slope of a Glen's flow law exponent of $n = 3$ is shown for comparison (dashed lines). Figure adapted from Millstein, Minchew, and Pegler (2022).

where u is the ice velocity. Due its non-linear, viscous flow, the relationship between strain rate and stress is modelled using Glen's flow law,

$$\dot{\varepsilon} = A\tau^n, \tag{3}$$

written here in its simplest form and elaborated on in Chapter 4. Here, $\dot{\varepsilon}$ is the strain rate tensor, τ is the deviatoric stress tensor, A is the ice fluidity and n is an exponent which describes the non-linear relationship between the deviatoric stress tensor and the strain rate tensor. Ice is a shear thinning fluid meaning that as an applied stress increases, its apparent viscosity decreases. This is explained by the structural organisation of ice crystals due to motion. The ice fluidity, A can be modelled as being dependent on a number of factors including the temperature or liquid content.

The non-linear relationship between the strain-rate tensor, $\dot{\varepsilon}$, and the deviatoric stress tensor, τ, has routinely been modelled with an exponent of $n = 3$, recent studies by Millstein, Minchew, and Pegler (2022) and Bons et al. (2018) have indicated that an exponent of $n = 4$ may be more appropriate (Fig. 5). An obstacle to the wide-spread application or testing of an alternative exponent is likely due to uncertainty in the conversion of the ice fluidity, A, whose coupling to ice temperature has been optimised for a flow law with an exponent of $n = 3$. A further explanation for an under-estimation of the Glen's flow law exponent is the inaccessibility of areas in ice sheets where the highest shear stresses occur, such as in lateral shear zones where crevasses are more likely and at the base of grounded ice, where ice core samples are limited.

A number of simplifications of the Stokes equations exist and are applied assuming that specific stress tensor components are negligible. Broadly speaking, the Stokes simplifications lie under the categories of (1) ice flow dominated by internal deformation and (2) ice flow dominated by longitudinal stretching. Within these categories, the ice flow approximations range in the number of stress tensor components ignored and a handful of hybrid models exist which couple two model types together (Ahlkrona et al., 2016; Seroussi et al., 2012).

1.2.2 *Shallow ice approximation (SIA)*

The shallow ice approximation (Greve and Blatter, 2009) is applicable in areas where vertical shear stresses dominate and longitudinal and transverse stresses are negligible. The Stokes equations (Eqs. 1) reduce to the following diagnostic equations for the velocity due to deformation,

$$\mathbf{u}_d = -2(\rho_i g)^n z_s |z_s|^{n-1} \int_{z_b}^{z_s} A(T)(z_s - \bar{z})^n d\bar{z}. \tag{4}$$

and the velocity due to sliding

$$\mathbf{u}_b(x, y) = -C_b(\rho_i g(z_s - z_b))^{p-q} |z_s|^{p-1} z_s. \tag{5}$$

Note that the gradient operator, , applies here only in the horizontal directions. The total velocity is the summation of the two components, $\mathbf{u} = \mathbf{u}_d + \mathbf{u}_b$. The upper and lower ice surfaces are defined as $z_s = z_s(x, y)$ and $z_b = z_b(x, y)$, respectively. The ice fluidity, $A(T)$, can be coupled to temperature, T. The constants p and q control the degree of non-linearity of the friction law. In transient shallow ice approximation simulations, fluxes are calculated from the velocity field and the upper ice surface is adjusted accordingly.

1.2.3 *Shallow shelf approximation (SSA)*

The shallow shelf approximation (Morland and Johnson, 1980) is used to approximate the Stokes equations in areas of floating ice or in ice streams where vertical variations in horizontal deviatoric stresses and horizontal variations in vertical velocities are neglected. Vertical variations in horizontal velocities are neglected, resulting in the ice flow approximation

$$\begin{aligned} 4\frac{\partial}{\partial x}\left(\bar{\eta}\frac{\partial v_x}{\partial x}\right) + 2\frac{\partial}{\partial x}\left(\bar{\eta}\frac{\partial v_y}{\partial y}\right) + \frac{\partial}{\partial y}\left(\bar{\eta}\left(\frac{\partial v_x}{\partial y} + \frac{\partial v_y}{\partial x}\right)\right) &= \rho_i g H \frac{\partial h}{\partial x} \\ 4\frac{\partial}{\partial y}\left(\bar{\eta}\frac{\partial v_y}{\partial y}\right) + 2\frac{\partial}{\partial y}\left(\bar{\eta}\frac{\partial v_x}{\partial x}\right) + \frac{\partial}{\partial x}\left(\bar{\eta}\left(\frac{\partial v_x}{\partial y} + \frac{\partial v_y}{\partial x}\right)\right) &= \rho_i g H \frac{\partial h}{\partial y}. \end{aligned} \tag{6}$$

The shallow shelf approximation is solved numerically as a two-dimensional problem.

1.2.4 *Blatter-Pattyn approximation*

In comparison to the shallow shelf approximation, the Blatter-Pattyn approximation includes two additional terms which allows for verti-

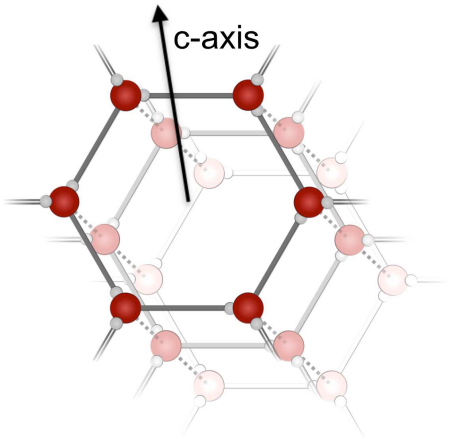

Figure 6: The hexagonal crystal lattice structure of ice, consisting of hydrogen tessellations of atoms (red) and oxygen atoms (grey) all connecting by bonds. When highly anisotropic, ice is made up layers of hexagonal rings, referred to as basal planes. The c-axis is defined as being perpendicular to the basal plane. Figure credit: TJ Young (modified here).

cal variations in horizontal velocities. The Blatter-Pattyn approximation (Pattyn et al., 2008) reads

$$\begin{aligned} 4\frac{\partial}{\partial x}\left(\bar{\eta}\frac{\partial v_x}{\partial x}\right)+2\frac{\partial}{\partial x}\left(\bar{\eta}\frac{\partial v_y}{\partial y}\right)+\frac{\partial}{\partial y}\left(\bar{\eta}\left(\frac{\partial v_x}{\partial y}+\frac{\partial v_y}{\partial x}\right)\right) \\ +\frac{\partial}{\partial z}\left(\bar{\eta}\frac{\partial v_x}{\partial z}\right)=\rho_i g H\frac{\partial h}{\partial x} \\ 4\frac{\partial}{\partial y}\left(\bar{\eta}\frac{\partial v_y}{\partial y}\right)+2\frac{\partial}{\partial y}\left(\bar{\eta}\frac{\partial v_x}{\partial x}\right)+\frac{\partial}{\partial x}\left(\bar{\eta}\left(\frac{\partial v_x}{\partial y}+\frac{\partial v_y}{\partial x}\right)\right) \\ +\frac{\partial}{\partial z}\left(\bar{\eta}\frac{\partial v_y}{\partial z}\right)=\rho_i g H\frac{\partial h}{\partial y}. \end{aligned} \tag{7}$$

The Blatter-Pattyn approximation is solved numerically as a three-dimensional problem, meaning that it is more computationally expensive than the shallow shelf approximation, but less computationally expensive than full Stokes.

1.2.5 *Ice as an anisotropic material*

Glen's flow law crudely accounts for the effects of anisotropy in that, in comparison with a Newtonian fluid description the power law mimics higher shearing at higher stresses due to the greater organisation of fluid molecules. However, Glen's flow law does not explicitly account for directional differences in physical processes, intrinsic to an anisotropic material. To account for anisotropy in models, it is necessary to understand small-scale properties of the ice structure and to be able to make comparison with observations for co-validation.

The ice found in ice sheets and glaciers, *ice* I_h, has a hexagonal crystal lattice structure composed of hydrogen and oxygen atoms (Fig. 6). The layers made up of the hexagonal rings are referred to as *basal*

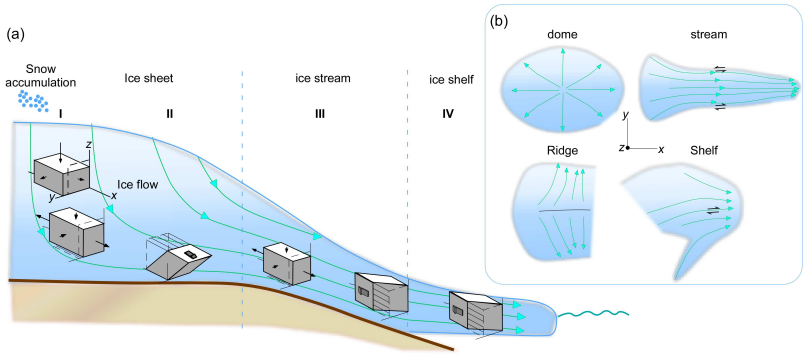

Figure 7: The typical deformation patterns experienced by ice at the divide, the flanks, in ice streams and ice shelves from a side view (a) and a top view (b). In Region I in Fig. 7a, the stress regime is dominated by vertical compression and as ice flows into Region II, the flow is dominated by vertical shear. In Region III, ice speeds up to form an ice stream. Extensional stresses dominate here with some friction due to contact with the bed. In Region IV, is floating and extensional stresses dominate. In Fig. 7b, typical flow regimes of various glaciological settings are shown. Examples of the streamlines which can occur at a dome, ice stream, ridge divide and ice shelf are shown. Figure from Llorens et al. (2022).

planes (not to be confused with basal sliding), with the perpendicular direction referred to as the c-axis. Laboratory experiments show that deformation of ice requires 60 times less applied stress along basal planes than in other directions (Duval, Ashby, and Anderman, 1983), meaning that the velocity field and crystal structure of ice are co-dependent. The directional dependence of physical properties of a material is referred to *anisotropy* and the general anisotropy pattern in a volume is referred to as *fabric* (Alley, 1988; Woodcock, 1977). In reality, ice sheets are made up of polycrystalline ice, with each crystal having its own c-axis direction, separated by *grain boundaries* where re-crystallisation can occur (Kennedy and Pettit, 2015). A particular stress direction may be conducive to basal slip in one crystal, whereas another crystal will respond with greater resistance to deformation due to a less optimal c-axis orientation. This results in a greater load on the crystal with a non-optimal c-axis orientation, resulting in a re-organisation towards an optimal crystal structure and orientation. An understanding of the rate and relative significance of competing processes acting during ice deformation is of particular importance in ice sheet modelling, as ice ranges from isotropic at the ice-atmosphere interface to highly anisotropic in areas of high shear stress (Llorens et al., 2022; Richards, Pegler, and Piazolo, 2022).

The c-axis patterns in ice sheets are dependent on the type of flow regime the ice is subject to. Under vertical compression as seen at an ice dome, the c-axes generally point upwards in the z-direction to form a fabric pattern called a *single maximum* (Figs. 7 and 8). As ice transitions to flank flow and then to faster plug-flow as in an ice stream or ice shelf, c-axes tend to develop into a girdle shape with c-axes organising in the plane perpendicular to the maximum strain-rate direction. Although the present flow regime has an influ-

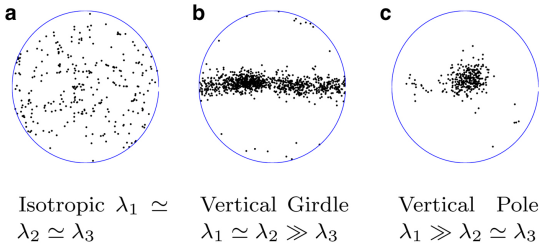

Figure 8: Schmidt diagrams showing c-axis vectors projected onto a circle, where (a) is typical of isotropic ice, (b) is typical of a vertical girdle and (c) is typical of a single maximum or vertical pole (Kluskiewicz et al., 2017). Here, λ_1, λ_2 and λ_3 are the eigenvalues of a crystal orientation tensor describing the spatial distribution of c-axes in a volume of ice. Note that the eigenvalue convention here is such that $\lambda_1 \geqslant \lambda_2 \geqslant \lambda_3$, and differs from the convention used in Chapter 4.

ence on the general c-axis orientation of ice, past flow regimes can also influence the present fabric pattern (Durand et al., 2007; Gerber et al., 2023). For example, ice which has undergone uni-axial vertical compression will develop a single maximum first and as the ice transitions into a region of flank flow dominated by vertical shear, the single maximum is further enhanced (Figs. 7 and 9).

In order to better capture the effect of anisotropy in ice sheet modelling, a number of methods have been developed ranging from simple, computationally efficient parameterisations (Graham et al., 2018; McCormack et al., 2022) to tensor descriptions of crystal orientation (Gagliardini et al., 2013; Gillet-Chaulet et al., 2005; Gillet-Chaulet et al., 2006; Iacopini et al., 2007; Lilien et al., 2021; Passchier, 1997; Pettit et al., 2007, 2011; Seddik et al., 2011; Thorsteinsson, Waddington, and Fletcher, 2003) bringing with them greater computational demands. Most often, the effects of a directional dependence is coupled to the viscosity via enhancement factors (Ma et al., 2010; Rathmann et al., 2021). Tensor descriptions of ice anisotropy are particularly useful in that decomposition of the crystal orientation tensor into its eigenvalues and eigenvectors allows direct comparison with observations (Fig. 8). Some parameterisations of anisotropy use flow enhancement factors dependent on the type of flow regime and offer computational efficiency on par with Glen's flow law, but have a downfall in that fabric history is not accounted for. On the other hand, Lagrangian evolution of a crystal orientation tensor describing the spatial distribution of c-axes allows for the modelling of more complex fabric types, but has been restricted to small-scale simulations mainly in two dimensions due to its computational expense and issues with numerical stability.

Until recently, the primary source of observational data has been in the form of ice cores from which c-axis directions can be inferred. Lately, and although there are limitations (Rathmann et al., 2022), progress has been made in inferring ice fabric using radar and seismic methods (Brisbourne et al., 2019; Brisbourne et al., 2021; Ershadi et al., 2022; Rathmann and Lilien, 2022; Smith et al., 2017; Young et al., 2021a; Young et al., 2021b) to reconstruct the eigenvalues and eigen-

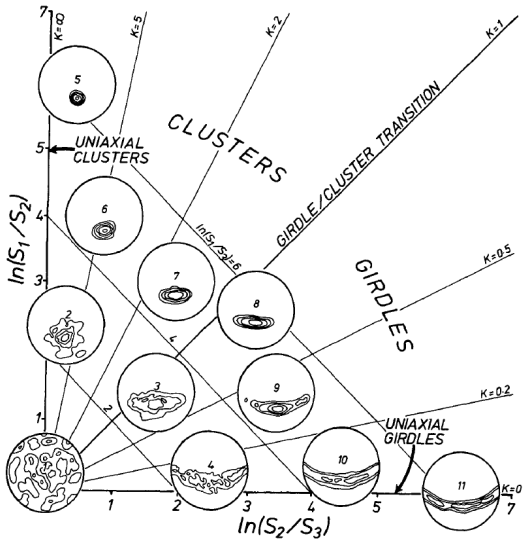

Figure 9: The fabric type determined by the ratios between eigenvalues (S_1, S_2 and S_3) of the crystal orientation tensor varying from isotropic to anisotropic and clustered to girdle fabrics (Woodcock, 1977). Note the eigenvalue convention here is such that $S_1 \geqslant S_2 \geqslant S_3$, which differs from the convention in Chapter 4.

vectors of a crystal orientation tensor. The lack of observational data has delayed comparisons with modelled ice fabric in order to constrain model parameters controlling the influence of strain rates and stresses. Another method for understanding the role of anisotropy in ice flow is the comparison of modelled and observed Raymond arches. Simulations have shown that the inclusion of anisotropy in a model allows the development of double Raymond arches, a feature that did not develop in an isotropic flow model applied to the same ice geometry (Martín and Gudmundsson, 2012; Martín, Hindmarsh, and Navarro, 2009).

1.2.6 *Finite element modelling*

In this thesis, the multiphysics simulation software *Elmer* is used when solving the Stokes problem, which allows for the simultaneous simulation of a number of physical fields. A package within the Elmer software framework has been developed specifically for solving glaciological problems and is referred to as *Elmer/Ice* (Gagliardini et al., 2013). Although the majority of the simulations in this thesis were performed using Elmer/Ice, it is also noted that for calculating the shallow shelf approximation and the Blatter-Pattyn approximation, the Python library *icepack* is used (Shapero et al., 2021).

A series of linear and non-linear iterations are performed to converge to an adequate solution of the Stokes equations, with each iteration reducing the error between the calculated and true solution. The non-linearity of the problem is a significant bottle-neck to quick convergence. In each timestep, a prognostic and diagnostic solution is solved for, with the velocity and pressure computed using an updated viscosity, from which the new geometry of the ice is deter-

mined. Although stabilisation algorithms exist for solving the Stokes problem (Arnold, Brezzi, and Fortin, 1984; Becker and Braack, 2001; Bochev, Dohrmann, and Gunzburger, 2006; Löfgren, Ahlkrona, and Helanow, 2022), a restrictive time-step size means that the Stokes problem can be quite computationally expensive. Furthermore, only few studies have investigated error estimation (Brezzi, 1974; Helanow and Ahlkrona, 2018), and issues such as unphysical velocity oscillations when ice is not in hydrostatic equilibrium remain (Berg and Bassis, 2020). Disagreement over the numerical representation of the grounding line and the treatment of basal properties here continue to be a challenge in the simulation of ice flow (Gagliardini et al., 2016).

Although many types of mesh exist for solving differential equations using the finite element method, the simulations presented here are performed using an unstructured mesh footprint with vertical extrusion of multiple layers, meaning the nodes are fixed in space in the horizontal. An unstructured grid is recommended for ease of grounding line migration. The uppermost and lowermost nodes vertically adjust with the movement of the upper and lower ice surfaces, respectively. The vertical coordinate is commonly taken to be relative to the mean sea level. In order to allow adequate movement of the grounding line, a higher resolution is recommended encompassing the grounding line, which can easily be implemented within the Elmer/Ice software architecture.

To overcome issues with computation time, domain decomposition is possible, with parallel computation of each domain partition allowing an overall increase in performance and/or the possibility of increasing mesh resolution. The sparse matrix multi-frontal parallel direct solver MUMPS can be used in combination with Elmer/Ice in order to divide the domain into multiple partitions. For inter-process communication, Elmer/Ice uses Message Passing Interface (MPI) for parallel computation. Although there are many advantages to parallel computing, a challenge in using domain decomposition is that solvers need to be adapted in order to deal with the adjusted computational environment.

1.2.7 *Data integration and comparison*

An important aspect of computational fluid dynamics is the incorporation of and validation with observational or laboratory data. There is a need for model predictions of physical phenomena or processes to be verified in two ways. Estimation of the errors incurred due to the discretisation of computational fluid dynamics equations must be made, but the equations being solved must also be verified as being an adequate description of the physical problem. Comparison between properties of modelled and observed ice flow dynamics are not only useful for verification of ice flow equations, but also allow the verification of prescribed model boundary conditions.

There are a vast number of parameters and mathematical descriptions of physical processes in ice sheet modelling, each with a certain

degree of uncertainty. These include, but are not limited to uncertainties in (1) the ice fluidity, A, (2) the Glen's flow law exponent, n, (3) alternatives to Glen's flow law incorporating a description of ice anisotropy, (4) the mathematical description of temperature coupling and the associated parameters, (5) the firn densification profile, (6) the basal friction (Brondex, Gillet-Chaulet, and Gagliardini, 2019; Gagliardini et al., 2007) and roughness (Gudmundsson, 2003; Sergienko and Wingham, 2022), and (7) boundary conditions such as the surface accumulation (Callens et al., 2016) and basal melt (Depoorter et al., 2013; Rignot et al., 2013; Seroussi and Morlighem, 2018).

Due to the vastness of Antarctica and challenges in gathering data due to its remote location, observational data is rather limited both spatially and temporally. The lack of data lays the ground for the need to infer properties of the ice and the contact with the bed or ocean using ice flow modelling. New methods such as comparing observed isochronal stratigraphy with modelled isochronal stratigraphy is allowing validation of ice flow models, and validation of assumptions about ice and bed properties. Given that the ice velocity field and boundary conditions dictate the geometry of the internal layers (Holschuh et al., 2017; Leysinger Vieli, Hindmarsh, and Siegert, 2007), the comparison between modelled and observed isochronal stratigraphy allows the validation of ice flow equations, surface accumulation and basal melt. Even more recently, radar measurements of the anisotropy of ice allow further validation of ice flow models through comparison.

Here, a description of the key objectives (O1-O5) of this thesis are provided with reference to the relevant chapters that follow.

- **O1. Investigation of the evolution of ice rises and ice rumples on glacial-interglacial timescales.** Ice rises and ice rumples regulate evolve and transition to alternative flow regimes over glacial-interglacial cycles. In Chapter 2, idealised, full Stokes simulations have been performed with variations in sea level to better understand how ice rises and ice rumples evolve.

- **O2. Investigation of the influence of ice rises and ice rumples on the upstream ice shelf.** Pinning points regulate the flow of ice towards the open ocean through buttressing forces, but questions remain open regarding the influence of a pinning point on the upstream ice shelf. In Chapter 2, the response of upstream ice shelf velocities are analysed in response to glacial-interglacial changes in ice rise geometry. In Chapter 5, full Stokes and lower-order models are used to investigate the dynamic response of the ice shelf to a pinning point for varying pinning point geometries and ice shelf fluxes.

- **O3. The three-dimensional simulation of the stratigraphy of an ice rise using a thermomechanically-coupled model for comparison with observed stratigraphy.** Observations of the internal stratigraphy of ice can be inferred from radargrams penetrating below the upper ice surface. In Chapter 3, a real-world ice rise in modelled using three-dimensional, full Stokes simulations. By calculating the age field from the steady-state velocity field, modelled stratigraphy is compared with observed stratigraphy.

- **O4. An investigation of the influence of the Glen's flow law exponent on the dynamics of an ice rise.** Ice is most often using a Glen's flow law exponent of $n = 3$, whereas recent studies have shown that a Glen's flow law exponent of $n = 4$ may be more appropriate. In Chapter 3, simulations of Derwael Ice Rise are performed with Glen's flow law exponents of $n = 3$ and $n = 4$ to investigate the influence on the age and velocity fields.

- **O5. The simulation of the anisotropy field of an ice rise with parameter choices from previous studies and investigation of the influence of the velocity field.** Recent advances in the processing of ice anisotropy data using quad-polarimetric radar has enabled a more wide-spread collection of anisotropy data. In Chapter 4, diagnostic simulations of the anisotropy field of Derwael Ice Rise are presented along with a framework for comparison with observations.

1.4 AUTHOR CONTRIBUTIONS

1.4.1 *First-author contributions*

Here, the respective author contributions are listed, with the name of the author of this thesis underlined. This thesis contains four chapters with first-author contributions.

Chapter 2:

Henry, A. C. J., Drews, R., Schannwell, C., and Višnjević, V.: Hysteretic evolution of ice rises and ice rumples in response to variations in sea level, The Cryosphere, 16, 3889–3905, https://doi.org/10.5194/tc-16-3889-2022, 2022. [Published in *The Cryosphere*, 2022].

ACJH, CS and RD designed the study, ACJH performed the simulations and carried out the analysis with help from CS, RD and VV, ACJH wrote the manuscript with help from CS, RD and VV.

Chapter 3:

A. Clara J. Henry, Clemens Schannwell, Vjeran Višnjević, Joanna Millstein, Paul D. Bons, Olaf Eisen, Reinhard Drews.: Predicting the three-dimensional age-depth field of an ice rise [Submitted to *The Journal of Geophysical Research: Earth Surface*].

ACJH, CS and RD designed the study, ACJH performed all simulations with help from CS and VV, ACJH performed the analysis with suggestions from JM, PDB and RD, ACJH wrote the manuscript which was edited by all co-authors.

Chapter 4:

A. Clara J. Henry, Carlos Martín, Reinhard Drews: Modelling the three-dimensional, diagnostic anisotropy field of an ice rise [Final edits before submission to *The Journal of Glaciology*].

ACJH and CM designed the study, ACJH performed all simulations with help from CM, ACJH performed all analysis with input from CM, ACJH wrote the manuscript which was edited by CM.

Chapter 5:

A. Clara J. Henry, Ian J. Hewitt and Guy Moss.: The dynamics of pinning point buttressing [Work in progress]

ACJH and IJH designed the study, ACJH performed the Elmer/Ice simulations, ACJH performed the icepack simulations with help from GM, ACJH performed the analysis with suggestions from IJH, ACJH wrote the draft which has not been edited and reviewed by co-authors.

1.5 CO-AUTHOR CONTRIBUTIONS

M. Reza Ershadi, Reinhard Drews, A. Clara J. Henry, Falk M. Oraschewski, Carlos Martín, Jean-Louis Tison, Veronica Tsibulskaya, Sainan Sun, Sarah Wauthy, Inka Koch, Paul D. Bons, Olaf Eisen and Frank Pattyn.: Investigating the dynamic history of a promontory ice rise using radar data [Submitted to *The Journal of Glaciology*].

Vjeran Višnjević, Reinhard Drews, Guy Moss, A. Clara J. Henry, Christian Wild.: Mapping the composition of Antarctic Ice Shelves as a metric for their susceptibility to future climate change [In preparation].

2

HYSTERETIC EVOLUTION OF ICE RISES AND ICE RUMPLES IN RESPONSE TO VARIATIONS IN SEA LEVEL

PUBLICATION DETAILS:

Henry, A. C. J., Drews, R., Schannwell, C., and Višnjević, V.: Hysteretic evolution of ice rises and ice rumples in response to variations in sea level, The Cryosphere, 16, 3889–3905, https://doi.org/10.5194/tc-16-3889-2022, 2022. [Published in *The Cryosphere*, 2022].

Hysteretic evolution of ice rises and ice rumples in response to variations in sea level

A. Clara J. Henry[1, 2, 3], Reinhard Drews[2], Clemens Schannwell[1], and Vjeran Višnjević[2]

[1]Max Planck Institute for Meteorology, Hamburg, Germany
[2]Department of Geosciences, University of Tübingen, Tübingen, Germany
[3]International Max Planck Research School on Earth System Modelling, Max Planck Institute for Meteorology, Hamburg, Germany

Abstract

Ice rises and ice rumples are locally grounded features found in coastal Antarctica and are surrounded by otherwise freely floating ice shelves. An ice rise has an independent flow regime, whereas the flow regime of an ice rumple conforms to that of the ice shelf and merely slows the flow of ice. In both cases, local highs in the bathymetry are in contact with the ice shelf from below, thereby regulating the large-scale ice flow, with implications for the upstream continental grounding line position. This buttressing effect, paired with the suitability of ice rises as a climate archive, necessitates a better understanding of the transition between ice rise and ice rumple, their evolution in response to a change in sea level, and their dynamic interaction with the surrounding ice shelf. We investigate this behaviour using a three-dimensional full Stokes ice flow model with idealised ice rises and ice rumples. The simulations span end-member basal friction scenarios of almost stagnant and fully sliding ice at the ice–bed interface. We analyse the coupling with the surrounding ice shelf by comparing the deviations between the non-local full Stokes surface velocities and the local shallow ice approximation (SIA). Deviations are generally high at the ice divides and small on the lee sides. On the stoss side, where ice rise and ice shelf have opposing flow directions, deviations can be significant. Differences are negligible in the absence of basal sliding where the corresponding steady-state ice rise is larger and develops a fully independent flow regime that is well described by SIA. When sea level is increased, and a transition from ice rise to ice rumple is approached, the divide migration is more abrupt the higher the basal friction. In each scenario, the transition occurs after the stoss-side grounding line has moved over the bed high and is positioned on a retrograde slope. We identify a hysteretic response of ice rises and ice rumples to changes in sea level, with grounded area being larger in a sea-level-increase scenario than in a sea-level-decrease scenario. This hysteresis shows not only irreversibility following an equal increase and subsequent decrease in sea level but also that the perturbation history is important when the ice rise or ice rumple geometry is not known. The initial grounded area needs to be carefully considered, as this will determine the formation of either an ice rise or an ice rumple, thereby causing different buttressing effects.

1 Introduction

Great progress in ice flow modelling has improved the physical representation of dynamical processes at the margins of the Antarctic Ice Sheet, but the transient evolution of the grounding line continues to be challenging, requiring high mesh resolution, small time steps, and advanced model physics (Schoof, 2007; Goldberg et al., 2009; Gudmundsson et al., 2012; Haseloff and Sergienko, 2018; Sergienko and Wingham, 2022). Moreover, the lack of past

observational constraints and ice sheet model initialisation inconsistencies result in spin-up simulation geometries which differ from observations (Seroussi et al., 2019) and result in parameter choice uncertainty (Albrecht et al., 2020).

Ice rises and ice rumples are locally grounded features surrounded by floating ice shelves and play a dual role in this context. Firstly, ice rises and ice rumples regulate the flow of ice towards the ocean through their buttressing effect (Favier and Pattyn, 2015; Barletta et al., 2018; Reese et al., 2018; Still et al., 2019; Still and Hulbe, 2021; Schannwell et al., 2020) and influence the migration of the continental grounding line (Favier et al., 2012). Secondly, past adjustments in local ice shelf flow dynamics can be inferred from ice rises by investigating, for example, isochronal structure and the development of features such as Raymond arches within ice rises (Raymond, 1983; Martín et al., 2006; Gillet-Chaulet and Hindmarsh, 2011; Hindmarsh et al., 2011; Drews et al., 2013, 2015; Schannwell et al., 2019; Goel et al., 2020). The importance of ice rise formation and decay for continental ice sheet evolution (e.g. due to glacial isostatic uplift or changes in sea level) has been recognised in a number of scenarios and shows the key role that ice rises play in large-scale grounding line migration patterns over glacial cycle timescales (Bindschadler et al., 1990, 2005; Barletta et al., 2018; Kingslake et al., 2018; Wearing and Kingslake, 2019).

In adopting terminology from Matsuoka et al. (2015), we identify ice rises as prominent grounded features with a distinct local radial flow regime, causing the flow of the surrounding ice shelves to divert either side of the feature. Ice rumples, however, generally form on less prominent bed highs and result in a predominantly unidirectional flow regime with the upstream ice shelf flowing over the bed anomaly. Ice rises and ice rumples are found all around the perimeter of the Antarctic Ice Sheet, but the mechanisms governing the transition from one flow regime to the other have not yet been investigated, and influences of the surrounding ice shelves on the local flow regimes have not yet been quantified. In order to explore these questions, we use the three-dimensional, full Stokes model Elmer/Ice to simulate idealised ice rises and ice rumples under various basal friction scenarios and sea level perturbations.

To quantify non-local effects from the surrounding ice shelves, we compare the full Stokes solutions with the shallow ice approximation (Hutter, 1983; Greve and Blatter, 2009) and the Vialov profile (Vialov, 1958), which do not capture the stress transfer between ice shelf and ice rise. Furthermore, we investigate whether the locality of flow and basal sliding can be determined by examining the mismatch between the full Stokes ice thickness and the Vialov profile, an idealised solution for the ice geometry. Using sea level perturbations, we explore whether ice rises and ice rumples respond hysteretically and whether multiple steady states exist for a given set of boundary conditions by tracking the grounded area, upstream ice shelf velocity, and dome position. Additionally, we investigate the formation scenarios under which ice rumples reach a steady state and the scenarios under which they are merely a transient feature during ice flow reorganisation.

2 Methods

Ice rises and ice rumples and their surrounding ice shelves are investigated in steady-state and transient scenarios using the three-dimensional full Stokes numerical model Elmer/Ice (Gagliardini et al., 2013).

2.1 Governing equations

We adopt a coordinate system in which the predominant along-flow direction is aligned with the x axis, the predominant across-flow direction is aligned with the y axis, and the z direction marks elevation relative to sea level. The flow of ice is governed by the full Stokes equations,

$$\boldsymbol{\nabla} \cdot (\boldsymbol{\tau} - P\mathbf{I}) + \rho_{\mathrm{i}} \boldsymbol{g} = 0, \tag{1}$$

where $\boldsymbol{\tau}$ is the deviatoric stress tensor, P is the pressure, ρ_{i} is the ice density, and $g = -g\hat{\boldsymbol{e}}_z$ is the gravitational acceleration. We assume the ice to be incompressible, and so, the mass

conservation equation reduces to

$$\boldsymbol{\nabla} \cdot \boldsymbol{u} = 0. \tag{2}$$

The non-linear rheology of ice is modelled using Glen's flow law, which relates the deviatoric stress tensor, $\boldsymbol{\tau}$, to the strain rate tensor, $\dot{\boldsymbol{\epsilon}}$, as

$$\boldsymbol{\tau} = 2\eta\dot{\boldsymbol{\epsilon}}, \tag{3}$$

where the effective viscosity, η, is

$$\eta = \frac{1}{2}A^{-1/n}\dot{\epsilon}_{\mathrm{e}}^{(1-n)/n}. \tag{4}$$

Here, n is the Glen's flow law exponent, and A is a rheological parameter primarily dependent on ice temperature. Since we assume ice to be isothermal, A is set to a constant value in all simulations. The effective strain rate, $\dot{\epsilon}_{\mathrm{e}}$, is calculated from the strain rate tensor, $\dot{\boldsymbol{\epsilon}}$, as

$$\dot{\epsilon}_{\mathrm{e}} = \sqrt{\mathrm{tr}(\dot{\boldsymbol{\epsilon}}^2)/2}. \tag{5}$$

2.1.1 Boundary conditions

The upper surface, $z = z_{\mathrm{s}}(x, y, t)$, evolves subject to

$$\left(\frac{\partial}{\partial t} + \boldsymbol{u} \cdot \boldsymbol{\nabla}\right)(z - z_{\mathrm{s}}) = \dot{a}_{\mathrm{s}}, \tag{6}$$

where $\dot{a}_{\mathrm{s}}$ is the accumulation rate at the upper ice shelf surface. The lower surface, $z = z_{\mathrm{b}}(x, y, t)$, evolves subject to

$$\left(\frac{\partial}{\partial t} + \boldsymbol{u} \cdot \boldsymbol{\nabla}\right)(z - z_{\mathrm{b}}) = \dot{a}_{\mathrm{b}}, \tag{7}$$

where $\dot{a}_{\mathrm{b}}$ is the melt rate at the ice shelf base. Furthermore, the grounded portion is constrained by the condition

$$b(x, y) \leq z_{\mathrm{b}}(x, y, t) \leq z_{\mathrm{s}}(x, y, t), \tag{8}$$

where $b(x, y)$ is the bed. The surface accumulation rate, $\dot{a}_{\mathrm{s}} = 1.2\,\mathrm{m\,a^{-1}}$, reflects the comparatively high rates observed at some ice rises in the Dronning Maud Land area of East Antarctica (Drews et al., 2013). The basal melt rate, $\dot{a}_{\mathrm{b}}$, beneath the ice shelf is defined as a function of ice thickness, H, based on the parameterisation used in Favier et al. (2016),

$$\dot{a}_{\mathrm{b}} = \begin{cases} 0, & \text{where ice is grounded, and} \\ \frac{1}{50}H^{\alpha}\tanh\left(\frac{|\boldsymbol{x}-\boldsymbol{x}_{\mathrm{g}}|}{100}\right), & \text{where ice is floating,} \end{cases} \tag{9}$$

where α is a tuning parameter, and $|\boldsymbol{x} - \boldsymbol{x}_{\mathrm{g}}|$ is the distance to the grounding line. During computation, x represents the position of the current node, and x_{g} represents the position of the grounding line node closest to the current node. Here, x and x_{g} are expressed in kilometres, H is expressed in metres, and $\dot{a}_{\mathrm{b}}$ has units of metres per year.

A constant flux of $Q\big|_{x=0} = 5.4 \times 10^9\,\mathrm{m^3\,a^{-1}}$ into the domain is prescribed at the upstream boundary, corresponding to an initial velocity of $300\,\mathrm{m\,a^{-1}}$. Ice flows through a fixed calving front, where ice is subject to sea pressure. At the lateral boundaries, a free-slip condition is applied, and the flow velocity is subject to the Dirichlet boundary condition $\boldsymbol{u} \cdot \boldsymbol{n} = 0$, where $\boldsymbol{n}$ is the normal vector pointing outwards.

Ice in contact with the bed is subject to a non-linear Weertman-type friction law,

$$\boldsymbol{\tau}_{\mathrm{b}} = -C|\boldsymbol{u}_{\mathrm{b}}|^{m-1}\boldsymbol{u}_{\mathrm{b}}, \tag{10}$$

where $\boldsymbol{\tau}_{\mathrm{b}}$ is the basal shear stress, C is a constant friction coefficient, $\boldsymbol{u}_{\mathrm{b}}$ is the velocity tangential to the bed, and m is the friction law exponent. The position of the grounding line at each time step is determined by solving a contact problem (Durand et al., 2009). The continuous *first floating* Elmer/Ice grounding line numerical implementation is used (Gagliardini et al., 2016) and was chosen because a discontinuity in basal friction at the grounding line caused undesired numerical artefacts in the ice surface.

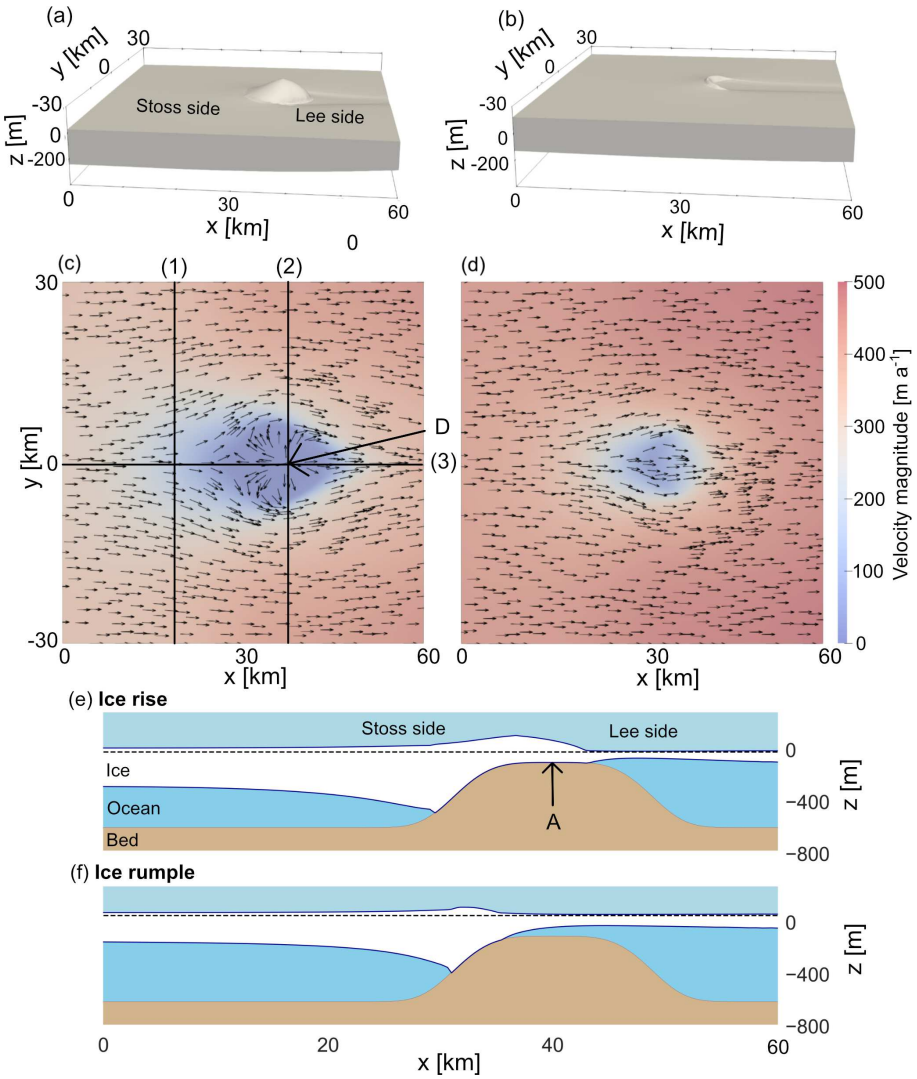

Figure 1: The 60 km × 60 km model domain is shown in the case of **(a)** an ice rise and **(b)** an ice rumple. A corresponding bird's eye view in **(c)** and **(d)** shows the surface velocity magnitude colour-coded and the ice flow direction with arrows. Corresponding along-flow cross-sections are shown in **(e)** and **(f)**. Sea level is at an elevation of 0 m in the case of the ice rise and 80 m in the case of the ice rumple. In **(c)**, (1), (2), and (3) indicate cross-sections used for analysis, and D is the ice rise dome. Both (2) and (3) are cross-sections through the ice rise dome. In **(e)**, A marks the highest point of the bed anomaly. The x direction corresponds with the along-flow direction, the y direction corresponds with the across-flow direction, and the z direction corresponds with the elevation.

Table 1: List of parameters used in the simulations.

Parameter	Symbol	Value	Unit
Rheological parameter	A	4.6×10^{-25}	$\mathrm{Pa}^{-3}\,\mathrm{s}^{-1}$
Ice temperature	T	-15	°C
Glen's exponent	n	3	
Accumulation rate	$\dot{a}_\mathrm{s}$	1.2	$\mathrm{m\,a}^{-1}$
Melt tuning parameter	α	0.76	
Glen's exponent	n	3	
Basal friction exponent	m	1/3	
Ocean density	ρ_w	1000	$\mathrm{kg\,m}^{-3}$
Ice density	ρ_i	900	$\mathrm{kg\,m}^{-3}$
Gravity	g	9.8	$\mathrm{m\,s}^{-2}$
Bed base	b_0	-580	m
Maximum bed height (above b_0)	M	500	m
Bed anomaly extent parameter	σ	8	km
Bed anomaly centre	(x_0, y_0)	$(40, 0)$	km
SIA basal drag exponents	(p, q)	$(3, 1)$	

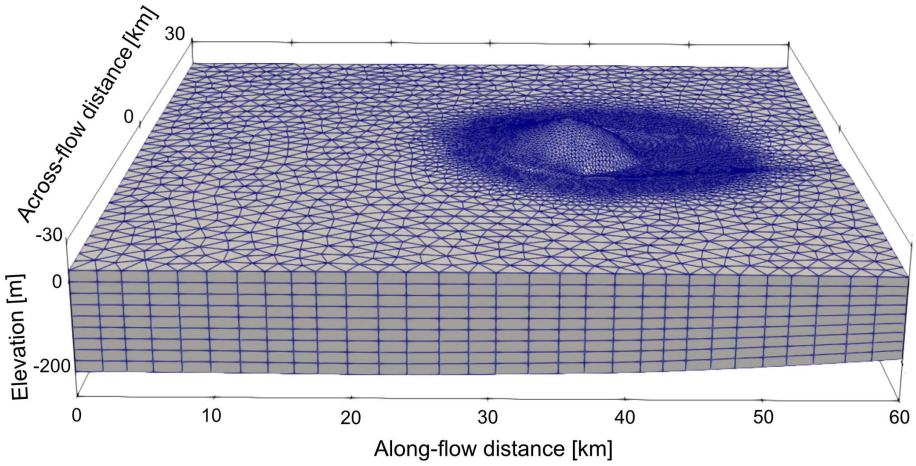

Figure 2: Shown is the mesh resolution. In the horizontal, the mesh is unstructured and has a resolution of 350 m in the area surrounding the ice rise or ice rumple. The background resolution (of the surrounding ice shelf) is 2000 m. The mesh is extruded in the vertical with 10 layers. Note that the geometry is exaggerated by a factor of 30 in the vertical direction.

2.2 Idealised model domain set-up

The evolution of ice rises and ice rumples is simulated in a 60 km × 60 km domain (Fig. 1). A bed anomaly is introduced and allows isle-type ice rises and ice rumples to form. The bed takes the form $b(x, y) = b_0 + b_\mathrm{a}$, where b_0 is a constant, and b_a is an anomaly with a flat top, defined as

$$b_\mathrm{a}(x, y) = M \exp\left\{\frac{-((x - x_0)^2 + (y - y_0)^2)^2}{2\sigma^4}\right\}. \tag{11}$$

The centre of the bed anomaly is located at (x_0, y_0), σ controls the horizontal extent, and M is the amplitude of the bed anomaly. The shape of the bed anomaly is broadly consistent with observations of ice rises, many of which have a plateau-shaped top that is near-horizontal (e.g. Derwael Ice Rise, Drews et al., 2015, and ice rises in the Fimbul Ice Shelf, Goel et al., 2020). All parameters used in the model are summarised in Table 1.

The ice thickness is initialised to 300 m throughout the domain, resulting in a geometry that is predominantly floating with a small grounded area at the bed anomaly. To ensure adequate resolution at the grounding line and ice divide, the mesh is refined in the area

encompassing the ice rise with a resolution of 350 m (Fig. 2). For this, we use the meshing software Mmg. This is in line with mesh resolution recommendations from other studies (Pattyn et al., 2013; Cornford et al., 2016) but is also the highest mesh resolution that is computationally feasible for the glacial–interglacial timescales considered here. To account for a possible migration of the ice rise, the radial extent of the area of high resolution is 5 km from the initial grounding line. In the remainder of the domain, a mesh resolution of 2000 m is used. The mesh is vertically extruded, resulting in 10 layers spaced equally apart, and the horizontal mesh size is kept constant throughout the simulations.

2.3 Shallow ice approximation (SIA) comparison

The shallow ice approximation (Hutter, 1983; Greve and Blatter, 2009) describes the flow of ice in the absence of longitudinal and transverse stress gradients and is composed of the deformational velocity ($\boldsymbol{u}_\mathrm{d}$) and basal sliding velocity ($\boldsymbol{u}_\mathrm{b}$) so that the total velocity is $\boldsymbol{u} = \boldsymbol{u}_\mathrm{d} + \boldsymbol{u}_\mathrm{b}$. In SIA, only the vertical shear stress gradients are considered so that the x-direction and y-direction deformational components of the velocity take the form

$$\boldsymbol{u}_\mathrm{d} = -2(\rho_\mathrm{i} g)^n \boldsymbol{\nabla} z_\mathrm{s} |\boldsymbol{\nabla} z_\mathrm{s}|^{n-1} \int_b^z A(T')(z_\mathrm{s} - \overline{z})^n \mathrm{d}\overline{z}. \tag{12}$$

We compare the velocity components only at the surface of the ice and also assume that temperature is constant, and so Eq. (12) reduces to

$$\boldsymbol{u}_\mathrm{d}(x, y, z_\mathrm{s}) = -\frac{2A(\rho_\mathrm{i} g)^n}{n+1}(z_\mathrm{s} - z_\mathrm{b})^{n+1} |\boldsymbol{\nabla} z_\mathrm{s}|^{n-1} \boldsymbol{\nabla} z_\mathrm{s}. \tag{13}$$

The x-direction and y-direction basal sliding components take the form

$$\boldsymbol{u}_\mathrm{b}(x, y) = -C_\mathrm{b}(\rho_\mathrm{i} g(z_\mathrm{s} - z_\mathrm{b}))^{p-q} |\boldsymbol{\nabla} z_\mathrm{s}|^{p-1} \boldsymbol{\nabla} z_\mathrm{s}, \tag{14}$$

where C_b is the basal friction coefficient and relates to the full Stokes basal friction coefficient, C, as follows:

$$C_\mathrm{b} = \frac{N_\mathrm{b}}{C^{1/m}} \tag{15}$$

with

$$N_\mathrm{b} = \rho_\mathrm{i} g(z_\mathrm{s} - z_\mathrm{b}), \tag{16}$$

where $N_\mathrm{b} = N_\mathrm{b} e_z$ is the basal normal stress. In Eq. (14), p and q are chosen for consistency with the non-linear Weertman-type friction law described above.

2.4 Comparison with the Vialov approximation

The Vialov profile (Vialov, 1958) is an analytical solution for an ice sheet profile in the case of a non-slip, flat-bed, and constant accumulation. The flow in an ice rise is predominantly radial from a point divide, and so we use a radial flux condition

$$\boldsymbol{\nabla} \cdot \boldsymbol{Q} = \frac{1}{R}\frac{\partial}{\partial R}(R\boldsymbol{Q}_\mathrm{R}) = \dot{a}_\mathrm{s}, \tag{17}$$

assuming no azimuthal variance. Here, $\boldsymbol{Q} = \boldsymbol{Q}_\mathrm{R} e_\mathrm{R}$ denotes the vertically integrated flux at a distance R from the origin (located at the ice rise divide). The resulting ice geometry profile is of the form

$$h(R) = h_0 \left[1 - \left(\frac{R}{L}\right)^{\frac{n+1}{n}}\right]^{\frac{n}{2n+2}}, \tag{18}$$

where

$$h_0 = 2^{\frac{n}{2n+2}} \left(\frac{\dot{a}_\mathrm{s}}{2A_0}\right)^{\frac{1}{2n+2}} L^{\frac{n+1}{n}} \tag{19}$$

and

$$A_0 = \frac{2A(\rho_\mathrm{i} g)^n}{n+2}. \tag{20}$$

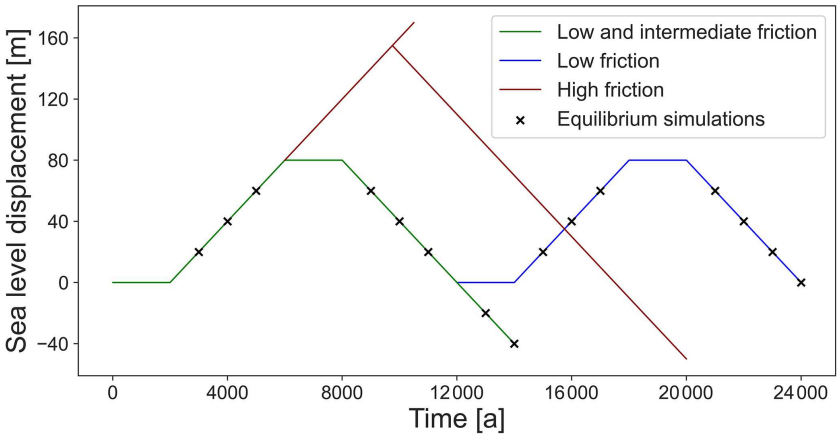

Figure 3: The change in sea level for the transient simulations. The low and intermediate scenarios follow the green curve. A second sea level increase-and-decrease cycle is performed for the low-friction scenario (blue). Sea level is increased to 170 m in the high-friction scenario, and a separate sea level decrease branch is simulated from 155 m (red curve). Sea level is increased and decreased at rates of $\pm 0.02\,\mathrm{m\,a^{-1}}$. The crosses indicate points in the low-friction scenario at which a steady-state branch is started with constant sea level in order to compare to the transient simulation.

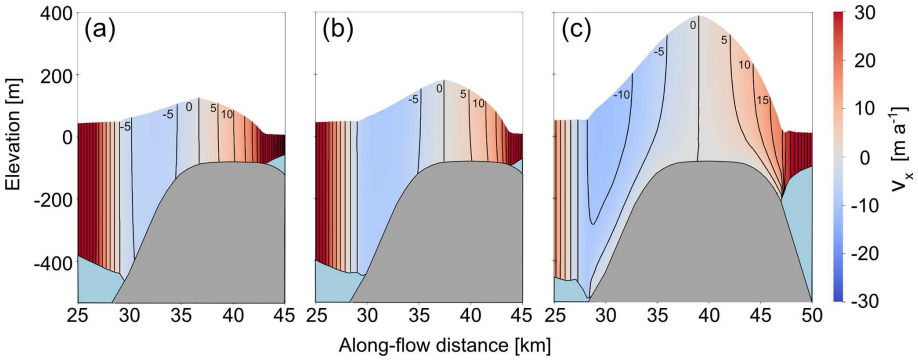

Figure 4: A cross-section of the ice rise in the along-flow direction for **(a)** the low-basal-friction, **(b)** the intermediate-basal-friction, and **(c)** the high-basal-friction scenarios. The contours show lines of equal velocity (full Stokes) in the x direction, i.e. in the along-flow direction.

L is the horizontal distance from the ice rise divide to the grounding line, and both h_0 and L are calculated from a reference point on the surface of the full Stokes simulation output.

We compare only the lee profile of the ice rises to the Vialov profile as the bed is relatively flat in this area, and we assume that small changes in bed topography are negligible. The profiles are compared for a central cross-section from the divide, extending in the along-flow direction into the ice shelf (Label (3) in Fig. 1c).

2.5 Design of transient simulations

To allow perturbation simulations to start from a steady-state geometry, all simulations are run for 2000 years under constant forcing. Simulations are performed for three different basal friction coefficients, $C = 3.812 \times 10^6$, $C = 7.624 \times 10^6$, and $C = 3.812 \times 10^8\,\mathrm{Pa\,m^{-1/3}\,s^{1/3}}$, which we refer to as *low*-, *intermediate*-, and *high*-friction scenarios, respectively. The intermediate-friction scenario has the same basal friction coefficient as that used in MISMIP (Pattyn et al., 2012) and in Favier and Pattyn (2015), where an ice rise is also modelled. The low-basal-friction coefficient is close to the suggested value of $3.16 \times 10^6\,\mathrm{Pa\,m^{-1/3}\,s^{1/3}}$ in MISMIP+

(Cornford et al., 2020). The high-basal-friction scenario essentially excludes basal sliding, mimicking ice frozen to the bed. For each basal friction coefficient, transient simulations with variable sea level are performed (Fig. 3). In the low- and intermediate-basal-friction scenarios, sea level is increased by 80 m at a rate of $0.02\,\mathrm{m\,a^{-1}}$ over 4000 years and then stays constant for another 2000 years. Sea level is then decreased at a rate of $0.02\,\mathrm{m\,a^{-1}}$ back to the initial level followed by a second phase of constant sea level for 2000 years. A second cycle is performed for the low-basal-friction scenario for a comparison with the first cycle. Branches of the low-basal-friction simulation are run to steady state (equilibrium) at discrete intervals while keeping sea level fixed. We run these simulation branches in order to understand how far from steady state the transient simulations are. The choice of sea level perturbation rate is in line with observations, showing periods of sea level rise of up to $0.04\,\mathrm{m\,a^{-1}}$ during the last deglaciation (Deschamps et al., 2012). Furthermore, we run branches of the simulation beyond the original sea level at the same sea level decrease rate of $0.02\,\mathrm{m\,a^{-1}}$.

In the low and intermediate scenarios, the ice rises transition to ice rumples at some stage during the sea level increase. In the high-friction scenario, no such transition occurs after a sea level increase of 80 m. We therefore continue the increase in sea level further at a constant rate of $0.02\,\mathrm{m\,a^{-1}}$ until the transition occurs. A reversal of the sea level perturbation is performed from a height of 155 m above the initial sea level.

3 Results

3.1 Steady-state analysis before sea level perturbation

After 2000 years of spin-up time, ice rises with a characteristic local flow regime develop in all three full Stokes scenarios (Fig. 4). From low to high friction, they vary in maximum thickness ($H_{\max} = 213$–$468\,\mathrm{m}$), grounded area (132–$225\,\mathrm{km^2}$), and characteristic timescale ($t_\mathrm{c} = 178$–$391\,\mathrm{a}$, defined as $t_\mathrm{c} = H_{\max}/\dot{a_s}$). The characteristic timescale is a metric that gives an indication of the rate of development of Raymond arches (Martín et al., 2009; Goel et al., 2020). The ice divide position in the high-friction scenario has a stossward offset of 0.9 km from the vertical symmetry axis of the bed protrusion. In the intermediate- and low-friction scenarios it is shifted stossward by 2.7 and 3.3 km, respectively. In all three cases, there is substantially more grounding on the stoss side of the bed protrusion than on the lee side.

Topographic and flow divides coincide in all three cases, and ice rise surface velocities are within tens of metres per year. There is negligible basal sliding in the high-friction scenario (with average absolute velocities of roughly $0.5 \times 10^{-4}\,\mathrm{m\,a^{-1}}$ at the bed–ice interface), whereas basal sliding in the along-flow cross-section (Label (3) in Fig. 1c) accounts for 90 % and 98 % of the local mean horizontal velocities in the intermediate- and low-friction scenarios, respectively. The width of the lateral shear zones, here defined as the lateral distance from the grounding line along a cross-section (Label (2) in Fig. 1c) in which v_x reaches 90 % of v_x at the domain boundary, varies marginally from 10 to 11.3 km from the low- to the high-friction scenarios. Ice fluxes upstream of the protrusion are approximately equal, but mean velocities are 15 % slower, and ice is about 15 % thicker in the high-friction scenario compared with the low-friction scenario.

All ice rises exhibit geometries and flow regimes which are comparable to observations. For example, the high-friction scenario is comparable to Derwael Ice Rise, where previous studies have assumed no basal sliding a priori (e.g. Drews et al., 2015). Basal sliding in the low- and intermediate-basal-friction scenarios means these ice rises are more susceptible to transition into ice rumples when sea level is raised, as shown later.

The comparison of full Stokes surface velocities to SIA surface velocities on ice rises illustrates where the local flow assumptions are violated. Figure 5 shows that all three basal friction scenarios have mismatches near the ice rise divides where longitudinal stress gradients are significant. The high-basal-friction scenario shows a good fit otherwise, as do the low- and intermediate-basal-friction scenarios on the lee sides. However, for these cases, surface velocities differ more on the stoss sides of the ice rises (Fig. 6). In the low-friction scenario, absolute deviations increase from 0 %–20 % in the vicinity of the divide (but not at the divide) to over 100 % closer to the grounding line. In the intermediate-friction scenario,

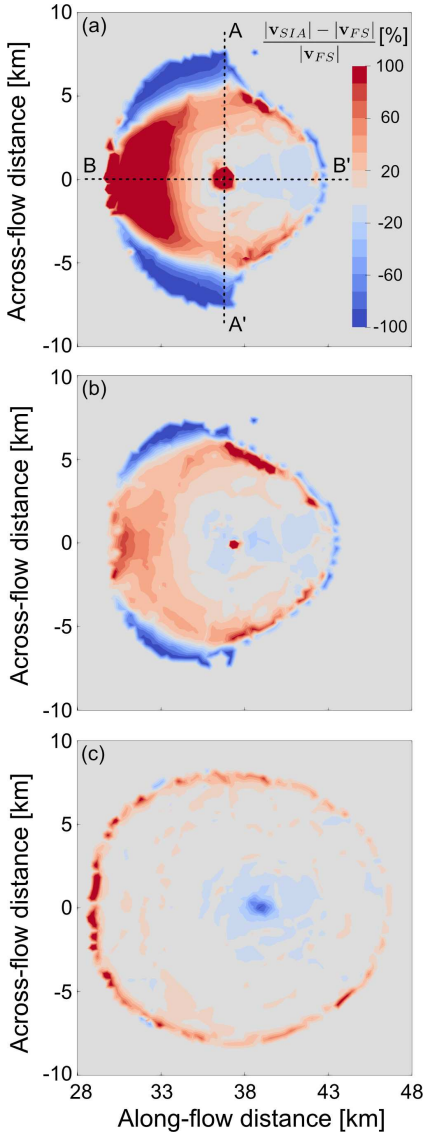

Figure 5: A bird's eye view of the grounded area corresponding to the steady states at $t = 2000$ years of the simulations with **(a)** a low-basal-friction, **(b)** an intermediate-basal-friction, and **(c)** a high-basal-friction scenario. In colour, the percentage difference is shown between the calculated SIA surface velocity magnitude and the full Stokes velocity magnitude.

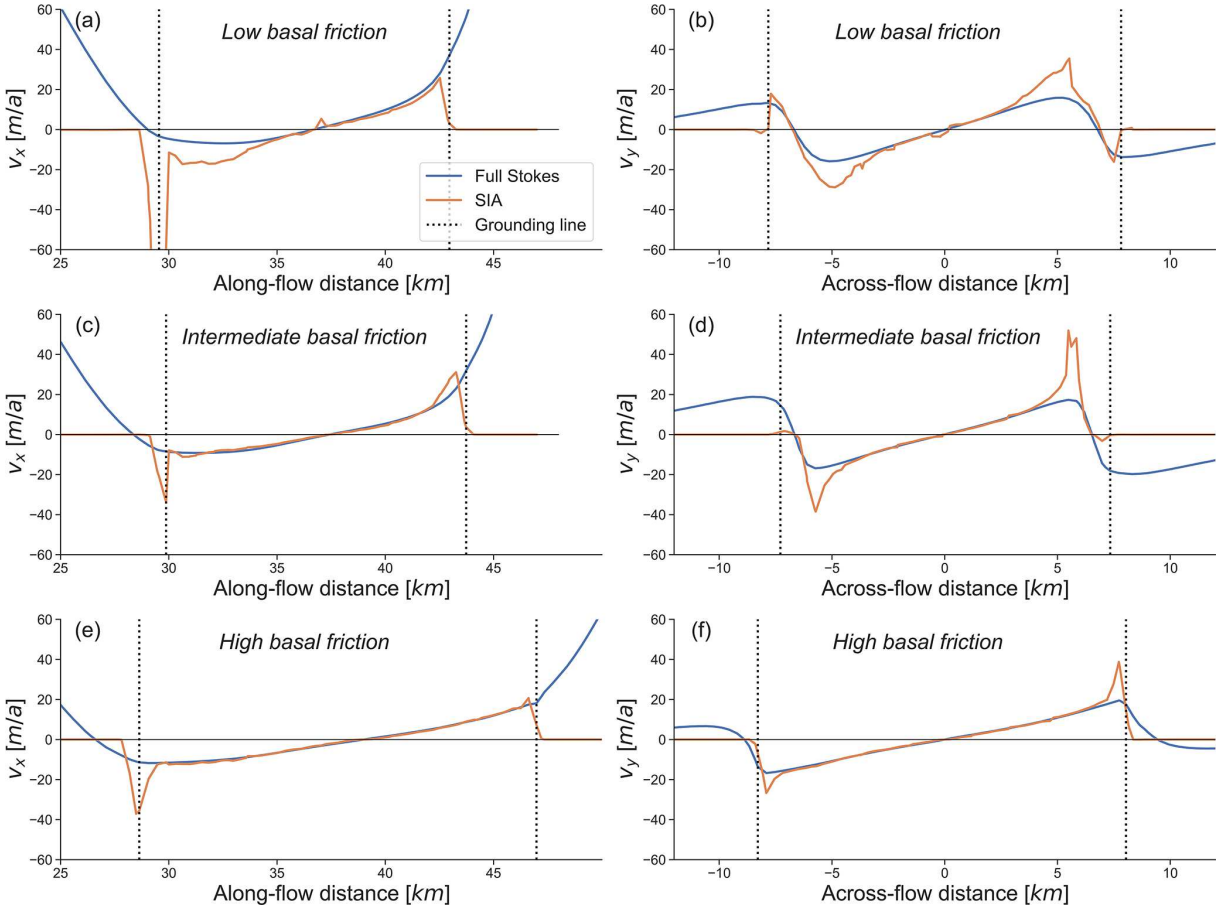

Figure 6: The full Stokes and SIA surface velocities at $t = 2000$ years in the along-flow direction (**a**, **c**, and **e**) and in the across-flow direction (**b**, **d**, and **f**), as indicated by the cross-sections A–A′ and B–B′ through the divide in Fig. 5. Panels **(a)** and **(b)** show the low-basal-friction scenario, **(c)** and **(d)** show the intermediate-basal-friction scenario, and **(e)** and **(f)** show the high-basal-friction scenario.

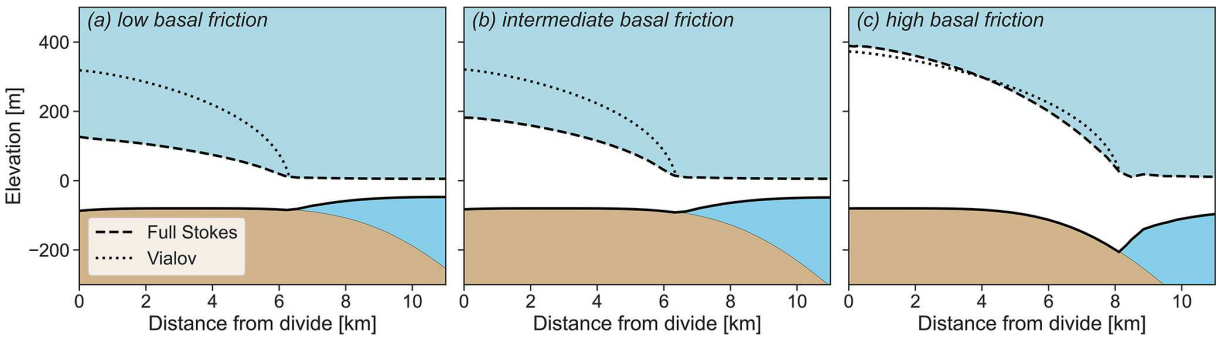

Figure 7: Cross-sections of the full Stokes simulations at $t = 2000$ years in the case of the **(a)** low-, **(b)** the intermediate-, and **(c)** the high-basal-friction coefficient. Using a reference point on the ice surface at the grounding line, a Vialov profile is calculated and plotted.

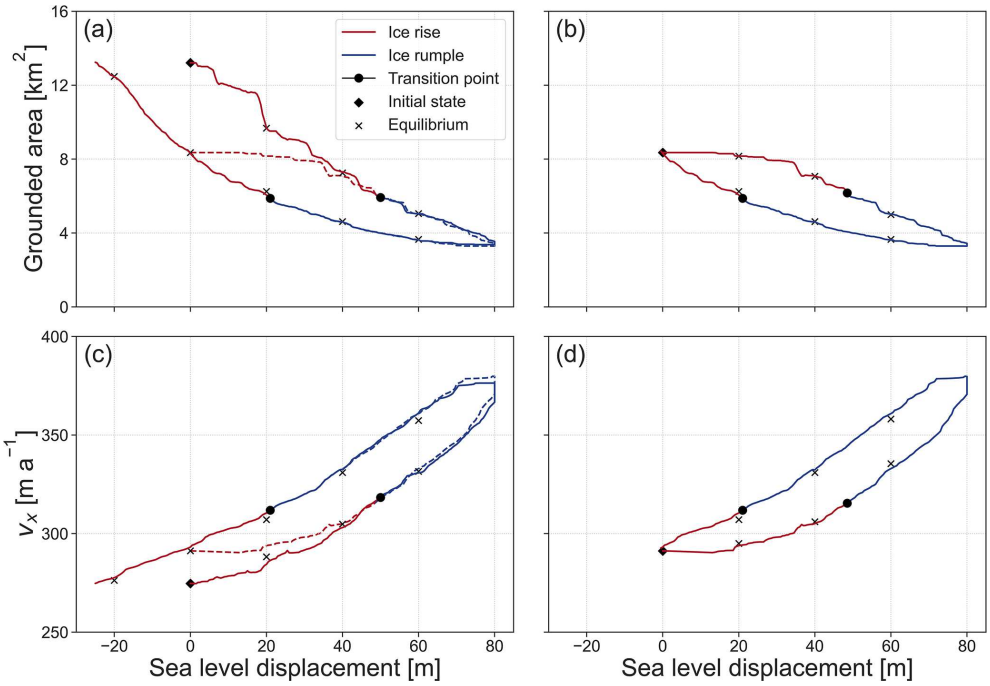

Figure 8: The response of grounded area and upstream ice shelf velocity to sea level perturbation in the case of low basal friction. Panels **(a)** and **(c)** show the evolution for the first sea level increase-and-decrease cycle in blue and red. Panels **(b)** and **(d)** show the evolution for the second increase-and-decrease cycle. These curves are also plotted in panels **(a)** and **(c)** with dashed red and blue lines for comparison. The crosses represent the results of steady-state branches of the transient simulations at corresponding sea levels. The transition from ice rise to rumple and vice versa is represented by the black dots and a change in colour of the curve.

deviations are not quite as significant but nonetheless reach deviations of 100 %. In terms of ice thickness, the Vialov approximation captures the high-friction scenario well despite the non-flat bed, while it significantly overestimates the low- and intermediate-basal-friction scenarios in which basal sliding is dominant (Fig. 7).

3.2 Ice-rise-to-ice-rumple transitions triggered by sea level variation

To understand the response of ice rises and ice rumples with differing basal friction to sea level perturbation, we analyse the grounded area (Figs. 8a, b and 9a), dome migration (Fig. 10), lee-side grounding line position, and the upstream ice shelf velocities (Figs. 8c, d and 9b). The upstream ice shelf velocity is defined as the mean velocity of ice in the x direction at $x = 20\,\mathrm{km}$, as marked by Label (1) in Fig. 1c. In terms of these metrics, the low- and intermediate-basal-friction scenarios behave distinctly differently than the high-basal-friction scenario. The former transition gradually to ice rumples if sea level is raised past a certain threshold and regrow into ice rises if sea level is reversed. The reversal is not symmetric, and the respective steady-state geometries depend on the history of their evolution (i.e. hysteresis). The high-basal-friction scenario, on the other hand, requires a much larger sea level perturbation to trigger transition into an ice rumple. Once this transition is reached, an ice rumple forms, but the system is unstable, and the ice rumple ungrounds entirely. Details of these differing states are provided in the following.

Before transitioning to an ice rumple, the dome position in the low-friction scenario migrates linearly at a rate of $1.7\,\mathrm{m\,a^{-1}}$ with increasing sea level (Fig. 10). The dome of the intermediate-friction ice rise migrates first at a rate of $0.8\,\mathrm{m\,a^{-1}}$ before increasing to a migration rate of $5.7\,\mathrm{m\,a^{-1}}$ after a sea level increase of 29 m. The dome of the high-basal-

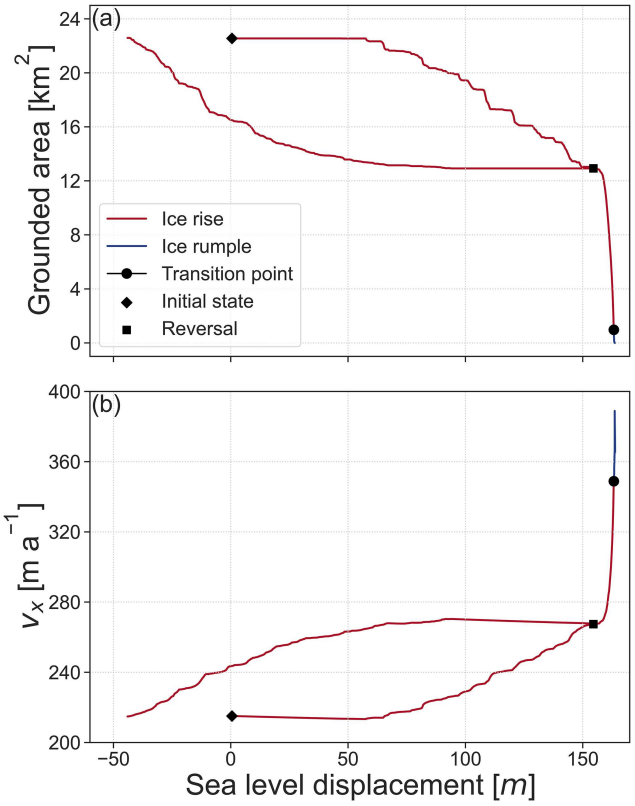

Figure 9: The response of grounded area and upstream ice shelf velocity to sea level perturbation in the case of high basal friction. In **(a)**, the grounded area is plotted against sea level displacement, and in **(b)**, the average velocity in the x direction in a cross-section upstream of the ice rise (at 20 km from the influx boundary) is plotted against sea level displacement. Red indicates that the system exhibits a characteristic flow regime of an ice rise, and blue indicates that of an ice rumple. The square indicates from where a reversal of the sea level perturbation is simulated.

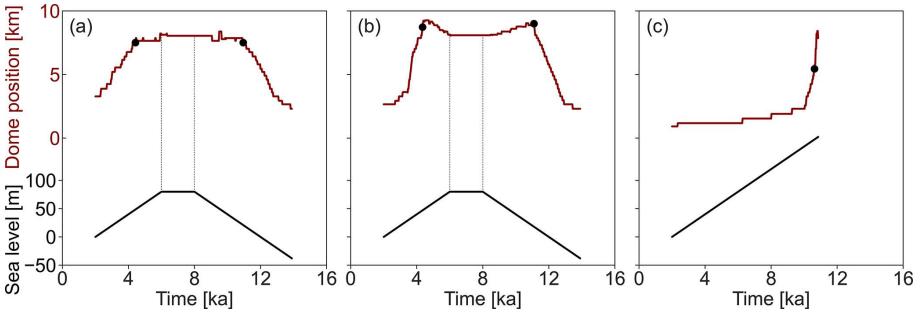

Figure 10: The response of the dome position to a raising and lowering of sea level in the case of **(a)** the low-, **(b)** the intermediate-, and **(c)** the high-basal-friction coefficients.

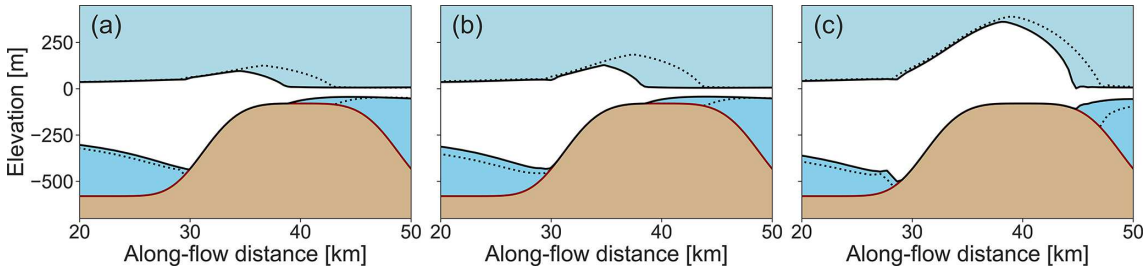

Figure 11: The figures show a cross-section of the ice rises in the along-flow direction for **(a)** the low-, **(b)** the intermediate-, and **(c)** the high-basal-friction scenario. The dotted lines show the geometry of the ice rises before sea level perturbation, and the solid lines show the geometry after a full cycle of sea level increase and decrease.

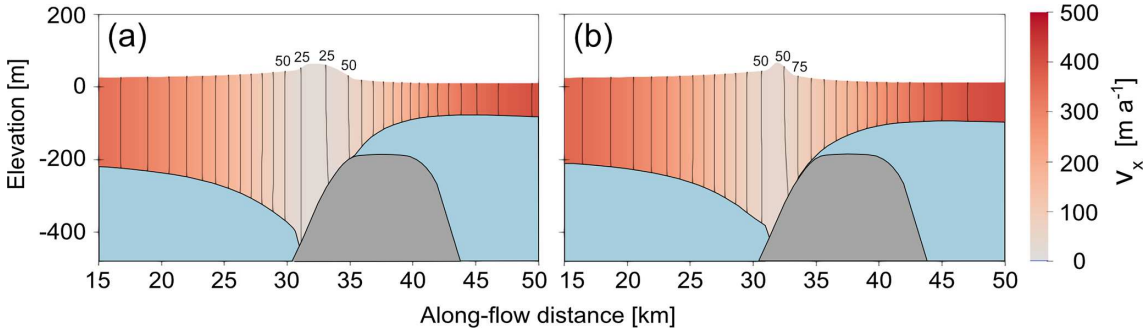

Figure 12: An along-flow cross-section of the ice rumple at $t = 8000$ years in the case of **(a)** the low-basal-friction and **(b)** the intermediate-basal-friction scenario. The contours show lines of equal velocity in the x direction and are spaced 25 m a^{-1} apart.

friction ice rise exhibits a slow response to sea level displacement during the first 152 m of sea level increase with a divide migration rate of 0.2 m a^{-1}, before increasing to a migration rate of 5.0 m a^{-1}.

After a sea level increase of 20 m in the case of the low-friction case, 30 m in the case of the intermediate-friction case, and 161 m in the high-friction case, the grounding line on the lee side of the ice rise migrates past the highest point of the bed anomaly (marked by A in Fig. 1e) and so is located on a retrograde slope. A transition from ice rise to ice rumple occurs at a further sea level displacement of 30, 16, and 1 m after the grounding line has reached this point in the case of the low-, intermediate-, and high-basal-friction scenarios, respectively.

A steady acceleration of the upstream ice shelf is seen in both the low- and intermediate-basal-friction scenarios, and there is no abrupt change once a transition from ice rise to ice rumple has occurred (Fig. 8). This is in contrast to the high-basal-friction scenario, where there is an abrupt change in the upstream ice shelf velocity as a transition from ice rise to ice rumple is approached.

After keeping the sea level constant for 2000 years at a sea level perturbation of 80 m, the low- and intermediate-basal-friction ice rumples evolve to their respective steady states, with minimum velocities of 20 and 38 m a^{-1} (Fig. 12). Reversal of the sea level perturbation then triggers an asymmetric reversal of the variables of interest described above, with grounded area and upstream ice shelf thickness increasing and upstream velocity decreasing. A transition from ice rumple to ice rise (Figs. 8 and 1) is observed when sea level is 21 and 19 m above the initial sea level in the low- and intermediate-basal-friction scenarios, respectively (as opposed to displacements of 50 and 45 m for low- and intermediate-basal-friction scenarios in the sea-level-increase scenarios, respectively). Once the original sea level is again reached, the ice rises in both the low- and intermediate-basal-friction scenarios are smaller, with a smaller grounded area and a lesser buttressing effect on the upstream ice shelf (Figs. 8, 1, and 11). The upstream ice shelf in the case of the low-basal-friction

scenario has a decrease in velocity of $18\,\mathrm{m\,a^{-1}}$, whereas the ice shelf in the intermediate-basal-friction scenario decreases in velocity by $25\,\mathrm{m\,a^{-1}}$. A second cycle of sea level increase and decrease is performed for the low-basal-friction scenario starting from the steady states that emerged from the previous sea level perturbation cycle. The response of the grounded area and ice shelf velocity is calculated as described above and presented in Fig. 8. The hysteresis cycle is now closed, with the final steady state corresponding to the state before the last sea level perturbation cycle.

When sea level rise is halted in the high-basal-friction scenario prior to the unstable grounding line retreat (here at a sea level perturbation of 155 m), the ice rise volume and grounded area also recover asymmetrically, resulting in two differing states for a given sea level displacement (Fig. 9).

We investigate the migration of the stoss- and lee-side grounding lines of the ice rise and make a comparison with the grounding line position in the case of hydrostatic equilibrium (video in the Supplement). The maximum differences in position are 0.5 km on the stoss side and 0.4 km on the lee side, with mean differences of 0.2 km in both cases. During sea level increase, the hydrostatic grounding line positions have a delayed response in comparison with the Elmer/Ice grounding line. On the other hand, during sea level decrease, the hydrostatic grounding lines have a more rapid response.

4 Discussion

4.1 The influence of basal sliding on the geometry and transient behaviour of ice rises

A number of previous studies have argued that basal sliding near ice rise divides is negligible because thermomechanically coupled models often predict ice significantly below the freezing point at the ice–bed interface near the summits (Martín et al., 2009; Drews et al., 2015; Goel et al., 2020) and because many ice rises exhibit isochronal features called Raymond arches, which do not form if basal sliding is dominant (Pettit et al., 2003; Martín et al., 2009). However, low and intermediate scenarios can be relevant in areas where Holocene marine sedimentation results in basal sliding in areas which have regrounded (Pollard et al., 2016). Moreover, differences between observed and simulated Raymond arches under a frozen bed assumption may indicate a delay or suppression of arch growth due to past or present basal sliding (Kingslake et al., 2016).

The simulations show that ice rises can form in scenarios where basal sliding is significant. Surface velocities in the low and intermediate scenarios are within a few metres per years near the crests, similar to the predictions in the high-friction scenario (Fig. 5). In this regard, surface velocities alone are a poor indicator for the presence or absence of basal sliding on ice rises. However, the geometries between the three scenarios differ significantly, and only the high-friction scenario can be adequately approximated with the Vialov profile, whereas the low and intermediate scenarios exhibit significant misfits (Fig. 8). This means that a simple fit with a Vialov profile can serve as a first-order metric for the absence or existence of basal sliding for specific ice rises. This is important, as the degree of basal sliding in the vicinity of the grounding line determines the local ice flow and the ice rise's transient behaviour in response to sea level perturbation. When comparing the grounding line positions of the full Stokes model and the hydrostatic grounding line position, we find that differences are small. However, over the millennial timescales considered here, together with the compounding effect of the small errors in grounding line position at each time step, it is possible that a hydrostatic assumption may result in differing ice rise and ice rumple geometries as well as a differing transition point.

Many ice rises are fully surrounded by ice shelves, and the extent to which isle-type ice rise velocities are affected by longitudinal and shear stresses transferred from the upstream ice shelf is not fully clear. This effect is analysed here using the differences between the non-local full Stokes simulations and the fully local SIA. The flow regime in the high-friction scenario is, to a large extent, independent of the surrounding ice shelf. In the low- and intermediate-basal-friction scenarios, however, the differences between full Stokes and SIA

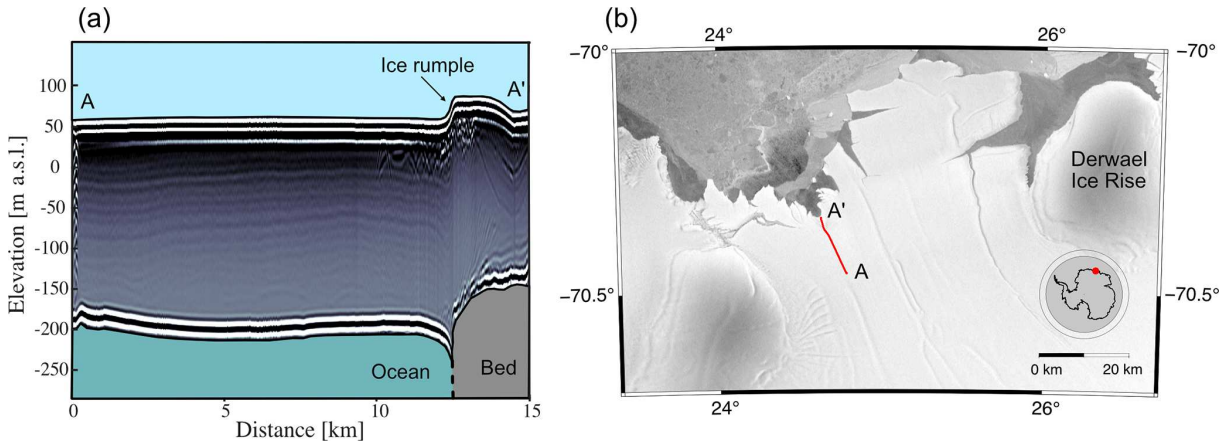

Figure 13: An along-flow ground-based radargram (Drews, 2019) showing an ice rumple in the Roi Baudouin Ice Shelf, East Antarctica, is shown in **(a)**. The flow of ice is from left (A) to right (A′). In **(b)**, the location of the radargram (A–A′) is shown (Jezek, 2003).

are greater and are especially evident on the stoss side of the ice rise. The greater velocity differences in the lower-friction scenarios show that these ice rises are influenced more by the stresses in the surrounding ice shelf. Implications for the presence or absence of a fully local flow regime are twofold: (1) if basal sliding is negligible even in areas close to the grounding zone, then SIA is an appropriate modelling framework, for example, when investigating the surface accumulation history using inverse methods (Callens et al., 2016), and (2) the basal boundary condition determines an ice rise's response to sea level perturbation.

The low- and intermediate-friction scenarios respond immediately to a rising sea level, with a retreat of the leeward grounding line accompanied by a stossward migration of the dome position. The ice rises progressively thin and eventually transition into ice rumples. There is no significant threshold behaviour between these two states, and once the sea level increase is halted, the system converges to a steady-state ice rumple with the lee-side grounding line located on the retrograde slope at the edge of the basal plateau. The summits are a few tens of metres above the ice shelf surface, and the overall geometry is consistent with, for example, the ice rumple located in the Roi Baudouin Ice Shelf (Fig. 13). The minimum overriding velocities of $20\,\mathrm{m\,a^{-1}}$ are, however, significantly faster than the example observed at the Roi Baudouin Ice Shelf, where the ice is effectively stagnant (Berger et al., 2016). The smooth transition of the low- and intermediate-friction ice rises into ice rumples reflects their strong coupling to the surrounding ice shelf, highlighted previously. From a larger-scale perspective there are no critical differences between ice rises and ice rumples in those scenarios other than the switch from a local to an overriding flow regime.

Conversely, the high-friction case only transitions to an ice rumple for sea level perturbations that are greater than what is expected in a glacial–interglacial cycle. In fact, there is no noticeable change in grounded area even for a sea level displacement of 50 m. This stability is in line with, for example, ice promontories at the Ekström Ice Shelf, which show a comparatively weak response to the thinning of their surrounding ice shelves (Schannwell et al., 2019). Grounding line retreat rates for higher sea level displacements then remain moderate as long as the leeward side remains grounded on a prograde slope. On a retrograde slope the ice rise becomes unstable, and complete ungrounding occurs. We therefore conclude that after a transition from ice rise, there is a threshold basal friction beyond which a steady-state ice rumple cannot form.

Interestingly, the low-friction ice rumple exhibits lower minimum velocities than the intermediate-friction ice rumple, most likely due to a greater grounded area (Fig. 12), and it is worth investigating whether inverse techniques used to predict the basal friction coefficient beneath pinning points produce results which remain valid regardless of horizontal resolution applied.

The required sea level perturbation for ungrounding clearly depends on the elevation below sea level of the bed protrusion, but the scenarios shown here with a maximum bed

elevation of 80 m below sea level have many real-world counterparts (e.g. Kupol Moskovskij, Kupol Coilkovskogo, Leningrad Ice Rise, Djupranen Ice Rise – Goel et al., 2020; Derwael Ice Rise – Drews et al., 2015). Our study suggests that features with a high basal friction have been and will remain stable local flow features even for comparatively large sea level perturbations. Moreover, it shows that ice rumples with comparatively low surface velocities as in the example provided in Fig. 13 are very unlikely a result of a deglaciated ice rise. An area that requires more investigation is the case of ice rises which do not conform to the plateau-shaped bed topography as prescribed here. The unstable retreat predicted in the high-basal-friction scenario suggests that ice rises located on retrograde slopes are critically less stable for an equal amount of sea level displacement.

4.2 The hysteretic behaviour of ice rises over glacial cycles

In all basal friction scenarios, there are two differing ice rises for a given sea level (Figs. 8 and 9). These pairs differ in the basal melt rate applied (which is thickness-dependent) and in the grounded area. Each pair corresponds to a low- and a high-buttressing case for which the averaged upstream ice velocity is used as a proxy (Figs. 8c, d, 9b, and 1b in the Appendix).

There is a difference in the individual pairs, with the grounded area being larger in the sea-level-increase scenario than in the sea-level-decrease scenario. In all cases, the pairs occupy virtually the same region on the obstacle's stoss side, but the extent of grounding on the plateau differs (Fig. 11). The thickness and slopes at the respective grounding lines are comparable, and therefore differences in basal melt (as parameterised in Eq. 9) are small, with differences of only 3.5 %, 3.0 %, and 2.4 % in the low-, intermediate-, and high-friction scenarios, respectively. The dynamic differences therefore stem mostly from the differing grounded areas that result in a differing form of drag (Still et al., 2019) and consequently a differing net resistance to the upstream ice shelf.

A self-stabilising feedback occurs, with divide migration opposing grounding line retreat in a sea-level-increase scenario. The ice rise height reduces, and the divide migrates stossward during lee-side grounding line retreat. Because the divide moves stossward, the area of accumulation adjacent to the divide on the lee side of the ice rise increases. The increased accumulation area promotes an increased flux across the grounding line, opposing grounding line retreat. Analogously, sea level decrease results in leeward divide migration. The resulting reduction in accumulation area adjacent to the divide on the lee side of the ice rise opposes grounding line advance. The existence of negative feedback mechanisms in both the sea-level-increase and sea-level-decrease scenario results in hysteretic behaviour (Figs. 8, 9 and 1).

Another mechanism that plays a role is the sensitivity of the grounding line to bed shape, with hysteretic behaviour occurring due to the positioning of retrograde and prograde slope segments (Schoof, 2007; Pattyn et al., 2012; Haseloff and Sergienko, 2018; Sergienko and Wingham, 2022). In our study, we also observe grounding line migration patterns linked to the shape of the three-dimensional bed protrusion. Consequently, it matters how the ice rise and ice rumple geometries are initialised to begin with.

Although in our study, we have used a constant surface accumulation, we would expect orographic precipitation to enhance the hysteretic behaviour. In future work it is worth investigating whether effects such as an increased melt rate also produce a hysteretic response in ice rises and ice rumples. Given that the grounded area and basal sliding determine the ice rise evolution, future simulations should include a more informative guess of the basal friction coefficients guided by, for example, seismic studies determining the bed properties (Smith et al., 2015). Inversion of the basal friction parameters from a thermomechanically coupled full Stokes model (Schannwell et al., 2019, 2020) does provide some information in this regard but also contains lumped uncertainties, e.g. from ice rheology and uncertain boundary conditions. Another process not considered here is changes in the bed protrusion through glacial isostatic adjustment (Kingslake et al., 2018; Wearing and Kingslake, 2019).

The existence of multiple steady states means that the grounding lines of ice rises and ice rumples observed today are dependent on the local ice flow history during the last glacial cycle. Inversely, the dynamics and buttressing effect of ice rises and ice rumples are

dependent on the initial geometry prescribed, which is typically unknown. The degree of buttressing is of importance for determining the stability and evolution of the continental grounding line (Favier and Pattyn, 2015; Reese et al., 2018). The representation of ice shelves has been identified as a key cause of continental-scale model spread (Seroussi et al., 2019), and a precise representation of ice rises and ice rumples would reduce spin-up and projection uncertainties.

We have shown that the difference between the simulated grounding line and the hydrostatic equilibrium grounding line is small at each time step. This small error may, however, lead to an error propagation during transient simulation, leading to inaccurate grounding line migration if a hydrostatic equilibrium assumption is used.

5 Conclusions

We examined the effect of basal friction and sea level variation on the evolution of ice rises and ice rumples using idealised simulations including the surrounding ice shelves. In a high-basal-friction scenario, there is negligible mismatch when comparing simulated steady-state full Stokes velocities with steady-state SIA velocities, whereas in a low-basal-friction scenario the mismatch is larger due to stronger mechanical coupling to the surrounding ice shelf. The locality of the ice flow and the degree of basal sliding can be diagnosed by examining the (mis-)fit of a Vialov profile to the observed thickness profile. In response to an increasing sea level, a transition from ice rise to ice rumple occurs. Steady-state ice rumples form in the low-basal-friction scenarios, whereas the ice rumple in the high-friction scenario is ephemeral and ungrounds rapidly. The higher-friction ice rise, on the other hand, is largely unresponsive to sea level variations, requiring more than double the sea level rise to trigger the transition compared to the lower-friction scenarios.

All basal friction scenarios show self-stabilising, hysteretic behaviour, with grounded area and upstream ice shelf buttressing dependent on the evolution history. As a consequence of this behaviour, we identify the importance of perturbation history for the formation of the correct feature. Although in our study, we have concentrated only on the response of ice rises to sea level perturbation, further processes such as an increase in basal melt are also likely to result in hysteretic and potentially irreversible behaviour in ice shelf buttressing upstream of ice rises.

A Appendix

A.1 The response of the grounded area and ice shelf velocity to sea level perturbation in the intermediate-basal-friction scenario

Presented in Fig. 1 is the response of the grounded area and upstream velocity to sea level perturbation in the case of the intermediate-basal-friction scenario ($C = 7.624 \times 10^6\,\mathrm{Pa\,m^{-1/3}\,s^{1/3}}$). The transition from ice rise to ice rumple occurs at a sea level displacement of 19 m, and the transition from ice rumple to ice rise occurs at a sea level displacement of 45 m, compared with 21 and 50 m, respectively, in the low-basal-friction scenario. Interestingly, the grounded area of the ice rumple follows a rather linear path in the intermediate-basal-friction scenario compared with the low-basal-friction scenario.

A.2 Comparison between the first floating and discontinuous grounding line numerical implementations

In the case of the low-basal-friction scenario, we have run equivalent simulations using a differing grounding line numerical implementation, namely the *discontinuous* method (Fig. 2). At the grounding line, basal friction is applied if the other two nodes in the element are also grounded, and a free-slip condition is applied if the other two nodes are ungrounded. The first floating numerical implementation, however, assumes a free-slip condition at the grounding line, and a linear reduction in basal friction between it and the upstream node is applied. Although the discontinuous numerical implementation has been shown to have the

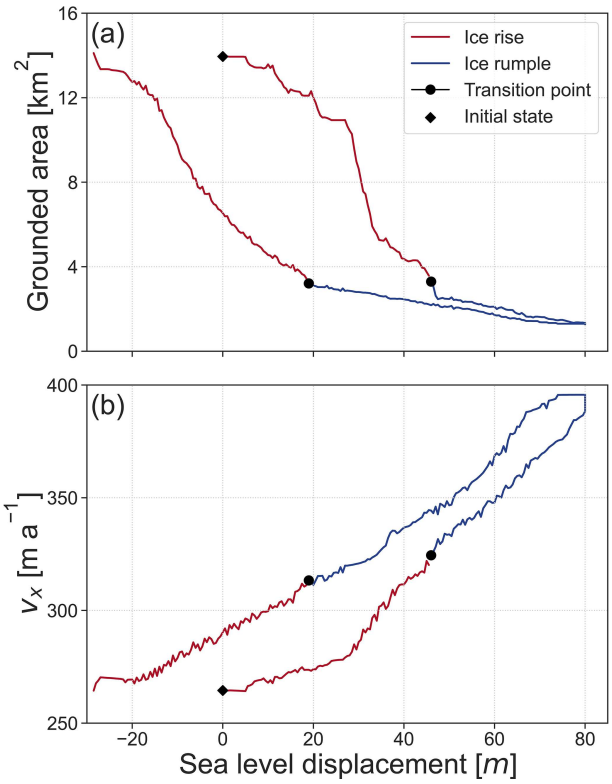

Figure 1: The response of the grounded area and ice shelf velocity to sea level perturbation in the intermediate-friction scenario. In **(a)**, the grounded area is plotted against sea level displacement, and in **(b)**, the average velocity in the x direction in a cross-section upstream of the ice rise (at 20 km from the influx boundary) is plotted against sea level displacement. Red indicates that the system exhibits a characteristic flow regime of an ice rise, and blue indicates that of an ice rumple.

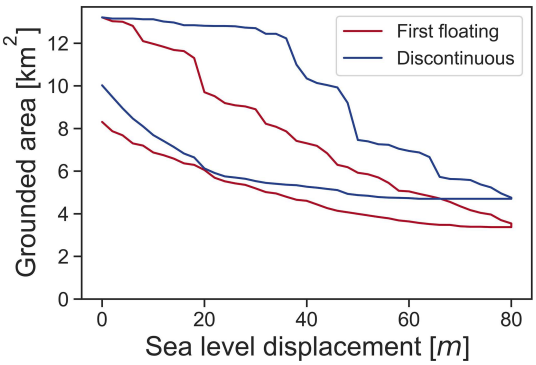

Figure 2: Shown is the response of the grounded area in the low-friction case of the first floating (red) and discontinuous (blue) Elmer/Ice numerical grounding line implementations.

least dependence on mesh resolution, it can be argued that the first floating is more plausible physically, with effective pressure disappearing at the grounding line (Gagliardini et al., 2016). The simulations show that regardless of the numerical implementation, hysteresis occurs.

Code availability

The code used to run the simulations and the post-processing code can be found at doi:10.5281/zenodo.7044134 (Henry et al., 2022a). The Elmer version is version 8.4 (revision 1c584234).

Data availability

The model output data are available for download (https://www.wdc-climate.de/ui/entry?acronym=ICERISE_Hysteresis; Henry, 2022).

Video supplement

A supplementary video is provided, showing the evolution of an ice rise in response to sea level perturbation as well as the position of the grounding line if the system were in hydrostatic equilibrium (DOI: 10.5446/56713; Henry et al., 2022b).

Author contribution

ACJH, CS, and RD conceived the idea for the study and designed the experiments. ACJH performed the simulations and analysis with support from all authors. The manuscript was written by ACJH with contributions from all authors.

Acknowledgements

This work used resources of the Deutsches Klimarechenzentrum (DKRZ) granted by its Scientific Steering Committee (WLA) under project ID bm1164. The authors gratefully acknowledge the Gauss Centre for Supercomputing e.V. (https://www.gauss-centre.eu, last access: 19 August 2022) for funding this project by providing computing time on the GCS Supercomputer SuperMUC-NG at Leibniz Supercomputing Centre (https://www.lrz.de, last access: 19 August 2022). Data for Fig. 13 (Drews, 2019) were collected with the support of the InBev Baillet Latour Antarctica Fellowship with logistic support from the International Polar Foundation.

Financial support

A. Clara J. Henry was supported by the Deutsche Forschungsgemeinschaft (DFG) in the framework of the priority programme 1158 "Antarctic Research with Comparative Investigations in Arctic Ice Areas" by grant SCHA 2139/1-1. Clemens Schannwell was supported by the German Federal Ministry of Education and Research (BMBF) as a Research for Sustainability initiative (FONA) through the PalMod project under the grant number 01LP1915C. Reinhard Drews and Vjeran Višnjević were supported by an Emmy Noether grant of the Deutsche Forschungsgemeinschaft (DR 822/3-1). The article processing charges for this open-access publication were covered by the Max Planck Society.

References

Mmg platform. `http://www.mmgtools.org/, version 5.3.10`. Accessed: 17-06-2022.

T. Albrecht, R. Winkelmann, and A. Levermann. Glacial-cycle simulations of the antarctic ice sheet with the parallel ice sheet model (pism) – part 1: Boundary conditions and climatic forcing. *The Cryosphere*, 14(2):599–632, 2020. doi: 10.5194/tc-14-599-2020. URL `https://tc.copernicus.org/articles/14/599/2020/`.

V. R. Barletta, M. Bevis, B. E. Smith, T. Wilson, A. Brown, A. Bordoni, M. Willis, S. A. Khan, M. Rovira-Navarro, I. Dalziel, R. Smalley, E. Kendrick, S. Konfal, D. J. Caccamise, R. C. Aster, A. Nyblade, and D. A. Wiens. Observed rapid bedrock uplift in Amundsen Sea Embayment promotes ice-sheet stability. *Science*, 360(6395):1335–1339, June 2018. ISSN 0036-8075, 1095-9203. doi: 10.1126/science.aao1447. URL `https://www.sciencemag.org/lookup/doi/10.1126/science.aao1447`.

S. Berger, L. Favier, R. Drews, J.-J. Derwael, and F. Pattyn. The control of an uncharted pinning point on the flow of an Antarctic ice shelf. *Journal of Glaciology*, 62(231):37–45, Feb. 2016. ISSN 0022-1430, 1727-5652. doi: 10.1017/jog.2016.7.

R. Bindschadler, P. Vornberger, and L. Gray. Changes in the ice plain of Whillans Ice Stream, West Antarctica. *Journal of Glaciology*, 51(175):620–636, 2005. ISSN 0022-1430, 1727-5652. doi: 10.3189/172756505781829070.

R. A. Bindschadler, E. P. Roberts, and A. Iken. Age of Crary Ice Rise, Antarctica, Determined from Temperature-Depth Profiles. *Annals of Glaciology*, 14:13–16, 1990. ISSN 0260-3055, 1727-5644. doi: 10.1017/S0260305500008168.

D. Callens, R. Drews, E. Witrant, M. Philippe, and F. Pattyn. Temporally stable surface mass balance asymmetry across an ice rise derived from radar internal reflection horizons through inverse modeling. *Journal of Glaciology*, 62(233):525–534, June 2016. ISSN 0022-1430, 1727-5652. doi: 10.1017/jog.2016.41.

S. L. Cornford, D. F. Martin, V. Lee, A. J. Payne, and E. G. Ng. Adaptive mesh refinement versus subgrid friction interpolation in simulations of Antarctic ice dynamics. *Annals of Glaciology*, 57(73):1–9, Sept. 2016. ISSN 0260-3055, 1727-5644. doi: 10.1017/aog.2016.13.

S. L. Cornford, H. Seroussi, X. S. Asay-Davis, G. H. Gudmundsson, R. Arthern, C. Borstad, J. Christmann, T. Dias dos Santos, J. Feldmann, D. Goldberg, M. J. Hoffman, A. Humbert, T. Kleiner, G. Leguy, W. H. Lipscomb, N. Merino, G. Durand, M. Morlighem, D. Pollard, M. Rückamp, C. R. Williams, and H. Yu. Results of the third Marine Ice Sheet Model Intercomparison Project (MISMIP+). *The Cryosphere*, 14(7):2283–2301, July 2020. ISSN 1994-0424. doi: 10.5194/tc-14-2283-2020. URL `https://tc.copernicus.org/articles/14/2283/2020/`.

P. Deschamps, N. Durand, E. Bard, B. Hamelin, G. Camoin, A. L. Thomas, G. M. Henderson, J. Okuno, and Y. Yokoyama. Ice-sheet collapse and sea-level rise at the Bølling warming 14,600 years ago. *Nature*, 483(7391):559–564, Mar. 2012. ISSN 0028-0836, 1476-4687. doi: 10.1038/nature10902. URL `http://www.nature.com/articles/nature10902`.

R. Drews. Ice thickness, surface-, and bed elevation of a pinning point in Roi Baudouin Ice Shelf, Dronning Maud Land Antarctica, 2019. URL https://doi.org/10.1594/PANGAEA.905997. Supplement to: Berger, Sophie; Favier, Lionel; Drews, Reinhard; Derwael, Jean-Jacques; Pattyn, Frank (2016): The control of an uncharted pinning point on the flow of an Antarctic ice shelf. Journal of Glaciology, 62(231), 37-45, https://doi.org/10.1017/jog.2016.7.

R. Drews, C. Martín, D. Steinhage, and O. Eisen. Characterizing the glaciological conditions at Halvfarryggen ice dome, Dronning Maud Land, Antarctica. *Journal of Glaciology*, 59 (213):9–20, 2013. ISSN 0022-1430, 1727-5652. doi: 10.3189/2013JoG12J134.

R. Drews, K. Matsuoka, C. Martín, D. Callens, N. Bergeot, and F. Pattyn. Evolution of Derwael Ice Rise in Dronning Maud Land, Antarctica, over the last millennia. *Journal of Geophysical Research: Earth Surface*, 120(3):564–579, Mar. 2015. ISSN 21699003. doi: 10.1002/2014JF003246. URL http://doi.wiley.com/10.1002/2014JF003246.

G. Durand, O. Gagliardini, B. de Fleurian, T. Zwinger, and E. Le Meur. Marine ice sheet dynamics: Hysteresis and neutral equilibrium. *Journal of Geophysical Research*, 114(F3):F03009, Aug. 2009. ISSN 0148-0227. doi: 10.1029/2008JF001170. URL http://doi.wiley.com/10.1029/2008JF001170.

L. Favier and F. Pattyn. Antarctic ice rise formation, evolution, and stability. *Geophysical Research Letters*, 42(11):4456–4463, June 2015. ISSN 0094-8276, 1944-8007. doi: 10.1002/2015GL064195. URL https://onlinelibrary.wiley.com/doi/abs/10.1002/2015GL064195.

L. Favier, O. Gagliardini, G. Durand, and T. Zwinger. A three-dimensional full Stokes model of the grounding line dynamics: effect of a pinning point beneath the ice shelf. *The Cryosphere*, 6(1):101–112, Jan. 2012. ISSN 1994-0424. doi: 10.5194/tc-6-101-2012. URL https://tc.copernicus.org/articles/6/101/2012/.

L. Favier, F. Pattyn, S. Berger, and R. Drews. Dynamic influence of pinning points on marine ice-sheet stability: a numerical study in Dronning Maud Land, East Antarctica. *The Cryosphere*, 10(6):2623–2635, Nov. 2016. ISSN 1994-0424. doi: 10.5194/tc-10-2623-2016. URL https://tc.copernicus.org/articles/10/2623/2016/.

O. Gagliardini, T. Zwinger, F. Gillet-Chaulet, G. Durand, L. Favier, B. de Fleurian, R. Greve, M. Malinen, C. Martín, P. Råback, J. Ruokolainen, M. Sacchettini, M. Schäfer, H. Seddik, and J. Thies. Capabilities and performance of Elmer/Ice, a new-generation ice sheet model. *Geoscientific Model Development*, 6(4):1299–1318, Aug. 2013. ISSN 1991-9603. doi: 10.5194/gmd-6-1299-2013. URL https://gmd.copernicus.org/articles/6/1299/2013/.

O. Gagliardini, J. Brondex, F. Gillet-Chaulet, L. Tavard, V. Peyaud, and G. Durand. Brief communication: Impact of mesh resolution for MISMIP and MISMIP3d experiments using Elmer/Ice. *The Cryosphere*, 10(1):307–312, Feb. 2016. ISSN 1994-0424. doi: 10.5194/tc-10-307-2016. URL https://tc.copernicus.org/articles/10/307/2016/.

F. Gillet-Chaulet and R. C. Hindmarsh. Flow at ice-divide triple junctions: 1. three-dimensional full-stokes modeling. *Journal of Geophysical Research: Earth Surface*, 116 (F2), 2011.

V. Goel, K. Matsuoka, C. D. Berger, I. Lee, J. Dall, and R. Forsberg. Characteristics of ice rises and ice rumples in Dronning Maud Land and Enderby Land, Antarctica. *Journal of Glaciology*, 66(260):1064–1078, Dec. 2020. ISSN 0022-1430, 1727-5652. doi: 10.1017/jog.2020.77.

D. Goldberg, D. M. Holland, and C. Schoof. Grounding line movement and ice shelf buttressing in marine ice sheets. *Journal of Geophysical Research*, 114 (F4):F04026, Dec. 2009. ISSN 0148-0227. doi: 10.1029/2008JF001227. URL http://doi.wiley.com/10.1029/2008JF001227.

R. Greve and H. Blatter. *Dynamics of ice sheets and glaciers*. Springer, Dordrecht, 2009. ISBN 9783642034145 9783642034152.

G. H. Gudmundsson, J. Krug, G. Durand, L. Favier, and O. Gagliardini. The stability of grounding lines on retrograde slopes. *The Cryosphere*, 6(6):1497–1505, Dec. 2012. ISSN 1994-0424. doi: 10.5194/tc-6-1497-2012. URL https://tc.copernicus.org/articles/6/1497/2012/.

M. Haseloff and O. V. Sergienko. The effect of buttressing on grounding line dynamics. *Journal of Glaciology*, 64(245):417–431, June 2018. ISSN 0022-1430, 1727-5652. doi: 10.1017/jog.2018.30.

A. C. J. Henry, R. Drews, C. Schannwell, and V. Višnjević. Hysteretic evolution of ice rises and ice rumples in response to variations in sea level. *The Cryosphere*, 16(9):3889–3905, 2022a. doi: 10.5194/tc-16-3889-2022. URL https://tc.copernicus.org/articles/16/3889/2022/.

C. Henry. Code for the publication "hysteretic evolution of ice rises and ice rumples in response to variations in sea level". *Zenodo [code]*, 2022. doi: doi: 10.5281/zenodo.7044134.

C. Henry, C. Schannwell, R. Drews, and V. Višnjević. The response of a low friction ice rise to sea level change. *TIB AV-Portal [video]*, 2022b. doi: doi: 10.5446/56713.

R. C. Hindmarsh, E. C. King, R. Mulvaney, H. F. Corr, G. Hiess, and F. Gillet-Chaulet. Flow at ice-divide triple junctions: 2. three-dimensional views of isochrone architecture from ice-penetrating radar surveys. *Journal of Geophysical Research: Earth Surface*, 116 (F2), 2011.

K. Hutter. *Theoretical glaciology: material science of ice and the mechanics of glaciers and ice sheets*. Dordrecht, D. Reidel Publishing Co./Tokyo, Terra Scientific Publishing Co., 1983. ISBN 9789027714732.

K. C. Jezek. Observing the antarctic ice sheet using the radarsat-1 synthetic aperture radar. *Polar Geography*, 27(3):197–209, 2003. doi: 10.1080/789610167. URL https://doi.org/10.1080/789610167.

J. Kingslake, C. Martín, R. J. Arthern, H. F. J. Corr, and E. C. King. Ice-flow reorganization in west antarctica 2.5 kyr ago dated using radar-derived englacial flow velocities. *Geophysical Research Letters*, 43(17): 9103–9112, 2016. doi: https://doi.org/10.1002/2016GL070278. URL https://agupubs.onlinelibrary.wiley.com/doi/abs/10.1002/2016GL070278.

J. Kingslake, R. P. Scherer, T. Albrecht, J. Coenen, R. D. Powell, R. Reese, N. D. Stansell, S. Tulaczyk, M. G. Wearing, and P. L. Whitehouse. Extensive retreat and re-advance of the West Antarctic Ice Sheet during the Holocene. *Nature*, 558(7710): 430–434, June 2018. ISSN 0028-0836, 1476-4687. doi: 10.1038/s41586-018-0208-x. URL http://www.nature.com/articles/s41586-018-0208-x.

C. Martín, R. C. A. Hindmarsh, and F. J. Navarro. Dating ice flow change near the flow divide at Roosevelt Island, Antarctica, by using a thermomechanical model to predict radar stratigraphy. *Journal of Geophysical Research*, 111(F1):F01011, 2006. ISSN 0148-0227. doi: 10.1029/2005JF000326. URL http://doi.wiley.com/10.1029/2005JF000326.

C. Martín, R. C. A. Hindmarsh, and F. J. Navarro. On the effects of divide migration, along-ridge flow, and basal sliding on isochrones near an ice divide. *Journal of Geophysical Research*, 114(F2):F02006, Apr. 2009. ISSN 0148-0227. doi: 10.1029/2008JF001025. URL http://doi.wiley.com/10.1029/2008JF001025.

K. Matsuoka, R. C. Hindmarsh, G. Moholdt, M. J. Bentley, H. D. Pritchard, J. Brown, H. Conway, R. Drews, G. Durand, D. Goldberg, T. Hattermann, J. Kingslake, J. T. Lenaerts, C. Martín, R. Mulvaney, K. W. Nicholls, F. Pattyn, N. Ross, T. Scambos, and P. L. Whitehouse. Antarctic ice rises and rumples: Their properties

and significance for ice-sheet dynamics and evolution. *Earth-Science Reviews*, 150: 724–745, Nov. 2015. ISSN 00128252. doi: 10.1016/j.earscirev.2015.09.004. URL https://linkinghub.elsevier.com/retrieve/pii/S0012825215300416.

F. Pattyn, C. Schoof, L. Perichon, R. C. A. Hindmarsh, E. Bueler, B. de Fleurian, G. Durand, O. Gagliardini, R. Gladstone, D. Goldberg, G. H. Gudmundsson, P. Huybrechts, V. Lee, F. M. Nick, A. J. Payne, D. Pollard, O. Rybak, F. Saito, and A. Vieli. Results of the Marine Ice Sheet Model Intercomparison Project, MISMIP. *The Cryosphere*, 6(3):573–588, May 2012. ISSN 1994-0424. doi: 10.5194/tc-6-573-2012. URL https://tc.copernicus.org/articles/6/573/2012/.

F. Pattyn, L. Perichon, G. Durand, L. Favier, O. Gagliardini, R. C. Hindmarsh, T. Zwinger, T. Albrecht, S. Cornford, D. Docquier, J. J. Fürst, D. Goldberg, G. H. Gudmundsson, A. Humbert, M. Hütten, P. Huybrechts, G. Jouvet, T. Kleiner, E. Larour, D. Martin, M. Morlighem, A. J. Payne, D. Pollard, M. Rückamp, O. Rybak, H. Seroussi, M. Thoma, and N. Wilkens. Grounding-line migration in plan-view marine ice-sheet models: results of the ice2sea MISMIP3d intercomparison. *Journal of Glaciology*, 59(215):410–422, 2013. ISSN 0022-1430, 1727-5652. doi: 10.3189/2013JoG12J129.

E. C. Pettit, H. P. Jacobson, and E. D. Waddington. Effects of basal sliding on isochrones and flow near an ice divide. *Annals of Glaciology*, 37:370–376, 2003. ISSN 0260-3055, 1727-5644. doi: 10.3189/172756403781815997.

D. Pollard, W. Chang, M. Haran, P. Applegate, and R. DeConto. Large ensemble modeling of the last deglacial retreat of the west antarctic ice sheet: comparison of simple and advanced statistical techniques. *Geoscientific Model Development*, 9 (5):1697–1723, May 2016. ISSN 1991-9603. doi: 10.5194/gmd-9-1697-2016. URL https://gmd.copernicus.org/articles/9/1697/2016/.

C. F. Raymond. Deformation in the Vicinity of Ice Divides. *Journal of Glaciology*, 29(103): 357–373, 1983. ISSN 0022-1430, 1727-5652. doi: 10.1017/S0022143000030288.

R. Reese, G. H. Gudmundsson, A. Levermann, and R. Winkelmann. The far reach of ice-shelf thinning in Antarctica. *Nature Climate Change*, 8(1):53–57, Jan. 2018. ISSN 1758-678X, 1758-6798. doi: 10.1038/s41558-017-0020-x. URL http://www.nature.com/articles/s41558-017-0020-x.

C. Schannwell, R. Drews, T. A. Ehlers, O. Eisen, C. Mayer, and F. Gillet-Chaulet. Kinematic response of ice-rise divides to changes in ocean and atmosphere forcing. *The Cryosphere*, 13(10):2673–2691, Oct. 2019. ISSN 1994-0424. doi: 10.5194/tc-13-2673-2019. URL https://tc.copernicus.org/articles/13/2673/2019/.

C. Schannwell, R. Drews, T. A. Ehlers, O. Eisen, C. Mayer, M. Malinen, E. C. Smith, and H. Eisermann. Quantifying the effect of ocean bed properties on ice sheet geometry over 40 000 years with a full-Stokes model. *The Cryosphere*, 14 (11):3917–3934, Nov. 2020. ISSN 1994-0424. doi: 10.5194/tc-14-3917-2020. URL https://tc.copernicus.org/articles/14/3917/2020/.

C. Schoof. Ice sheet grounding line dynamics: Steady states, stability, and hysteresis. *Journal of Geophysical Research*, 112(F3):F03S28, July 2007. ISSN 0148-0227. doi: 10.1029/2006JF000664. URL http://doi.wiley.com/10.1029/2006JF000664.

O. V. Sergienko and D. J. Wingham. Bed topography and marine ice-sheet stability. *Journal of Glaciology*, 68(267):124–138, 2022. doi: 10.1017/jog.2021.79.

H. Seroussi, S. Nowicki, E. Simon, A. Abe-Ouchi, T. Albrecht, J. Brondex, S. Cornford, C. Dumas, F. Gillet-Chaulet, H. Goelzer, N. R. Golledge, J. M. Gregory, R. Greve, M. J. Hoffman, A. Humbert, P. Huybrechts, T. Kleiner, E. Larour, G. Leguy, W. H. Lipscomb, D. Lowry, M. Mengel, M. Morlighem, F. Pattyn, A. J. Payne, D. Pollard, S. F. Price, A. Quiquet, T. J. Reerink, R. Reese, C. B. Rodehacke, N.-J. Schlegel,

A. Shepherd, S. Sun, J. Sutter, J. Van Breedam, R. S. W. van de Wal, R. Winkelmann, and T. Zhang. initmip-antarctica: an ice sheet model initialization experiment of ismip6. *The Cryosphere*, 13(5):1441–1471, 2019. doi: 10.5194/tc-13-1441-2019. URL https://tc.copernicus.org/articles/13/1441/2019/.

E. C. Smith, A. M. Smith, R. S. White, A. M. Brisbourne, and H. D. Pritchard. Mapping the ice-bed interface characteristics of Rutford Ice Stream, West Antarctica, using microseismicity: Mapping ICE-Bed Interface, Rutford. *Journal of Geophysical Research: Earth Surface*, 120(9):1881–1894, Sept. 2015. ISSN 21699003. doi: 10.1002/2015JF003587. URL http://doi.wiley.com/10.1002/2015JF003587.

H. Still and C. Hulbe. Mechanics and dynamics of pinning points on the Shirase Coast, West Antarctica. *The Cryosphere*, 15(6):2647–2665, June 2021. ISSN 1994-0424. doi: 10.5194/tc-15-2647-2021. URL https://tc.copernicus.org/articles/15/2647/2021/.

H. Still, A. Campbell, and C. Hulbe. Mechanical analysis of pinning points in the Ross Ice Shelf, Antarctica. *Annals of Glaciology*, 60(78):32–41, Apr. 2019. ISSN 0260-3055, 1727-5644. doi: 10.1017/aog.2018.31.

S. Vialov. Regularities of glacial shields movement and the theory of plastic viscous flow. *Physics of the Movements of Ice IAHS*, 47:266–275, 1958.

M. G. Wearing and J. Kingslake. Holocene Formation of Henry Ice Rise, West Antarctica, Inferred From Ice-Penetrating Radar. *Journal of Geophysical Research: Earth Surface*, 124(8):2224–2240, Aug. 2019. ISSN 2169-9003, 2169-9011. doi: 10.1029/2018JF004988. URL https://onlinelibrary.wiley.com/doi/abs/10.1029/2018JF004988.

3

PREDICTING THE THREE-DIMENSIONAL AGE-DEPTH FIELD OF AN ICE RISE

MANUSCRIPT DETAILS:

A. Clara J. Henry, Clemens Schannwell, Vjeran Višnjević, Joanna Millstein, Paul D. Bons, Olaf Eisen, Reinhard Drews.: Predicting the three-dimensional age-depth field of an ice rise [Submitted to *The Journal of Geophysical Research: Earth Surface*].

Predicting the three-dimensional age-depth field of an ice rise

A. Clara J. Henry[1, 2, 3], Clemens Schannwell[1], Vjeran Višnjević[2], Joanna D. Millstein[4], Paul D. Bons[2], Olaf Eisen[5, 6], and Reinhard Drews[2]

[1]Max Planck Institute for Meteorology, Hamburg, Germany
[2]Department of Geosciences, University of Tübingen, Tübingen, Germany
[3]International Max Planck Research School on Earth System Modelling, Max Planck Institute for Meteorology, Hamburg, Germany
[4]Massachusetts Institute of Technology—Woods Hole Oceanographic Institute Joint Program in Oceanography/Applied Ocean Science and Engineering, Cambridge, MA, USA
[5]Alfred Wegener Institute Helmholtz Centre for Polar and Marine Research, Bremerhaven, Germany
[6]University of Bremen, Bremen, Germany

Key Points

- First three-dimensional simulations of the stratigraphy of an ice rise allowing comparison of model results with radar observations.
- Choice of the Glen's flow law exponent influences deformation in the grounding zones.
- Reduction in surface elevation at the divide relative to observations points at missing processes in the model such as anisotropy.

Abstract

Ice rises situated around the perimeter of Antarctica buttress ice flow and contain information about the past climate and changes in flow regime. Moreover, ice rises contain convergent and divergent flow regimes, and both floating and grounded ice over comparatively small spatial scales, meaning they are ideal locations to study ice-flow dynamics. Here, we introduce a new modelling framework that permits the comparison between modelled and observed stratigraphy. A thermo-mechanically coupled, isotropic, Stokes ice flow model with a dynamic grounding line is used (Elmer/Ice). The result is the simulated age-depth field of a three-dimensional, steady-state ice rise which is dynamically coupled to the surrounding ice shelf. Applying the model to Derwael Ice Rise, results show a good match between observed and modelled stratigraphy over most of the ice rise and predict approximately 8000 year old ice at a depth of 95 %. Differences in the prediction of age between simulations using Glen's flow law exponents of $n = 3$ and $n = 4$ are generally small (< 5 % over most areas). In the ice rise shear zones, large differences in shear strain rates in the velocity direction are found between the $n = 3$ and the $n = 4$ simulations. Our simulations indicate that a Glen's flow law exponent of $n = 4$ may be better suited when modelling ice rises due to a steady-state geometry which is closer to the observed geometry. Our three-dimensional modelling framework can easily be transferred to other ice rises and has relevance for researchers interested in ice core dating and understanding ice-flow re-organisation.

Plain Language Summary

Ice rises are features which form in coastal Antarctica when the ice shelf comes into contact with the bathymmetry. These features provide a backstress on the ice shelf and can influence grounding line position. We simulate an ice rise in East Antarctica called Derwael Ice Rise, outlining the steps necessary to model the three-dimensional stratigraphy of an ice rise and compare the modelled stratigraphy with observed stratigraphy derived from radar measurements. Comparisons between the observed and modelled stratigraphy allow us to validate boundary conditions and the parameterisations used in our model. This work is relevant as a blueprint for simulating other ice rises for those interested in comparison with ice core records, and investigating ice rises formation and evolution.

1 Introduction

Ice rises form where ice shelves ground locally on topographic highs in the bathymmetry and are important in coastal Antarctic ice flow dynamics as they regulate the flow of ice towards the ocean (Favier and Pattyn, 2015; Favier et al., 2016; Henry et al., 2022). Moreover, ice rises are valuable as a climate archive because they often provide high-resolution and undisturbed records throughout the Holocene. Ice-core drill sites are often located at local summits to avoid lateral flow. However, it is a significant challenge to predict the age-depth fields prior to drilling. This is due to strong variations in surface mass balance (SMB, Cavitte et al. (2022)) and also because the ice-flow regimes change over a few tens of kilometres. Divide flow at the summit (where arches in the internal stratigraphy may form) turns into flank flow, and finally to the grounding zone where coupling with the surrounding ice shelves takes place. Compared to Antarctica's interior, ice rises at the coast are comparatively easy to reach and consequently a number of them , Derwael Ice Rise being one of them, have been densely surveyed with radar to image the isochronal stratigraphy. This enables the comparison of model predictions across various flow regimes with observations which can help calibrate model parameters such as Glen's flow law exponent, the fundamental constitutive relation for ice flow.

The non-Newtonian flow of ice (Glen, 1955; Weertman, 1983; Budd and Jacka, 1989) results in Raymond arches (Raymond, 1983) which form in the stratigraphy under the ice-rise divides and have been used to estimate how stationary ice-divide flow is. This effect can be dampened, for example, by along-ridge flow or changing conditions, thus inhibiting their formation. Under a changing climate, the geometry of an ice rise often changes, thereby causing a change in the isochronal structure (Nereson et al., 1998; Martín et al., 2009). The onset of stability of an ice rise is indicated by the amplitude of the Raymond arches and a change in the size of an ice rise is indicated by the migration of Raymond arches visible in the stratigraphy as side arches or tilted anticline stacks. Simulations of the stratigraphy of specific ice rises have thus far been performed in two dimensions (Martín et al., 2006, 2009, 2014; Drews et al., 2015; Goel et al., 2018), with Gillet-Chaulet and Hindmarsh (2011) performing simulations of the stratigraphy of an idealised ice rise in three dimensions without the inclusion of the surrounding ice shelf.

In this paper, we build on previous ice-rise modelling studies (Martín et al., 2009; Drews et al., 2015; Schannwell et al., 2019, 2020) and extend them by introducing a modelling framework that allows us to model ice rises including the surrounding ice shelves and their stratigraphy in three dimensions. This not only permits the prediction of the stratigraphy, but also accounts for three-dimensional effects that are of importance for comparisons with radar observations and ice cores. Whilst having proven important in the development of an understanding of Raymond arches, the two-dimensional studies do not allow for along-ridge flow. Studies investigating the observed stratigraphy in shear zones (Franke et al., 2022) and zones of convergence (Bons et al., 2016) have been performed, but a comparison between observed and modelled stratigraphy in such settings has not yet been performed. In idealised simulations (Hindmarsh et al., 2011; Gillet-Chaulet et al., 2011), it has been shown that along-ridge flow has a dampening effect on Raymond arch evolution. Where these simulations lack, however, is in the use of idealised boundary forcing conditions, which do

Table 1: List of parameters used in the simulations

Parameter	Symbol	Value	Unit
Basal friction exponent	m	1/3	
Local ocean density	ρ_w	1000	kg m^{-3}
Ice density	ρ_i	900	kg m^{-3}
Gravity	g	9.8	m s^{-2}
Universal gas constant	R	8.314	$mol^{-1}K^{-1}$
Geothermal heat flux	ϕ_q	50	mWm^{-2}
Basal melt parameter	b_0	0.95	ma^{-1}

not sufficiently produce the differing flow regime conditions on the stoss and lee sides of an ice rise.

The introduction of our new modelling framework provides a blueprint for modelling a real-world ice rise in three dimensions using the thermo-mechanically coupled model Elmer/Ice (Gagliardini et al., 2013) in order to predict the age field ice-rise wide. We investigate how robust those results are compared to observations with two Glen's flow law exponents. We choose to compare simulations using the typical exponent of $n = 3$ with simulations using an exponent of $n = 4$, closer to the value of $n = 4.1 \pm 0.4$ found to work best for Antarctic ice shelves (Millstein et al., 2022) and similar values suggested by Bons et al. (2018) for Greenland. The conversion from using a Glen's flow law with an exponent of $n = 3$ to an exponent of $n = 4$ is made using an initial scalar stress estimate along with simulations for the evaluation of an appropriate Arrhenius pre-factor for $n = 4$.

The three-dimensional, steady-state simulations presented here have relevance for comparisons with ice cores and in the context of understanding the link between isochronal structures and changes in ice geometry and external forcing. Steady-state simulations allow the deduction of changes due to misfits and provide an important step towards the use of ice rises as a constraint for paleo ice-sheet simulations. This study not only successfully demonstrates three-dimensional modelling to bridge Stokes models with observed radar stratigraphy, but also delves into the implications of model parameter choice by exploiting variables in Glen's flow law.

2 Derwael Ice Rise

Derwael Ice Rise has a grounded area of roughly 1050 km^2 and is an isle-type ice rise with a ridge divide. The grounded area has a maximum width of roughly 35 km perpendicular to the predominant flow direction of the ice shelf. The ice rise has a maximum ice thickness of roughly 630 m with an estimated accuracy of 5 % (Morlighem et al., 2020) and is thickest in the south of the ice rise, where there is convergence of flow from the ice rise and the ice shelf. The maximum ice thickness at the ridge divide is roughly 540. We choose Derwael Ice Rise because of the availability of radar data across the ice rise divide and the shear margins, and also because Derwael Ice Rise is close to steady-state, perhaps with some current thinning (Drews et al., 2015; Callens et al., 2016). Derwael Ice Rise has well expressed isochrone arches beneath the ridge divide. A pecularity is, that arches (referred to as side arches later on) also occur in the south-eastern flanks close to the divide (Drews et al., 2015). An ice rumple is located in the north-western corner of the domain.

3 Methods

The model setup is based on Henry et al. (2022), and here we extend the framework to real-world geometries. In the following sections, we describe the required modifications to accomplish this. We use the finite element software Elmer/Ice (Gagliardini et al., 2013) to solve the Stokes equations. Here, we describe the coupled equations, model parameters boundary conditions and mesh resolution.

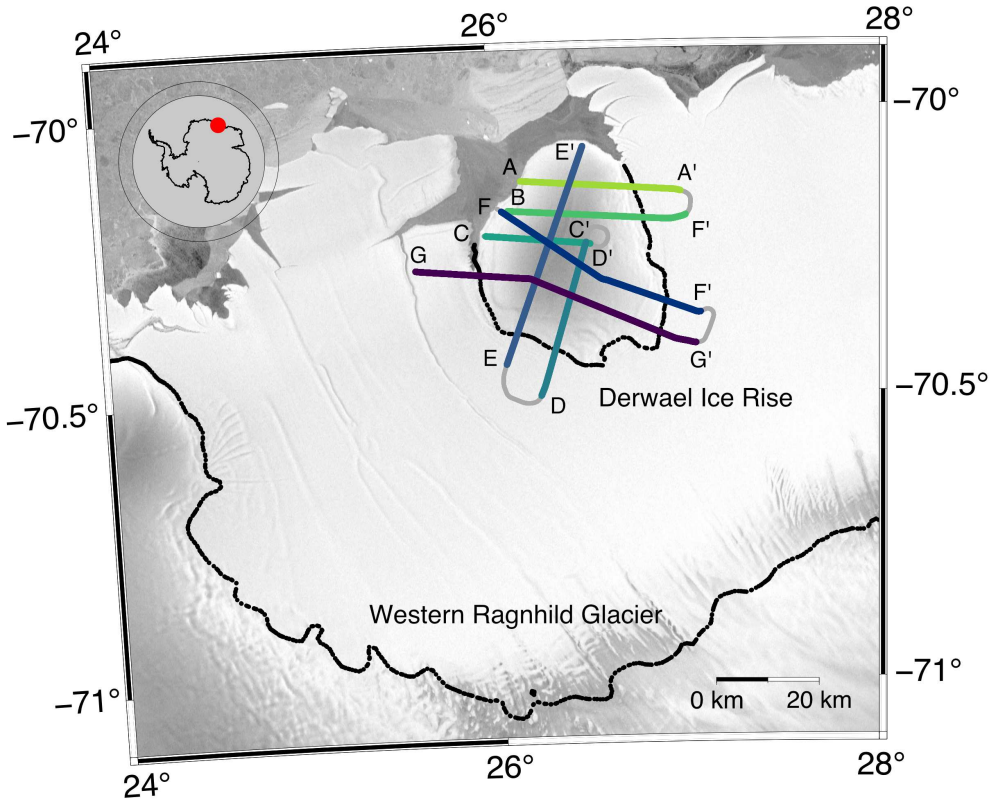

Figure 1: The location of Derwael Ice Rise within the Roi Baudouin Ice Shelf in East Antarctica. The coloured line segments $A - A'$ to $G - G'$ indicate the locations of radar measurements taken using airborne radar. The continental and ice rise grounding lines are indicated by the black lines. The RADARSAT mosaic Jezek (2003) is shown in the background, and the grounding line (black dots) is from Morlighem et al. (2020).

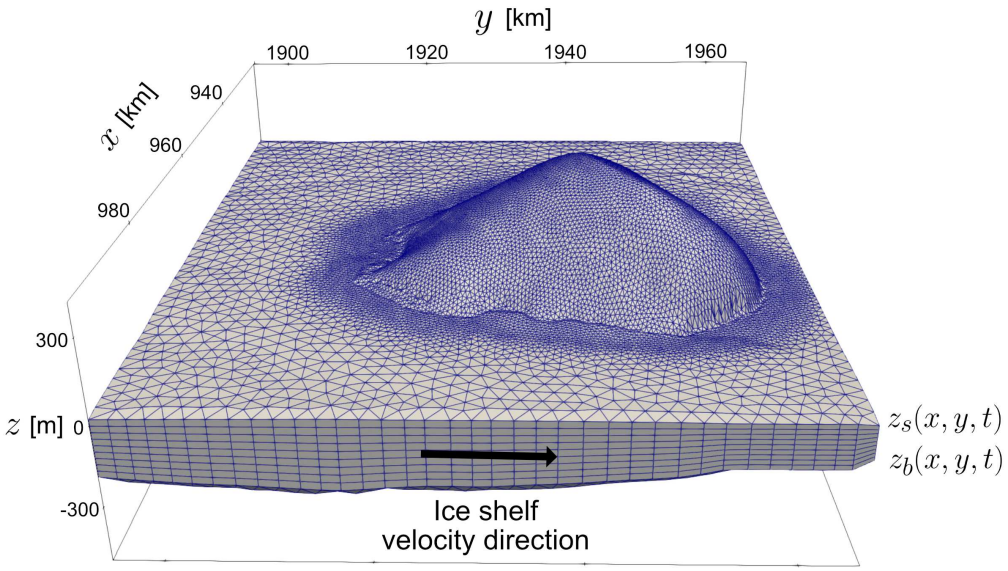

Figure 2: The model set up with horizontal distances in Antarctic polar stereographic projection. The area encompassing the ice rise has a characteristic resolution of 500 m and the surrounding area has a resolution of 2000 m. The upper ice surface is denoted by $z_s = z_s(x, y, t)$ and the lower ice surface by $z_b = z_b(x, y, t)$, where x and y are the horizontal directions and z is the vertical direction relative to sea level. Note: for visualisation, the vertical is scaled by a factor of 30.

3.1 Governing equations

The Stokes equations,

$$\boldsymbol{\nabla} \cdot (\boldsymbol{\tau} - P\mathbf{I}) + \rho_i \mathbf{g} = 0, \tag{1}$$

describe the flow of ice, where $\boldsymbol{\tau}$ is the deviatoric stress tensor, P is the pressure, $\mathbf{I}$ is the identity matrix, ρ_i is the ice density and $\mathbf{g} = -g\hat{\mathbf{e}}_z$ is the gravitational acceleration. The ice is subject to an incompressibility condition,

$$\boldsymbol{\nabla} \cdot \mathbf{u} = 0. \tag{2}$$

The Glen's power flow law,

$$\boldsymbol{\tau} = 2\eta\dot{\boldsymbol{\varepsilon}}, \tag{3}$$

describes the nonlinear dependence between the strain rate tensor, $\dot{\boldsymbol{\varepsilon}}$, and the deviatoric stress tensor. The effective viscosity, η, is

$$\eta = \frac{1}{2} A(T)^{-1/n} \dot{\varepsilon}_e^{(1-n)/n}, \tag{4}$$

where $A(T)$ is the ice fluidity which is dependent on temperature, T, and is described in detail below. The effective strain rate, $\dot{\varepsilon}_e^2$, is the square of the second invariant of the strain rate tensor, $\dot{\boldsymbol{\varepsilon}}$. As in Gagliardini et al. (2013), the temperature of the ice evolves subject to

$$\rho_i c_v \left(\frac{\delta T}{\delta t} + \mathbf{u} \cdot \boldsymbol{\nabla} T \right) = \nabla \cdot (\kappa \boldsymbol{\nabla} T) + \mathbf{D} : \boldsymbol{\sigma}, \tag{5}$$

where : is the double inner product,

$$c_v = 146.3 + 7.253T \tag{6}$$

is the specific heat capacity of the ice and

$$\kappa = 9.828 \exp\left(-5.7 \times 10^{-03} T\right) \tag{7}$$

is the thermal conductivity Ritz (1987). The temperature is coupled to the Glen's flow law using an Arrhenius law

$$A(T, p) = E A_0 \exp(-Q/RT), \tag{8}$$

where A_0 is a constant pre-factor, Q is the activation energy and R is the universal gas constant. The Arrhenius law is multiplied by a constant, E, called an enhancement factor, in order to obtain an optimal coefficient in the Arrhenius law. The combination of the parameters A_0 and E are used in ice sheet modelling to account for effects such as grain size, crystal orientation, impurities, porosity and water content. An exploration of the influence of each process is beyond the scope of this study, but we will note here that processes which soften ice cause either an increase in the parameter A_0 or E. For calculating the equivalent Arrhenius factor for a Glen's flow law exponent of $n = 3$, we take a similar approach to Zeitz et al. (2020) and use a first estimate of the stress magnitude of $[\tau_0] = 0.25 \times 10^6$ Pa, so that

$$A_0\big|_{n=4} \exp\left(-Q\big|_{n=4}\right) = \frac{A_0\big|_{n=3} \exp\left(-Q\big|_{n=3}\right)}{[\tau_0]}. \tag{9}$$

The first estimate of τ_0 is to compensate for the multiplication of an additional deviatoric stress tensor in Glen's flow law. The upper surface temperature is set equal to the temperature field data (Comiso, 2000). Initially, a linear temperature profile from the lower ice surface to the upper ice surface is prescribed. During transient simulation, the upper and lower surface temperatures evolve subject to a Neumann boundary condition. During initialisation, the lower ice surface temperature is prescribed to be the pressure melting point temperature,

$$T_p = 273.15 - \beta \rho_i g (z_s - z). \tag{10}$$

Here, β denotes the Clausius-Clapeyron constant, $\beta = 9.8 \times 10^{-8}$ K Pa^{-1} (Zwinger et al., 2007). In order to solve for the isochronal stratigraphy of the ice, the age of the ice is solved according to

$$\frac{\partial \psi}{\partial t} + \mathbf{u} \cdot \nabla(\psi) = 1 \tag{11}$$

where ψ is the age of the ice (Zwinger and Moore, 2009). Eq. 11 is solved using a semi-Lagrangian scheme implemented in Elmer/Ice (Martín and Gudmundsson, 2012).

The upper ice surface, $z = z_s(x, y, t)$, and the lower ice surface, $z = z_b(x, y, t)$, evolve subject to

$$\left(\frac{\partial}{\partial t} + \mathbf{u} \cdot \boldsymbol{\nabla}\right)(z - z_s) = \dot{a}_s, \tag{12}$$

and

$$\left(\frac{\partial}{\partial t} + \mathbf{u} \cdot \boldsymbol{\nabla}\right)(z - z_b) = \dot{a}_b, \tag{13}$$

respectively, where $\dot{a}_s = \dot{a}_s(x, y)$ is the ice-equivalent SMB. The basal melt rate, $\dot{a}_b = \dot{a}_b(x, y)$, is set to a suitable constant of 0.95 m a^{-1} which resulted in minimal adjustment of ice shelf thickness and grounding line position and is close to the average spatial value of 0.8 m a^{-1} across the Roi Baudouin Ice Shelf (Drews et al., 2020). The SMB, $\dot{a}_s$, is described in further detail below. Where ice is in contact with the bed, a non-linear Weertman friction law (Weertman, 1957) is used,

$$\boldsymbol{\tau}_b = -C|\mathbf{u}_b|^{m-1}\boldsymbol{u}_b, \tag{14}$$

where $\boldsymbol{\tau}_b$ is the basal shear stress, C is a constant friction coefficient, $\boldsymbol{u}_b$ is the velocity tangential to the bed, and m is the friction law exponent and has the value $m = 1/3$ in all simulations.

For all our simulations, we use a horizontal resolution of 500 m in the area encompassing the ice rise up to a distance from the grounding line of 5000 m and the surrounding area has a resolution of 2000 m (Fig. 2). In the vertical, the mesh is made up of 10 layers. The higher resolution is needed in order to better resolve the stratigraphy of the ice rise. The Elmer/Ice grounding line implementation *Discontinous* is used.

3.2 Observational data, initial conditions and boundary conditions

3.2.1 Observational stratigraphy

Airborne radar data were acquired in the 2018/19 Antarctic field season as part of the CHIPSM survey using the Polar 6 aircraft of the Alfred Wegener Institute with an ultra-wideband radar (MCoRDS v5) and eight-element fuselage antenna array operating in the 150–520 MHz frequency range. Details on data processing and tracing of isochronal internal layers is laid out in Koch et al. (2023), which use the same data set. Dating of the two shallowest internal layers along the radar profiles is based on an ice-core depth scale (Philippe et al., 2016) under the assumption of a steady-state age-depth relation (Koch et al., 2023). This yields a total of seven profiles across the ice rise (Fig. 1).

In order to make comparisons between the modelled isochronal stratigraphy and the observed internal reflection horizons possible, a density adjustment needs to be made. This can be done either by adjusting the modelled isochrone elevation to match the density profile of the real-world ice rise or vice versa. We choose the latter. The adjustment results in isochrone elevations equivalent to a constant density of 900 kg m^{-3} and is calculated according to the density profile of Derwael Ice Rise in Callens et al. (2014). Throughout the paper, when referring to depth below surface in relation to observations, these are relative to the BedMachine surface elevation, adjusted to an equivalent of 900 kg m^{-3} as opposed to the 917 kg m^{-3} assumed in BedMachine. On the other hand, when referring to depth below surface in relation to model results, depths are relative to the steady-state modelled surface using a denisty of 900 kg m^{-3}. Note that this choice does not have an effect on the final comparison between the modelled and observed isochrones.

3.2.2 Surface and basal mass balances, velocity, bed and ice geometry

Over the ice rise, we derive the SMB along transects from the shallow radar stratigraphy using the standard approach of the shallow layer approximation (Waddington et al., 2007). Isochrones are dated using an ice core drilled at the summit (Philippe et al., 2016). Details of this are presented in Koch et al. (2023) accompanied by the dataset Koch et al.. We interpolated between radar transects using an interpolation scheme and merge the SMB

Table 2: List of simulations

Simulation	n	E	Pre-factor 1 [$\mathrm{Pa}^{-n}\ \mathrm{a}^{-1}$]	Pre-factor 2 [$\mathrm{Pa}^{-n}\ \mathrm{a}^{-1}$]
n3E0.2	3	0.2	1.258×10^7	6.046×10^{22}
n3E0.4	3	0.4	1.258×10^7	6.046×10^{22}
n3E0.5	3	0.5	1.258×10^7	6.046×10^{22}
n3E0.6	3	0.6	1.258×10^7	6.046×10^{22}
n3E0.8	3	0.8	1.258×10^7	6.046×10^{22}
n3E1.0	3	1.0	1.258×10^7	6.046×10^{22}
lightgreyheightn4E1.2	4	1.2	5.032×10^7	2.419×10^{23}
n4E1.6	4	1.6	5.032×10^7	2.419×10^{23}
n4E1.8	4	1.8	5.032×10^7	2.419×10^{23}
n4E2.0	4	2.0	5.032×10^7	2.419×10^{23}
n4E2.4	4	2.4	5.032×10^7	2.419×10^{23}
n4E2.8	4	2.8	5.032×10^7	2.419×10^{23}

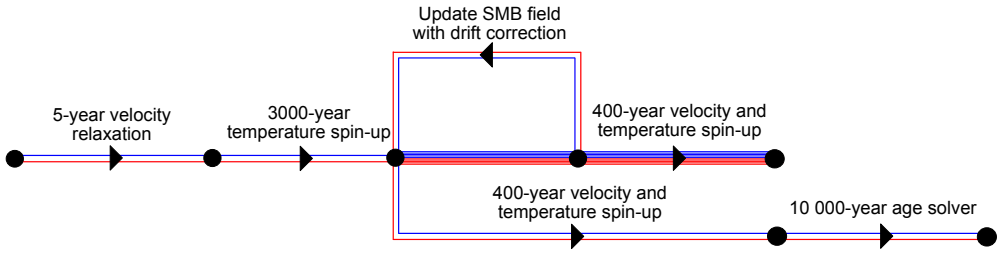

Figure 3: The schematic shows the spin-up procedure for the simulations in Table 2. The blue lines refer to the $n = 3$ simulations and the red lines refer to the $n = 4$ simulations. The black dots indicate the points when the simulation was restarted with a change in model set up as indicated by the schematic labels. Further details regarding the sequence of steps are given in Section 3.3.

field at the ice-rise edges with reanalysis data from RACMO2.3p1 mean annual SMB from the years 1979-2014 (van den Broeke, 2019). Including the SMB estimates from radar observations is a critical step in the analysis because the reanalysis data are too coarsely resolved on the ice rise. In order to avoid model drift due to uncorrected offsets in the SMB field, we correct the SMB field by subtracting it by the rate of change of the surface elevation after 50 years of simulation time.

At the domain boundary on the oceanward side of the ice rise, the ice is allowed to flow subject to hydrostatic pressure. At all other boundaries, depth-independent fluxes are prescribed and are derived from observed velocities (Rignot and Scheuchl., 2017). The bed elevation and the initial ice geometry is prescribed using BedMachine Antarctica data (Morlighem et al., 2020). When comparing BedMachine bed elevation with observations from our radar survey, we found significant mismatches of roughly 150 m in the north-eastern corner of Derwael Ice Rise (Fig. 4). This is surprising given that the radar survey is part of the BedMachine dataset. We see some interpolation artefacts where the grounded ice bed elevation dataset is merged with the bed elevation data below floating ice.

3.3 Model spin-up procedure

In order to model the three-dimensional isochronal stratigraphy of an ice rise, the following steps are taken to spin-up the model. The details are as follows and can be seen in Fig. 3.

Step 1: Simulate the ice rise for 5 years with the Stokes, temperature, and upper and lower free surface solvers on for Glen's flow law exponents of $n = 3$ and $n = 4$.

Step 2: Spin up the temperature for 3000 years with the Stokes and free surface solvers off.

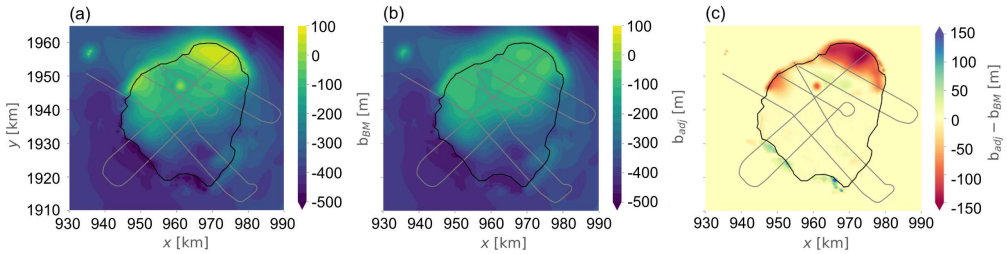

Figure 4: The BedMachine Antarctica bed elevation is shown in (a) and the adjusted bed elevation after re-interpolation and smoothing of unphysical anomalies is shown in (b). The difference between the adjusted bed elevation and the original BedMachine bed elevation is shown in (c). The grey lines show the location of radargrams with which the simulations are compared. The bed elevation data from these radar lines has been used in the BedMachine data.

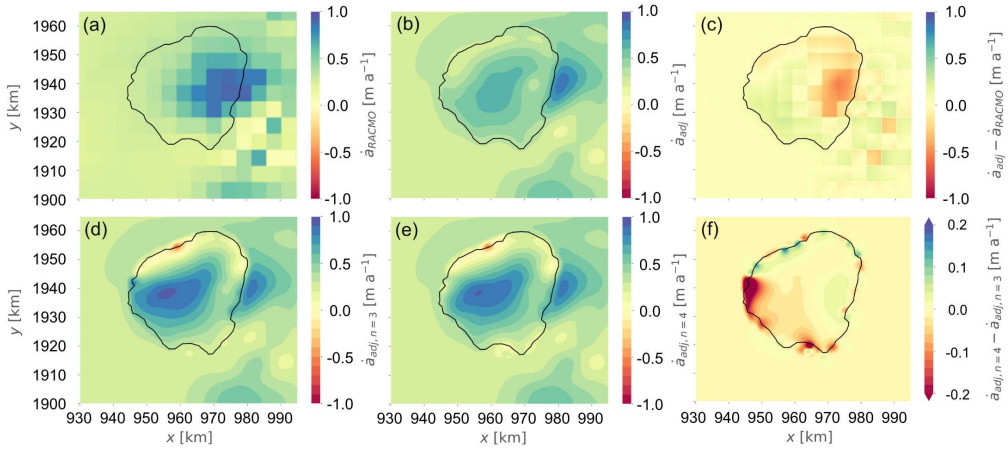

Figure 5: Surface mass balance (SMB) (a) based on RACMO2.3p1 data; (b) the adjusted product from a combination of stratigraphy-derived data in the grounded area and RACMO2.3p1 data in the surrounding area; (c) difference between the adjusted and the RACMO2.3p1 SMB. The SMB in (d) and (e) use a drift correction made with the $\partial z_s/\partial t$ field after a simulation time of 50 years for the $n = 3$ and the $n = 4$ simulations, respectively and (f) shows the difference in SMB between the $n = 3$ and $n = 4$ simulations for the stratigraphy-derived and drift-corrected SMB.

Step 3: Simulate with the chosen set of parameters (Table 2) for 400 years.

Step 4: Choose the optimal $n = 3$ and $n = 4$ simulation based on the least volume change (Fig. 6).

Step 5: Compute SMB from model drift after allowing the surface elevation to evolve for 50 years. The SMB is adjusted using the model drift over the grounded area and is incorporated with the combined stratigraphy-derived and RACMO2.3p1 SMB field. A Gaussian filter is applied to remove steep gradients.

Step 6: Simulate with the temperature, free surface and Stokes solvers activated for 400 years.

Step 7: Run the age solver with the Stokes, free surface and temperature solvers off for 10000 years.

4 Results

4.1 Model parameter choice and applied surface mass balance

In contrast to the SMB field from the RACMO2.3p1 simulation, the highest values of the stratigraphy-derived and drift-corrected SMB are concentrated in the centre of the ice rise (Fig. S6 in the Supporting Information). Here, the differences in spatial variation before and after the drift correction are evident, with the drift-corrected SMB being concentrated more towards the west of the ice rise. RACMO2.3p1 data shows higher values on the eastern and northern sides of the ice rise, whereas the stratigraphy-derived and drift-corrected SMB has higher values in the centre and on the south-western side of the ice rise. The results are close to mean SMB values of 0.47 ± 0.02 m w.e. a^{-1} (for comparison with our results, this is equivalent to 0.52 ± 0.02 m a^{-1} assuming an ice density of 900 kg m^{-3}) for the period $1816 - 2011$ found by Philippe et al. (2016), derived from an ice core at the summit of Derwael Ice Rise.

In order to find the optimal combination of parameters in the simulations of Derwael Ice Rise, an ensemble of simulations for various enhancement factors were performed. Here we note that in this work we take the enhancement factor to simply be a constant multiplier that adjusts the Arrhenius factor, A_0 and is equivalent to adjusting the Arrhenius pre-factor itself. As a performance evaluation metric in order to find the optimal enhancement factor, we use the change in surface elevation with respect to time across the grounded ice (Fig. 6), assuming that Derwael Ice Rise is in steady state. We found that an enhancement factor of $E = 0.5$ (simulation $n3E0.5$) produced an ice rise with the least cumulative volume change in the $n = 3$ simulations. For the $n = 4$ simulations, a corresponding enhancement factor of $E = 1.8$ (simulation $n4E1.8$) is found. Henceforth, we refer to the $n3E0.5$ and the $n4E1.8$ simulations simply as the $n = 3$ and $n = 4$ simulations, respectively. Large fluctuations seen in Fig. 6 (c) and (d) are due to sudden changes in grounding line position and temporary localised decreases in elevation. Simulations with an underestimated or overestimated enhancement factor result in elevation and volumetric changes.

In both the $n = 3$ and the $n = 4$ simulation, there is a slight reduction in ice thickness at the divide compared with the BedMachine data of roughly 15 m (corresponding to 3 % of the ice thickness at the divide). This reduction in ice thickness is less in the $n = 4$ than the $n = 3$ simulation. On the western side of the ice rise excess thinning of the ice occurs, whereas in all other grounding zones, too much thickening occurs. Comparing the elevation change between the $n = 3$ and $n = 4$ simulations (Fig. 8), it can be seen that the steady-state $n = 3$ simulation has a lower elevation in the centre of the ice rise than the $n = 4$ simulation. In the north-eastern flank of the ice rise, the $n = 3$ simulation has a lower steady-state surface elevation than the $n = 4$ simulation, but all other flanks show a tendency for a higher surface elevation in the case of the $n = 3$ simulation.

4.2 Comparisons between modelled and observed stratigraphy

Our new modelling framework allows us to further understand the similarities and differences between the observational data of Derwael Ice Rise and the simulated ice rise. Modelled isochrones are compared with dated isochrones derived from the radargrams obtained using airborne radar measurements. The radar measurements cover areas of Derwael Ice Rise including the ridge divide, flanks and grounding zones. The data is divided into seven cross-sections, each of which is compared with the model output for both $n = 3$ and $n = 4$ (Fig. 9). The modelled isochrones broadly reproduce the observed isochrones. The largest discrepancies between modelled and observed stratigraphy correspond to regions of the domain where the modelled and observed surface geometry do not match. For example, due to the tendency of the ice rise to broaden and thicken at the grounding zones and decrease in elevation in the centre during transient evolution, the elevation of the isochrones in these regions is generally under-estimated in the centre of the ice rise and over-estimated in the grounding zones. Evidence for this is provided by the cross-section $A - A'$ (Fig. 9a). There is a significant mismatch of up to 50 m between the modelled and observed isochrones, particularly on the eastern side which is likely due to an incorrect bed elevation. Mismatches with similar characteristics are also present in cross-sections $B - B'$, $C - C'$ and $F - F'$.

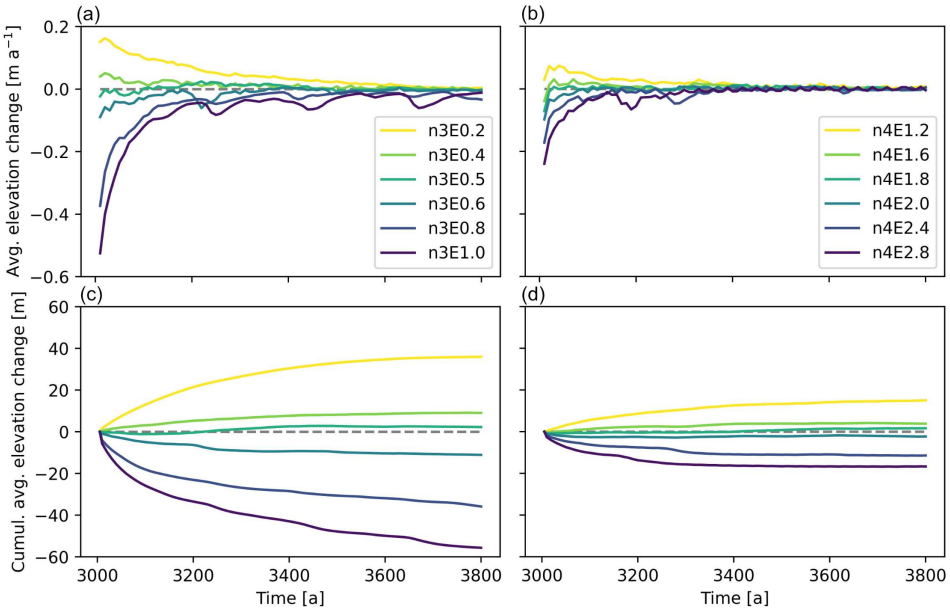

Figure 6: Elevation changes for different simulations: (a) and (b) show the average elevation changes, and (c) and (d) show the cumulative elevation changes for Glen's flow law exponents of $n = 3$ and $n = 4$, respectively, for varying enhancement factors. Legends indicate the different model runs in colour.

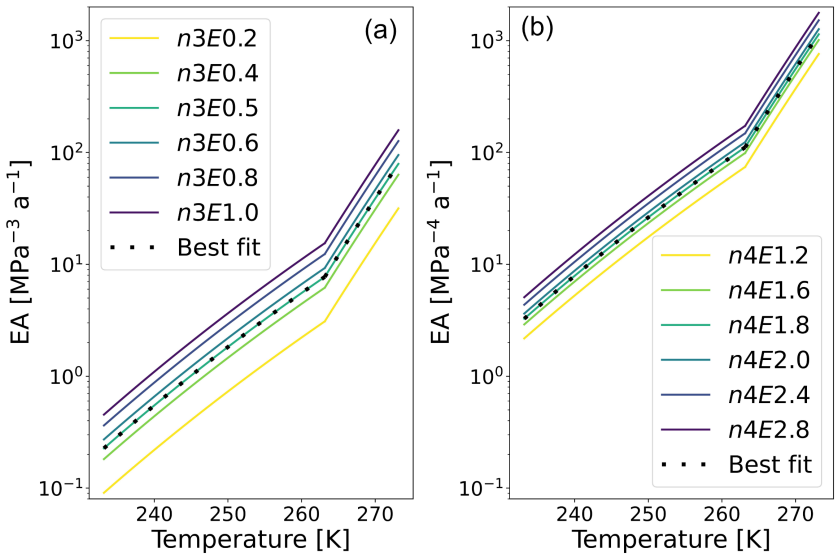

Figure 7: The relationship between the temperature and the Arrhenius law multiplied by varying enhancement factors, E; (a) corresponds with the $n = 3$ simulations and (b) with the $n = 4$ simulations. Note the y-axes have a logarithmic scale. In (a) and (b), the dotted lines indicate the most suitable combination of parameters for the simulations of Derwael Ice Rise.

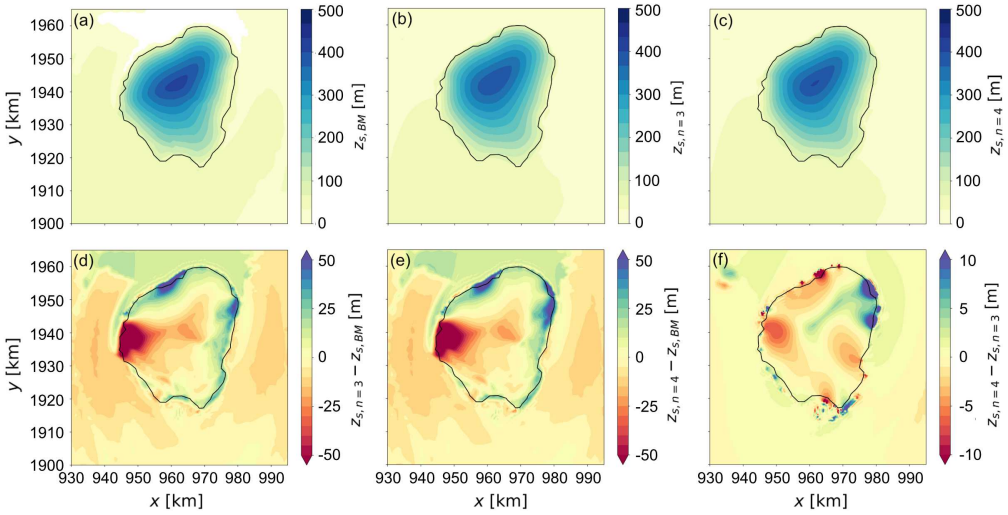

Figure 8: Surface elevation (a) from BedMachine Antarctica data, and (b) and (c) show the surface elevation of the $n = 3$ and $n = 4$ simulations, respectively, after the 400 year transient velocity spin up. The difference in surface elevation between the $n = 3$ simulation and the BedMachine data is shown in (d), the difference in surface elevation between the $n = 4$ simulation and the BedMachine data is shown in (e) and the difference in surface elevation between the $n = 4$ simulation and the $n = 3$ simulation is shown in (f). Note that (f) has a different colour scale than (d) and (e).

Fig. 10 shows the difference between the observed and modelled $n = 3$ isochronal slope for the cross-sections $A-A'$ to $F-F'$ in Fig. 1. Generally, the slopes of the modelled isochrones match well with the observed isochronal slopes. Areas where there is a close match between observed and modelled isochrones are indicated by white in Fig. 10. At all grounding lines around the ice rise, there is significant steepening of isochrones due to the downward motion of ice. Given the general tendency of the ice rise to broaden in the grounding zones, the steepening of the modelled isochrones tend to be located a small distance from the observed isochrones, but reproduce similar patterns in isochrone geometry. On the stoss side of the ice rise, thinning of the stratigraphy indicates sudden acceleration of ice a few kilometres away from the grounding line. This is particularly evident in the cross-sections $A - A'$.

In the observational data, the Raymond arch at the ridge divide is visible in the cross-sections $B - B'$, $C - C'$, $F - F'$ and $G - G'$. The side arch identified in Drews et al. (2015) is also visible in the cross-section $F - F'$. In Fig. 9e, the side arch visible in the observed isochrones is noticeable at a depth corresponding to the first modelled isochrone below the surface, which has an age of 100 years.

4.3 Velocities and strain rates

Simulated ice-shelf velocities on the western side of the ice rise are over 300 ma^{-1} and roughly 200 ma^{-1} on the eastern side. This is because of the location of the tributary Western Ragnhild Glacier. The asymmetry of the surrounding ice shelf results in an asymmetry in the divergence of the flow of ice around the ice rise. The simulated velocity field of the ice rise shows a distinct ridge divide on the northern side of the ice rise, with the divide positioned diagonally from the north east to the south west.

Absolute surface velocity differences between the $n = 3$ and the $n = 4$ simulations are generally below 10 % with the exception of the divide and the north-eastern and south-eastern sides of the ice rise (Fig. S2 in the Supporting Information). The largest negative velocity differences occur in north-eastern and south-eastern sides of the ice rise with higher velocities in the $n = 3$ simulation. In the talwegs, velocities are higher in the $n = 4$ simulation. Note that talweg is a term first introduced in relation to ice rises in Gillet-Chaulet et al. (2011) and is a geomorphological term describing a valley. At the ridge divide,

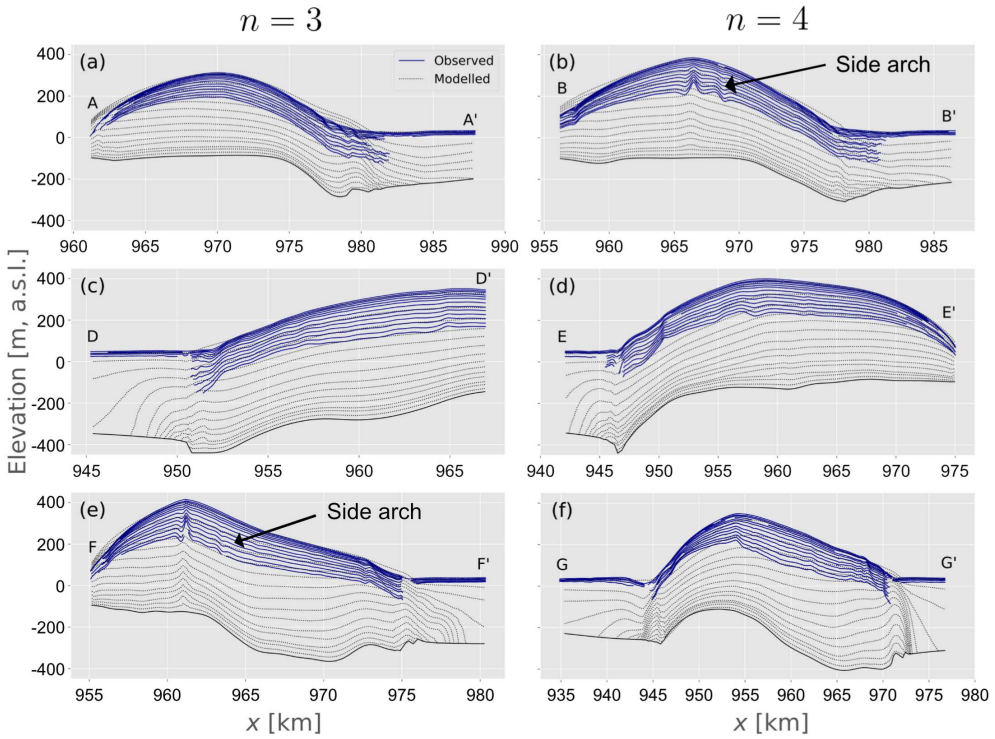

Figure 9: Comparisons between modelled and observed stratigraphy along radar profiles marked in 1 in the vertical domain of the model. Graphs in left columns, (a), (c), and (e), show comparisons for a Glen's flow law exponent of $n = 3$ (cross-sections $A - A'$, $D - D'$ and $F - F'$), and the right column, (b), (d), and (f), show comparisons for a Glen's flow law exponent of $n = 4$ (cross-sections $B - B'$, $E - E'$ and $G - G'$). The blue solid lines show the observed stratigraphy and the dotted black lines show the modelled stratigraphy.

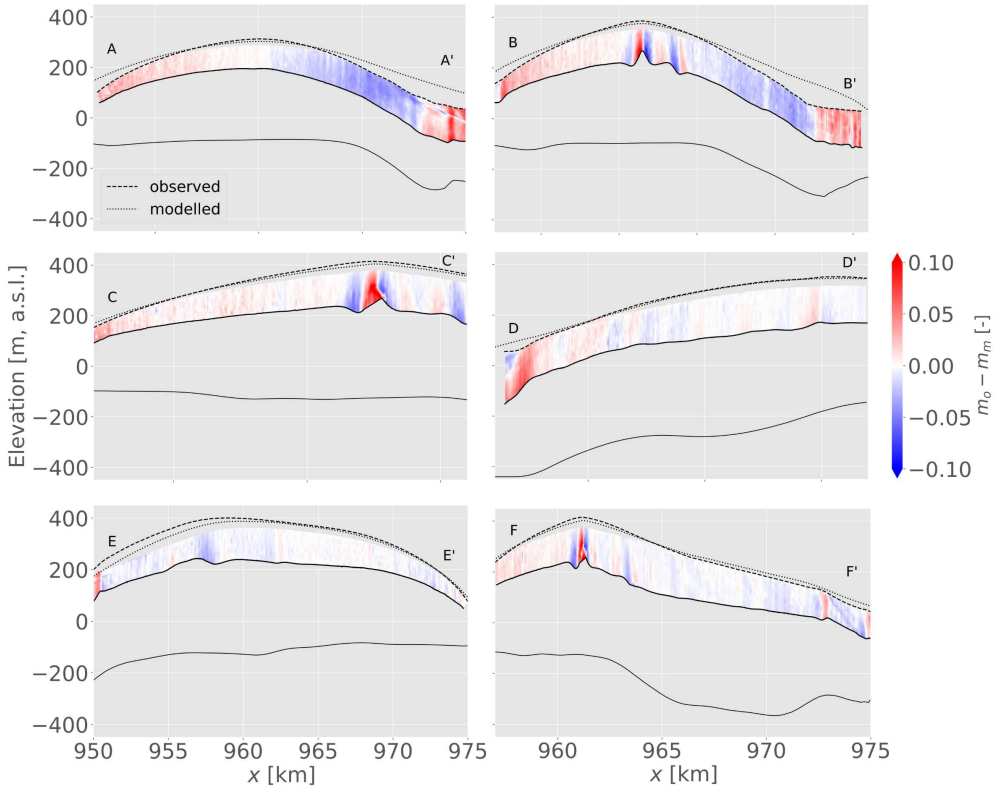

Figure 10: Difference between observed isochrone slope (m_o) and the $n = 3$ modelled isochrone slope (m_m) at locations where data is available for both. The cross-sections $A - A'$ to $F - F'$ correspond with the radar profiles in Fig. 1. The dashed lines show the observed ice surface and the dotted lines show the modelled surface. The lower extent of the area of comparison and the lower ice surface are shown with solid black lines.

the velocities are significantly lower in the $n = 4$ simulation than the $n = 3$ simulation. In the areas perpendicular to the centre of the ridge divide, the $n = 4$ simulation has higher velocities than the $n = 3$ simulation. Elsewhere, the $n = 3$ simulation has higher velocities than the $n = 4$ simulation. A similar pattern of velocity difference between the $n = 3$ and the $n = 4$ simulations is observed at the depth of the 1000 year isochrone (Fig. S2 in the Supporting Information). Percentage differences in velocities are more pronounced in the talwegs at the 1000 year isochrone than at the ice surface. The flanks perpendicular to the ridge divide show higher velocities in the case of the $n = 4$ simulation than the $n = 3$ simulation. Furthermore, there are pronounced higher velocities in the $n = 3$ simulation in the south of the ice rise. Here, there is higher divergence of the velocity vectors (Fig. 12a), but not enough for an additional ridge or Raymond arches to form.

At the base of the ice rise, some basal sliding occurs. Lowest basal velocities of < 1 ma^{-1} are simulated under the ridge divide and increase towards the flanks of the ice rise (Fig. S3a in the Supporting Information). Interestingly, from the centre of the ice rise to the south-eastern corner, there is an area of low velocity compared with elsewhere in the flanks of the ice rise. In three locations in the grounded ice, close to the grounding line, there is a higher basal sliding velocity of 5 ma^{-1}. This indicates that there is a higher effective stress in these areas, leading to acceleration of the ice. In both the $n = 3$ and $n = 4$ simulations, the same basal friction parameterisation is used, and so differences in the basal velocities are due to feedbacks with the overlying ice. A comparison of the basal velocities between the two simulations reveals that the largest differences are seen in the grounding zones, where basal velocities in the $n = 4$ simulation are higher than in the $n = 3$ simulation (Fig. S3b in the Supporting Information). In the interior of the ice rise at the flanks of the ridge divide, velocities in the $n = 3$ simulation are higher than in the $n = 4$ simulation.

The computed ice surface shear strain rate in the direction of ice flow shows a similar pattern to the ice velocity. Higher shear strain rates are observed on the western side of the ice rise. These result from the larger velocities in the ice shelf (Fig. 11). On the eastern side of the ice rise, the shear strain rates are lower than on the western side. The areas of higher shear strain rate on the eastern side are concentrated in two areas; in the north east and the south east of the ice rise. The area of lower shear strain rate between the areas of higher shear strain rate are a consequence of velocities from the ice rise and ice shelf being more similar in magnitude. Differences in shear strain rates between the $n = 3$ and $n = 4$ simulations primarily occur on the western side of the ice rise. Differences on the eastern side of the ice rise are negligible in comparison and localised differences are likely due to slight differences in grounding line position.

Differences in ice velocity between the simulations also affect the computed internal stratigraphy. For both simulations, the oldest ice at a depth of 95 % is located at the ridge and on the stoss side of the ice rise. Here, convergence of flow from the ice rise and the ice shelf results in relatively stagnant ice velocities (Fig. S1 in the Supporting Information). The age field at a depth of 95 % shows that ice is on average 335 years older in the case of the $n = 3$ simulation. This reflects the higher strain rates and thus enhanced thinning of ice under a higher Glen's flow law exponent. At a depth of 50 %, differences in age are much less, with ice being between 25 and 50 years older at the divide in the case of the $n = 4$ simulation. The largest differences in age at a depth of 50 % are seen in the area of compression between the ice rise and the ice shelf and in the north-eastern corner of the ice rise, with ice being more than 50 years older in the case of the $n = 4$ simulation. The opposite is seen in the talwegs, where ice is older in the case of the $n = 3$ simulation at a depth of 50 %.

5 Discussion

5.1 Progress and challenges for three-dimensional ice rise modelling

Previous research has highlighted the importance of ice rises in deciphering past re-organisation of flow. Until now, the comparison between observed and modelled internal stratigraphy has

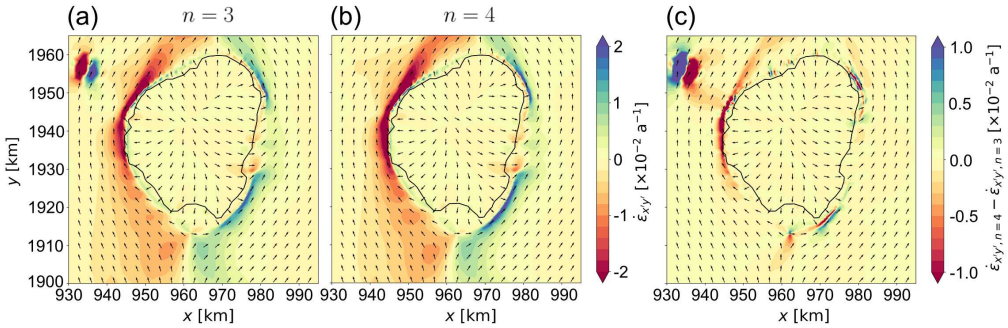

Figure 11: Shown in (a) and (b) is the shear strain rate for the $n = 3$ and $n = 4$ simulations, respectively, calculated by rotating the strain rate tensor to align with the velocity direction. In (c), the difference between the shear strain rate in the direction of the velocity of the $n = 4$ and $n = 3$ simulations is shown.

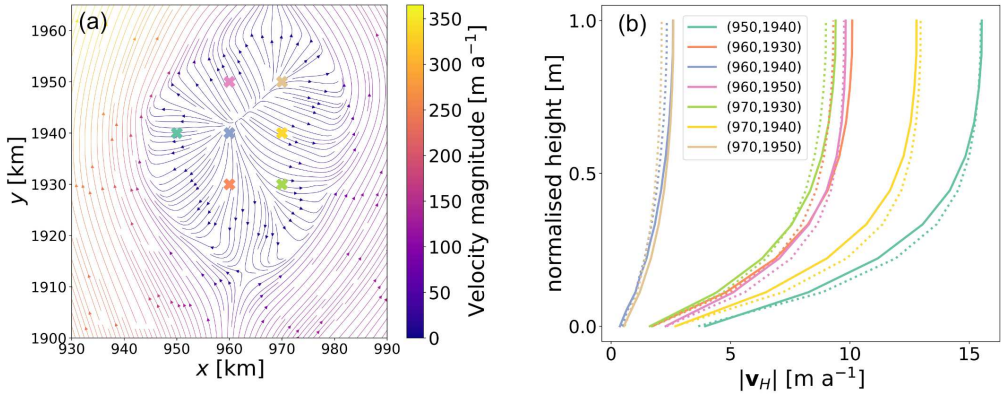

Figure 12: (a) shows the velocity field of Derwael Ice Rise, (b) shows the horizontal velocity magnitude for the (x, y) coordinates marked in (a), for the $n = 3$ simulation (solid lines) and the $n = 4$ simulation (dashed lines).

been restricted to flow-line setups, providing a spatially limited assessment (Martín et al., 2006, 2009; Drews et al., 2015). We introduce a new three-dimensional modelling framework that overcomes these limitations and allows us to provide a spatially continuous age field that can be compared with radar observations. This provides an important step towards the routine simulation of ice rises and the ultimate goal of using them to constrain paleo ice-sheet simulations.

During the development of our modelling framework, we encountered a number of challenges. Given their small size, ice rises are often insufficiently resolved in continental-scale boundary datasets such as BedMachine or RACMO2.3p1. This can only be overcome if in-situ and high-resolution datasets are available to correct for these mismatches. The multiple steps necessary to spin-up the model are in parts subjective and a different sequence of spin-up steps of different simulation lengths may result in slightly differing results. As highlighted previously, it is important to note that interpolation errors in the bed elevation do occur and it may be necessary to make comparisons with the raw data. Failure to correct anomalies in the bed elevation data can result in artefacts in transient simulations, for example, a thickening of the ice rise after initialisation. This highlights the importance of such measurements to allow such studies for other ice rises around Antarctica.

The drift correction to the SMB implemented in our study results in an SMB field which is higher than the RACMO2.3p1 dataset (roughly 0.5 m a^{-1} higher) in the centre of the ice rise and lower closer to the margins of the ice rise than in the stratigraphy-adjusted SMB field. This points to a slight over-compensation of the ice softness and perhaps missing processes at the margins of the ice rise such as fracturing, higher melt rates or an anisotropic fabric or another process which would increase the velocity of the ice in that area. Another explanation is that the ice in the centre of the ice rise is stiffer in reality than in the model. As shown in Martín et al. (2009) and Martín and Gudmundsson (2012), anisotropic evolution of ice is a mechanism which enhances the stiffness of ice at an ice divide and the lack of this mechanism in our model is a likely reason for excess thinning of ice at the divide.

5.2 Comparison between modelled and observed stratigraphy

Much progress has been made in comparing modelled and observed internal stratigraphy (Sutter et al. (2021) and Born and Robinson (2021)) on large scales. For Stokes simulations, comparisons between modelled and observed stratigraphy have only been performed for two-dimensional simulations (Martín et al., 2009; Martín and Gudmundsson, 2012; Drews et al., 2015) and have so far not included the grounding line and the surrounding shelf. Including the ice shelf in the simulation domain means that grounding zone processes are included in the simulations and the domain boundaries are no longer within the bounds of the grounded area of the ice rise. Such a setup also allows investigation of isochrones in the shear zone between the ice rise and ice shelf which is characterised by steep isochrone geometries that are difficult to capture with radar observations.

The comparisons between the observed and modelled isochronal slopes in Fig. 10 show a close fit overall, with larger differences in the north east of the ice rise where issues with the bed elevation were found. Furthermore, differences are larger at the main Raymond arch where too coarse vertical resolution results in greater mismatches. Differences in isochrone slopes are primarily due to a mismatch in the surface elevation between modelled and observed results. The largest differences are seen in the north east of the ice rise and at the main Raymond arch and the side arch, which is not captured in the model. The side arch visible in the observed isochrones in Fig. 9e is visible at a depth corresponding to the first modelled isochrone below the surface which has an age of 100 years.

By studying areas where the surface elevation between the observed and modelled stratigraphy is similar, we can identify processes in ice dynamics which are not reproduced by the model. In cross-section $D - D'$, there is a deviation in isochrone slope at $x = 957$ km when comparing the modelled isochrones to the observed isochrones. A greater thinning of the isochrones in the observed stratigraphy indicates that the modelled ice may not adequately reproduce speed-up of the ice in this area. In the cross-section $G - G'$, the acceleration of ice seen in the observed stratigraphy is not reproduced to the same extent in the model on the western side of the cross-section. On the eastern side of the $G - G'$ cross-section, the mod-

elled stratigraphy shows more gentle slopes than the observed stratigraphy, indicating that in the direction of the grounding zone, modelled ice is accelerating more than the observed ice.

The side arch marked in Fig. 9b was discussed in previous work and it was suggested that it may be a result of unresolved three-dimensional effects (Drews et al., 2015). The lack of a side arch in our three-dimensional simulations indicates that this is not the case and we instead hypothesise that Derwael Ice Rise was previously a triple junction ice rise and that a ridge was previously located where the side arch is seen in the observed stratigraphy. If this is the case, then a transition from a triple junction ice rise to a ridge divide ice rise is quite recent (¡ 100 years) as the side arches are also evident close to the surface. This then suggests that ice rises can have signatures of both ice-divide stability (evidenced by the oversized Raymond arches beneath the contemporary divide) and instability (evidenced by the side arch interpreted as a remnant of a ice-divide triple junction). Furthermore, it cannot be ruled out that the flow divide had switched more than once between the main arch and the side arch.

Comparing the modelled isochrones to the observed isochrones in the shear zone, we see that in the grounding zone, the observed isochrones steepen closer to the ice rise interior than the modelled isochrones. This is due to a grounding line advance in the simulations as a result of too little shear softening in the modelled shear zones around the ice rise, perhaps due to missing processes such as fracturing or an anisotropic fabric. An alternative approach to reducing the grounding line advance would be to alter the Arrhenius pre-factor to allow for softer ice, but this would result in a reduction of the ice rise elevation.

5.3 Glen's flow law exponent

In our study, we have investigated the influence of using a Glen's flow law exponent of $n = 3$ and $n = 4$. The $n = 4$ simulation results in a more peaked shape (Fig. 8). Both the $n = 3$ and the $n = 4$ simulations result in a slight lowering of the surface elevation in the ridge divide area, with the $n = 4$ simulation resulting in a surface elevation closer to that of the observed surface elevation. This is an indicator that a Glen's flow law exponent of $n = 4$ is more suitable, but a general tendency for excess thickening in the grounding zones means this result is not without uncertainty. The lower velocities in the $n = 4$ simulation compared with the $n = 3$ simulation align with our understanding of the Raymond effect, with lower velocities and greater Raymond arch amplitude associated with a higher Glen's flow law exponent. Interestingly, the differences in the flanks of the ice rise indicate different responses to the non-linearity that result in slight differences in flow regime.

Predicted age–depth relationships differ by < 5 % in most areas for simulations with $n = 3$ and $n = 4$ (Fig. S1 in the Supporting Information). This suggests that tuning of the Arrhenius factor and the drift-correction for the $n = 3$ and $n = 4$ simulations lead to similar velocity fields in both cases. Exceptions are the divide regions and the shear zones at the ice-rise boundaries where differences are significant. Larger differences are seen in areas where stresses are significantly higher or lower than average stresses. Strain rates in the ice are higher in the $n = 4$ than the $n = 3$ simulation in the shear zones and near the ice-bed interface. Despite these differences, the modelled stratigraphy does not differ significantly. Studies for which an appropriate Arrhenius factor for an exponent of $n = 4$ have so far only been performed with two-dimensional simulations (Martín et al., 2006; Drews et al., 2015), resulting in uncertainties due to the lack of through-plane velocities. A conversion of the Glen's flow law from an exponent of $n = 3$ to $n = 4$ is further complicated by the dependence of the Arrhenius law on the temperature, activation energy, and n itself. Notably, significant uncertainty exists within these parameters as they have been calibrated through few laboratory studies in specific conditions (Zeitz et al., 2020). In our conversion, we neglect differences in activation energies and use a typical stress, $[\tau_0]$, to calculate an initial guess for an appropriate Arrhenius Law for $n = 4$. This simplified scaling is useful as we are able to compare parameters within our model to observed stratigraphy, highlighting the most appropriate values for the flow law. The chosen typical stress is within a reasonable range as in Goldsby and Kohlstedt (2001) and Goldsby (2006). In conjunction with known uncertainties in our understanding of the kinetics of glacier ice, implies that constraints

on mechanisms such as temperature, activation energy, and grain size implicit within the Arrhenius relation are necessary to better understand the kinetics of creep on natural glacier ice.

Due to the assumption that ice is incompressible, the horizontal dilation (Figs. S4 and S5 in the Supporting Information) is the equivalent of the vertical strain rate, $\dot{\varepsilon}_{zz}$, with a sign change. We assume that differences in strain rate with and without a firn column do not differ greatly. The higher horizontal dilation in the north-western and eastern talwegs in the $n = 4$ simulation than the $n = 3$ simulation implies that there is greater stretching occurring in the ice. The opposite effect is seen in the vicinity of the ice rise ridge divide, with a lower dilation in the case of the $n = 4$ simulation. These small-scale results, which are in agreement with those presented in Gillet-Chaulet et al. (2011), are an analogy for larger scale situations. On larger scales, the higher dilation in areas of high velocity is likely to have consequences for the timing of the onset of an ice stream. Interestingly, in our simulations of Derwael Ice Rise, the south-western region of the ice rise shows a large area where the dilation is lower in the case of the $n = 4$ simulation than the $n = 3$ simulation, resulting in a region which does not contain a ridge divide, but also does not have strain rate differences which one would expect in the talweg of an ice rise. These characteristics are indicative of an ice rise which is in a state close to having a triple junction flow regime. Furthermore, the spatial variation in dilation and the resulting change in distance between isochrones could help in future to determine a correct Glen's flow law exponent.

In Fig. 11, it can be seen that there are higher shear strain rates in the direction of flow in the shear margins in the case of the $n = 4$ simulation than in the $n = 3$ simulation. This result implies softer ice in shear margins when using a $n = 4$ simulation, indicative of viscous deformation at the higher strain rates. When investigating threshold shear strain rates or shear stresses beyond which fracturing occurs, it is important to bear in mind that a differing Glen's flow law exponent will have a differing effect in simulations. An important observation is that the ice rumple north-west of Derwael Ice Rise becomes less grounded in the case of the $n = 4$ simulation, which we attribute to the greater strain-rate softening of the ice for the higher Glen's flow law exponent. This has consequences for simulations including pinning points as the choice of Glen's flow law exponent may have an influence on the buttressing due to that pinning point. Moreover, the higher flux of ice into the ice shelf coming from the talweg on the eastern side of Derwael Ice Rise, results in low shear strain rates in the grounding zone compared with the shear zones upstream and downstream.

5.4 Model limitations and future research directions

We have assumed that Derwael Ice Rise is in steady state and have found parameter values which result in a steady-state geometry close to the present-day observed geometry. Extra care would need to be taken when modelling other ice rises which do not satisfy the steady-state criterion. The boundary and initial conditions of our model are dependent on both observational data and model output (from regional atmospheric climate model RACMO2.3p1). It is important to check for interpolation errors using the raw data. Failure to correct for the bed elevation led to a series of flawed transient simulations in our case. Furthermore, we have not coupled anisotropy evolution to our model as there is insufficient anisotropy data available to constrain the model. Inclusion of ice-anisotropy will increase Raymond arch amplitudes. In future work, three-dimensional ice rises will provide ideal locations for the analysis of differing anisotropy schemes as well as other physical processes such as ice fracture in the shear margins.

Ice rises are good locations to study the effect of ice flow parameters across different flow regimes. The isochronal patterns observed near the base and surface are directly linked to the SMB and BMB fields. Simply adjusting the SMB and BMB fields using the change in surface elevation after initialisation does not, however, suffice for inferring the correct boundary conditions. We have therefore first adjusted A and n in the Glen's flow law (Glen, 1958). The parameter n has an influence on the proportions of the dome shape of the ice rise as shown in, for example, Gillet-Chaulet et al. (2011). A range of Arrhenius factors, A, then need to be tested with the various Glen's flow law exponents, n, in order to obtain an optimal ice rise geometry. A further source of uncertainty is in the basal friction parameterisation. Assuming

that there is negligible basal sliding where there is substantial horizontal divergence of ice flow, an adjustment of the basal friction parameter can be made until there is sufficient thinning of ice in the talweg and no thinning elsewhere. We acknowledge that although we aim to independently adjust the ice flow parameterisations and boundary conditions they are none-the-less dependent on one-another. We argue, however, that with the steps we have taken in model calibration and comparison with isochrones, we have moved a step closer to independently determining model parameters.

6 Conclusions

We have introduced a new three-dimensional ice-rise modelling framework that includes an ice rise, a grounding line, and the surrounding ice shelf. This framework allows us to compare the modelled three-dimensional stratigraphy with the observed stratigraphy. The modelling framework presented here can be transferred as is to other ice rises of interest to predict the age-depth fields prior to ice-core drilling and also to continue constraining ice-flow parameters relevant for continent-wide simulations. Overall, we find that the modelled stratigraphy of Derwael Ice Rise matches well with observed stratigraphy except in regions where there is uncertainty in the bed elevation. We predict 8000 year old ice at 95 % depth and spatial age gradients at intermediate depth are significant reflecting the spatial variability in SMB. Observed arches in the ice-rise flanks cannot be reproduced and are likely a remnant of a former ice-divide triple junction that has disappeared in the last 100 years.

The presented modelling framework provides a blueprint for the simulation of other ice rises with Glen's flow exponents of $n = 3$ and $n = 4$ to make comparisons with ice cores or observational stratigraphy with the hopes of narrowing down uncertainties in other model parameters in the future, such as temperature and grain size. Simulations with differing $n = 3$ and $n = 4$ broadly result in similar velocity and age-depth fields if the temperature dependent viscosity factors are tuned accordingly. Exceptions are areas close to the ice divide, the peripherial shear zones and in the ice close to the ice-bed interface, helping to establish limits on the strain rates that permit viscous flow. Furthermore, this framework is a valuable first step towards testing and constraining various physical processes such as fracturing and anisotropy, perhaps constrained with quad-polarimetric radar measurements (Ershadi et al., 2022).

Code and data availability

The code for the simulations can be found at https://github.com/henryclara/Derwael/ and the code to produce the figures in the paper can be found at:
https://github.com/henryclara/DerwaelAccompanyingCode.

Data for producing the figures and the data used as input to the model can be found at:
https://nc-geophysik.guz.uni-tuebingen.de/index.php/s/7PdWiGeFJdFGMKH.

Acknowledgements

C. Henry was supported by the Deutsche Forschungsgemeinschaft (DFG) in the framework of the priority programme 1158 "Antarctic Research with comparative investigations in Arctic ice areas" by a grant SCHA 2139/1-1. C. Schannwell was supported by the German Federal Ministry of Education and Research (BMBF) as a Research for Sustainability initiative (FONA) through the PalMod project under the grant number 01LP1915C. R. Drews and V. Višnjević were supported by an Emmy Noether Grant of the Deutsche Forschungsgemeinschaft (DR 822/3-1). This work used resources of the Deutsches Klimarechenzentrum (DKRZ) granted by its Scientific Steering Committee (WLA) under project ID bm1164.

References

P. D. Bons, D. Jansen, F. Mundel, C. C. Bauer, T. Binder, O. Eisen, M. W. Jessell, M.-G. Llorens, F. Steinbach, D. Steinhage, et al. Converging flow and anisotropy cause large-scale folding in greenland's ice sheet. *Nature communications*, 7(1):1–6, 2016.

P. D. Bons, T. Kleiner, M.-G. Llorens, D. J. Prior, T. Sachau, I. Weikusat, and D. Jansen. Greenland ice sheet: Higher nonlinearity of ice flow significantly reduces estimated basal motion. *Geophysical Research Letters*, 45(13):6542–6548, 2018.

A. Born and A. Robinson. Modeling the greenland englacial stratigraphy. *The Cryosphere*, 15(9):4539–4556, 2021.

W. Budd and T. Jacka. A review of ice rheology for ice sheet modelling. *Cold Regions Science and Technology*, 16(2):107–144, 1989. ISSN 0165-232X. doi: https://doi.org/10.1016/0165-232X(89)90014-1. URL `https://www.sciencedirect.com/science/article/pii/0165232X89900141`.

D. Callens, K. Matsuoka, D. Steinhage, B. Smith, E. Witrant, and F. Pattyn. Transition of flow regime along a marine-terminating outlet glacier in East Antarctica. *The Cryosphere*, 8(3):867–875, May 2014. ISSN 1994-0424. doi: 10.5194/tc-8-867-2014.

D. Callens, R. Drews, E. Witrant, M. Philippe, and F. Pattyn. Temporally stable surface mass balance asymmetry across an ice rise derived from radar internal reflection horizons through inverse modeling. *Journal of Glaciology*, 62(233):525–534, June 2016. ISSN 0022-1430, 1727-5652. doi: 10.1017/jog.2016.41.

M. G. Cavitte, H. Goosse, S. Wauthy, T. Kausch, J.-L. Tison, B. Van Liefferinge, F. Pattyn, J. T. Lenaerts, and P. Claeys. From ice core to ground-penetrating radar: representativeness of smb at three ice rises along the princess ragnhild coast, east antarctica. *Journal of Glaciology*, 68(272):1221–1233, 2022. doi: 10.1017/jog.2022.39.

J. C. Comiso. Variability and trends in antarctic surface temperatures from in situ and satellite infrared measurements. *Journal of Climate*, 13(10):1674–1696, May 2000. ISSN 0894-8755, 1520-0442. doi: 10.1175/1520-0442(2000)013¡1674:VATIAS¿2.0.CO;2.

R. Drews, K. Matsuoka, C. Martín, D. Callens, N. Bergeot, and F. Pattyn. Evolution of Derwael Ice Rise in Dronning Maud Land, Antarctica, over the last millennia. *Journal of Geophysical Research: Earth Surface*, 120(3):564–579, Mar. 2015. ISSN 21699003. doi: 10.1002/2014JF003246. URL `http://doi.wiley.com/10.1002/2014JF003246`.

R. Drews, C. Schannwell, T. Ehlers, R. Gladstone, F. Pattyn, and K. Matsuoka. Atmospheric and oceanographic signatures in the ice shelf channel morphology of roi baudouin ice shelf, east antarctica, inferred from radar data. *Journal of Geophysical Research: Earth Surface*, 125(7):e2020JF005587, 2020.

M. R. Ershadi, R. Drews, C. Martín, O. Eisen, C. Ritz, H. Corr, J. Christmann, O. Zeising, A. Humbert, and R. Mulvaney. Polarimetric radar reveals the spatial distribution of ice fabric at domes and divides in east antarctica. *The Cryosphere*, 16(5):1719–1739, 2022. doi: 10.5194/tc-16-1719-2022. URL `https://tc.copernicus.org/articles/16/1719/2022/`.

L. Favier and F. Pattyn. Antarctic ice rise formation, evolution, and stability. *Geophysical Research Letters*, 42(11):4456–4463, June 2015. ISSN 0094-8276, 1944-8007. doi: 10.1002/2015GL064195. URL `https://onlinelibrary.wiley.com/doi/abs/10.1002/2015GL064195`.

L. Favier, F. Pattyn, S. Berger, and R. Drews. Dynamic influence of pinning points on marine ice-sheet stability: a numerical study in Dronning Maud Land, East Antarctica. *The Cryosphere*, 10(6):2623–2635, Nov. 2016. ISSN 1994-0424. doi: 10.5194/tc-10-2623-2016. URL `https://tc.copernicus.org/articles/10/2623/2016/`.

S. Franke, P. D. Bons, J. Westhoff, I. Weikusat, T. Binder, K. Streng, D. Steinhage, V. Helm, O. Eisen, J. D. Paden, et al. Holocene ice-stream shutdown and drainage basin reconfiguration in northeast greenland. *Nature Geoscience*, pages 1–7, 2022.

O. Gagliardini, T. Zwinger, F. Gillet-Chaulet, G. Durand, L. Favier, B. de Fleurian, R. Greve, M. Malinen, C. Martín, P. Råback, J. Ruokolainen, M. Sacchettini, M. Schäfer, H. Seddik, and J. Thies. Capabilities and performance of Elmer/Ice, a new-generation ice sheet model. *Geoscientific Model Development*, 6(4):1299–1318, Aug. 2013. ISSN 1991-9603. doi: 10.5194/gmd-6-1299-2013. URL `https://gmd.copernicus.org/articles/6/1299/2013/`.

F. Gillet-Chaulet and R. C. Hindmarsh. Flow at ice-divide triple junctions: 1. three-dimensional full-stokes modeling. *Journal of Geophysical Research: Earth Surface*, 116 (F2), 2011.

F. Gillet-Chaulet, R. C. A. Hindmarsh, H. F. J. Corr, E. C. King, and A. Jenkins. *In-situ* quantification of ice rheology and direct measurement of the Raymond Effect at Summit, Greenland using a phase-sensitive radar. *Geophysical Research Letters*, 38(24):n/a–n/a, Dec. 2011. ISSN 00948276. doi: 10.1029/2011GL049843. URL `http://doi.wiley.com/10.1029/2011GL049843`.

J. Glen. The flow law of ice: A discussion of the assumptions made in glacier theory, their experimental foundations and consequences. *IASH Publ*, 47(171):e183, 1958.

J. W. Glen. The creep of polycrystalline ice. *Proceedings of the Royal Society of London. Series A. Mathematical and Physical Sciences*, 228(1175):519–538, 1955.

V. Goel, C. Martín, and K. Matsuoka. Ice-rise stratigraphy reveals changes in surface mass balance over the last millennia in dronning maud land. *Journal of Glaciology*, 64(248): 932–942, 2018. doi: 10.1017/jog.2018.81.

D. L. Goldsby. Superplastic flow of ice relevant to glacier and ice-sheet mechanics. *Glacier science and environmental change*, pages 308–314, 2006.

D. L. Goldsby and D. L. Kohlstedt. Superplastic deformation of ice: Experimental observations. *Journal of Geophysical Research: Solid Earth*, 106(B6):11017–11030, 2001.

A. C. J. Henry, R. Drews, C. Schannwell, and V. Višnjević. Hysteretic evolution of ice rises and ice rumples in response to variations in sea level. *The Cryosphere*, 16(9):3889–3905, 2022. doi: 10.5194/tc-16-3889-2022. URL `https://tc.copernicus.org/articles/16/3889/2022/`.

R. C. Hindmarsh, E. C. King, R. Mulvaney, H. F. Corr, G. Hiess, and F. Gillet-Chaulet. Flow at ice-divide triple junctions: 2. three-dimensional views of isochrone architecture from ice-penetrating radar surveys. *Journal of Geophysical Research: Earth Surface*, 116 (F2), 2011.

K. C. Jezek. Observing the antarctic ice sheet using the radarsat-1 synthetic aperture radar. *Polar Geography*, 27(3):197–209, 2003. doi: 10.1080/789610167. URL `https://doi.org/10.1080/789610167`.

I. Koch, R. Drews, L. S. Muhle, S. Franke, D. Jansen, F. Oraschewski, H. Spiegel, V. Višnjević, K. Matsuoka, F. Pattyn, and O. Eisen. Internal reflection horizons of ice shelves and ice rises in eastern dronning maud land (east antarctica) from multisystem radio-echo sounding data [in review]. *PANGAEA*. doi: https://doi.pangaea.de/10.1594/PANGAEA.950383.

I. Koch, R. Drews, S. Franke, D. Jansen, F. M. Oraschewski, L. Muhle, V. Višnjević, K. Matsuoka, F. Pattyn, and O. Eisen. Radar internal reflection horizons from multisystem data reflect ice dynamic and surface accumulation history along the princess ragnhild coast, dronning maud land, east antarctica [in review]. *Journal of Glaciology*, 2023.

C. Martín and G. H. Gudmundsson. Effects of nonlinear rheology, temperature and anisotropy on the relationship between age and depth at ice divides. *The Cryosphere*, 6(5):1221–1229, 2012. doi: 10.5194/tc-6-1221-2012. URL https://tc.copernicus.org/articles/6/1221/2012/.

C. Martín, R. C. A. Hindmarsh, and F. J. Navarro. Dating ice flow change near the flow divide at Roosevelt Island, Antarctica, by using a thermomechanical model to predict radar stratigraphy. *Journal of Geophysical Research*, 111(F1):F01011, 2006. ISSN 0148-0227. doi: 10.1029/2005JF000326. URL http://doi.wiley.com/10.1029/2005JF000326.

C. Martín, R. C. A. Hindmarsh, and F. J. Navarro. On the effects of divide migration, along-ridge flow, and basal sliding on isochrones near an ice divide. *Journal of Geophysical Research*, 114(F2):F02006, Apr. 2009. ISSN 0148-0227. doi: 10.1029/2008JF001025. URL http://doi.wiley.com/10.1029/2008JF001025.

C. Martín, G. H. Gudmundsson, and E. C. King. Modelling of Kealey Ice Rise, Antarctica, reveals stable ice-flow conditions in East Ellsworth Land over millennia. *Journal of Glaciology*, 60(219):139–146, 2014. ISSN 0022-1430, 1727-5652. doi: 10.3189/2014JoG13J089.

J. D. Millstein, B. M. Minchew, and S. S. Pegler. Ice viscosity is more sensitive to stress than commonly assumed. *Communications Earth & Environment*, 3(1):1–7, 2022.

M. Morlighem, E. Rignot, T. Binder, D. Blankenship, R. Drews, G. Eagles, O. Eisen, F. Ferraccioli, R. Forsberg, P. Fretwell, et al. Deep glacial troughs and stabilizing ridges unveiled beneath the margins of the antarctic ice sheet. *Nature Geoscience*, 13(2):132–137, 2020.

N. A. Nereson, C. F. Raymond, E. D. Waddington, and R. W. Jacobel. Migration of the siple dome ice divide, west antarctica. *Journal of Glaciology*, 44(148):643–652, 1998. ISSN 0022-1430, 1727-5652. doi: 10.3189/S0022143000002148.

M. Philippe, J.-L. Tison, K. Fjøsne, B. Hubbard, H. A. Kjær, J. Lenaerts, R. Drews, S. G. Sheldon, K. De Bondt, P. Claeys, et al. Ice core evidence for a 20th century increase in surface mass balance in coastal dronning maud land, east antarctica. *The Cryosphere*, 10 (5):2501–2516, 2016.

C. F. Raymond. Deformation in the Vicinity of Ice Divides. *Journal of Glaciology*, 29(103): 357–373, 1983. ISSN 0022-1430, 1727-5652. doi: 10.1017/S0022143000030288.

J. M. Rignot, E. and B. Scheuchl. Measures insar-based antarctica ice velocity map, version 2, 2017. URL https://nsidc.org/data/NSIDC-0484/versions/2.

C. Ritz. *Time dependent boundary conditions for calculation of temperature fields in ice sheets. In: E. D. Waddington and J. S. Walder (Eds.), The Physical Basis of Ice Sheet Modelling, IAHS Publication No. 170, pp. 207–216.* IAHS Press, Wallingford, UK, 1987.

C. Schannwell, R. Drews, T. A. Ehlers, O. Eisen, C. Mayer, and F. Gillet-Chaulet. Kinematic response of ice-rise divides to changes in ocean and atmosphere forcing. *The Cryosphere*, 13(10):2673–2691, Oct. 2019. ISSN 1994-0424. doi: 10.5194/tc-13-2673-2019. URL https://tc.copernicus.org/articles/13/2673/2019/.

C. Schannwell, R. Drews, T. A. Ehlers, O. Eisen, C. Mayer, M. Malinen, E. C. Smith, and H. Eisermann. Quantifying the effect of ocean bed properties on ice sheet geometry over 40 000 years with a full-Stokes model. *The Cryosphere*, 14 (11):3917–3934, Nov. 2020. ISSN 1994-0424. doi: 10.5194/tc-14-3917-2020. URL https://tc.copernicus.org/articles/14/3917/2020/.

J. Sutter, H. Fischer, and O. Eisen. Investigating the internal structure of the antarctic ice sheet: the utility of isochrones for spatiotemporal ice-sheet model calibration. *The Cryosphere*, 15(8):3839–3860, 2021.

M. R. van den Broeke. RACMO2.3p1 annual surface mass balance Antarctica (1979-2014), 2019. URL https://doi.org/10.1594/PANGAEA.896940.

E. D. Waddington, T. A. Neumann, M. R. Koutnik, H.-P. Marshall, and D. L. Morse. Inference of accumulation-rate patterns from deep layers in glaciers and ice sheets. *Journal of Glaciology*, 53(183):694–712, 2007. doi: 10.3189/002214307784409351.

J. Weertman. On the sliding of glaciers. *Journal of Glaciology*, 3(21):33–38, 1957. doi: 10.3189/S0022143000024709.

J. Weertman. Creep deformation of ice. *Annual Review of Earth and Planetary Sciences*, 11(1):215–240, May 1983. ISSN 0084-6597, 1545-4495. doi: 10.1146/annurev.ea.11.050183.001243. URL https://www.annualreviews.org/doi/10.1146/annurev.ea.11.050183.001243.

M. Zeitz, A. Levermann, and R. Winkelmann. Sensitivity of ice loss to uncertainty in flow law parameters in an idealized one-dimensional geometry. *The Cryosphere*, 14(10): 3537–3550, 2020.

T. Zwinger and J. C. Moore. Diagnostic and prognostic simulations with a full stokes model accounting for superimposed ice of midtre lovénbreen, svalbard. *The Cryosphere*, 3(2):217–229, 2009. doi: 10.5194/tc-3-217-2009. URL https://tc.copernicus.org/articles/3/217/2009/.

T. Zwinger, R. Greve, O. Gagliardini, T. Shiraiwa, and M. Lyly. A full stokes-flow thermomechanical model for firn and ice applied to the gorshkov crater glacier, kamchatka. *Annals of Glaciology*, 45:29–37, 2007.

4

MODELLING THE THREE-DIMENSIONAL, DIAGNOSTIC ANISOTROPY FIELD OF AN ICE RISE

MANUSCRIPT DETAILS:

A. Clara J. Henry, Carlos Martín, Reinhard Drews: Modelling the three-dimensional, diagnostic anisotropy field of an ice rise [Final edits before submission to *The Journal of Glaciology*].

Modelling the three-dimensional, diagnostic anisotropy field of an ice rise

A. Clara J. Henry[1, 2, 3], Carlos Martín[4], and Reinhard Drews[2]

[1]Max Planck Institute for Meteorology, Hamburg, Germany
[2]Department of Geosciences, University of Tübingen, Tübingen, Germany
[3]International Max Planck Research School on Earth System Modelling, Max Planck Institute for Meteorology, Hamburg, Germany
[4]British Antarctic Survey, Natural Environmental Research Council, Cambridge, UK

Abstract

Polar ice develops anisotropic crystal orientation fabrics under deformation, yet ice is most often modelled as an isotropic fluid. We present three-dimensional simulations of the crystal orientation fabric of Derwael Ice Rise including the surrounding ice shelf using a crystal orientation tensor evolution equation corresponding to a fixed velocity field. We use a semi-Lagrangian numerical method that constrains the degree of crystal orientation evolution to solve the field equations in complex flow areas. We perform four simulations based on previous studies, altering the rate of evolution of the crystal anisotropy and its dependence on a combination of the strain rate and deviatoric stress tensors. We provide a framework for comparison with radar observations of the anisotropy field, outlining areas where the assumption of one vertical eigenvector may not hold and provide resulting errors in measured eigenvalues. We recognise the areas of high horizontal divergence at the tails of the flow divide as important areas to make comparisons with observations. At these locations, poorly constrained model parameters result in the largest difference in fabric type. These results are important in the planning of future campaigns for gathering data in order to constrain model parameters and as a link between observations and computationally-efficient, simplified model representations of ice anisotropy.

1 Introduction

Ice varies from isotropic to anisotropic, with crystals developing a preferred orientation fabric due to ice flow dynamics. Ice crystals tend to align with the direction of an applied force and shearing of ice is enhanced along basal planes perpendicular to the applied force (Alley, 1988). The orientation of the basal planes is described by a vector referred to as the *c*-axis. The snow grain orientation is initially isotropic and anisotropic ice fabric develops at a rate dependent on a variety of physical factors including the temperature, pressure and strain rate of the ice. These dependencies allow the investigation of both the steady-state and transient behaviour of ice through the analysis of observational anisotropy data and ice flow models.

Ice cores have long been used to quantify the the direction of ice crystals and the degree of anisotropy with depth (Durand et al., 2009; Montagnat et al., 2014; Weikusat et al., 2017). However, the lack of horizontal spatial information hinders the study of the relationship between ice flow and anisotropy. Apart from ice cores sites, anisotropic information is sparse and relies on geophysical methods such as seismics, both active (Diez et al., 2014; Brisbourne et al., 2019) and passive (Smith et al., 2017; Kufner et al., 2023) or radar (Fujita et al., 2006; Matsuoka et al., 2012; Drews et al., 2012). The main limitation is that, generally,

seismic methods only provide depth-averaged anisotropy and radar only provide anisotropy information in the horizontal plane, perpendicular to the direction of wave propagation. Recent advances in phase coherent radar systems, and data processing for use in inferring ice anisotropy have resulted in an increase in the acquisition of observational fabric data (Dall, 2010; Young et al., 2021a,b; Jordan et al., 2022; Ershadi et al., 2022). These surveys provide the spatial variability of fabric in more extensive areas and aid understanding of the relation between ice anisotropy and ice flow. Prior to this, the lack of observational data to compare with and constrain models has long hindered the progression of ice fabric modelling.

Although we concentrate only on the coupling of the anisotropy field to the velocity and stress fields in the presented study, we note that advances in a full coupling of crystal orientation tensor evolution with viscosity are ongoing with challenges remaining regarding numerical instability (Gerber et al., 2023). Several modelling studies investigating the effects of an anisotropic rheology on ice flow dynamics at ice divides in two dimensions (Martín et al., 2009; Martín and Gudmundsson, 2012; Lilien et al., 2023) and in ice streams along flow lines (Gerber et al., 2023) have shown the importance of including anisotropy evolution in ice flow models. In idealised, two-dimensional simulations, Richards et al. (2022) investigate the influence of the strain-rate and spin on the fabric type. Building on the work of Thorsteinsson et al. (2003), Gillet-Chaulet et al. (2006), and Pettit et al. (2007), Rathmann et al. (2021) investigated the coupling between anisotropy and viscosity through enhancement factors which result in greater shearing perpendicular to the predominant c-axis direction in two-dimensional numerical ice-flow simulations. Using a computationally-efficient anisotropic flow model with a simplified representation of anisotropy coupled to the viscosity via enhancement factors, McCormack et al. (2022) studied the effect of anisotropy on larger-scale three-dimensional models.

The coupling of anisotropy evolution in ice flow models is not without complication due to challenges with numerical stability, the parameter choice within the anisotropy evolution equation, and the coupling with viscosity in the Glen's flow law equation. Furthermore, because an isotropic assumption has traditionally been employed in ice sheet models, model parameters have been optimised to fit isotropic rather than anisotropic ice flow dynamics. For these reasons, a thorough investigation of each step in the process of modelling ice anisotropy is needed.

In this paper, we present the first model of the three-dimensional anisotropy field of an ice rise using the finite element model Elmer/Ice (Gagliardini et al., 2013) across 100 partitions and applied to Derwael Ice Rise. We investigate the dependence of the anisotropy field on the strain rate and deviatoric stress fields without coupling with the viscosity and without re-crystallisation terms, which allows analysis in the absence of the additional feedback complexity. Our simulations provide novel ice fabric predictions for a number of three-dimensional ice-flow settings including areas of vertical-shear-dominated flank flow, grounding zones and shear zones. We highlight areas where geophysical measurements of ice-fabric types would be most informative to constrain relevant model parameters. Furthermore, the direction of the c-axis across the ice rise is investigated to identify regions where a vertical c-axis assumption is valid in radar measurements of anisotropy, providing a novel method for determining the error in eigenvalues with such an assumption.

1.1 Motivation

Our study is motivated by a lack of progress in large-scale ice-sheet models considering crystal orientation fabric. This is despite observations of strong crystal orientation fabric in polar ice (Alley, 1988), knowledge of how anisotropic polar ice is (Duval et al., 1983) and field evidence of the effect crystal orientation fabric has on ice flow (Gerber et al., 2023). After the introduction of the crystal orientation tensor (Gödert, 2003), the flow-induced crystal orientation fabric evolution can be considered by large-scale ice-sheet models (Gagliardini et al., 2013).

We believe that the main reasons for the lack of progress are: (a) the numerical implementation of crystal orientation fabric evolution is challenging (Seddik et al., 2011), (b) the interpretation of model output and comparison with non-comprehensive observations is

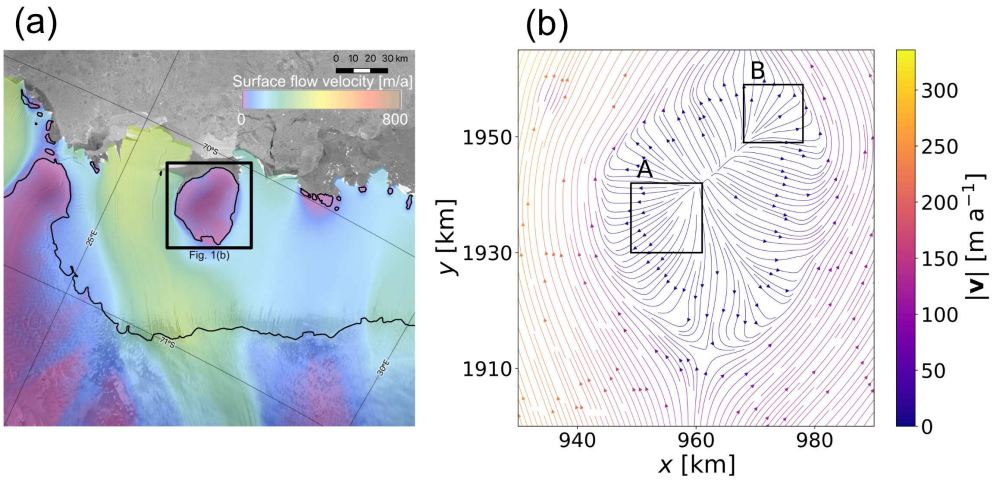

Figure 1: In (a), an overview is shown of Derwael Ice Rise, with the surrounding ice shelves and the grounding line (Jezek et al., 2013; Rignot et al., 2017) The velocity field is shown in colour. In (b), the simulated upper surface velocity field of Derwael Ice Rise is shown, based on simulations in Henry et al. (2023). The boxes A and B show the areas referred to as the areas of high horizontal divergence at the tails of the flow divide.

complex (Jordan et al., 2022), and (c) essential model parameters within the theory are not yet constrained by observations (Ma et al., 2010).

Numerically, the main issue is that numerical dispersion tends to break down the orientation tensor properties. Here, we present a numerically-robust, three-dimensional model, discuss a framework to interpret model output for comparison with observations, and highlight areas where observations could better constrain model parameters.

1.2 Derwael Ice Rise (DIR)

Ice rises are an ideal study location for understanding ice-flow processes, because transitions between different flow regimes occur over comparatively short spatial scales. Furthermore, ice rises regulate flow from the Antarctic Ice Sheet towards the open ocean, controlling ice shelf velocities and the continental grounding line position (Favier and Pattyn, 2015; Schannwell et al., 2019, 2020; Henry et al., 2022). Formation, evolution and disintegration of ice rises occur over glacial-interglacial timescales, meaning that remnants of ice properties such as temperature and anisotropy from previous flow regimes may become stored in the slow flowing ice of an ice rise.

Ice rises typically have clear ice divides transitioning into a flank-flow regime on all sides with little to no basal sliding (Matsuoka et al., 2015). The grounding line is typically located a few tens of kilometres away from the divide, and the flow field transitions to the surrounding ice shelves through narrow shear zones with large horizontal shear strain rates. We chose Derwael Ice Rise (DIR, Fig. 1) in East Antarctica as our study site for two reasons. First, we can rely on a predicted three-dimensional steady-state velocity field developed in a previous study (Henry et al., 2023). This velocity field is based on a transient, thermomechanically-coupled full Stokes model with an isotropic rheology. The model was forced with an observationally-constrained surface mass balance field and predictions of the model output were validated with extensive radar observations which are available for this Ice Rise (Koch et al., 2023). Second, previous studies suggest that DIR is likely close to steady state (Callens et al., 2016) possibly with a minor amount of thinning (Drews et al., 2015). This justifies the steady-state assumption applied here. DIR is a marine-based ice rise and has a flow divide in the form of a curved arc extended south-west to north-east. The maximum ice thickness is roughly 630 m and flow velocities in the flank are typically slower than $10\,\mathrm{m\,a^{-1}}$.

2 Methods

The simulations use output from Henry et al. (2023) as a starting point in which the finite element model Elmer/Ice (Gagliardini et al., 2013) was applied to DIR. Most importantly, we use the predicted three-dimensional, steady-state velocity field to make predictions of the anisotropic ice properties resulting from a one-way coupling with the crystal orientation evolution equations detailed below.

2.1 Governing equations

The equations of motion for Stokes flow are written as

$$\boldsymbol{\nabla} \cdot (\boldsymbol{\tau} - P\mathbf{I}) + \rho_i \mathbf{g} = 0, \tag{1}$$

where $\boldsymbol{\tau}$ is the deviatoric stress tensor, P is the pressure, $\mathbf{I}$ is the identity matrix, ρ_i is the ice density and $\mathbf{g} = g\hat{\mathbf{e}}_z$ is the gravitational acceleration. The ice is subject to an incompressibility condition,

$$\boldsymbol{\nabla} \cdot \mathbf{u} = 0, \tag{2}$$

and the Glen's flow law,

$$\boldsymbol{\tau} = 2\eta\dot{\boldsymbol{\varepsilon}}, \tag{3}$$

which describes the nonlinear dependence between the strain rate tensor, $\dot{\boldsymbol{\varepsilon}}$, and the deviatoric stress tensor. The effective viscosity, η, is

$$\eta = \frac{1}{2} E A(T')^{-1/n} \dot{\varepsilon}_e^{(1-n)/n}. \tag{4}$$

where E is an enhancement factor which is spatially and temporally constant here, $A(T')$ is the ice fluidity which is dependent on the ice temperature relative to the pressure melting point, T', which is solved using a temperature evolution equation as described in Henry et al. (2023). Here, n is the Glen's flow law exponent, and $\dot{\varepsilon}_e = \sqrt{\mathrm{tr}\,\dot{\boldsymbol{\varepsilon}}^2/2}$ is the effective strain rate.

Fixing the velocity and stress fields, a semi-Lagrangian anisotropy evolution equation is coupled and simulations are performed for 20000 years. The simulation time was deemed appropriate given that in Henry et al. (2023), it was predicted that the ice in DIR is roughly 8000 years old at a depth of 95 %.

The anisotropy of ice is described by the second and fourth order orientation tensors, $\mathbf{a}^{(2)}$ and $\mathbf{a}^{(4)}$, respectively defined by

$$a_{ij}{}^{(2)} = \langle c_i c_j \rangle \tag{5}$$

and

$$a_{ijkl}{}^{(4)} = \langle c_i c_j c_k c_l \rangle, \tag{6}$$

where $\mathbf{c}$ is the c-axis unit vector and the operator $\langle\rangle$ denotes the average over all the grains that compose the ice polycrystal.

The representation of the anisotropy field using a crystal orientation tensor,

$$\mathbf{a}^{(2)} = \begin{pmatrix} a_{xx}^{(2)} & a_{xy}^{(2)} & a_{xz}^{(2)} \\ a_{yx}^{(2)} & a_{yy}^{(2)} & a_{yz}^{(2)} \\ a_{zx}^{(2)} & a_{zy}^{(2)} & a_{zz}^{(2)} \end{pmatrix},$$

describing the c-axis distribution is ideal for comparison with ice core or radar observations in that an equivalent crystal orientation tensor can be constructed from observational data by determining the cross products of cosines of each c-axis and summing up such that

$$\mathbf{a}^{(2)} = \begin{pmatrix} a_{xx}^{(2)} & a_{xy}^{(2)} & a_{xz}^{(2)} \\ a_{yx}^{(2)} & a_{yy}^{(2)} & a_{yz}^{(2)} \\ a_{zx}^{(2)} & a_{zy}^{(2)} & a_{zz}^{(2)} \end{pmatrix} = \frac{1}{N} \begin{pmatrix} \sum l_i^2 & \sum l_i m_i & \sum l_i n_i \\ \sum m_i l_i & \sum m_i^2 & \sum m_i n_i \\ \sum n_i l_i & \sum n_i m_i & \sum n_i^2 \end{pmatrix}.,$$

where N is the number of c-axes being summed over. The cosines of the c-axis vectors are defined by taking the cosine of the angle between the c-axis vector, $\boldsymbol{c}_i$, and each positive coordinate axis, $\hat{\boldsymbol{e}}_x$, $\hat{\boldsymbol{e}}_y$ and $\hat{\boldsymbol{e}}_z$, so that

$$\begin{aligned} l_i &= \boldsymbol{c}_i \cdot \hat{\boldsymbol{e}}_x \\ m_i &= \boldsymbol{c}_i \cdot \hat{\boldsymbol{e}}_y \\ n_i &= \boldsymbol{c}_i \cdot \hat{\boldsymbol{e}}_x. \end{aligned} \tag{7}$$

From the orientation tensor, a number of metrics can be calculated to investigate the degree of crystal orientation, the predominant c-axes directions and the fabric type. The eigenvalues, namely λ_1, λ_2 and λ_3, and the corresponding eigenvectors, $\mathbf{v}_1$, $\mathbf{v}_2$ and $\mathbf{v}_3$, of the crystal orientation tensor $\mathbf{a}^{(2)}$ satisfy

$$\mathbf{a}^{(2)}\mathbf{v} = \lambda\mathbf{v} \tag{8}$$

defining each eigenvalue by its subscript such that $\lambda_1 \leq \lambda_2 \leq \lambda_3$. In the case of randomly oriented c-axes or isotropic ice, all three eigenvalues are similar in size such that $\lambda_1 \approx \lambda_2 \approx \lambda_3 \approx 1/3$. In areas where $\lambda_3 \geq \lambda_1 \approx \lambda_2$, ice fabric is said to have a single maximum fabric with the majority of c-axes pointing in a single direction. Where $\lambda_2 \approx \lambda_3 \geq \lambda_2$, ice is said to have a girdle fabric, with c-axes following an arc or circle.

The evolution of the second-order orientation tensor can be described by

$$\begin{aligned} \left(\frac{\partial}{\partial t} + \mathbf{u}\cdot\boldsymbol{\nabla}\right)\mathbf{a}^{(2)} = \mathbf{W}\mathbf{a}^{(2)} - \mathbf{a}^{(2)}\mathbf{W} \\ - \iota(\mathbf{C}\mathbf{a}^{(2)} + \mathbf{a}^{(2)}\mathbf{C} - 2\mathbf{a}^{(4)} : \mathbf{C}), \end{aligned} \tag{9}$$

where the tensor C is defined by

$$\mathbf{C} = (1-\alpha)\dot{\boldsymbol{\varepsilon}} + \alpha\frac{1}{2\eta_0}\boldsymbol{\tau}, \tag{10}$$

and α is the so-called interaction parameter, which describes the relative influence of the strain rate and stress tensors. The parameter ι determines the rate at which the crystal orientation tensor is influences by the weighted combination of strain-rate and deviatoric stress tensors. The last term, $\alpha\frac{1}{2\eta_0}\boldsymbol{\tau}$, in Eq. (10) is represented as $\alpha k_s A \tau_e^{n-1}\boldsymbol{\tau}$ in Gagliardini et al. (2013), but the simulation calculations are equivalent. The spin of the ice is denoted by the spin tensor, $\mathbf{W}$, and

$$\eta_0 = \frac{1}{2}(EA)^{-1/n}\left(\frac{1}{2}\mathrm{tr}(\dot{\boldsymbol{\varepsilon}}^2)^{\frac{1-n}{2n}}\right). \tag{11}$$

Early work recognised the influence of the cumulative strain and stress on ice crystal c-axis orientation (Alley, 1988), which led to the development of a crystal orientation tensor evolution equation (Eq. (9)) dependent on the velocity gradient through the spin and strain rate tensors, and the deviatoric stress tensor (Gillet-Chaulet et al., 2006). Although it is known that the velocity and stress fields have an influence on the anisotropy field of ice, it remains unclear what the relative influence is. The anisotropy evolution equation (Eq. (9)) is made up of various terms, with the spin tensor, $\boldsymbol{W}$, acting to rotate the crystal orientation tensor to follow the spin of the ice. Acting opposite to the spin tensor is the tensor, $\boldsymbol{C}$, which is a weighted combination of the strain rate tensor, $\dot{\boldsymbol{\varepsilon}}$, and the deviatoric stress tensor, $\boldsymbol{\tau}$. This combination comes from the fact that the behaviour of macroscopic materials can be limited by two extreme approximations: uniform stress, where the stress in the crystals is assumed to be identical to the macroscopic stress, and Taylor or uniform strain rate, where the strain rate in the crystals is assumed to be identical to the macroscopic strain rate (Gagliardini et al., 2009). The choice of α and ι in previous studies have been motivated by assumptions of the relative influence of stress and strain rate on crystal orientation evolution. The last term in the equation describes the influence of the higher-order crystal orientation tensor, $\boldsymbol{a}^{(4)}$ on the 3×3 crystal orientation tensor, $\boldsymbol{a}^{(2)}$. In reality, $\boldsymbol{a}^{(2)}$ is dependent on further, higher-order tensors, but it has been shown that this dependence is negligible (Chung and Kwon, 2002).

Table 1: Parameter combinations

	α	ι	Source
(a)	0	1	Martín et al. (2009)
(b)	0	0.6	Seddik et al. (2011)
(c)	1	1	Martín and Gudmundsson (2012)
(d)	0.06	1	Gagliardini et al. (2013)

To solve Eq. (9) we also require a relation between $\mathbf{a}^{(2)}$ and $\mathbf{a}^{(4)}$, a closure approximation, and we use an invariant-based optimal fitting closure approximation (Gillet-Chaulet et al., 2006). The distribution of c-axes can be described by tensors of ever-increasing order, but a compromise is found by using the closure approximation in order to reduce computation time. The effect of the choice of α and ι on the anisotropy field is investigated using combinations of parameters from previous literature presented in Table 1.

The value of α determines the relative influence of the strain rate and deviatoric stress tensors on anisotropy evolution. For example, a value of $\alpha = 0$, means that there is dependence on the strain rate tensor but no dependence on the deviatoric stress. Alternatively, a value of $\alpha = 1$ provides dependence on the deviatoric stress tensor but no dependence on the strain rate tensor. The parameter ι adjusts the rate at which the anisotropy field develops in response to the weighted combination of the strain rate and deviatoric stress fields and takes a value between $\iota = 0$ and $\iota = 1$.

Initially, all ice in the model domain is isotropic, described by the tensor $\mathbf{a}^{(2)} = \frac{1}{3}\mathbf{I}$, where $\mathbf{I}$ is the 3×3 identity matrix. During transient simulation of the anisotropy field dependent on the velocity field, the upper surface is assigned an isotropic boundary conditions on all ice entering the domain due to accumulation.

The anisotropic evolution model described in Eq. (9) together with its boundary and initial conditions is solved using a semi-Lagrangian method as described in Martín et al. (2009). The determinant of $\mathbf{a}^{(2)}$ gives information about the degree of crystal orientation of the fabric (Advani and Tucker, 1987). We define here the degree of crystal orientation with the scalar value,

$$d = 1 - 3^3 \det\Big(\mathbf{a}^{(2)}\Big). \tag{12}$$

The degree of crystal orientation varies from zero for isotropic ice to one for single-maximum fabric, and is independent of the frame of reference as the determinant is an invariant. We constrain Eq. (9) with the condition,

$$\left(\frac{\partial}{\partial t} + \mathbf{u} \cdot \boldsymbol{\nabla}\right) d \geq 0, \tag{13}$$

meaning that ice is constrained to increase in degree of crystal orientation over time. This constraint on the degree of crystal orientation stops numerical dispersion breaking the simulation in areas with high strain rates. Our method is also straightforward to implement in large scale models that run in parallel environments.

3 Results

3.1 Analysis of simulated anisotropy field

We display predicted eigenvalues for the $\alpha = 0$, $\iota = 1$ simulation at an elevation of $z = 0$ which encompasses an ice-depth range of close to 0 m in the ice shelf to over 300 m at the ice rise flow divide where stresses are dominated by vertical compression and lateral extension (Fig. 2). The main characteristic, which is evident in all simulations, is that the ice fabric evolves from an isotropic material at the surface and under deformation, develops into an anisotropic fabric varying from a single maximum to a girdle fabric (Fig. 3). In the ice rise interior, the largest eigenvalue, λ_3, is much larger than λ_1 and λ_2, particularly at and surrounding the flow divide (Figs. 1b and 2). This results in greater fabric anisotropy here. Further south in the ice rise, where ice flow is hindered by the convergence of flow

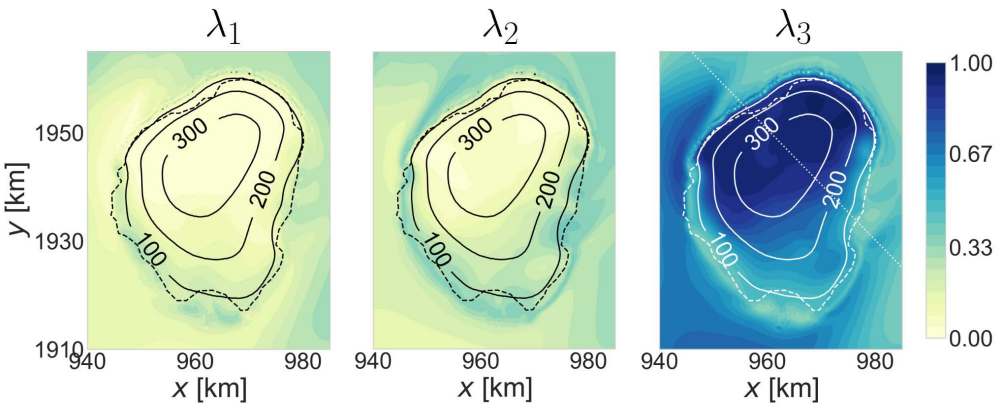

Figure 2: The eigenvalues, λ_1, λ_2 and λ_3, of the crystal orientation tensor in the $\alpha = 0$, $\iota = 1$ simulation at an elevation of $z = 0$, corresponding to sea level. The solid lines, black in the plots showing λ_1 and λ_2, and white in the plot showing λ_3, are contours of depth below the upper ice surface and the dashed lines show the grounding line. The dotted line in the λ_3 figure shows where the cross-section in Fig. 3 is taken.

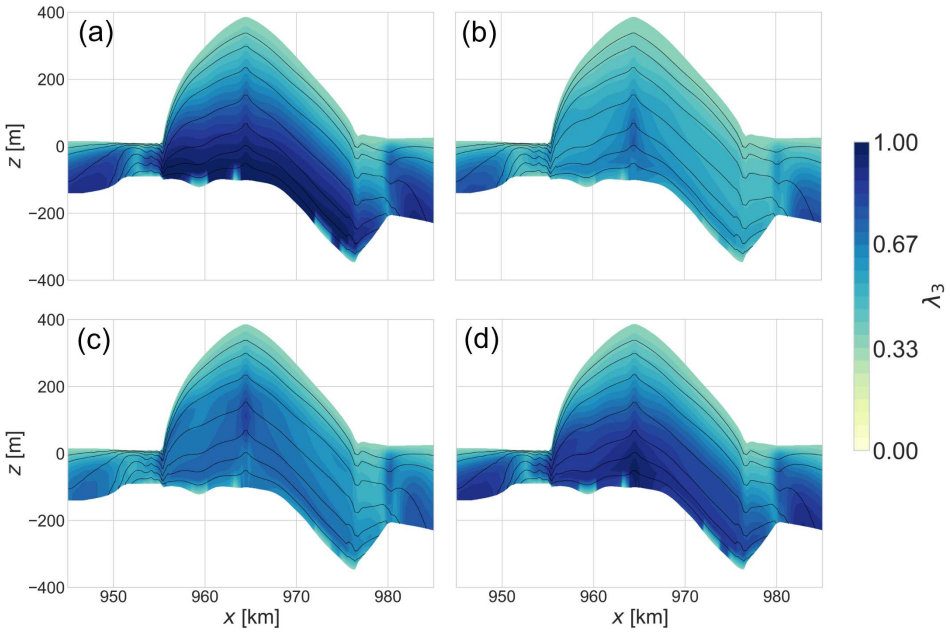

Figure 3: Cross-sections through the flow divide as shown in the Fig. 2 showing λ_3, the largest eigenvalue for (a) the $\alpha = 0$, $\iota = 1$ simulation, (b) the $\alpha = 0$, $\iota = 0.6$ simulation, (c) the $\alpha = 1$, $\iota = 1$ simulation and (d) the $\alpha = 0.06$, $\iota = 1$ simulation. The solid lines show isochrones.

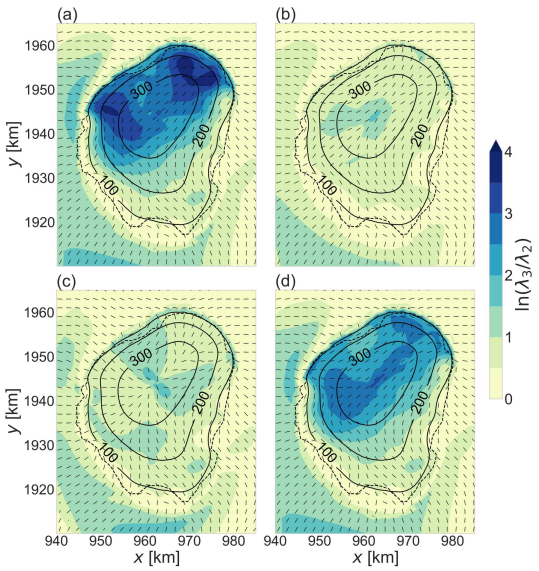

Figure 4: The ratio of the two larger eigenvalues of the 3×3 crystal orientation tensor at $z = 0$ for (a) the $\alpha = 0$, $\iota = 1$ simulation, (b) the $\alpha = 0$, $\iota = 0.6$ simulation, (c) the $\alpha = 1$, $\iota = 1$ simulation and (d) the $\alpha = 0.06$, $\iota = 1$ simulation. The dashes show the maximum horizontal anisotropy direction. The dashed line shows the grounding line and the solid line show contours of the depth below the upper ice surface.

between the ice rise and the ice shelf, differences are not as substantial. In the ice rise interior away from the grounding line, differences between the smaller two eigenvalues, λ_1 and λ_2 are mostly small, increasing slightly on the stoss side of the ice rise. The stoss side is defined as the side of the ice rise with a flow direction opposing the upstream ice shelf flow direction (Figs. 1b and 2). At the grounding zone on the stoss side of the ice rise, where horizontal convergence of flow occurs, the three eigenvalues are similar in magnitude, whereas at the transition from grounded to floating ice on the lee side of the ice rise, where flow is dominated be extension, a slightly larger difference is seen between the smaller two eigenvalues, λ_1 and λ_2. In the ice shelves away from the grounding zone, there are differing patterns in the relative magnitude of the three eigenvalues. In the ice shelf west of the ice rise where velocities are higher than east of the ice rise and extension dominates, the largest eigenvalue is significantly larger in magnitude compared with the two smaller eigenvalues. In the ice shelf to the east of the ice rise, where extension of flow is an active process, differences in magnitude are generally much lower. The ice shelf south of the ice rise, on the stoss side, shows one eigenvalue much larger than the other two, similar to the magnitudes in the ice shelf on the western side of the ice rise.

3.2 Comparison of simulations with differing parameter choice

In order to compare simulation results across the four combinations of the parameters α and ι in Eq. (9) used in the previous studies stated in Table 1, we use a number of metrics to understand the fabric types evolving in the various flow regimes at Derwael Ice Rise. First, we describe the differences in relative magnitude of the eigenvalues of the crystal orientation tensor across the four simulations. If the logarithmic ratio (Woodcock, 1977), $\ln(\lambda_3/\lambda_2)$, is large, then the c-axes are more concentrated in a single direction. The direction of the largest horizontal crystal orientation eigenvector, $\boldsymbol{v}_{2,H}$, shows the predominant horizontal c-axis direction.

The simulations with parameter choices of $\alpha = 0$, $\iota = 1$ (Fig. 4a) and $\alpha = 0.06$, $\iota = 1$ (Fig. 4d) have comparable results, with a much greater $\ln(\lambda_3/\lambda_2)$ than predicted by the other two simulations. The simulation results differ, however, in the spatial variation of $\ln(\lambda_3/\lambda_2)$. The $\alpha = 0$, $\iota = 1$ simulation shows larger values of $\ln(\lambda_3/\lambda_2)$ at the tails of the ice rise flow divide (Boxes A and B in Fig. 1b), whereas the $\alpha = 0.06$, $\iota = 1$ simulation

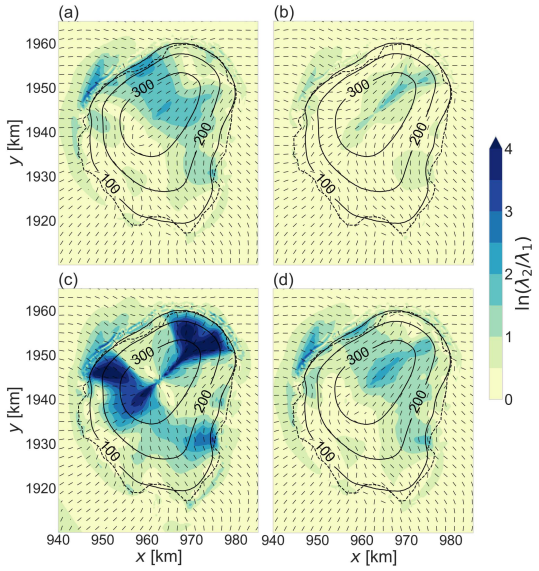

Figure 5: The ratio of the two smaller eigenvalues of the 3×3 crystal orientation tensor at $z = 0$ for (a) the $\alpha = 0$, $\iota = 1$ simulation, (b) the $\alpha = 0$, $\iota = 0.6$ simulation, (c) the $\alpha = 1$, $\iota = 1$ simulation and (d) the $\alpha = 0.06$, $\iota = 1$ simulation. The dashes show the maximum horizontal anisotropy direction. The dashed line shows the grounding line and the solid line show contours of the depth below the upper ice surface.

shows slightly greater relative values along the flow divide. Although not negligible, the simulations with parameter choices of $\alpha = 0$, $\iota = 0.6$ (Fig. 4b) and $\alpha = 1$, $\iota = 1$ (Fig. 4c) show much lower ratios between the largest and second largest eigenvalues, with the $\alpha = 0$, $\iota = 0.6$ simulation showing a slightly higher value at the centre of the flow divide. In the $\alpha = 1$, $\iota = 1$ simulation, a differing pattern of horizontal eigenvectors originating at a point source at the flow divide, whereas the other simulations show alignment of the eigenvector direction along the flow divide. Of note is also the differing eigenvector directions at the tails of the flow divide, with differing patterns of vector divergence and convergence.

The two smaller eigenvalues, λ_1 and λ_2 are investigated using the metric $\ln(\lambda_2/\lambda_1)$ (Fig. 5). Large ratios between the two smaller eigenvalues indicates that c-axis directions for a given volume of ice are concentrated along an arc. In all simulations, there are high values of $\ln(\lambda_2/\lambda_1)$ at the flow divide and generally low values in the vicinity of the grounding zone on the stoss side of the ice rise, with values differing between simulations elsewhere. The $\alpha = 0$, $\iota = 0.6$ (Fig. 5b) simulation show the lowest values overall. The simulations with parameter choices of $\alpha = 0$, $\iota = 1$ and $\alpha = 0.06$, $\iota = 1$ show relatively similar results, with the highest eigenvalue ratio at the flow divide and in the areas of the ice rise perpendicular to the flow divide. The $\alpha = 1$, $\iota = 1$ simulation (Fig. 5c) has areas of a large ratio between λ_2 and λ_1, much larger than any other simulation and highlights the effect of a strong dependence on the strain-rate tensor on the crystal orientation tensor evolution. Rather than having high values perpendicular to the flow divide, the highest values are along a small band following the flow divide and in the areas of high horizontal divergence at the tails of the flow divide, extending in some areas as far as the grounding line. There are no large differences between λ_2 and λ_1 in the ice shelves, with the largest values being concentrated north-west of the ice rise in all simulations.

The Woodcock k value (Woodcock, 1977), defined as

$$k = \frac{\ln(\lambda_3/\lambda_2)}{\ln(\lambda_2/\lambda_1)}, \tag{14}$$

provides a metric by which to investigate which areas are characterised by a single maximum fabric and which are characterised by girdle fabric. Note that k can have values between $k = 0$ and $k = \infty$. In order to better investigate small values of k, we plot $\ln(k)$ for each simulation in Table 1. If $\ln(k) > 0$, then the ice is defined as having a single maximum fabric

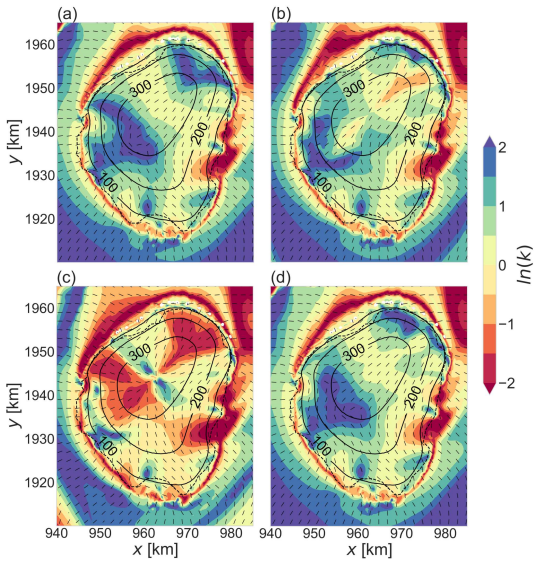

Figure 6: The logarithm of the Woodcock k value at an elevation of $z = 0$ for (a) the $\alpha = 0$, $\iota = 1$ simulation, (b) the $\alpha = 0$, $\iota = 0.6$ simulation, (c) the $\alpha = 1$, $\iota = 1$ simulation and (d) the $\alpha = 0.06$, $\iota = 1$ simulation. The dashes show the maximum horizontal anisotropy direction. The dashed line shows the grounding line and the solid line show contours of the depth below the upper ice surface.

and if $\ln(k) < 0$, the ice is defined as having a girdle fabric. Furthermore, if $\ln(k) >> 0$ and $\ln(\lambda_3/\lambda_2) >> 0$, then the ice has a strong single maximum. If, on the other hand, $\ln(k) << 0$ and $\ln(\lambda_2/\lambda_1) >> 0$, then ice has a strong girdle fabric.

In the $\alpha = 0$, $\iota = 1$ simulation, there are relatively high $\ln(k)$ values at the tails of the flow divide (Fig. 6a), extending in some areas almost to the grounding line. Elsewhere on the ice rise, values of $\ln(k)$ are generally close to zero. The $\alpha = 0.06$, $\iota = 1$ simulation (Fig. 6d) shows similar results except at the north-east of the ice rise, where high values of $\ln(k)$ are concentrated closer to the grounding line. The $\alpha = 0$, $\iota = 0.6$ simulation (Fig. 6b) shows higher values of $\ln(k)$ even further from the flow divide and a small area with negative $\ln(k)$ values at the north-eastern end of the flow divide. The $\alpha = 1$, $\iota = 1$ simulation (Fig. 6c) shows, by far, the most negative values of $\ln(k)$, concentrated at the two tails of the flow divide and small areas with positive values of $\ln(k)$ perpendicular to the flow divide. All four simulations show an almost-continuous band of negative values of $\ln(k)$ at the grounding line or a small distance away from the grounding line in the ice shelf. Moving away from the grounding line, a general increase in values of $\ln(k)$ is seen, with some exceptions.

3.3 Metrics for comparison with radar data

In quad-polarimetric radar processing, it is often assumed that because of the dominance of vertical compression, one eigenvector aligns with the vertical direction. In areas where this assumption holds, signal processing can be simplified (Jordan et al., 2022; Ershadi et al., 2022). Obliquely oriented fabric types can, in theory, also be detected (Matsuoka et al., 2009; Rathmann et al., 2022), but thus far this has not been done for observations which are typically only collected in a nadir-viewing geometry. Here, we present results evaluating the applicability of the assumption of one vertical eigenvector across all four simulations.

In general, the predicted tilt angle is small in the grounded area across all simulations(Fig. 7). Note that the grounded area is the area within the dashed line marking the grounding line. The angle remains small, with similar spatial patterns in the simulations with parameter choices of $\alpha = 0$, $\iota = 1$ and $\alpha = 0.06$, $\iota = 1$ (Figs. 7a and 7d, respectively). In the $\alpha = 0$, $\iota = 0.6$ simulation (Fig. 7b), differences between the z-direction and $\boldsymbol{v}_3$ are generally small, with the exception of slightly higher values on either side of the flow divide. Spatial patterns on the stoss side of the ice rise are similar to those in the above-mentioned

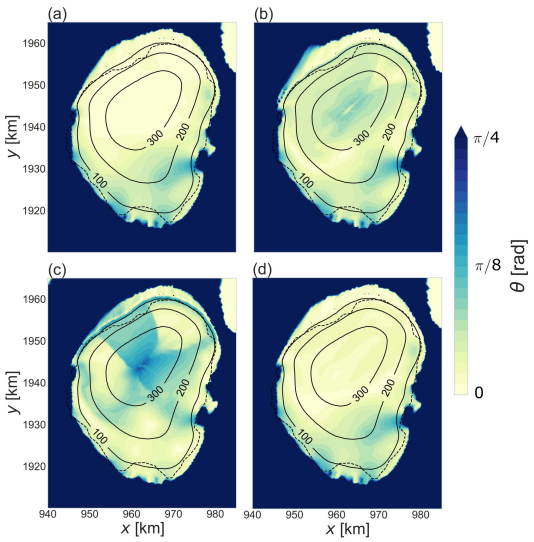

Figure 7: The angle between the eigenvector corresponding to the largest eigenvalue and the vertical direction at an elevation of $z = 0$ corresponding to sea level for (a) the $\alpha = 0$, $\iota = 1$ simulation, (b) the $\alpha = 0$, $\iota = 0.6$ simulation, (c) the $\alpha = 1$, $\iota = 1$ simulation and (d) the $\alpha = 0.06$, $\iota = 1$ simulation. The dashed line shows the grounding line and the solid lines show contours for the depth below the surface in metres.

$\alpha = 0$, $\iota = 1$ and $\alpha = 0.06$, $\iota = 1$ simulations. The simulation with the largest tilt angles is the $\alpha = 1$, $\iota = 1$ simulation (Fig. 7c), with differences of $\pi/8$ to $\pi/4$ radians at and perpendicular to the flow divide. In all simulations, the tilt angle in the ice shelf is larger a short distance away from the grounding line, except for small, isolated areas.

We furthermore calculate the eigenvectors and eigenvalues of the horizontal crystal orientation tensor, i.e. the upper left 2×2 part of the 3×3 tensor $\mathbf{a}^{(2)}$. The reason for this is that if the 3×3 crystal orientation tensor has one strictly vertical eigenvector, the eigenvalues and eigenvectors of the 2×2 tensor correspond to the horizontal eigenvalues and eigenvectors of the 3×3 tensor. We denote the eigenvalues of the 2×2 tensor by $\lambda_{1,H}$ and $\lambda_{2,H}$, and the corresponding eigenvectors by $\mathbf{v}_{1,H}$ and $\mathbf{v}_{2,H}$, respectively. By comparing the eigenvalues of the 2×2, horizontal crystal orientation tensor with the eigenvalues of the 3×3 crystal orientation tensor, an error estimate can be found for assuming that the eigenvector corresponding to the largest eigenvalue is aligned with the z-axis.

We present percentage differences between λ_1 and $\lambda_{1,H}$ (Fig. 8), as well as λ_2 and $\lambda_{2,H}$ (Fig. 9). We find that if a difference exists between λ_1 and $\lambda_{1,H}$, or λ_2 and $\lambda_{2,H}$, then the 2×2 tensor eigenvalues always underestimate the smaller two 3×3 tensor eigenvalues. Furthermore, percentage differences tend to be higher for the smaller eigenvalues λ_1 and $\lambda_{1,H}$ than for λ_2 and $\lambda_{2,H}$, but exceptions to this are seen. The $\alpha = 0$, $\iota = 1$ simulation shows a negligible percentage difference between λ_1 and $\lambda_{1,H}$ (Fig. 8a) and small percentage differences for λ_2 and $\lambda_{2,H}$ of up to 10 % (Fig. 9a). A similar spatial distribution of percentage differences appears for λ_2 and $\lambda_{2,H}$ in the $\alpha = 0.06$, $\iota = 1$ simulation (Fig. 9d). Most notable is the percentage difference between λ_1 and $\lambda_{1,H}$ in the $\alpha = 1$, $\iota = 1$ simulation (Fig. 8c), where values are above 20 % in a large area at and perpendicular to the flow divide. In this simulation ($\alpha = 1$, $\iota = 1$), percentage differences between λ_2 and $\lambda_{2,H}$ (Figs. 9c) are high compared to other simulations, but the high values localised at and in the area perpendicular to the flow divide occupy a smaller area than the percentage differences between λ_1 and $\lambda_{1,H}$ (Fig. 8c). In the $\alpha = 0$, $\iota = 0.6$ and the $\alpha = 0.06$, $\iota = 1$ simulations, percentage differences between λ_1 and $\lambda_{1,H}$ are negligible across a large portion of the ice rise, in particular on the stoss side (Figs. 8b,d). The highest percentage differences are either side of the flow divide with values up to and over 20 %, reducing further away from the flow divide. Percentage differences between λ_2 and $\lambda_{2,H}$ in the $\alpha = 0$, $\iota = 0.6$ simulation are negligible except for small areas at the flow divide (Fig. 9b). As the assumption that

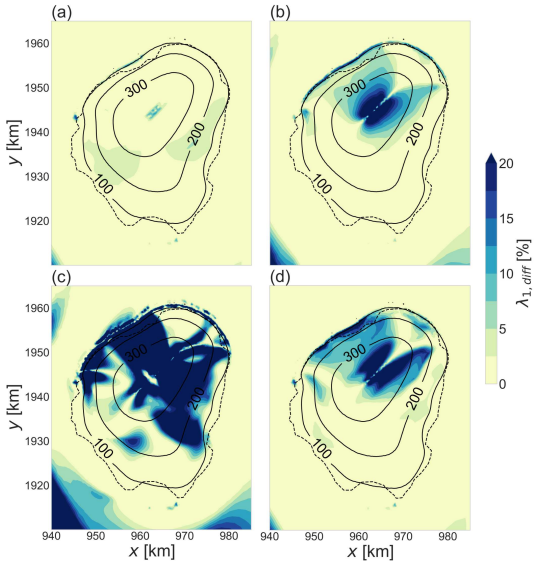

Figure 8: The percentage difference between $\lambda_{1,H}$ and λ_1 at an elevation of $z = 0$ for (a) the $\alpha = 0$, $\iota = 1$ simulation, (b) the $\alpha = 0$, $\iota = 0.6$ simulation, (c) the $\alpha = 1$, $\iota = 1$ simulation and (d) the $\alpha = 0.06$, $\iota = 1$ simulation. The solid line contours show depth below surface and the dashed line is the grounding line.

the eigenvector corresponding with the largest eigenvalue is made for grounded ice, we do not analyse the differences between eigenvalues of the 2×2 and the 3×3 crystal orientation tensors in the ice shelves.

Next, we present results for the difference between the eigenvalues, $\lambda_{2,H} - \lambda_{1,H}$, of the 2×2 horizontal part of the 3×3 crystal orientation tensor. This metric corresponds directly with results from radar data where a vertical eigenvector assumption is made (Fig. 10). The $\alpha = 0$, $\iota = 1$ (Fig. 10a) and the $\alpha = 0.06$, $\iota = 1$ (Fig. 10d) simulations show similar results both spatially and in terms of the magnitude of differences, with differences staying below 0.1 at and in the vicinity of the flow divide. The largest differences in the eigenvalues occur on the eastern side of the ice rise, close to the grounding line as well as in small isolated areas elsewhere on the stoss side of the ice rise in the vicinity of the grounding line. Although eigenvalue differences differ substantially in magnitude between the two simulations, the $\alpha = 0$, $\iota = 0.6$ (Fig. 10b) and the $\alpha = 1$, $\iota = 1$ (Fig. 10c) simulations show similar spatial patterns. In the $\alpha = 0$, $\iota = 0.6$ simulation (Fig. 10b), the highest differences between $\lambda_{2,H}$ and $\lambda_{1,H}$ area seen at the tails of the flow divide, extending towards the grounding line north-east of the ice rise and in isolated areas on the east of the ice rise. Elsewhere, differences between $\lambda_{2,H}$ and $\lambda_{1,H}$ remain below 0.1. The $\alpha = 1$, $\iota = 1$ simulation (Fig. 10c) shows large differences between $\lambda_{2,H}$ and $\lambda_{1,H}$ of over 0.3 at the flow divide and extending to the grounding line, particularly on the lee side of the ice rise. As in all other simulations, differences of over 0.3 are seen on the eastern side of the ice rise close to the grounding line.

Finally, we investigate the dependence of the anisotropy field on the strain rate field, and in particular the relationship between the largest horizontal anisotropy direction and the largest horizontal strain rate direction. Given that we expect c-axes to point perpendicular to the direction of maximum stretching, we calculate the largest horizontal strain rate direction by calculating the eigenvalues and eigenvectors of the upper left 2×2 tensor of the 3×3 strain rate tensor, $\dot{\boldsymbol{\varepsilon}}$. We denote the eigenvectors of the horizontal strain rate tensor by $\boldsymbol{w}_{1,H}$ and $\boldsymbol{w}_{2,H}$, where $\boldsymbol{w}_{1,H} \leq \boldsymbol{w}_{2,H}$. We then calculate the angle between the maximum horizontal strain rate direction, $\boldsymbol{w}_{2,H}$, and the maximum horizontal anisotropy direction, $\boldsymbol{v}_{2,H}$ (Fig. 11). In the $\alpha = 0$, $\iota = 1$ simulation (Fig. 11a) and the $\alpha = 0.06$, $\iota = 1$ simulation (Fig. 11d), the angle between $\boldsymbol{w}_{2,H}$ and $\boldsymbol{v}_{2,H}$ remains close to $\pi/2$, meaning that the two vectors are mostly close to perpendicular. Exceptions are in small areas of divergence at the two tails of the flow divide. In the $\alpha = 0$, $\iota = 0.6$ simulation (Fig. 11b), the angle between $\boldsymbol{w}_{2,H}$ and $\boldsymbol{v}_{2,H}$ is mainly high everywhere on the ice rise except at the two tails of the flow

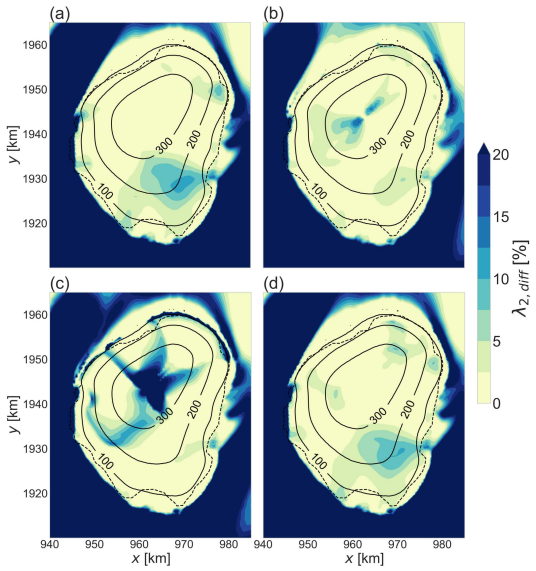

Figure 9: The percentage difference between $\lambda_{2,H}$ and λ_2 at an elevation of $z = 0$ for (a) the $\alpha = 0$, $\iota = 1$ simulation, (b) the $\alpha = 0$, $\iota = 0.6$ simulation, (c) the $\alpha = 1$, $\iota = 1$ simulation and (d) the $\alpha = 0.06$, $\iota = 1$ simulation. The solid line contours show depth below surface and the dashed line is the grounding line.

divide where values are consistently closer to zero. Lastly, the $\alpha = 1$, $\iota = 1$ simulation (Fig. 11c) shows a large area on the stoss side of the ice rise, away from the flow divide, where $\boldsymbol{w}_{2,H}$ and $\boldsymbol{v}_{2,H}$ are mostly close to perpendicular. At the flow divide, there is a thin line where the two vectors are perpendicular and in the areas perpendicular to the flow divide, the angle between the two vectors is generally $> \pi/4$. This simulation shows the largest areas where the angle between $\boldsymbol{w}_{2,H}$ and $\boldsymbol{v}_{2,H}$ is close to zero from the extremes of the flow divide as far, or almost as far as the grounding line.

4 Discussion

We present the results of three-dimensional simulations of the full-tensor anisotropy field of Derwael Ice Rise via a coupling with the velocity and stress fields. The simulated domain includes the surrounding ice shelf, allowing analysis of the anisotropy field across the grounding zone. Based on four previous studies (Martín et al., 2009; Seddik et al., 2011; Martín and Gudmundsson, 2012; Gagliardini et al., 2013), we simulate the anisotropy field varying parameter choices controlling the relative influence of the strain rate and deviatoric stress tensors. By decomposition of the simulated crystal orientation tensor into eigenvalues and eigenvectors, our results provide a necessary step towards the comparison of observed ice fabric with three-dimensional modelled results for a variety of flow regimes.

4.1 Dependence of the anisotropy field on the velocity and stress fields

The various flow regimes in the ice rise influence the anisotropy field in different ways, with past flow regimes of a volume of ice also having an effect on the present anisotropy, which is captured due to the semi-Lagrangian implementation of the crystal orientation tensor evolution in the simulations in this study.

Based on previous choices (Martín et al., 2009; Seddik et al., 2011; Martín and Gudmundsson, 2012; Gagliardini et al., 2013), we adjust the parameters α and ι in Eq. (9). The parameter α, taking values $\alpha \in [0, 1]$, controls the relative influence of the strain rate and deviatoric stress tensors, with a value of $\alpha = 0$ meaning that the deviatoric stress tensor is ignored and a value of $\alpha = 1$ meaning that the strain rate tensor is ignored. The parameter

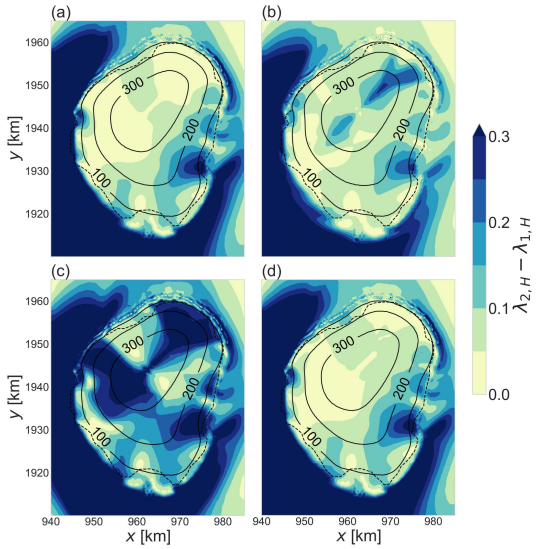

Figure 10: The difference between the two eigenvalues of the 2×2 horizontal crystal orientation tensor for (a) the $\alpha = 0$, $\iota = 1$ simulation, (b) the $\alpha = 0$, $\iota = 0.6$ simulation, (c) the $\alpha = 1$, $\iota = 1$ simulation and (d) the $\alpha = 0.06$, $\iota = 1$ simulation. The solid lines show contours for the depth below the surface in metres and the dashed line is the grounding line.

ι, taking values of $\iota \in [0, 1]$, controls the rate of change the crystal orientation tensor, $\boldsymbol{a}^{(2)}$, undergoes in response to the combination of the strain rate and deviatoric stress tensor. For example, for a value of ι close to zero, apart from rotational changes due to the spin tensor, the crystal orientation tensor changes minimally in response to the combination of the strain rate and deviatoric stress tensors. Because the strain rate and deviatoric stress tensor are co-dependent via Glen's flow law (Eq. (3)), differentiation between the various combinations of α and ι is not trivial. Broadly speaking, though this is not always the case, the behaviour of the anisotropy field in the $\alpha = 0$, $\iota = 0.6$ simulation shows similar results to the $\alpha = 1$, $\iota = 1$ simulation, despite the relatively large differences in parameter choice. Conversely, the $\alpha = 0$, $\iota = 1$ and the $\alpha = 0.06$, $\iota = 1$ simulations show only slightly differing results, likely explained by the similarity in values of α and ι.

While certain anisotropic fabric types can be expected under particular flow and stress regimes, the length of time the ice has undergone deformation in this regime also has an influence on the reflected anisotropy field. In Fig. 4, it can be seen that at the elevation $z = 0$, the ice has developed into a relatively strong single maximum fabric in the $\alpha = 0$, $\iota = 1$ simulation (Fig. 4a) and the $\alpha = 0.06$, $\iota = 1$ simulation (Fig. 4d) compared with the other two simulations. On the other hand, the $\alpha = 1$, $\iota = 1$ simulation (Fig. 4c) does not show a strong single maximum. This indicates that the strain rate term of Eq. (10) has a stronger influence on the development of a single maximum under vertical compression at a flow divide than the deviatoric stress tensor term of Eq. (10). Interestingly, in the $\alpha = 0$, $\iota = 1$ simulation (Fig. 4a) and the $\alpha = 0.06$, $\iota = 1$ simulation (Fig. 4d), the areas with a higher single maximum are located at the two tails of the flow divide. Although not explicitly simulated in this study, we expect that the fabric type in the area of high horizontal divergence at the tails of the flow divide would show a similar fabric to that forming at a dome flow divide, defined by a flow divide with horizontal flowlines originating at a point source. In the vicinity of the flow divide, the $\alpha = 1$, $\iota = 1$ simulation shows a vastly different horizontal anisotropy direction than the other simulations (Fig. 5c). The eigenvector corresponding to the largest horizontal eigenvalue originate at a point source as opposed to being parallel to the flow divide in the other simulations. Values of $\ln(\lambda_2/\lambda_1)$ are high along the flow divide and in relatively large areas where there is high horizontal divergence at the tails of the flow divide meaning that the ice has a girdle fabric. Of note is that Fig. 11c shows that in the areas of girdle fabric, the maximum horizontal strain rate direction is not perpendicular to the maximum horizontal anisotropy direction. The

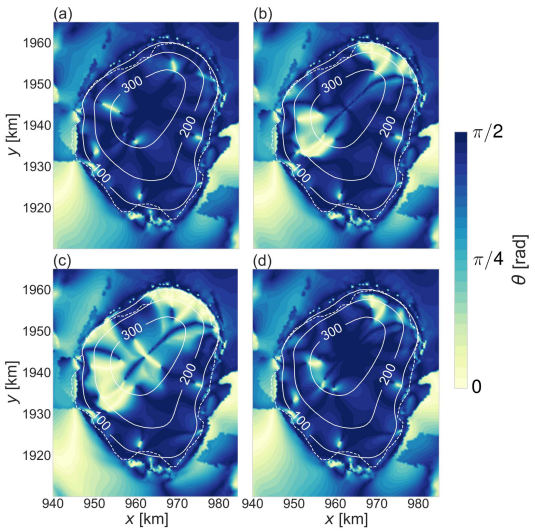

Figure 11: The angle between the eigenvectors corresponding to the larger horizontal crystal orientation eigenvalue and the larger horizontal strain rate eigenvalue for (a) the $\alpha = 0$, $\iota = 1$ simulation, (b) the $\alpha = 0$, $\iota = 0.6$ simulation, (c) the $\alpha = 1$, $\iota = 1$ simulation and (d) the $\alpha = 0.06$, $\iota = 1$ simulation.

reason for the differences between the $\alpha = 1$, $\iota = 1$ and the other three simulations is due to the largely different α value, which in this case results in ignoring the strain rate tensor completely.

Moving into the flanks of the ice rise, where vertical shear dominates, although the flow of ice in the grounded areas is horizontally divergent, the fabric types vary substantially. We identify a number of factors as having an influence on the ice fabric type: (a) whether flank flow is perpendicular to the flow divide or at the tails of the flow divide, (b) whether the ice is on the stoss or lee side of the ice rise, and (c) how close ice is to the grounding line and what type of flow regime is active at the grounding zone. In flow regimes dominated by vertical shear, as is the case in the areas perpendicular to the flow divide, it is expected that fabric shows a single maximum with a slight offset to the vertical (Llorens et al., 2022). However, the $\alpha = 0$, $\iota = 1$ (Fig. 4a) and the $\alpha = 0.06$, $\iota = 1$ (Fig. 4d) simulations show the strongest single maxima perpendicular to the flow divide, but Figs. 7a and d, show that these simulations have the smallest tilt angle compared to the other simulations.

Across the grounding line, the predicted ln(k) values allow differentiation between single maximum fabric ($\ln(k) > 0$) and girdle fabrics ($\ln(k) < 0$, Fig. 6). It must be noted, however, that a large positive or negative value of $\ln(k)$ does not necessarily imply that the ice has a strong single maximum or strong girdle fabric, respectively. Any analysis of the $\ln(k)$ field must be done in conjunction with plots of $\ln(\lambda_2/\lambda_1)$ (Fig. 5) and $\ln(\lambda_3/\lambda_2)$ (Fig. 4) (Woodcock, 1977). In all simulations, $(\ln(\lambda_3/\lambda_2))$ is the lowest at the grounding zone and in the northern and eastern sides of the ice shelf, meaning that there is no single maximum in these areas. Contrary to this, the metric for a girdle fabric $(\ln(\lambda_2/\lambda_1))$ shows a small band at the grounding zone with values of $\ln(\lambda_2/\lambda_1) = 0.5$ to 1. This weak girdle fabric may be due to the transition from a fabric with a vertical single maximum, to a single maximum aligned with the horizontal plane, via a transition across the grounding zone.

4.2 Implications for viscosity coupling

One ultimate goal in modelling the anisotropy field of ice is to be able to fully couple the velocity and stress fields to the anisotropy field and *vice versa* (note, we will refer to these simulations as *fully-coupled* hereafter). In this study, we have explored the influence of the velocity and stress fields on the anisotropy field using three-dimensional simulations, but have not investigated the coupling of the anisotropy field to the velocity field via a direction-dependent viscosity. Here, we discuss areas of Derwael Ice Rise where we expect the fabric

type to influence viscosity as well as barriers to fully-coupled, three-dimensional anisotropic simulations.

Generally-speaking, ice crystal c-axes rotate in a direction which allows for optimal shearing, with studies showing that if ice is highly anisotropic, deformation in the plane perpendicular to the c-axis is significantly enhanced compared with deformation in other directions (Duval et al., 1983). Areas where ice has a single maximum will experience ease of deformation parallel to basal planes and stiffening in response to deformation parallel to the c-axes. In the simulations of Derwael Ice Rise, a single maximum fabric is most apparent in the $\alpha = 0$, $\iota = 1$ and the $\alpha = 0.06$, $\iota = 1$ simulations (Fig. 4). If enhancement factors were used (Gillet-Chaulet et al., 2005; Ma et al., 2010) in a coupling with the ice viscosity, this would allow more ease of vertical shear in these areas which is important in the evolution of Raymond arches at flow divides, as shown in two-dimensional, anisotropic simulations (Martín et al., 2009; Martín and Gudmundsson, 2012; Drews et al., 2015).

A number of hurdles hinder the three-dimensional simulation of a fully-coupled anisotropy field including computational expense, numerical instabilities, a lack of comparison with observations, parameter uncertainty and challenges associated with parallelisation. In a study by Gerber et al. (2023) in which flow tube simulations the Elmer/Ice model of a fully-coupled anisotropy field were performed, it was noted that numerical instabilities significantly hindered the simulation of areas with high velocities. Furthermore, computational expense and an increased memory load means that a directionally-dependent viscosity creates a further hindrance. Despite this, simulations such as those presented in this paper allow ease of comparison with observations and should be included in comparisons between a hierarchy of models with varying complexity.

4.3 Model representation of anisotropy

Ice rises are an ideal location for testing models of anisotropy as they contain various flow regimes which are relevant for other locations in the Antarctic Ice Sheet. Ice rises contain many of the same features as entire ice sheets, and results can inform expectations on studies in larger scales (Matsuoka et al., 2003). The shear zones on the western and eastern sides of Derwael Ice Rise are representative of behaviour typical at lateral shear zones in ice shelves or ice streams (Smith et al., 2017). Similarly, flow divides, flank flow and ice shelf flow are typical in many areas of Antarctica. More studies are needed to examine whether an anisotropic flow law is needed in order to make accurate projections of sea level rise. This is especially important as sudden speed up of ice, for example in the initiation of an ice stream, is associated with anisotropic behaviour (Thorsteinsson et al., 2003; Lilien et al., 2021; Gerber et al., 2023). This necessitates further studies for comparison between various hierarchies of isotropic and anisotropic ice flow models with varying model complexity as well as comparison with observations. In our approach, anisotropy is modelled using a crystal orientation tensor, which can describe many fabric types, but does not capture cone fabric shapes as modelled by Pettit et al. (2007) or multiple single maxima. An example of a representation of crystal orientation which can capture more complex fabrics has been developed by Rathmann et al. (2021).

In addition to difficulties in choosing a correct mathematical representation of an anisotropic fabric, Eq. (9) is challenging to solve numerically as it is an advection equation, with no diffusive term. We find that the use of semi-Lagrangian methods reduce dispersion, as they introduce diffusion through interpolation (Advani and Tucker, 1987). However, in areas with strong gradients in the velocity field we nonetheless find that numerical dispersion deteriorates the solution with time. The alternative approach to this numerical problem has been to either explicitly incorporate numerical diffusion in Eq. (9) as in Seddik et al. (2011), or to include re-crystallisation terms as in Gagliardini et al. (2013). We find it to be more effective to constrain the degree of orientation, but our approach can easily be adapted to include a re-crystallisation term in Eq. (9).

4.4 Framework for comparison with observations

A crucial component of accurate modelling of the anisotropy field of ice is the comparison with observations, which, until recently have been possible only by comparison with a limited number of ice cores. From ice core data, it is possible to construct a crystal orientation tensor which is directly comparable to simulations such as those presented in this work. Recently, advances in the measurement of anisotropic fabric using radar has allowed the acquisition of a significant amount of data with much greater ease than expensive ice coring projects (Young et al., 2021a,b; Ershadi et al., 2022). However, assumptions made in the processing of data mean that the methods currently used are only valid where the dominant c-axis direction is exactly vertical (Rathmann et al., 2022).

Thus far, observational anisotropy data has been used for inferring ice flow history including flow re-organisation (Durand et al., 2007; Matsuoka et al., 2012; Brisbourne et al., 2019, 2021) as well as for investigation of the state of the ice fabric in ice conditions such as ice streams (Smith et al., 2017; Kufner et al., 2023), in layers of enhanced shear (Pettit et al., 2011) and at ice rises (Drews et al., 2015). In terms of making comparisons between observations and anisotropic models, matching of isochrones and velocities has been performed (Drews et al., 2015; McCormack et al., 2022), but few studies have compared directly the observed and modelled anisotropy fields (Lilien et al., 2023).

Although we do not explicitly make comparisons between the observed and modelled anisotropy fields of Derwael Ice Rise, we have described steps necessary for such a comparison. Our results show very differing three-dimensional anisotropy fields depending on the chosen influence of the strain rate and deviatoric stress tensors in Eq. (9) used in previous studies (Martín et al., 2009; Seddik et al., 2011; Martín and Gudmundsson, 2012; Gagliardini et al., 2013) and draw attention to the need to constrain equation parameters. We have provided a method to compare the difference between the two horizontal eigenvalues (Fig. 10), sometimes referred to as the *horizontal anisotropy*, which is directly comparable to radar observations. We recommend radar surveys in the areas of high horizontal flow divergence at the tails of flow divides, as these are areas where differing values of α and ι show significantly differing anisotropy fields.

5 Conclusions

In this study, we have modelled the three-dimensional anisotropy field of Derwael Ice Rise (DIR) including domain partitioning using a crystal orientation tensor evolution equation describing the spatial distribution of ice crystal c-axes in a given ice volume. Simulations are performed varying the relative influence of the strain rate and deviatoric stress tensors in the crystal orientation tensor evolution equation as used in four previous studies (Martín et al., 2009; Seddik et al., 2011; Martín and Gudmundsson, 2012; Gagliardini et al., 2013), with results showing significantly differing ice fabrics across the flow divide and the flanks of DIR. Lastly, we provide a modelling framework for comparison with radar observations, outlining areas where the assumption of one vertical eigenvector may not hold and resulting errors in horizontal eigenvalues.

Data and code availability

Repositories for the code and data of this manuscript are currently being prepared.

Acknowledgements

C. Henry was supported by the Deutsche Forschungsgemeinschaft (DFG) in the framework of the priority programme 1158 "Antarctic Research with comparative investigations in Arctic ice areas" by a grant SCHA 2139/1-1. R. Drews was partially supported by an Emmy Noether Grant of the Deutsche Forschungsgemeinschaft (DR 822/3-1). This work used resources of the Deutsches Klimarechenzentrum (DKRZ) granted by its Scientific Steering

Committee (WLA). We would like to thank Luca Schmidt for comments which improved the manuscript.

References

S. G. Advani and I. Tucker, Charles L. The Use of Tensors to Describe and Predict Fiber Orientation in Short Fiber Composites. *Journal of Rheology*, 31(8):751–784, 11 1987. ISSN 0148-6055. doi: 10.1122/1.549945. URL https://doi.org/10.1122/1.549945.

R. B. Alley. Fabrics in polar ice sheets: development and prediction. *Science*, 240(4851): 493–495, 1988.

A. M. Brisbourne, C. Martín, A. M. Smith, A. F. Baird, J. M. Kendall, and J. Kingslake. Constraining Recent Ice Flow History at Korff Ice Rise, West Antarctica, Using Radar and Seismic Measurements of Ice Fabric. *Journal of Geophysical Research: Earth Surface*, 124(1):175–194, Jan. 2019. ISSN 21699003. doi: 10.1029/2018JF004776. URL http://doi.wiley.com/10.1029/2018JF004776.

A. M. Brisbourne, M. Kendall, S.-K. Kufner, T. S. Hudson, and A. M. Smith. Downhole distributed acoustic seismic profiling at skytrain ice rise, west antarctica. *The Cryosphere*, 15(7):3443–3458, July 2021. ISSN 1994-0424. doi: 10.5194/tc-15-3443-2021. URL https://tc.copernicus.org/articles/15/3443/2021/.

D. Callens, R. Drews, E. Witrant, M. Philippe, and F. Pattyn. Temporally stable surface mass balance asymmetry across an ice rise derived from radar internal reflection horizons through inverse modeling. *Journal of Glaciology*, 62(233):525–534, June 2016. ISSN 0022-1430, 1727-5652. doi: 10.1017/jog.2016.41.

D. H. Chung and T. H. Kwon. Invariant-based optimal fitting closure approximation for the numerical prediction of flow-induced fiber orientation. *Journal of Rheology*, 46(1): 169–194, Jan. 2002. ISSN 0148-6055, 1520-8516. doi: 10.1122/1.1423312.

J. Dall. Ice sheet anisotropy measured with polarimetric ice sounding radar. In *2010 IEEE International Geoscience and Remote Sensing Symposium*, pages 2507–2510, 2010. doi: 10.1109/IGARSS.2010.5653528.

A. Diez, O. Eisen, I. Weikusat, J. Eichler, C. Hofstede, P. Bohleber, T. Bohlen, and U. Polom. Influence of ice crystal anisotropy on seismic velocity analysis. *Annals of Glaciology*, 55(67):97–106, 2014. ISSN 0260-3055, 1727-5644. doi: 10.3189/2014AoG67A002.

R. Drews, O. Eisen, D. Steinhage, I. Weikusat, S. Kipfstuhl, and F. Wilhelms. Potential mechanisms for anisotropy in ice-penetrating radar data. *Journal of Glaciology*, 58(209): 613–624, 2012. ISSN 0022-1430, 1727-5652. doi: 10.3189/2012JoG11J114.

R. Drews, K. Matsuoka, C. Martín, D. Callens, N. Bergeot, and F. Pattyn. Evolution of Derwael Ice Rise in Dronning Maud Land, Antarctica, over the last millennia. *Journal of Geophysical Research: Earth Surface*, 120(3):564–579, Mar. 2015. ISSN 21699003. doi: 10.1002/2014JF003246. URL http://doi.wiley.com/10.1002/2014JF003246.

G. Durand, F. Gillet-Chaulet, A. Svensson, O. Gagliardini, S. Kipfstuhl, J. Meyssonnier, F. Parrenin, P. Duval, and D. Dahl-Jensen. Change in ice rheology during climate variations–implications for ice flow modelling and dating of the epica dome c core. *Climate of the Past*, 3(1):155–167, 2007.

G. Durand, O. Gagliardini, B. de Fleurian, T. Zwinger, and E. Le Meur. Marine ice sheet dynamics: Hysteresis and neutral equilibrium. *Journal of Geophysical Research*, 114(F3):F03009, Aug. 2009. ISSN 0148-0227. doi: 10.1029/2008JF001170. URL http://doi.wiley.com/10.1029/2008JF001170.

P. Duval, M. Ashby, and I. Anderman. Rate-controlling processes in the creep of polycrystalline ice. *The Journal of Physical Chemistry*, 87(21):4066–4074, 1983.

M. R. Ershadi, R. Drews, C. Martín, O. Eisen, C. Ritz, H. Corr, J. Christmann, O. Zeising, A. Humbert, and R. Mulvaney. Polarimetric radar reveals the spatial distribution of ice fabric at domes and divides in east antarctica. *The Cryosphere*, 16(5):1719–1739, May 2022. ISSN 1994-0424. doi: 10.5194/tc-16-1719-2022. URL https://tc.copernicus.org/articles/16/1719/2022/.

L. Favier and F. Pattyn. Antarctic ice rise formation, evolution, and stability. *Geophysical Research Letters*, 42(11):4456–4463, June 2015. ISSN 0094-8276, 1944-8007. doi: 10.1002/2015GL064195. URL https://onlinelibrary.wiley.com/doi/abs/10.1002/2015GL064195.

S. Fujita, H. Maeno, and K. Matsuoka. Radio-wave depolarization and scattering within ice sheets: a matrix-based model to link radar and ice-core measurements and its application. *Journal of Glaciology*, 52(178):407–424, 2006. doi: 10.3189/172756506781828548.

O. Gagliardini, F. Gillet-Chaulet, and M. Montagnat. A review of anisotropic polar ice models: from crystal to ice-sheet flow models. *Physics of Ice Core Records II*, 68, 01 2009.

O. Gagliardini, T. Zwinger, F. Gillet-Chaulet, G. Durand, L. Favier, B. de Fleurian, R. Greve, M. Malinen, C. Martín, P. Råback, J. Ruokolainen, M. Sacchettini, M. Schäfer, H. Seddik, and J. Thies. Capabilities and performance of Elmer/Ice, a new-generation ice sheet model. *Geoscientific Model Development*, 6(4):1299–1318, Aug. 2013. ISSN 1991-9603. doi: 10.5194/gmd-6-1299-2013. URL https://gmd.copernicus.org/articles/6/1299/2013/.

T. A. Gerber, D. A. Lilien, N. M. Rathmann, S. Franke, T. J. Young, F. Valero-Delgado, M. R. Ershadi, R. Drews, O. Zeising, A. Humbert, et al. Crystal orientation fabric anisotropy causes directional hardening of the northeast greenland ice stream. *Nature Communications*, 14(1):2653, 2023.

F. Gillet-Chaulet, O. Gagliardini, J. Meyssonnier, M. Montagnat, and O. Castelnau. A user-friendly anisotropic flow law for ice-sheet modeling. *Journal of glaciology*, 51(172): 3–14, 2005.

F. Gillet-Chaulet, O. Gagliardini, J. Meyssonnier, T. Zwinger, and J. Ruokolainen. Flow-induced anisotropy in polar ice and related ice-sheet flow modelling. *Journal of non-newtonian fluid mechanics*, 134(1-3):33–43, 2006.

G. Gödert. A mesoscopic approach for modelling texture evolution of polar ice including recrystallization phenomena. *Annals of Glaciology*, 37:23–28, 2003. doi: 10.3189/172756403781815375.

A. C. J. Henry, R. Drews, C. Schannwell, and V. Višnjević. Hysteretic evolution of ice rises and ice rumples in response to variations in sea level. *The Cryosphere*, 16(9):3889–3905, 2022. doi: 10.5194/tc-16-3889-2022. URL https://tc.copernicus.org/articles/16/3889/2022/.

A. C. J. Henry, C. Schannwell, V. Višnjević, J. Millstein, P. Bons, O. Eisen, and D. R. Predicting the three-dimensional age-depth field of an ice rise. 2023. doi: 10.22541/essoar.169230234.44865946/v1.

K. C. Jezek, J. C. Curlander, F. Carsey, C. Wales, and R. G. Barry. Ramp amm-1 sar image mosaic of antarctica, version 2, 2013. URL https://nsidc.org/data/NSIDC-0103/versions/2.

T. M. Jordan, C. Martín, A. M. Brisbourne, D. M. Schroeder, and A. M. Smith. Radar characterization of ice crystal orientation fabric and anisotropic viscosity within an antarctic ice stream. *Journal of Geophysical Research: Earth*

Surface, 127(6):e2022JF006673, 2022. doi: https://doi.org/10.1029/2022JF006673. URL https://agupubs.onlinelibrary.wiley.com/doi/abs/10.1029/2022JF006673. e2022JF006673 2022JF006673.

I. Koch, R. Drews, S. Franke, D. Jansen, F. M. Oraschewski, L. Muhle, V. Višnjević, K. Matsuoka, F. Pattyn, and O. Eisen. Radar internal reflection horizons from multisystem data reflect ice dynamic and surface accumulation history along the princess ragnhild coast, dronning maud land, east antarctica [in review]. *Journal of Glaciology*, 2023.

S. Kufner, J. Wookey, A. M. Brisbourne, C. Martín, T. S. Hudson, J. M. Kendall, and A. M. Smith. Strongly depth-dependent ice fabric in a fast-flowing antarctic ice stream revealed with icequake observations. *Journal of Geophysical Research: Earth Surface*, 128 (3):e2022JF006853, Mar 2023. ISSN 2169-9003, 2169-9011. doi: 10.1029/2022JF006853. URL https://agupubs.onlinelibrary.wiley.com/doi/10.1029/2022JF006853.

D. A. Lilien, N. M. Rathmann, C. S. Hvidberg, and D. Dahl-Jensen. Modeling ice-crystal fabric as a proxy for ice-stream stability. *Journal of Geophysical Research: Earth Surface*, 126(9), Sep 2021. ISSN 2169-9003, 2169-9011. doi: 10.1029/2021JF006306. URL https://onlinelibrary.wiley.com/doi/10.1029/2021JF006306.

D. A. Lilien, N. M. Rathmann, C. S. Hvidberg, A. Grinsted, M. R. Ershadi, R. Drews, and D. Dahl-Jensen. Simulating higher-order fabric structure in a coupled, anisotropic ice-flow model: application to dome c. *Journal of Glaciology*, page 1–20, Nov. 2023. ISSN 0022-1430, 1727-5652. doi: 10.1017/jog.2023.78.

M.-G. Llorens, A. Griera, P. D. Bons, I. Weikusat, D. J. Prior, E. Gomez-Rivas, T. De Riese, I. Jimenez-Munt, D. García-Castellanos, and R. A. Lebensohn. Can changes in deformation regimes be inferred from crystallographic preferred orientations in polar ice? *The Cryosphere*, 16(5):2009–2024, May 2022. ISSN 1994-0424. doi: 10.5194/tc-16-2009-2022. URL https://tc.copernicus.org/articles/16/2009/2022/.

Y. Ma, O. Gagliardini, C. Ritz, F. Gillet-Chaulet, G. Durand, and M. Montagnat. Enhancement factors for grounded ice and ice shelves inferred from an anisotropic ice-flow model. *Journal of Glaciology*, 56(199):805–812, 2010. ISSN 0022-1430, 1727-5652. doi: 10.3189/002214310794457209.

C. Martín and G. H. Gudmundsson. Effects of nonlinear rheology, temperature and anisotropy on the relationship between age and depth at ice divides. *The Cryosphere*, 6(5):1221–1229, Oct 2012. ISSN 1994-0424. doi: 10.5194/tc-6-1221-2012. URL https://tc.copernicus.org/articles/6/1221/2012/.

C. Martín, R. C. A. Hindmarsh, and F. J. Navarro. On the effects of divide migration, along-ridge flow, and basal sliding on isochrones near an ice divide. *Journal of Geophysical Research*, 114(F2):F02006, Apr. 2009. ISSN 0148-0227. doi: 10.1029/2008JF001025. URL http://doi.wiley.com/10.1029/2008JF001025.

K. Matsuoka, T. Furukawa, S. Fujita, H. Maeno, S. Uratsuka, R. Naruse, and O. Watanabe. Crystal orientation fabrics within the antarctic ice sheet revealed by a multipolarization plane and dual-frequency radar survey. *Journal of Geophysical Research: Solid Earth*, 108(B10):2003JB002425, Oct. 2003. ISSN 0148-0227. doi: 10.1029/2003JB002425. URL https://agupubs.onlinelibrary.wiley.com/doi/10.1029/2003JB002425.

K. Matsuoka, L. Wilen, S. Hurley, and C. Raymond. Effects of birefringence within ice sheets on obliquely propagating radio waves. *IEEE Transactions on Geoscience and Remote Sensing*, 47(5):1429–1443, May 2009. ISSN 0196-2892, 1558-0644. doi: 10.1109/TGRS.2008.2005201. URL http://ieeexplore.ieee.org/document/4682732/.

K. Matsuoka, D. Power, S. Fujita, and C. F. Raymond. Rapid development of anisotropic ice-crystal-alignment fabrics inferred from englacial radar polarimetry, central west antarctica. *Journal of Geophysical Research: Earth*

Surface, 117(F3), 2012. doi: https://doi.org/10.1029/2012JF002440. URL https://agupubs.onlinelibrary.wiley.com/doi/abs/10.1029/2012JF002440.

K. Matsuoka, R. C. Hindmarsh, G. Moholdt, M. J. Bentley, H. D. Pritchard, J. Brown, H. Conway, R. Drews, G. Durand, D. Goldberg, T. Hattermann, J. Kingslake, J. T. Lenaerts, C. Martín, R. Mulvaney, K. W. Nicholls, F. Pattyn, N. Ross, T. Scambos, and P. L. Whitehouse. Antarctic ice rises and rumples: Their properties and significance for ice-sheet dynamics and evolution. *Earth-Science Reviews*, 150: 724–745, Nov. 2015. ISSN 00128252. doi: 10.1016/j.earscirev.2015.09.004. URL https://linkinghub.elsevier.com/retrieve/pii/S0012825215300416.

F. S. McCormack, R. C. Warner, H. Seroussi, C. F. Dow, J. L. Roberts, and A. Treverrow. Modeling the deformation regime of thwaites glacier, west antarctica, using a simple flow relation for ice anisotropy (estar). *Journal of Geophysical Research: Earth Surface*, 127 (3):e2021JF006332, Mar. 2022. ISSN 2169-9003, 2169-9011. doi: 10.1029/2021JF006332. URL https://agupubs.onlinelibrary.wiley.com/doi/10.1029/2021JF006332.

M. Montagnat, N. Azuma, D. Dahl-Jensen, J. Eichler, S. Fujita, F. Gillet-Chaulet, S. Kipfstuhl, D. Samyn, A. Svensson, and I. Weikusat. Fabric along the neem ice core, greenland, and its comparison with grip and ngrip ice cores. *The Cryosphere*, 8(4):1129–1138, 2014. doi: 10.5194/tc-8-1129-2014. URL https://tc.copernicus.org/articles/8/1129/2014/.

E. C. Pettit, T. Thorsteinsson, H. P. Jacobson, and E. D. Waddington. The role of crystal fabric in flow near an ice divide. *Journal of Glaciology*, 53(181):277–288, 2007. ISSN 0022-1430, 1727-5652. doi: 10.3189/172756507782202766.

E. C. Pettit, E. D. Waddington, W. D. Harrison, T. Thorsteinsson, D. Elsberg, J. Morack, and M. A. Zumberge. The crossover stress, anisotropy and the ice flow law at siple dome, west antarctica. *Journal of Glaciology*, 57(201):39–52, 2011. ISSN 0022-1430, 1727-5652. doi: 10.3189/002214311795306619.

N. M. Rathmann, C. S. Hvidberg, A. Grinsted, D. A. Lilien, and D. Dahl-Jensen. Effect of an orientation-dependent non-linear grain fluidity on bulk directional enhancement factors. *Journal of Glaciology*, 67(263):569–575, Jun 2021. ISSN 0022-1430, 1727-5652. doi: 10.1017/jog.2020.117.

N. M. Rathmann, D. A. Lilien, A. Grinsted, T. A. Gerber, T. J. Young, and D. Dahl-Jensen. On the limitations of using polarimetric radar sounding to infer the crystal orientation fabric of ice masses. *Geophysical Research Letters*, 49(1):e2021GL096244, Jan. 2022. ISSN 0094-8276, 1944-8007. doi: 10.1029/2021GL096244.

D. H. Richards, S. S. Pegler, and S. Piazolo. Ice fabrics in two-dimensional flows: beyond pure and simple shear. *The Cryosphere*, 16(10):4571–4592, Oct 2022. ISSN 1994-0424. doi: 10.5194/tc-16-4571-2022. URL https://tc.copernicus.org/articles/16/4571/2022/.

E. Rignot, J. Mouginot, and B. Scheuchl. Measures insar-based antarctica ice velocity map, version 2, 2017. URL https://nsidc.org/data/NSIDC-0484/versions/2.

C. Schannwell, R. Drews, T. A. Ehlers, O. Eisen, C. Mayer, and F. Gillet-Chaulet. Kinematic response of ice-rise divides to changes in ocean and atmosphere forcing. *The Cryosphere*, 13(10):2673–2691, Oct. 2019. ISSN 1994-0424. doi: 10.5194/tc-13-2673-2019. URL https://tc.copernicus.org/articles/13/2673/2019/.

C. Schannwell, R. Drews, T. A. Ehlers, O. Eisen, C. Mayer, M. Malinen, E. C. Smith, and H. Eisermann. Quantifying the effect of ocean bed properties on ice sheet geometry over 40 000 years with a full-Stokes model. *The Cryosphere*, 14 (11):3917–3934, Nov. 2020. ISSN 1994-0424. doi: 10.5194/tc-14-3917-2020. URL https://tc.copernicus.org/articles/14/3917/2020/.

H. Seddik, R. Greve, T. Zwinger, and L. Placidi. A full stokes ice flow model for the vicinity of dome fuji, antarctica, with induced anisotropy and fabric evolution. *The Cryosphere*, 5(2):495–508, 2011. doi: 10.5194/tc-5-495-2011. URL https://tc.copernicus.org/articles/5/495/2011/.

E. C. Smith, A. F. Baird, J. M. Kendall, C. Martín, R. S. White, A. M. Brisbourne, and A. M. Smith. Ice fabric in an antarctic ice stream interpreted from seismic anisotropy. *Geophysical Research Letters*, 44(8):3710–3718, Apr 2017. ISSN 0094-8276, 1944-8007. doi: 10.1002/2016GL072093. URL https://onlinelibrary.wiley.com/doi/10.1002/2016GL072093.

T. Thorsteinsson, E. D. Waddington, and R. C. Fletcher. Spatial and temporal scales of anisotropic effects in ice-sheet flow. *Annals of Glaciology*, 37:40–48, 2003. ISSN 0260-3055, 1727-5644. doi: 10.3189/172756403781815429.

I. Weikusat, D. Jansen, T. Binder, J. Eichler, S. H. Faria, F. Wilhelms, S. Kipfstuhl, S. Sheldon, H. Miller, D. Dahl-Jensen, and T. Kleiner. Physical analysis of an antarctic ice core—towards an integration of micro- and macrodynamics of polar ice. *Philosophical Transactions of the Royal Society A: Mathematical, Physical and Engineering Sciences*, 375(2086):20150347, Feb. 2017. ISSN 1364-503X, 1471-2962. doi: 10.1098/rsta.2015.0347. URL https://royalsocietypublishing.org/doi/10.1098/rsta.2015.0347.

N. H. Woodcock. Specification of fabric shapes using an eigenvalue method. *Geological Society of America Bulletin*, 88(9):1231, 1977. ISSN 0016-7606. doi: 10.1130/0016-7606(1977)88¡1231:SOFSUA¿2.0.CO;2. URL https://pubs.geoscienceworld.org/gsabulletin/article/88/9/1231-1236/202166.

T. J. Young, C. Martín, P. Christoffersen, D. M. Schroeder, S. M. Tulaczyk, and E. J. Dawson. Rapid and accurate polarimetric radar measurements of ice crystal fabric orientation at the western antarctic ice sheet (wais) divide ice core site. *The Cryosphere*, 15 (8):4117–4133, 2021a.

T. J. Young, D. M. Schroeder, T. M. Jordan, P. Christoffersen, S. M. Tulaczyk, R. Culberg, and N. L. Bienert. Inferring ice fabric from birefringence loss in airborne radargrams: Application to the eastern shear margin of thwaites glacier, west antarctica. *Journal of Geophysical Research: Earth Surface*, 126(5):e2020JF006023, May 2021b. ISSN 2169-9003, 2169-9011. doi: 10.1029/2020JF006023. URL https://agupubs.onlinelibrary.wiley.com/doi/10.1029/2020JF006023.

5

ICE-SHELF DYNAMICS DUE TO PINNING POINT BUTTRESSING

MANUSCRIPT DETAILS:

A. Clara J. Henry, Ian J. Hewitt and Guy Moss.: The dynamics of pinning point buttressing [Work in progress]

Ice-shelf dynamics due to pinning point buttressing

Abstract

Pinning points located within ice shelves regulate ice flow dynamics in coastal Antarctica, and influence the continental grounding line position. Despite remaining questions regarding the contribution of a pinning point to the force balance in an ice shelf, there have been no sensitivity studies investigating the buttressing force due to pinning points. We perform a range of full Stokes simulations varying the pinning point geometry and ice shelf flux, and investigate the relative influence of ice flow parameters. We decompose forces in the ice shelf into those due to ocean pressure and due to pinning point buttressing. We furthermore perform baseline simulations without a pinning point comparing full Stokes, shallow shelf approximation (SSA) and Blatter-Pattyn approximation (BPA) simulations to an analytical ice shelf solution. The SSA simulations allow the simulation of pinning points with computational efficiency and without the need to perform parallelised simulations. These preliminary results are of importance for those wishing to investigate the buttressing force due to individual pinning points.

1 Introduction

The location and stability of the Antarctic grounding line is dependent on a variety of factors including the slope of the bed (Schoof, 2007) and the stresses incurred by the buttressing of ice shelves (Goldberg et al., 2009; Favier and Pattyn, 2015; Haseloff and Sergienko, 2018). Accurate predictions of the continental grounding line position are important because a retreat of the grounding line causes a loss of grounded ice and an increase in sea level. The regulation of the flow of ice shelves can occur due to lateral buttressing whereby stresses at the sides of confined ice shelves cause a slowing of ice shelf velocities (Pegler, 2016, 2018). Regulation of ice shelf flow can also occur due to the forces caused by a pinning point, defined as an area of grounded ice within an ice shelf which is otherwise surrounded by floating ice (Favier and Pattyn, 2015; Reese et al., 2018a; Fürst et al., 2015). The ice shelf is diverted either side of the obstacle in the case of an ice rise and slowed down in the case of an ice rumple. The buttressing force due to a pinning point depends on a variety of factors. The larger the width of a pinning point perpendicular to the predominant ice shelf velocity direction determines, the more obstructive a pinning point is to ice shelf flow. Furthermore, the greater the flux of the upstream ice shelf, the greater the vertical contact with a pinning point due to a thicker ice column. Changes in ice shelf thickness have a significant effect on the continental grounding line flux with a thinning of the ice shelf causing a speed up of ice across the grounding line (Reese et al., 2018a). Furthermore, the geometry of a pinning point has an influence on upstream ice shelf velocities, with a larger pinning point resulting in lower velocities (Henry et al., 2022).

Despite their influence on coastal ice flow dynamics, pinning points are often neglected in large-scale simulations due to limited resolution and large uncertainties in bed elevation data. Apart from causing an incorrect force balance in an ice shelf, neglecting a pinning point results in incorrect fluidity parameters if these are inferred from observations (Berger et al., 2016) causing excess stiffening and a reduction in sea-level contribution in transient simulations (Favier et al., 2016). Unpinning of pinning points has an influence on ice shelf velocities (Favier et al., 2016; Still and Hulbe, 2021; Wild et al., 2022), a mechanism that

is missed if a pinning point is not resolved in a model, causing incorrect transient evolution. Furthermore, some models prescribe the flux at the grounding line using an analytical expression (Schoof, 2007) which provides inaccurate predictions of ice fluxes when the downstream ice shelf is buttressed (Reese et al., 2018b). Other models use an alternative approach, including parameterisation in an attempt to account for pinning point buttressing (Pollard and DeConto, 2012).

Calculating forces due to pinning points in the Ross Ice Shelf, Macayeal et al. (1987) and Still et al. (2019) showed that the buttressing force on the upstream ice shelf varied largely from one pinning point to another. The significance of components of the force balance was shown by calculating the driving force due to changes in ice shelf thickness, the viscous force, and the ocean pressure. Given that pinning points provide a non-negligible force on the upstream ice shelf, they change in geometry over time (Favier and Pattyn, 2015; Kingslake et al., 2016, 2018; Wearing and Kingslake, 2019; Brisbourne et al., 2019; Henry et al., 2022) and are found in every ice shelf around the Antarctic perimeter (Matsuoka et al., 2015), it is important to understand the dominant factor influencing the pinning point buttressing force. This is particularly important for understanding how buttressing may change in ice shelves most vulnerable to a changing climate (Višnjević et al., 2022).

In this manuscript, we present preliminary results investigating (1) the dominant factors influencing pinning point buttressing, (2) a comparison between three models to investigate the ability to capture ice shelf dynamics due to an obstacle and (3) first results of a decomposition of ice shelf forces to isolate the force due to the pinning point. Using a full Stokes model, we simulate pinning points varying the upstream ice shelf flux and the extent of the underlying bed anomaly thereby causing varying grounded areas. We investigate the relative influence of parameters controlling buttressing dynamics, namely the gravitational constant and the ice fluidity. Following previous work by Macayeal et al. (1987) and Still et al. (2019), we calculate the force on the upstream ice shelf due to ocean pressure and due to the pinning point. Although not presented here, we discuss an alternative method for calculating the pinning point force for future work. We perform comparable simulations using the SS) and a simplified representation of pinning points, and compare these against the benchmark full Stokes simulations. Reasons for comparisons between model hierarchies are (1) investigation of the ability of ice flow approximations to capture the dynamic response due to pinning point buttressing, and (2) to provide a computationally-efficient method for calculation of the buttressing force due to a pinning point.

2 Methods

A number of formulations exist for the equations describing the flow of ice, varying in complexity and computational expense. The Stokes equations, often referred to as the full Stokes equations, are used to compute the stress field, and are applicable across both floating and grounded ice. Therefore, they are appropriate for describing ice flow at pinning points. Computationally-efficient approximations to the Stokes equations exist for flow regimes with negligible stress tensor components that can be ignored in the force balance. For example, the shallow shelf approximation (SSA, Morland (1987)) is appropriate for floating ice where vertical gradients of horizontal velocities are negligible. Here, we present simulations of pinning points of varying sizes and varying domain boundary fluxes using the Stokes equations. Alongside full-Stokes simulations of fully-resolved pinning points, we perform comparable simulations representing the pinning point as a vertical cylinder in full Stokes, SSA and Blatter-Pattyn approximation (BPA) simulations. The diameter of the cylinder is determined by the grounded width of the pinning point perpendicular to the predominant flow direction in the fully-resolved pinning point simulations. Simplifications are made for two reasons; (1) a significant reduction in computational expense and (2) isolated investigation of ice shelf dynamics due an obstacle without additional uncertainties regarding friction laws and accurate ice velocities in the pinning point.

Fully-resolved simulations of pinning points, solved with the full Stokes equations, are performed with variations of the inflow velocity, $v_0 = \{50, 100, 150, 200, 250, 300\}$ m a^{-1}, and variations of a parameter controlling the pinning point extent, $\sigma_R = 1000, 2000, 3000, 4000, 5000$

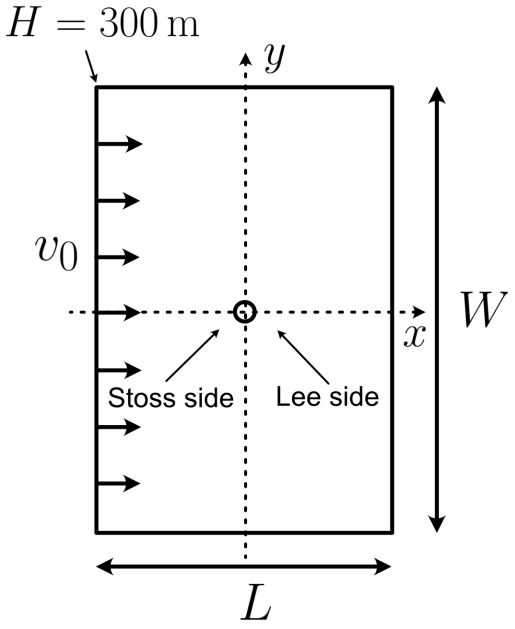

Figure 1: The simulation domain from above showing the x- and y-axes. The dimensions of the domain are defined by the width perpendicular to the predominant ice shelf velocity direction, W, and the length of the domain, L. On the left, the inflow domain boundary is shown where a fixed inflow velocity, v_0, and ice thickness, $H = 300\,\mathrm{m}$, are specified. In the centre of the domain, at $(x, y) = (0, 0)$, the pinning point is shown.

m. Simulations are performed for a period of 1000 years to allow evolution to a steady state. The width of the domain for all simulations is $W = 300$ km and the length is $L = 150$ km (Fig. 1).

2.1 Stokes equations

We use the finite element model *Elmer/Ice* (Gagliardini et al., 2013) to solve the full Stokes equations. The equations of motion for Stokes flow are

$$\boldsymbol{\nabla} \cdot (\boldsymbol{\tau} - P\mathbf{I}) + \rho_i \mathbf{g} = 0, \tag{1}$$

where $\boldsymbol{\tau}$ is the deviatoric stress tensor, P is the pressure, $\mathbf{I}$ is the identity matrix, ρ_i is the ice density and $\mathbf{g} = g\hat{\mathbf{e}}_z$ is the gravitational acceleration. The ice is subject to an incompressibility condition,

$$\boldsymbol{\nabla} \cdot \mathbf{u} = 0. \tag{2}$$

Glen's flow law,

$$\boldsymbol{\tau} = 2\eta\dot{\boldsymbol{\varepsilon}}, \tag{3}$$

describes the nonlinear dependence between the strain rate tensor, $\dot{\boldsymbol{\varepsilon}}$, and the deviatoric stress tensor. The effective viscosity, η, is given by

$$\eta = \frac{1}{2} A(T)^{-1/n} \dot{\varepsilon}_e^{(1-n)/n}, \tag{4}$$

where $A(T)$ is the ice fluidity which is dependent on temperature, T, and is isothermal in our case, and n is the Glen's flow factor, usually taken to be $n = 3$. The effective strain rate is defined as $\sqrt{\mathrm{tr}\,\dot{\varepsilon}^2/2}$.

The upper ice surface, $z = z_s(x, y, t)$, and the lower ice surface, $z = z_b(x, y, t)$, evolve subject to

$$\left(\frac{\partial}{\partial t} + \mathbf{u} \cdot \boldsymbol{\nabla}\right)(z - z_s) = \dot{a}_s, \tag{5}$$

Table 1: Stokes simulations parameters

Parameter	Symbol	Value	Unit
Domain length	L	150	km
Domain width	W	300	km
Inflow ice thickness	H_0	300	m
Rheological parameter	A	4.6×10^{-25}	$\mathrm{Pa}^{-3}\ \mathrm{s}^{-1}$
Glen's exponent	n	3	
Basal friction exponent	m	1/3	
Ocean density	ρ_w	1000	$\mathrm{kg\ m}^{-3}$
Ice density	ρ_i	900	$\mathrm{kg\ m}^{-3}$
Gravity	g	9.8	$\mathrm{m\ s}^{-2}$
Bed base	b_0	-600	m
Maximum bed height (above b_0)	M	600	m
Bed anomaly centre	(x_0, y_0)	$(0, 0)$	km
Bed anomaly extent	σ_R	$[1000, 2000, 3000, 4000, 5000]$	m
Inflow velocity	v_0	$[50, 100, 150, 200, 250, 300]$	$\mathrm{m\ a}^{-1}$

and

$$\left(\frac{\partial}{\partial t} + \mathbf{u} \cdot \boldsymbol{\nabla}\right)(z - z_b) = \dot{a}_b, \tag{6}$$

respectively, where $\dot{a}_s$ is the accumulation rate and $\dot{a}_b$ is the basal melt rate. The initial ice thickness is 300 m everywhere in the domain. A surface mass balance of 1 m a^{-1} is prescribed throughout the domain and a basal mass balance of 1 m a^{-1} is prescribed where the ice is floating.

In the horizontal, a resolution of 250 m is used in the area encompassing the pinning point, defined as the area within a distance of 5000 m from the initial grounding line. A lower resolution of 2000 m is used in the surrounding area. In the vertical, 10 nodes are used. Following Henry et al. (2022), the bed elevation is defined by the function

$$b_a(x, y) = b_0 + M \exp\{-R^4/\sigma_R^4\}. \tag{7}$$

where $R = \sqrt{x^2 + y^2}$. Simulations are performed with σ_R values of $1000, 2000, 3000, 4000$ and 5000 m. Simulations varying the inflow velocity are performed for every combination of inflow velocities, v_0, of $50, 100, 150, 200, 250$ and 300 m a^{-1}. Simulations are performed for a period of 1000 years to allow evolution to a steady state.

2.2 Shallow shelf approximation (SSA)

The shallow shelf approximation (SSA, Hutter (1983)) reduces the Stokes equations to

$$\begin{aligned} 4\frac{\partial}{\partial x}\left(\bar{\eta}\frac{\partial v_x}{\partial x}\right) + 2\frac{\partial}{\partial x}\left(\bar{\eta}\frac{\partial v_y}{\partial y}\right) + \frac{\partial}{\partial y}\left(\bar{\eta}\left(\frac{\partial v_x}{\partial y} + \frac{\partial v_y}{\partial x}\right)\right) &= \rho_i g H \frac{\partial h}{\partial x} \\ 4\frac{\partial}{\partial y}\left(\bar{\eta}\frac{\partial v_y}{\partial y}\right) + 2\frac{\partial}{\partial y}\left(\bar{\eta}\frac{\partial v_x}{\partial x}\right) + \frac{\partial}{\partial x}\left(\bar{\eta}\left(\frac{\partial v_x}{\partial y} + \frac{\partial v_y}{\partial x}\right)\right) &= \rho_i g H \frac{\partial h}{\partial y}. \end{aligned} \tag{8}$$

It is used to solve ice flow in ice shelves (see, for example, Greve and Blatter (2009) for a full derivation). Here, H is the ice thickness, $\bar{\eta}$ is the vertically-integrated viscosity,

$$\bar{\eta} = \int_{z_b}^{z_s} \eta \, dz, \tag{9}$$

and h is the surface elevation relative to sea level. As opposed to three-dimensional Stokes equations, the SSA is vertically-integrated and is thus a two-dimensional partial differential equation. The SSA equations are implemented in the finite element model *icepack* (Shapero et al., 2021).

In icepack, a regularisation term is introduced to account for very small strain rates as is the case in the simulations presented here. An unstructured grid is used with an approximate resolution of 1000 m and we assume zero net accumulation.

2.3 Blatter-Pattyn approximation (BPA)

Simulations of flow around an obstacle are performed with the BPA and are also solved using *icepack* Shapero et al. (2021). The BPA solving the following set of equations,

$$\begin{aligned} 4\frac{\partial}{\partial x}\left(\bar{\eta}\frac{\partial v_x}{\partial x}\right) + 2\frac{\partial}{\partial x}\left(\bar{\eta}\frac{\partial v_y}{\partial y}\right) + \frac{\partial}{\partial y}\left(\bar{\eta}\left(\frac{\partial v_x}{\partial y} + \frac{\partial v_y}{\partial x}\right)\right) + \frac{\partial}{\partial z}\left(\bar{\eta}\frac{\partial v_x}{\partial z}\right) = \rho_i g H \frac{\partial h}{\partial x} \\ 4\frac{\partial}{\partial y}\left(\bar{\eta}\frac{\partial v_y}{\partial y}\right) + 2\frac{\partial}{\partial y}\left(\bar{\eta}\frac{\partial v_x}{\partial x}\right) + \frac{\partial}{\partial x}\left(\bar{\eta}\left(\frac{\partial v_x}{\partial y} + \frac{\partial v_y}{\partial x}\right)\right) + \frac{\partial}{\partial z}\left(\bar{\eta}\frac{\partial v_y}{\partial z}\right) = \rho_i g H \frac{\partial h}{\partial y} \end{aligned} \tag{10}$$

In comparison with the SSA, additional terms to incorporate vertical gradients in horizontal velocities are included. These additional terms mean that the BPA must be solved in three dimensions. Simulations are therefore significantly more expensive than SSA simulations. In icepack, the extruded vertical direction is not solved with Lagrange elements, as has been standard practice, but with a Legendre-polynomial basis. In simulations, the degree of the Legendre polynomial must be chosen. A Legendre-polynomial degree of 0 results in a system of equations equivalent to the SSA, whereas higher degrees allow a better representation of vertical shear.

In the simulations presented here, we have used a Legendre-polynomial degree of 1, which allows only minimal representation of vertical shear. The simulations presented are significantly more expensive than the SSA simulations, and would likely require partitioning of the domain when using a higher order polynomial. As in the SSA simulations, we use an unstructured grid with an approximate resolution of 1000 m and we assume zero net accumulation.

2.4 Analytical ice shelf solution

In order to validate the numerical simulations, we make comparisons with a simplified ice shelf geometry without a pinning point for which an analytical solution is known (Greve and Blatter, 2009). With no net accumulation, the ice velocity is given by

$$v_x(x) = \left(v_0^{n+1} + \frac{A(\rho_i g \delta H_0 v_0)^n}{4^n}(n+1)(x - x_0)\right)^{1/(n+1)}, \tag{11}$$

and the ice thickness by

$$H(x) = \frac{H_0 v_0}{v_x(x)}, \tag{12}$$

where $\delta = 1 - \rho_i/\rho_w$, ρ_w is the ocean density and H_0 is the ice thickness at the inflow boundary.

2.5 Calculation of stress

In order to make comparisons with the Stokes simulations and because the SSA simulations, BPA simulations and the analytical ice shelf solution, we calculate the stress field from the velocity field for selected simulations. First, we calculate the membrane stresses in the x- and y-directions using Glen's flow law (Eq. (3)), assuming that horizontal velocity derivatives do not change with depth,

$$\begin{aligned} N_{xx} &= 2\bar{\eta}\dot{\varepsilon}_{xx} = 2\bar{\eta}\frac{\partial v_x}{\partial x} \\ N_{yy} &= 2\bar{\eta}\dot{\varepsilon}_{yy} = 2\bar{\eta}\frac{\partial v_y}{\partial y} \\ N_{xy} &= 2\bar{\eta}\dot{\varepsilon}_{xy} = \bar{\eta}\left(\frac{\partial v_x}{\partial y} + \frac{\partial v_y}{\partial x}\right), \end{aligned} \tag{13}$$

where N_{xx}, N_{yy} and $N_{xy} = N_{yx}$ are the components of the membrane stress tensor, $\mathbf{N}$, which are equal to the vertically-integrated deviatoric stress tensor components,

$$N_{ij} = \int_{z_b}^{z_s} \tau_{ij}\, dz. \tag{14}$$

We assume that the first two terms in the first equation in Glen's flow law (Eq. (3))

$$\frac{\partial \sigma_{xz}}{\partial x} + \frac{\partial \sigma_{yz}}{\partial y} + \frac{\partial \sigma_{zz}}{\partial z} = \rho_i g \tag{15}$$

are negligible, which is a reasonable assumption for an ice shelf Hutter (1983). This allows us to integrate Eq. (15), giving

$$\frac{\partial \sigma_{zz}}{\partial z} = \rho_i g. \tag{16}$$

Assuming no stress at the upper ice surface,

$$\sigma_{zz}|_{z=z_s} = 0, \tag{17}$$

which results in an expression for the vertical stress component,

$$\sigma_{zz} = -\rho_i g(z_s - z). \tag{18}$$

To calculate the other stress tensor components, we first observe that the trace of the deviatoric stress tensor satisfies

$$\tau_{xx} + \tau_{yy} + \tau_{zz} = 0. \tag{19}$$

Using the defined relationship between pressure, stress and deviatoric stress,

$$\boldsymbol{\tau} - p\mathbf{I} = \boldsymbol{\sigma}, \tag{20}$$

we find an expression for pressure

$$\begin{aligned} p &= \tau_{zz} - \sigma_{zz} \\ &= -\tau_{xx} - \tau_{yy} - \sigma_{zz}. \end{aligned} \tag{21}$$

Using Eq. (20) and Eq. (21), the x-component of the stress tensor is

$$\begin{aligned} \sigma_{xx} &= -p + \tau_{xx} \\ &= 2\tau_{xx} + \tau_{yy} - \rho_i g(z_s - z). \end{aligned} \tag{22}$$

Integrating Eq. (22) over the vertical we find an expression for the stress in the x-direction in terms of the membrane stresses as defined in Eqs. 13 and 14, so that

$$\bar{\sigma}_{xx} = 2N_{xx} + N_{yy} - \frac{1}{2}\rho_i g(z_s - z_b)^2. \tag{23}$$

Note that because we investigate only the forces and stresses in the x-direction in the remaing sections, we drop the subscript when referring to the vertically-integrated stress, such that $\bar{\sigma} = \bar{\sigma}_{xx}$.

2.6 Ice shelf forces

We use a number of metrics for comparison between full Stokes and the SSA simulations. We define the vertically-integrated stress exerted on the ice shelf upstream of a pinning point at the cross-section, $x = -45$ km, by

$$\bar{\boldsymbol{\sigma}}(y) = \bar{\sigma}(y)\hat{\mathbf{e}}_x = \int_{z_b}^{z_s} \sigma_{xx}\, dz\, \hat{\mathbf{e}}_x \tag{24}$$

and integrated over the width of the domain,

$$\mathbf{F}_{tot} = \int_{-W/2}^{W/2} \int_{z_b}^{z_s} \sigma_{xx}\, dz\, dy\, \hat{\mathbf{e}}_x \tag{25}$$

where σ_{xx} is the normal stress in the x-direction. The total force on the upstream ice shelf, $\mathbf{F}_{tot}$, is the superposition of two forces, $\mathbf{F}_{tot} = \mathbf{F}_{pp,tot} + \mathbf{F}_{op,tot}$, where $\mathbf{F}_{pp,tot}$ is the force due

to the pinning point and $\mathbf{F}_{op,tot}$ is the ocean pressure applied to the ice shelf if the calving front were at that position. The vertically-integrated stress due to ocean pressure over the cross-section $x = c$ is

$$\bar{\boldsymbol{\sigma}}_{op}(y) = \bar{\sigma}_{op}(y)\hat{\mathbf{e}}_x = \int_{z_b}^{o} -\rho_w g z \; dz \; \hat{\mathbf{e}}_x, \tag{26}$$

and integrated over the width of the domain is,

$$\mathbf{F}_{op,tot} = \int_{-W/2}^{W/2} \int_{z_b}^{o} -\rho_w g z \; dz \; dy \; \hat{\mathbf{e}}_x, \tag{27}$$

where ρ_w is the ocean density. Therefore, the vertically-integrated stress on the upstream ice shelf due to the pinning point can be expressed as

$$\bar{\boldsymbol{\sigma}}_{pp}(y) = \bar{\sigma}_{pp}(y)\hat{\mathbf{e}}_x = \left\{ \int_{z_b}^{z_s} \sigma_{xx} \; dz \; + \int_{z_b}^{o} \rho_w g z \; dz \right\} \; \hat{\mathbf{e}}_x \tag{28}$$

and integrated over the width of the domain,

$$\mathbf{F}_{pp,tot} = \int_{-W/2}^{W/2} \left\{ \int_{z_b}^{z_s} \sigma_{xx} \; dz \; + \int_{z_b}^{o} \rho_w g z \; dz \right\} \; dy \; \hat{\mathbf{e}}_x \tag{29}$$

The distribution of vertically-integrated stresses in the x-direction, $\bar{\boldsymbol{\sigma}} = \bar{\boldsymbol{\sigma}}_{pp}(y) + \bar{\boldsymbol{\sigma}}_{op}(y)$ are of interest to study the spatial influence of a pinning point. A further quantity of interest is the ocean pressure in the upstream direction with complete removal of the pinning point, $\mathbf{F}_{npp}$, written

$$\bar{\boldsymbol{\sigma}}_{npp}(y) = \bar{\sigma}_{npp}(y)\hat{\mathbf{e}}_x = \int_{z_b}^{o} -\rho_w g z \; dz \; \hat{\mathbf{e}}_x = \int_{z_b}^{z_s} \sigma_{xx} \; dz \; \hat{\mathbf{e}}_x. \tag{30}$$

which is independent of the y-coordinate, and so the upstream force integrated over the width of the domain with no pinning point is written

$$\mathbf{F}_{npp,tot} = W \int_{z_b}^{o} -\rho_w g z \; dz \; \hat{\mathbf{e}}_x = W \int_{z_b}^{z_s} \sigma_{xx} \; dz \; \hat{\mathbf{e}}_x. \tag{31}$$

3 Results

3.1 Benchmark simulations

Benchmark comparisons of unbuttressed ice shelves are made between full Stokes simulations and analytical solutions. Fig. 2a and b show the x-direction velocities, v_x, and ice thickness, H, for ice shelves with inflow velocities of $v_0 = \{100, 200, 300\}$ m a^{-1}. At the inflow boundary, velocities and thicknesses do not differ due to equal boundary conditions, whereas moving in the x-direction towards the calving front, small differences occur between the full Stokes simulations and the analytical solutions, with the full Stokes simulations resulting in slightly thicker ($4 - 5$ m thicker) and slower ice ($3 - 14$ m a^{-1} slower).

3.2 Full Stokes simulations

In all full Stokes simulations, the initial ice thickness is 300 m and the simulations are allowed to evolve to a steady-state geometry for 1000 years. A total of 30 full Stokes simulations with fully-resolved pinning points are performed for every combination of inflow velocity $v_0 = \{50, 100, 150, 200, 250, 300\}$ m a^{-1} and bed anomaly extent parameter $\sigma_R = \{1000, 2000, 3000, 4000, 5000\}$ m. The bed anomaly parameter, σ_R, results in a grounded width of the pinning point of roughly double the value of σ_R (Fig. 10 in the Appendix). First, we analyse differences between the four extreme simulations, with combinations of (a) $v_0 = 50$ m a^{-1}, $\sigma_R = 1000$ m, (b) $v_0 = 50$ m a^{-1}, $\sigma_R = 5000$ m, (c) $v_0 = 300$ m a^{-1}, $\sigma_R = 1000$ m and (d) $v_0 = 300$ m a^{-1}, $\sigma_R = 5000$ m. All simulations show a thinning of ice from the inflow boundary towards the pinning point, localised thickening at and on the

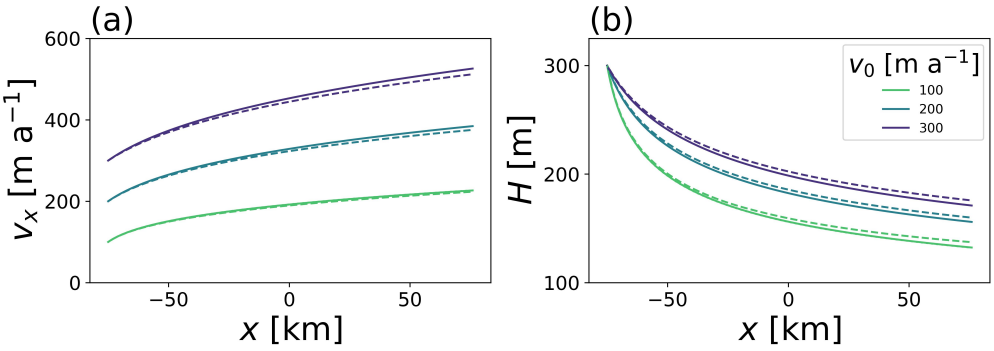

Figure 2: A comparison between (a) the velocity in the x-direction and (b) the ice thickness for full Stokes simulations without a pinning point (dashed lines) and the analytical solution ice shelf solution (solid lines) for selected simulations.

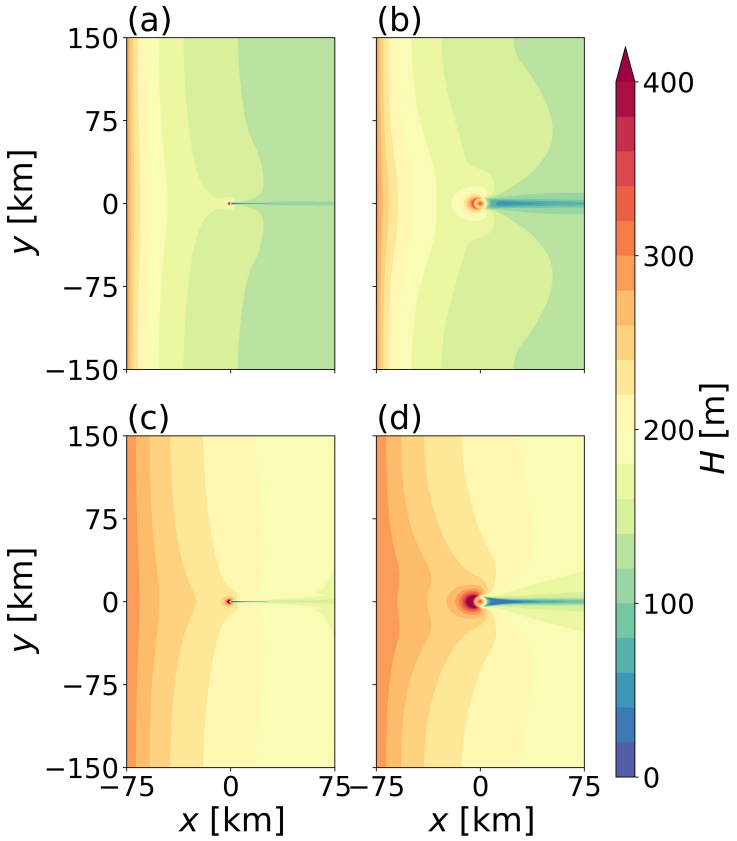

Figure 3: The ice thickness, H, in full Stokes simulations of pinning points with combinations of inflow velocities, v_0, and bed extent parameters, σ_R, of (a) $v_0 = 50$ m a^{-1}, $\sigma_R = 1000$ m, (b) $v_0 = 50$ m a^{-1}, $\sigma_R = 5000$ m, (c) $v_0 = 300$ m a^{-1}, $\sigma_R = 1000$ m and (d) $v_0 = 300$ m a^{-1}, $\sigma_R = 5000$ m.

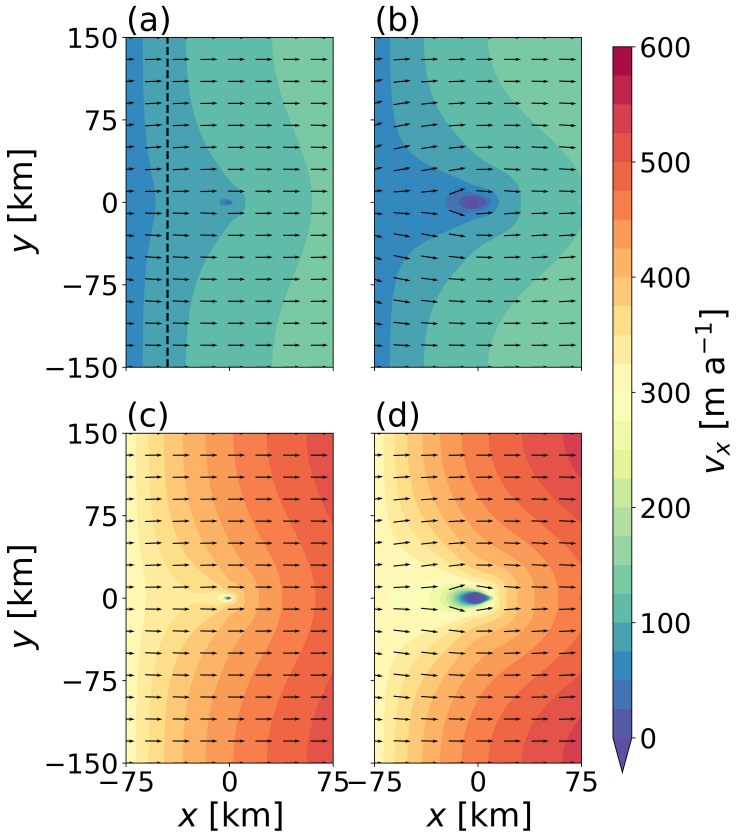

Figure 4: The upper ice surface velocity fields of full Stokes simulations of pinning points with combinations of inflow velocities, v_0, and bed extent parameters, σ_R, of (a) $v_0 = 50$ m a^{-1}, $\sigma_R = 1000$ m, (b) $v_0 = 50$ m a^{-1}, $\sigma_R = 5000$ m, (c) $v_0 = 300$ m a^{-1}, $\sigma_R = 1000$ m and (d) $v_0 = 300$ m a^{-1}, $\sigma_R = 5000$ m. The colour represents the velocity in the x-direction and the arrows show the horizontal velocity direction. The dashed line in (a) represents the location, $x = -45$ km where cross-sections are taken for simulation analysis.

stoss side of the pinning point, and further thinning on the lee side of the pinning point (Fig. 3). More thinning occurs in simulations with a lower inflow velocity, with differences in ice thickness between simulations of a fixed inflow velocity and varying pinning point size being minimal. In each simulation, the most thinning occurs on the lee side of the pinning point, with a greater pinning point size causing a broader area of thinning. Away from the pinning point, at the lateral boundaries, the ice thickness reaches a minimum of roughly 110 m in both simulations with an inflow velocity of $v_0 = 50$ m a^{-1} compared to a minimum ice thickness of roughly 190 m in the simulations with an inflow velocity of $v_0 = 300$ m a^{-1}.

The upper surface velocities of the simulations with combinations of (a) $v_0 = 50$ m a^{-1}, $\sigma_R = 1000$ m, (b) $v_0 = 50$ m a^{-1}, $\sigma_R = 5000$ m, (c) $v_0 = 300$ m a^{-1}, $\sigma_R = 1000$ m and (d) $v_0 = 300$ m a^{-1}, $\sigma_R = 5000$ m are presented in Fig. 4. In both simulations with an inflow velocity of $v_0 = 50$ m a^{-1}, the maximum x-direction velocity reaches roughly 150 m a^{-1}, whereas in the simulations with an inflow velocity of 300 m a^{-1}, maximum x-direction velocities attain maximum values of roughly $525 - 550$ m a^{-1}. At the pinning points, velocities are very slow in comparison with the surrounding ice shelf, with velocities below 25 m a^{-1}.

3.2.1 Influence of ice flow parameters

In order to understand the relative influence of parameters in the ice flow equations, we perform sensitivity analysis on the ice fluidity and the gravitational constant. Although the gravitational constant differs only very slightly in reality across Antarctica, we investigate

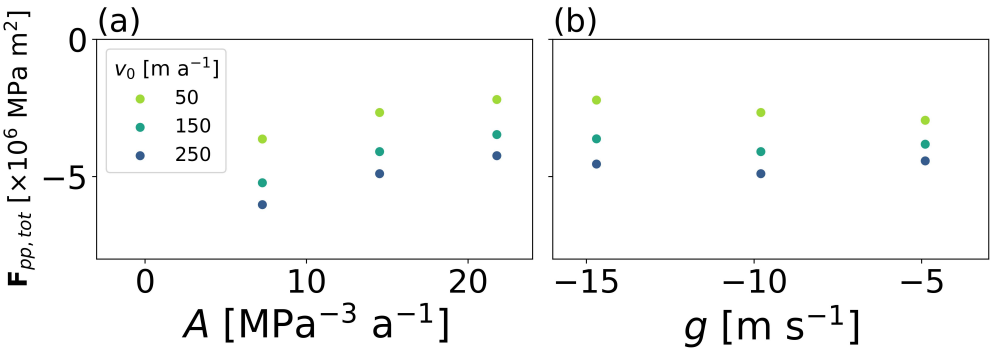

Figure 5: The total force in the x-direction as defined in Eq. (25) for simulations varying (a) the ice fluidity and (b) the gravitational constant. The varying colours represent differing inflow velocities, v_0.

the influence of variations in g (as well as A) for the potential future non-dimensionalisation of this model. Keeping a fixed bed anomaly extent parameter, σ_R, we perform simulations with the combinations of inflow velocities $v_0 = \{50, 150, 250\}$, ice fluidity values of $0.5A$, A, $1.5A$ and gravitational constant values of $0.5g$, g, $1.5g$.The values A and g are defined in Table 2.1.

Percentage differences between the total force on the upstream ice shelf for simulations with ice fluidity parameters of A and $0.5A$ range from 21 to 31 %, with a higher percentage difference the lower the inflow velocity. Total forces on the upstream ice show percentage differences between ice fluidity parameters of A and $1.5A$ ranging from 14 to 19 %, also with a higher percentage difference for a lower inflow velocity.

Percentage differences between total forces in simulations with gravitational constants of g and $0.5g$ range from 7 to 10 %, with the lowest percentage difference occurring in the simulation with an inflow velocity of 150 m (Fig. 5a). In simulations with gravitational constants of g and $1.5g$, percentage differences range from 7 to 19 %, with the largest percentage difference occuring in the simulation with an inflow velocity of $v_0 = 50$ m a^{-1} (Fig. 5b).

3.2.2 Subdivision of buttressing forces

A number of factors determine the force on the upstream ice in an ice shelf due to a pinning point. In Fig. 6, vertically-integrated stresses at the cross-section defined by $x = -45$ km are plotted for the four extreme simulations performed by solving the full Stokes equations. Shown are the simulations with inflow velocities and bed anomaly extent parameters of (1) $v_0 = 50$ m a^{-1}, $\sigma_R = 1000$ m (2) $v_0 = 50$ m a^{-1}, $\sigma_R = 5000$ m, (3) $v_0 = 300$ m a^{-1}, $\sigma_R = 1000$ m and (4) $v_0 = 300$ m a^{-1}, $\sigma_R = 5000$ m. The total, vertically-integrated stress in the x-direction is shown as well as a subdivision of the stresses into the component due to ocean pressure and that due to the pinning point. The ocean pressure at the cross-section is defined as the ocean pressure in the upstream direction if the calving front were at that position. For the range of simulation set ups chosen, the total integrated force differs more significantly for a differing inflow velocity than for pinning point size. At the centre of the cross-section, defined by $y = 0$, the vertically-integrated stress in the x-direction due to the pinning point makes up 3.3 to 3.8 % of the total vertically-integrated stress for the simulations with a bed anomaly parameter of $\sigma_R = 1000$ m. In the case of the $\sigma_R = 5000$ m simulations, the vertically-integrated stress due to the pinning point makes up 8.2 to 10.6 % of the total vertically-integrated stress at the centre of the cross-section.

3.2.3 Pinning point buttressing forces

We now investigate only the total force due to the pinning points in the 30 full Stokes simulations with every combination of inflow velocity and bed anomaly extent parameters of $v_0 = 50, 100, 150, 200, 250, 300$ m a^{-1} and $\sigma_R = 1000, 2000, 3000, 4000, 5000$ m (Fig. 7).

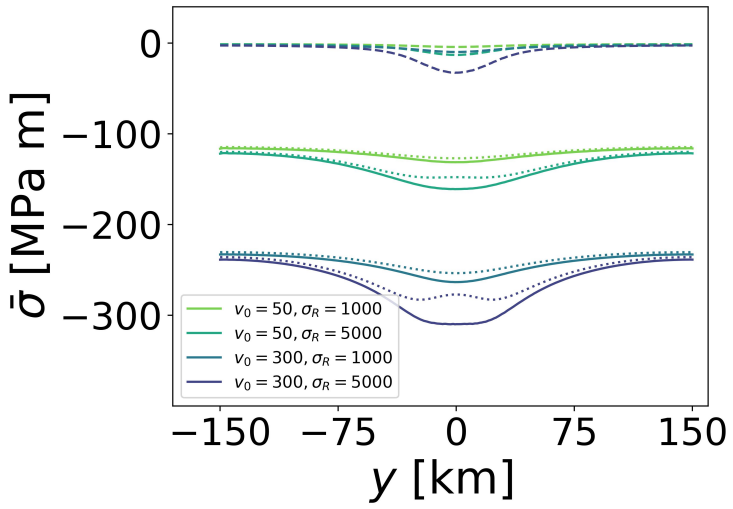

Figure 6: The vertically-integrated stress in the x-direction at the $x = -45$ km cross-section for the extreme simulations; (1) $v_0 = 50$ m a^{-1}, $\sigma_R = 1000$ m (2) $v_0 = 50$ m a^{-1}, $\sigma_R = 5000$ m, (3) $v_0 = 300$ m a^{-1}, $\sigma_R = 1000$ m and (4) $v_0 = 300$ m a^{-1}, $\sigma_R = 5000$ m as indicated by the legend colours. The solid lines show the vertically-integrated stress in the x-direction. The dotted lines shows the vertically-integrated ocean pressure, which is equivalent to the total vertically-integrated stress in the x-direction if the calving front were at the cross-section. The dashed lines show the vertically-integrated stress in the x-direction due to the pinning point, defined as the total vertically-integrated stress minus the vertically integrated ocean pressure.

The total force in the x-direction due to a pinning point is defined in Eq. (29). For each set of buttressing forces with a fixed σ_R, a line of best fit is calculated. The average slope of these lines is $\bar{m} = 0.4293$, meaning that the buttressing force due to a pinning point scales as approximately $F \propto v_0^{0.4293}$ (Fig. 7b). Lines of best fit are calculated for each set of buttressing forces with a fixed inflow velocity, v_0. The mean slope is $\bar{m} = 0.4563$, meaning that the total buttressing scales as approximately $F \propto v_0^{0.4563}$.

3.3 Comparison with lower-order models

In order to investigate the ability of models of varying complexity to capture an accurate stress field due to an obstacle in an ice shelf, we present results across full Stokes, SSA and BPA simulations (Fig. 9). Mean total percentage differences between the full Stokes and the SSA simulations vary between 4 % and 7 %, with the smaller obstacles resulting

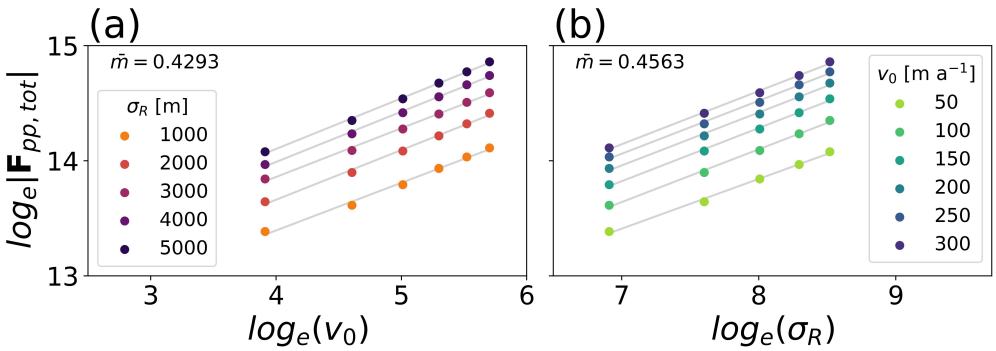

Figure 7: The influence of (a) the inflow velocity, v_0, and (b) the bed anomaly extent parameter, σ_R, on the total force due to the pinning point as defined in Eq. (29).

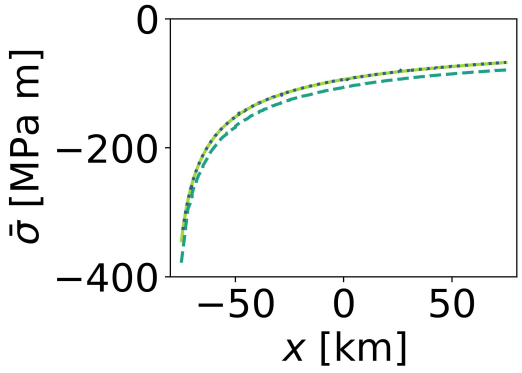

Figure 8: The vertically-integrated stress in the x-direction in the absence of a pinning point, for the analytical stress solution (solid line), the full Stokes simulation stress solution (dashed line) and the SSA stress solution (dotted line).

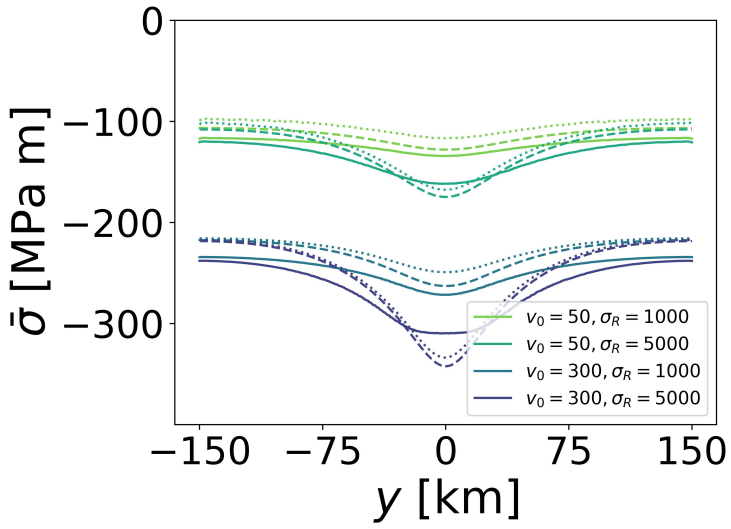

Figure 9: The vertically-integrated stress in the x-direction as defined in Eq. (24) for full Stokes simulations (solid lines), BPA simulations (dotted lines) and SSA simulations (dashed lines). The colours indicate the simulation setup with varying inflow velocities, v_0, and bed anomaly extents, controlled by σ_R. All simulations are flow around a cylinder.

in slightly greater total percentage differences. Spatially, the full Stokes simulations vary less than the SSA and BPA simulations. The most prominent spatial differences occur in the simulations with a larger obstacle in the ice shelf. In both the $v_0 = 50$, $\sigma_R = 5000$ and the $v_0 = 300$, $\sigma_R = 5000$ simulations, forces are higher in the SSA simulations than in the full Stokes simulations, whereas the opposite is true away from the obstacle. Slight differences occur between the SSA and BPA simulations, with the force on the upstream ice shelf being higher in the SSA simulation. Further investigation with a higher degree Legendre-polynomial in the BPA simulations is needed in order to investigate whether BPA can capture the stress field on par with the full Stokes simulations.

4 Discussion

4.1 Implications for ice shelves

Given that a significant proportion of total precipitation and melting occurs at the Antarctic coastline, it is important that we understand how changes here may influence changes

in buttressing forces. It has been predicted that in West Antarctica, ocean melt rates will significantly increase (Naughten et al., 2023), reducing buttressing strength within ice shelves. Furthermore, predictions show a decrease in surface accumulation in coastal regions (Kittel et al., 2021; Dunmire et al., 2022), leaving ice shelves with predominantly locally-accumulated ice vulnerable to ice shelf thinning Višnjević et al. (2023).

It has been found in previous studies that pinning points have an influence on ice shelf conditions and grounding line position through buttressing forces (Favier and Pattyn, 2015; Fürst et al., 2015; Reese et al., 2018a; Henry et al., 2022). Furthermore, pinning points have the potential to delay sea level contribution (Favier et al., 2016). During deglaciation, the existence of an ice rise can result in a delay of continental grounding line retreat (Favier and Pattyn, 2015). Conversely, glacial isostatic adjustment can result in an enlargement of a pinning point and a resulting advance of the continental grounding line (Wearing and Kingslake, 2019).

In this study, we have investigated the influence of a number of factors on the forces on the upstream ice shelf due to pinning points using idealised numerical simulations. We found that the buttressing force due to a pinning point scales as $F \propto v_0^{0.4293}$ for a varying ice shelf inflow velocity, with a fixed inflow ice thickness and as $F \propto \sigma_R^{0.4563}$ for a varying bed anomaly extent parameter controlling the grounded area of the pinning point. The bed anomaly parameter, σ_R, results in a grounded width of the pinning point of roughly double the value of σ_R. Although the buttressing force due to the pinning point scales almost equally with v_0 and σ_R, we expect that buttressing forces are more susceptible to changes in v_0 than σ_R given how slowly changes in the grounded area of pinning points occur over glacial-interglacial timescales (Favier and Pattyn, 2015; Henry et al., 2022).

An alternative approach for calculating the forces due to a pinning point has been performed in previous work (Macayeal et al., 1987; Still et al., 2019) and could be used for comparison with the work presented here. The method involves taking a contour around a pinning point and calculating various components of the force balance based on observations; (1) the glaciostatic contribution, (2) the dynamic drag and (3) the ocean pressure. Once these have been calculated, the ocean pressure can be subtracted from the glaciostatic contribution and the dynamic drag to calculate the force due to the pinning point.

4.2 Limitations and outlook

Calculating the force balance using observations gives estimates of the buttressing force for just one point in time, whereas the method presented here can be used for sensitivity analysis to investigate the possible future or past scenarios. In the idealised simulations presented here, we have not investigated the buttressing force due to having a number of pinning points in one simulation domain and we suggest that cross-validation be used between modelled results and those presented in Macayeal et al. (1987) and Still et al. (2019) in future studies.

One area in need of further investigation is the calculation of the buttressing force due to a pinning point. Here, we have followed Macayeal et al. (1987) and Still et al. (2019), but in reality, a significant portion of the force due to ocean pressure is due to a thickening of the ice shelf due to pinning point buttressing. In further work, it may be best to calculate the force due to a pinning point by subtracting the force in simulations without a pinning point from the force in the presence of a pinning point. However, this has a disadvantage in that it requires additional simulations and does not allow direct comparison with the method presented in Macayeal et al. (1987) and Still et al. (2019).

In the simulations with a simplified representation of a pinning point with a cylinder, we use boundary conditions specifying horizontal velocities of $v_x = 0$ and $v_y = 0$. This assumption means that our results are only valid at pinning points where velocities are negligible compared to the surrounding ice shelf. The low velocities result in very small strain rates and can cause numerical instabilities. In icepack, the model used to solve the SSA and the BPA, this is remedied by introducing a regularisation term. None-the-less, we found that for small pinning points, calculations had to be made with small time steps of 0.25 years initially, which could be increased later in the simulations.

The main difference between the full Stokes and SSA simulations is the number of stress tensor or velocity gradient components which are solved for. In the SSA, velocities are

vertically-integrated, meaning that vertical differences in horizontal velocities are ignored. Furthermore, a cryostatic assumption is assumed resulting in vertical resistive stresses being neglected. These assumptions mean that the vertical differences in horizontal velocities characteristic of the velocity field of ice rises are not captured in this approximation.

4.3 Model representation of pinning points

In this work, we have presented results of fully-resolved pinning points using a full Stokes model. We have furthermore simulated equivalent pinning points using the SSA and the BPA, simplifying the representation of pinning points by modelling the flow around cylinder with the same diameter as the grounded width perpendicular to the ice shelf flow direction of the full Stokes pinning points. The reasons for the comparison between model hierarchies are twofold: (1) the investigation of the ability of a lower-order model to capture the dynamic response of an ice shelf to the buttressing due to an obstacle and (2) to provide a computationally-efficient method for calculating ice shelf buttressing.

In continental-scale simulations, coastal regions are predominantly modelled using the SSA or the BPA. We have investigated the ability of lower-order ice flow approximations to model the dynamic response of the surrounding ice shelf to a pinning point and suggest that future studies investigate the ability to model a fully-resolved pinning point with a lower-order model.

5 Conclusions

In these preliminary results, we have investigated the buttressing forces in ice shelves due to pinning points with full Stokes, partitioned simulations, varying the upstream ice shelf velocity and the pinning point size. Results show that the force due to a pinning point scales as $F \propto v_0^{0.4293}$ in response to a changing inflow velocity and as $F \propto v_0^{0.4563}$ in response to a changing bed anomaly extent, when following a buttressing force calculation method as presented in Macayeal et al. (1987) and Still et al. (2019).

We have performed benchmark simulations between the full Stokes simulations, lower-order simulations and an analytical solution without a pinning point. Building on this, we investigate the ability of lower-order ice flow approximations to model the dynamics of buttressing due to a pinning point in an ice shelf.

Appendix

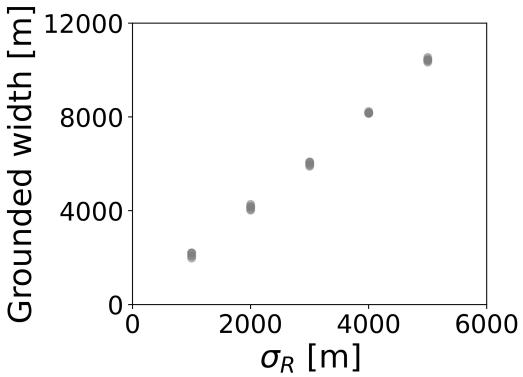

Figure 10: The grounded width of the pinning point against the bed anomaly extent parameter, σ_R for all full Stokes simulations with a fully resolved pinning point.

References

S. Berger, L. Favier, R. Drews, J.-J. Derwael, and F. Pattyn. The control of an uncharted pinning point on the flow of an Antarctic ice shelf. *Journal of Glaciology*, 62(231):37–45, Feb. 2016. ISSN 0022-1430, 1727-5652. doi: 10.1017/jog.2016.7.

A. M. Brisbourne, C. Martín, A. M. Smith, A. F. Baird, J. M. Kendall, and J. Kingslake. Constraining Recent Ice Flow History at Korff Ice Rise, West Antarctica, Using Radar and Seismic Measurements of Ice Fabric. *Journal of Geophysical Research: Earth Surface*, 124(1):175–194, Jan. 2019. ISSN 21699003. doi: 10.1029/2018JF004776.

D. Dunmire, J. T. M. Lenaerts, R. T. Datta, and T. Gorte. Antarctic surface climate and surface mass balance in the community earth system model version 2 during the satellite era and into the future (1979–2100). *The Cryosphere*, 16 (10):4163–4184, Oct. 2022. ISSN 1994-0424. doi: 10.5194/tc-16-4163-2022. URL `https://tc.copernicus.org/articles/16/4163/2022/`.

L. Favier and F. Pattyn. Antarctic ice rise formation, evolution, and stability. *Geophysical Research Letters*, 42(11):4456–4463, June 2015. ISSN 0094-8276, 1944-8007. doi: 10.1002/2015GL064195.

L. Favier, F. Pattyn, S. Berger, and R. Drews. Dynamic influence of pinning points on marine ice-sheet stability: a numerical study in Dronning Maud Land, East Antarctica. *The Cryosphere*, 10(6):2623–2635, Nov. 2016. ISSN 1994-0424. doi: 10.5194/tc-10-2623-2016.

J. J. Fürst, G. Durand, F. Gillet-Chaulet, N. Merino, L. Tavard, J. Mouginot, N. Gourmelen, and O. Gagliardini. Assimilation of Antarctic velocity observations provides evidence for uncharted pinning points. *The Cryosphere*, 9(4):1427–1443, Aug. 2015. ISSN 1994-0424. doi: 10.5194/tc-9-1427-2015.

O. Gagliardini, T. Zwinger, F. Gillet-Chaulet, G. Durand, L. Favier, B. de Fleurian, R. Greve, M. Malinen, C. Martín, P. Råback, J. Ruokolainen, M. Sacchettini, M. Schäfer, H. Seddik, and J. Thies. Capabilities and performance of Elmer/Ice, a new-generation ice sheet model. *Geoscientific Model Development*, 6(4):1299–1318, Aug. 2013. ISSN 1991-9603. doi: 10.5194/gmd-6-1299-2013.

D. Goldberg, D. M. Holland, and C. Schoof. Grounding line movement and ice shelf buttressing in marine ice sheets. *Journal of Geophysical Research*, 114(F4):F04026, Dec. 2009. ISSN 0148-0227. doi: 10.1029/2008JF001227.

R. Greve and H. Blatter. *Dynamics of ice sheets and glaciers*. Springer, Dordrecht, 2009. ISBN 9783642034145 9783642034152.

M. Haseloff and O. V. Sergienko. The effect of buttressing on grounding line dynamics. *Journal of Glaciology*, 64(245):417–431, June 2018. ISSN 0022-1430, 1727-5652. doi: 10.1017/jog.2018.30.

A. C. J. Henry, R. Drews, C. Schannwell, and V. Višnjević. Hysteretic evolution of ice rises and ice rumples in response to variations in sea level. *The Cryosphere*, 16(9):3889–3905, 2022. doi: 10.5194/tc-16-3889-2022. URL `https://tc.copernicus.org/articles/16/3889/2022/`.

K. Hutter. *Theoretical glaciology: material science of ice and the mechanics of glaciers and ice sheets*. Dordrecht, D. Reidel Publishing Co./Tokyo, Terra Scientific Publishing Co., 1983. ISBN 9789027714732.

J. Kingslake, C. Martín, R. J. Arthern, H. F. J. Corr, and E. C. King. Ice-flow reorganization in west antarctica 2.5 kyr ago dated using radar-derived englacial flow velocities. *Geophysical Research Letters*, 43(17):9103–9112, 2016. doi: https://doi.org/10.1002/2016GL070278.

J. Kingslake, R. P. Scherer, T. Albrecht, J. Coenen, R. D. Powell, R. Reese, N. D. Stansell, S. Tulaczyk, M. G. Wearing, and P. L. Whitehouse. Extensive retreat and re-advance of the West Antarctic Ice Sheet during the Holocene. *Nature*, 558(7710):430–434, June 2018. ISSN 0028-0836, 1476-4687. doi: 10.1038/s41586-018-0208-x.

C. Kittel, C. Amory, C. Agosta, N. C. Jourdain, S. Hofer, A. Delhasse, S. Doutreloup, P.-V. Huot, C. Lang, T. Fichefet, and X. Fettweis. Diverging future surface mass balance between the antarctic ice shelves and grounded ice sheet. *The Cryosphere*, 15(3):1215–1236, Mar. 2021. ISSN 1994-0424. doi: 10.5194/tc-15-1215-2021. URL `https://tc.copernicus.org/articles/15/1215/2021/`.

D. Macayeal, R. Bindschadler, S. Shabtaie, S. Stephenson, and C. Bentley. Force, Mass, and Energy Budgets of the Crary Ice Rise Complex, Antarctica. *Journal of Glaciology*, 33(114):218–230, 1987. ISSN 0022-1430, 1727-5652. doi: 10.1017/S0022143000008728.

K. Matsuoka, R. C. Hindmarsh, G. Moholdt, M. J. Bentley, H. D. Pritchard, J. Brown, H. Conway, R. Drews, G. Durand, D. Goldberg, T. Hattermann, J. Kingslake, J. T. Lenaerts, C. Martín, R. Mulvaney, K. W. Nicholls, F. Pattyn, N. Ross, T. Scambos, and P. L. Whitehouse. Antarctic ice rises and rumples: Their properties and significance for ice-sheet dynamics and evolution. *Earth-Science Reviews*, 150:724–745, Nov. 2015. ISSN 00128252. doi: 10.1016/j.earscirev.2015.09.004.

L. W. Morland. Unconfined ice-shelf flow. In C. J. Van der Veen and J. Oerlemans, editors, *Dynamics of the West Antarctic Ice Sheet*, pages 99–116, Dordrecht, 1987. Springer Netherlands. ISBN 978-94-009-3745-1.

K. A. Naughten, P. R. Holland, and J. De Rydt. Unavoidable future increase in west antarctic ice-shelf melting over the twenty-first century. *Nature Climate Change*, 13(11): 1222–1228, Nov. 2023. ISSN 1758-678X, 1758-6798. doi: 10.1038/s41558-023-01818-x. URL `https://www.nature.com/articles/s41558-023-01818-x`.

S. S. Pegler. The dynamics of confined extensional flows. *Journal of Fluid Mechanics*, 804: 24–57, 2016. doi: 10.1017/jfm.2016.516.

S. S. Pegler. Marine ice sheet dynamics: the impacts of ice-shelf buttressing. *Journal of Fluid Mechanics*, 857:605–647, Dec. 2018. ISSN 0022-1120, 1469-7645. doi: 10.1017/jfm.2018.741.

D. Pollard and R. M. DeConto. Description of a hybrid ice sheet-shelf model, and application to antarctica. *Geoscientific Model Development*, 5(5):1273–1295, 2012. doi: 10.5194/gmd-5-1273-2012. URL `https://gmd.copernicus.org/articles/5/1273/2012/`.

R. Reese, G. H. Gudmundsson, A. Levermann, and R. Winkelmann. The far reach of ice-shelf thinning in Antarctica. *Nature Climate Change*, 8(1):53–57, Jan. 2018a. ISSN 1758-678X, 1758-6798. doi: 10.1038/s41558-017-0020-x.

R. Reese, R. Winkelmann, and G. H. Gudmundsson. Grounding-line flux formula applied as a flux condition in numerical simulations fails for buttressed Antarctic ice streams. *The Cryosphere*, 12(10):3229–3242, Oct. 2018b. ISSN 1994-0424. doi: 10.5194/tc-12-3229-2018.

C. Schoof. Ice sheet grounding line dynamics: Steady states, stability, and hysteresis. *Journal of Geophysical Research*, 112(F3):F03S28, July 2007. ISSN 0148-0227. doi: 10.1029/2006JF000664.

D. R. Shapero, J. A. Badgeley, A. O. Hoffman, and I. R. Joughin. icepack: a new glacier flow modeling package in python, version 1.0. *Geoscientific Model Development*, 14(7):4593–4616, 2021. doi: 10.5194/gmd-14-4593-2021. URL `https://gmd.copernicus.org/articles/14/4593/2021/`.

H. Still and C. Hulbe. Mechanics and dynamics of pinning points on the Shirase Coast, West Antarctica. *The Cryosphere*, 15(6):2647–2665, June 2021. ISSN 1994-0424. doi: 10.5194/tc-15-2647-2021.

H. Still, A. Campbell, and C. Hulbe. Mechanical analysis of pinning points in the Ross Ice Shelf, Antarctica. *Annals of Glaciology*, 60(78):32–41, Apr. 2019. ISSN 0260-3055, 1727-5644. doi: 10.1017/aog.2018.31.

V. Višnjević, R. Drews, C. Schannwell, I. Koch, S. Franke, D. Jansen, and O. Eisen. Predicting the steady-state isochronal stratigraphy of ice shelves using observations and modeling. *The Cryosphere*, 16(11):4763–4777, 2022. doi: 10.5194/tc-16-4763-2022. URL `https://tc.copernicus.org/articles/16/4763/2022/`.

V. Višnjević, R. Drews, G. Moss, A. Henry, and C. Wild. Mapping the composition of antarctic ice shelves as a metric for their susceptibility to future climate change [in preparation]. 2023.

M. G. Wearing and J. Kingslake. Holocene Formation of Henry Ice Rise, West Antarctica, Inferred From Ice-Penetrating Radar. *Journal of Geophysical Research: Earth Surface*, 124(8):2224–2240, Aug. 2019. ISSN 2169-9003, 2169-9011. doi: 10.1029/2018JF004988.

C. T. Wild, K. E. Alley, A. Muto, M. Truffer, T. A. Scambos, and E. C. Pettit. Weakening of the pinning point buttressing thwaites glacier, west antarctica. *The Cryosphere*, 16(2):397–417, 2022. doi: 10.5194/tc-16-397-2022. URL `https://tc.copernicus.org/articles/16/397/2022/`.

6 SUMMARY, CONCLUSIONS AND IMPLICATIONS

6.1 MAJOR FINDINGS

This thesis contains four first-author chapters covering the numerical modelling of ice rises and ice rumples in coastal Antarctica. I present the first three-dimensional, full Stokes simulations of an isle-type ice rise including the surrounding ice shelf with calculation of the age field, the anisotropy field and providing an alternative to the classical Glen's flow law exponent of $n = 3$. In addition to the real-world ice rise simulations, a number of experiments are performed using idealised simulations to quantify the buttressing effect of ice rises and ice rumples on the upstream ice shelf and to understand their response to a changing forcings. The research objectives outlined in Section 1.3 are investigated using the Elmer/Ice model, along with comparisons with the icepack model.

O1: Advances in the understanding of ice rise evolution

The Antarctic ice sheet undergoes hysteresis in response to a changing climate, with the volume and extend of the ice sheet depending on previous states (Garbe et al., 2020; Schoof, 2007). In other words, a change in forcing (e.g. warming) of the Earth results in changes to the geometry of the Antarctic ice sheet with geometry changed being slow to respond or are irreversible for a return to the previous forcing (e.g. temperature). We simulate a three-dimensional, idealised ice rise, solving the Stokes equations and perform experiments by varying sea level for three end-member basal friction coefficients, mimicking glacial-interglacial cycles. We simulate a transition from ice rise to ice rumple, with our findings showing almost immediate ungrounding of the ice rumple in the case of a high basal friction coefficient, but stable ice rumples in the case of the two lower basal friction coefficients. A major finding of the study presented in Chapter 2 is that our numerical simulations indicate that the grounded area of ice rises and ice rumples responds with hysteresis to sea level perturbation. Physically, this can be explained by non-linear relationships between the sea level, the divide position and the area of accumulation on the oceanward side of the ice rise. Our simulations furthermore indicate that the non-linear response of pinning points to sea level variation also has a hysteretic effect on the velocities in the upstream ice shelf, showing that the buttressing due to a pinning point depends on the ice shelf and pinning point history.

O2: Advances in our understanding of pinning point buttressing

Although previous studies have shown that pinning points provide a buttressing effect on upstream ice shelves (Fürst et al., 2016; Reese et al., 2018) due to the drag induced, the differences in buttressing due to differing pinning point sizes and ice shelf conditions have not previously been studied systematically. We simulate three-dimensional, idealised pinning points, varying the extent of the underlying bed anomaly and the upstream ice flux. We find that changes in the upstream ice shelf have a more dominant influence on changes in the force, scaling on the order of $F \propto v_0^{0.4293}$ compared with changes due to differing pinning point sizes, scaling on the order of $F \propto v_0^{0.4563}$. With the goal of creating a modelling framework of pinning points with low computational cost, in Chapter 5 comparisons between full Stokes simulations of the buttressing due to fully-resolved pinning points and simplified representations including flow around a cylinder and lower order models. We furthermore compare ice shelf conditions with pinning points to analytical and numerical solutions with no pinning point providing estimations of the loss in force due to an ungrounding pinning point. Our results show that changes in buttressing due to a pinning point are largely due to changes in ice shelf fluxes rather than changes in pinning point geometry. This work is a step towards a better understanding of the role of pinning points in ice sheet evolution, the influence of the various parameters in ice flow equations and a quantification of the loss of force when a pinning point is not accurately resolved in continental-scale models.

O3: Modelling the stratigraphy of an ice rise

Investigation of the internal isochronal stratigraphy of ice is useful in that the geometry of the isochronal stratigraphy is dependent on the accumulation rate and the velocity field within the ice and can be used for inferring past flow re-organisation (Franke et al., 2022; Martín, Hindmarsh, and Navarro, 2009). Comparison between the modelled and observed isochronal stratigraphy allows validation of the equations of motion and boundary conditions. Building on two-dimensional simulations of ice rise stratigraphy restricted to grounded ice, we simulate the three-dimensional age field of Derwael Ice Rise in East Antarctica, including the surrounding ice shelf and by calculating isochrones, make comparisons between the modelled and observed isochronal stratigraphy. We find good agreement in the flanks of the ice rise, with the location of the Raymond arches being correct, albeit with lower amplitudes due to limitations in the vertical resolution. Our results allow prediction of the isochronal stratigraphy in the grounding zones where real-world isochrones are too steep to be adequately captured by radar surveys. This work is an important step towards a more routine use of the observed isochronal stratigraphy not just for validation of the modelled isochronal stratigraphy but also for constraining parameters in the equations of motion.

O4: Understanding the role of the Glen's flow law exponent

Ice exhibits shear-thinning behaviour and is thus best described as a non-Newtonian fluid, whereby strain rate depends non-linearly on the stress. A stress exponent of $n = 3$ has commonly been used in modelling studies, but more recent studies on both grounded and floating ice have indicated that an exponent of $n = 4$ may be more suitable (Bons et al., 2016; Millstein, Minchew, and Pegler, 2022). In Chapter 3, three-dimensional simulations of Derwael Ice Rise are presented with Glen's flow law exponents of $n = 3$ and $n = 4$, with adjustments to the ice fluidity for each exponent to minimise the surface elevation change of the ice rise. Although this does not result in a large difference in the geometry of the modelled isochronal stratigraphy, we find that differences in the age of the ice at 95 % depth are roughly 5 % due to greater thinning of the ice in the case of the $n = 4$ simulation. The most significant differences between using a Glen's flow law exponent of $n = 3$ or $n = 4$ is in the shear zones of the ice rise, with shear strain rate being significantly higher in the case of the $n = 4$ simulation. This work using a real-world ice geometry is a major step towards routine modelling of Glen's flow law exponents other than $n = 3$ in three dimensional simulations.

O5: Advances in anisotropy modelling

The ice in ice sheets ranges from isotropic at the upper ice surface to anisotropic due to crystal re-organisation under deformation. A number of methods exist for coupling anisotropy into ice flow models ranging from simple, computationally-efficient approaches to full tensor descriptions of the anisotropy field. Using a semi-Lagrangian solver coupled to the spin, strain rate and deviatoric stress tensors, we simulate the full-tensor anisotropy field of Derwael Ice Rise. We compare simulation results for four different parameters choices used in previous studies (Gagliardini et al., 2013; Martín and Gudmundsson, 2012; Martín, Hindmarsh, and Navarro, 2009; Seddik et al., 2011) and find that simulated anisotropy fields differ significantly. We furthermore develop a framework for future comparison between the modelled anisotropy field and quad-polarimetric radar observations of the anisotropy field with the ultimate goal of constraining parameters in the coupling between the anisotropy and velocity fields in simulations. We provide estimates of the errors incurred in radar observations by assuming that the majority of ice crystals point in the z-direction.

6.2 IMPLICATIONS AND OUTLOOK

In this thesis, I have investigated ice rises and ice rumples with the aim of gaining a better understanding of their role in Antarctic ice sheet evolution, but also to investigate the model representation of physical processes. The methods and findings of this work have im-

plications for ice sheet modelling and as a tool to complement observational studies.

The work in this thesis has demonstrated the three-dimensional, full Stokes modelling of isle-type ice rises and ice rumples which has implications for a wide range of scientific disciplines within Antarctic research. First of all, given that the majority of changes in the Antarctic Ice Sheet will occur in coastal areas where flow regimes are more complicated, the validation of the representation of pinning points in lower-order ice sheet models should be made with full Stokes simulations. Further investigation should be made regarding the most appropriate Glen's flow law exponent as this is likely to have an influence, for example, on the timing of ice stream initiation. Following on from the three-dimensional simulation of the anisotropy field of an ice rise, a full coupling of the anisotropy field and the velocity field should be made in a three-dimensional modelling framework, with validation of parameter choices with observations. Given that the results in this thesis provides quantification of the force due to pinning point buttressing, this framework allows calculation of buttressing loss under a changing climate for specific pinning points.

Ice sheet models are a predictive tool and should not be taken to completely reflect reality. As the field of ice sheet modelling continues to advance along with ever-increasing computational power, I believe that we should continue to question both model representation of physical processes and the accuracy of numerical methods. Despite this, models are an invaluable tool which allow us to understand fluid dynamics in ways which are impossible using other techniques.

APPENDIX A

Supporting Information for "Predicting the three-dimensional age-depth field of an ice rise"

A. Clara J. Henry[1, 2, 3], Clemens Schannwell[1], Vjeran Višnjević[2], Joanna D. Millstein[4], Paul D. Bons[2], Olaf Eisen[5, 6], and Reinhard Drews[2]

[1]Max Planck Institute for Meteorology, Hamburg, Germany
[2]Department of Geosciences, University of Tübingen, Tübingen, Germany
[3]International Max Planck Research School on Earth System Modelling, Max Planck Institute for Meteorology, Hamburg, Germany
[4]Massachusetts Institute of Technology—Woods Hole Oceanographic Institute Joint Program in Oceanography/Applied Ocean Science and Engineering, Cambridge, MA, USA
[5]Alfred Wegener Institute Helmholtz Centre for Polar and Marine Research, Bremerhaven, Germany
[6]University of Bremen, Bremen, Germany

Contents of this file

1. Figures S1 to S10

Introduction

The supporting information contains additional figures pertaining to the simulations described in the main article. Figures included show (1) the age at 50 and 95 % depth for the simulations using Glen's flow law exponents of $n = 3$ and $n = 4$, (2) the percentage difference in velocity magnitude at the surface and at the 1000 year isochrone for the $n = 3$ and $n = 4$ simulations, (3) the basal velocity magnitude for the $n = 4$ simulation and the difference in basal velocity magnitude between the $n = 3$ and $n = 4$ simulations, (4) the horizontal surface dilation for the $n = 3$ and $n = 4$ simulations and the difference between the two, (5) comparisons between RACMO2.3p1, stratigraphy-derived and drift-corrected surface mass balance (SMB) fields, (6) vertical temperature evolution profiles sampled at two coordinates, (7) comparisons between observed and modelled stratigraphy for all $n = 3$ and $n = 4$ simulation cross-sections not included in the main article and (8) the slope difference between the modelled and observed stratigraphy for the cross-section $G - G'$.

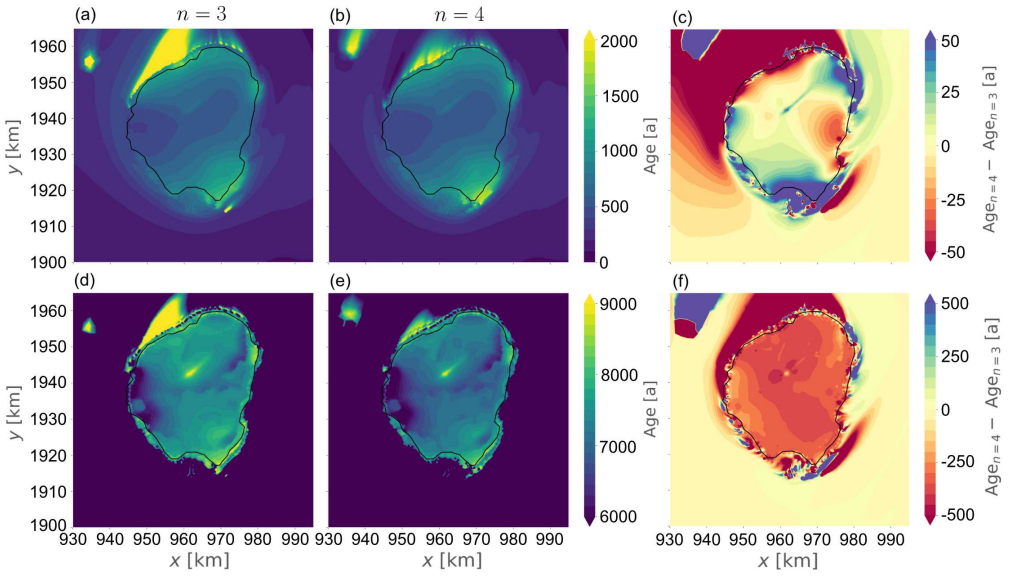

Figure 1: In (a) and (b), the age of the ice is shown at a depth of 50 % for the $n = 3$ and $n = 4$ simulations, respectively, and in (c), the difference between the $n = 4$ and the $n = 3$ simulations. In (d) and (e), the age of the ice is shown at a depth of 95 % for the $n = 3$ and $n = 4$ simulations, respectively. In (c) and (f), the difference between the age in the $n = 4$ and the $n = 3$ simulations is shown for a depth of 50 % and 95 %, respectively.

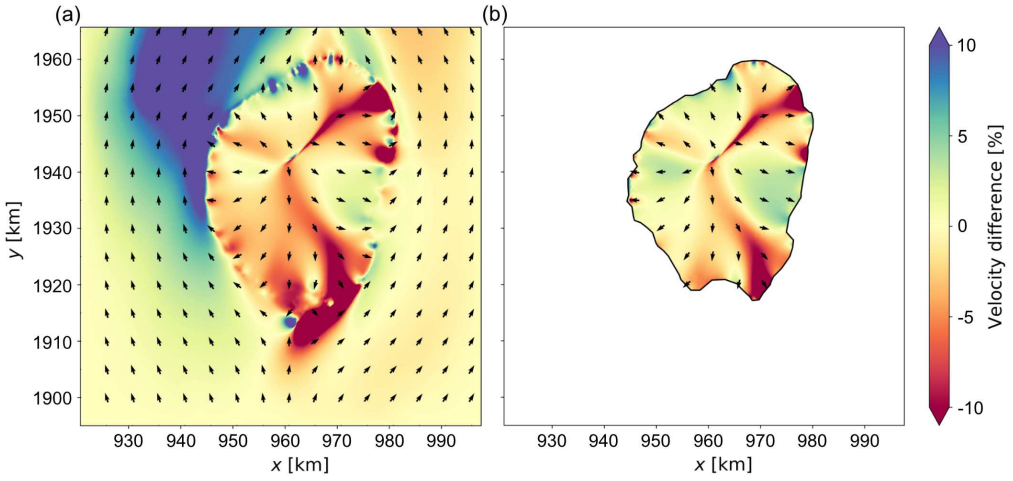

Figure 2: In (a), the percentage difference between the surface velocity magnitudes in the case of the $n = 4$ simulation and the $n = 3$ simulation. In (b), the percentage difference between the velocity magnitudes at the $Age = 1000$ a isochrone in the case of the $n = 4$ simulation and the $n = 3$ simulation. The arrows indicate the velocity directions of the $n = 3$ simulation. Note that the velocity magnitude of the $n = 3$ simulation is subtracted from the velocity magnitude of the $n = 4$ simulation.

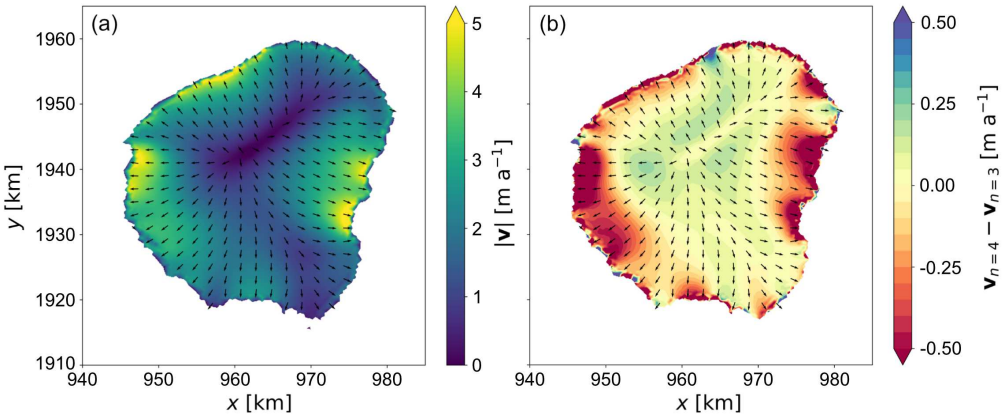

Figure 3: The basal velocity of the $n = 4$ simulation is shown in (a). The colour indicates the velocity magnitude and the arrows indicate the velocity direction. The basal velocity magnitude difference between the $n = 3$ and the $n = 4$ simulation is shown in (b). Note that the basal velocity magnitude of the $n = 3$ simulation is subtracted from the basal velocity magnitude of the $n = 4$ simulation.

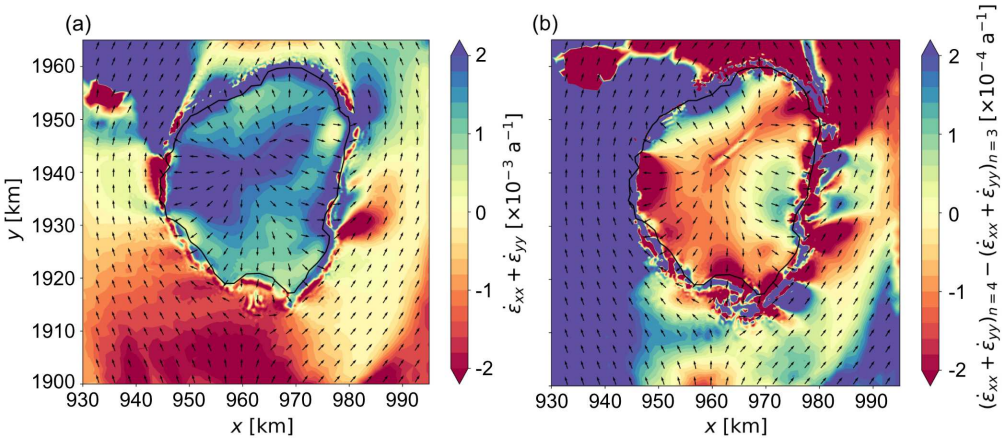

Figure 4: In (a), the horizontal dilation of the velocity field in the case of the $n = 3$ simulation is shown. In (b), the difference between the horizontal dilation in the case of the $n = 4$ and $n = 3$ simulations is shown. Note that the dilation of the $n = 3$ simulation is subtracted from the dilation of the $n = 4$ simulation.

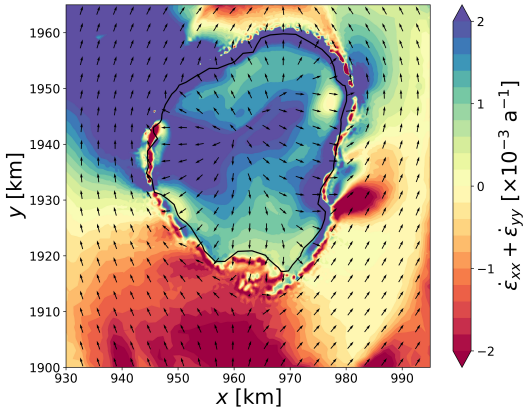

Figure 5: The horizontal dilation of the velocity field in the case of the $n = 4$ simulation.

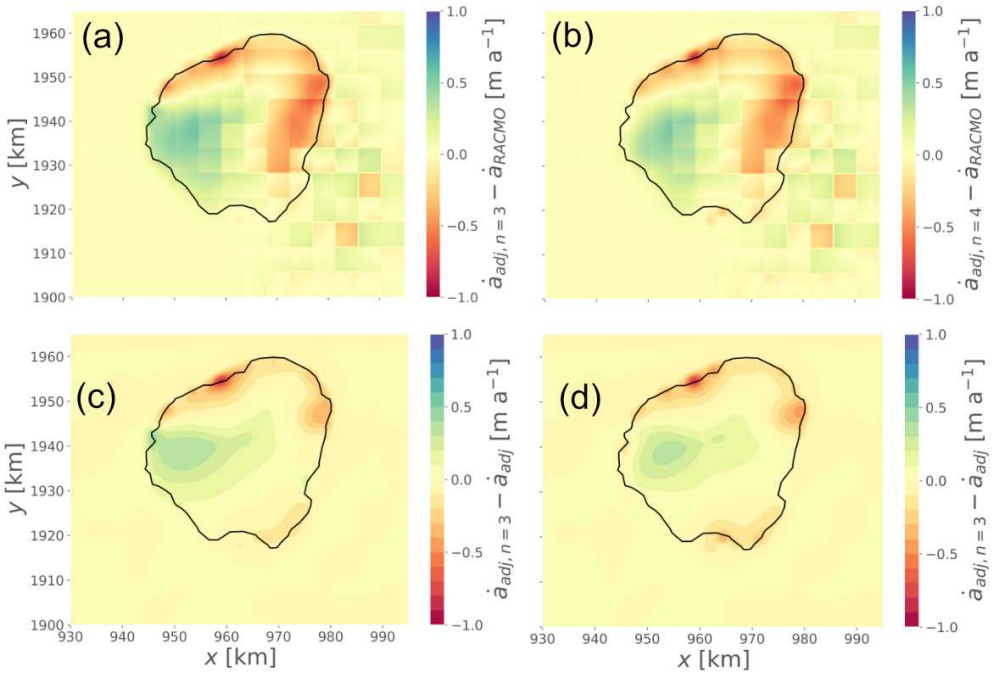

Figure 6: (a) and (b) show the difference between the SMB of the $n = 3$ and the RACMO2.3p1 data, and between the $n = 4$ simulations and the RACMO2.3p1 data , respectively. (c) and (d) show the difference between the SMB after and before the $\partial z_s/\partial t$ field adjustment for the simulations $n = 3$ and $n = 4$, respectively. Note: all SMB data is in ice-equivalent.

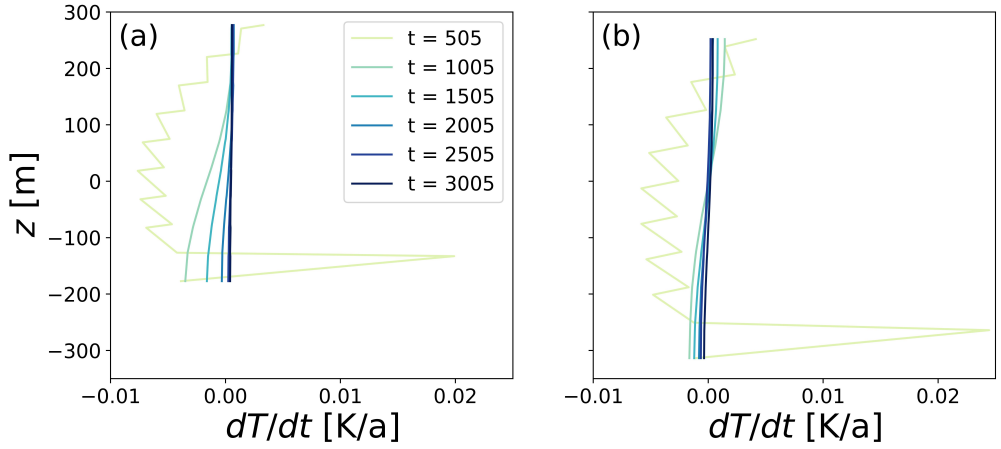

Figure 7: Figures (a) and (b) show the temperature evolution profiles at the horizontal coordinates $(x, y) = (970, 1940)$ and $(x, y) = (960, 1930)$, respectively, during the temperature spin up.

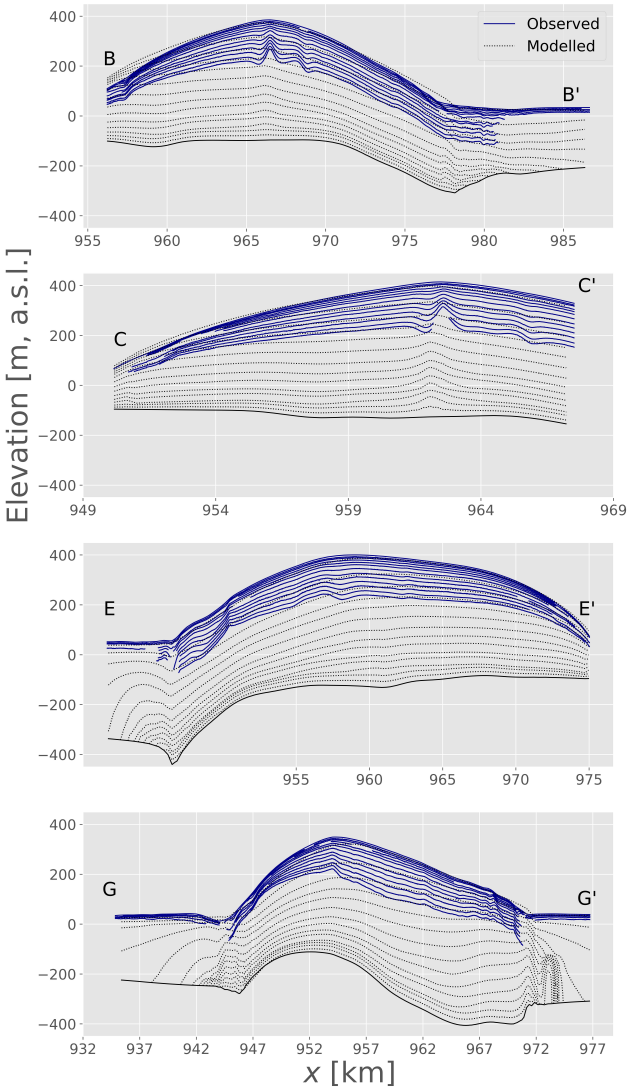

Figure 8: Comparisons between modelled and observed stratigraphy along radar profiles marked in the vertical domain of the model. Modelled isochrones correspond to the $n = 3$ simulation. The blue solid lines show the observed stratigraphy and the dotted black lines show the modelled stratigraphy.

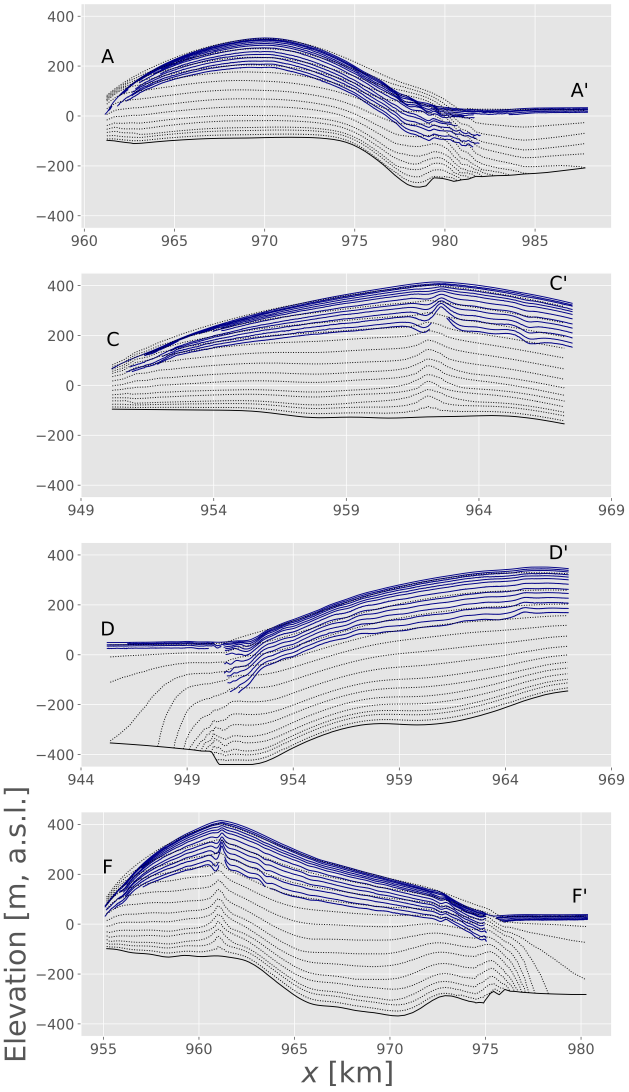

Figure 9: Comparisons between modelled and observed stratigraphy along radar profiles marked in the vertical domain of the model. Modelled isochrones correspond to the $n = 4$ simulation. The blue solid lines show the observed stratigraphy and the dotted black lines show the modelled stratigraphy.

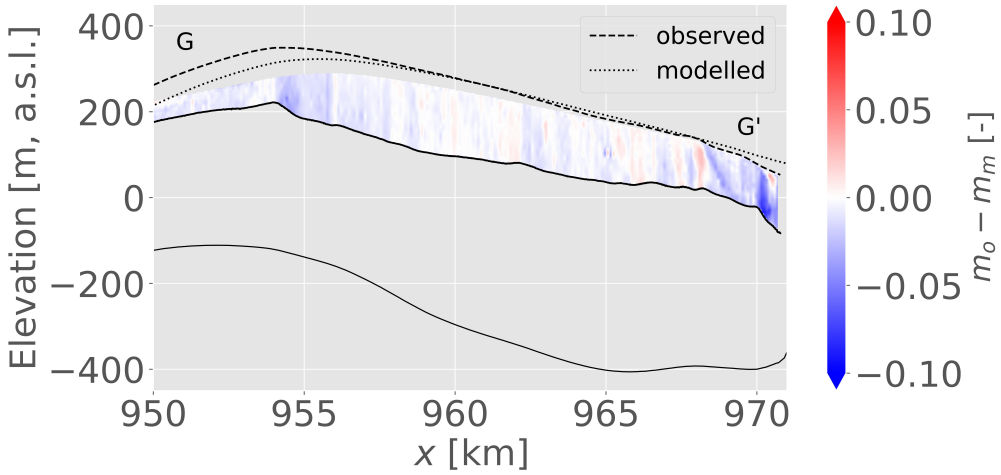

Figure 10: Difference between observed isochrone slope (m_o) and the $n = 3$ modelled isochrone slope (m_m) at locations where data is available for both. The cross-section $G - G'$ corresponds with the radar profile in Fig. 1 in the main article. The dashed lines show the observed ice surface and the dotted lines show the modelled surface. The lower extent of the area of comparison and the lower ice surface are shown with solid black lines.

BIBLIOGRAPHY

Ahlkrona, Josefin, Per Lötstedt, Nina Kirchner, and Thomas Zwinger (Mar. 2016). "Dynamically coupling the non-linear Stokes equations with the shallow ice approximation in glaciology: Description and first applications of the ISCAL method." en. In: *Journal of Computational Physics* 308, 1–19. ISSN: 00219991. DOI: 10.1016/j.jcp.2015.12.025. URL: https://linkinghub.elsevier.com/retrieve/pii/S002199911500844X.

Albrecht, T., R. Winkelmann, and A. Levermann (2020). "Glacial-cycle simulations of the Antarctic Ice Sheet with the Parallel Ice Sheet Model (PISM) – Part 1: Boundary conditions and climatic forcing." In: *The Cryosphere* 14.2, pp. 599–632. DOI: 10.5194/tc-14-599-2020. URL: https://tc.copernicus.org/articles/14/599/2020/.

Alley, Richard B (1988). "Fabrics in polar ice sheets: development and prediction." In: *Science* 240.4851, pp. 493–495.

Arnold, D. N., F. Brezzi, and M. Fortin (Dec. 1984). "A stable finite element for the stokes equations." en. In: *Calcolo* 21.4, 337–344. ISSN: 0008-0624, 1126-5434. DOI: 10.1007/BF02576171. URL: http://link.springer.com/10.1007/BF02576171.

Barletta, Valentina R. et al. (June 2018). "Observed rapid bedrock uplift in Amundsen Sea Embayment promotes ice-sheet stability." en. In: *Science* 360.6395, pp. 1335–1339. ISSN: 0036-8075, 1095-9203. DOI: 10.1126/science.aao1447. URL: https://www.sciencemag.org/lookup/doi/10.1126/science.aao1447 (visited on 08/16/2021).

Becker, R. and M. Braack (Dec. 2001). "A finite element pressure gradient stabilization¶for the Stokes equations based on local projections." In: *Calcolo* 38.4, 173–199. ISSN: 0008-0624, 1126-5434. DOI: 10.1007/s10092-001-8180-4. URL: http://link.springer.com/10.1007/s10092-001-8180-4.

Berg, B. and J. Bassis (2020). "Brief communication: Time step dependence (and fixes) in Stokes simulations of calving ice shelves." In: *The Cryosphere* 14.9, pp. 3209–3213. DOI: 10.5194/tc-14-3209-2020. URL: https://tc.copernicus.org/articles/14/3209/2020/.

Berger, Sophie, Lionel Favier, Reinhard Drews, Jean-Jacques Derwael, and Frank Pattyn (Feb. 2016). "The control of an uncharted pinning point on the flow of an Antarctic ice shelf." en. In: *Journal of Glaciology* 62.231, pp. 37–45. ISSN: 0022-1430, 1727-5652. DOI: 10.1017/jog.2016.7. URL: https://www.cambridge.org/core/product/identifier/S0022143016000071/type/journal_article (visited on 08/16/2021).

Bindschadler, Robert A., Eric P. Roberts, and Almut Iken (1990). "Age of Crary Ice Rise, Antarctica, Determined from Temperature-Depth Profiles." en. In: *Annals of Glaciology* 14, pp. 13–16. ISSN: 0260-3055, 1727-5644. DOI: 10.1017/S0260305500008168. URL: https://www.cambridge.org/core/product/identifier/S0260305500008168/type/journal_article (visited on 08/16/2021).

Bindschadler, Robert A. et al. (2013). "Ice-sheet model sensitivities to environmental forcing and their use in projecting future sea level (the SeaRISE project)." en. In: *Journal of Glaciology* 59.214, pp. 195–224. ISSN: 0022-1430, 1727-5652. DOI: 10.3189/2013JoG12J125. (Visited on 08/16/2021).

Bindschadler, Robert (1993). "Siple Coast Project research of Crary Ice Rise and the mouths of Ice Streams B and C, West Antarctica: review and new perspectives." en. In: *Journal of Glaciology* 39.133, pp. 538–552. ISSN: 0022-1430, 1727-5652. DOI: 10.1017/S0022143000016439. URL: https://www.cambridge.org/core/product/identifier/S0022143000016439/type/journal_article (visited on 08/16/2021).

Bindschadler, Robert, Patricia Vornberger, and Laurence Gray (2005). "Changes in the ice plain of Whillans Ice Stream, West Antarctica." en. In: *Journal of Glaciology* 51.175, pp. 620–636. ISSN: 0022-1430, 1727-5652. DOI: 10.3189/172756505781829070. URL: https://www.cambridge.org/core/product/identifier/S0022143000210824/type/journal_article (visited on 08/16/2021).

Bochev, Pavel B., Clark R. Dohrmann, and Max D. Gunzburger (Jan. 2006). "Stabilization of Low-order Mixed Finite Elements for the Stokes Equations." en. In: *SIAM Journal on Numerical Analysis* 44.1, 82–101. DOI: 10.1137/S0036142905444482.

Bons, Paul D, Daniela Jansen, Felicitas Mundel, Catherine C Bauer, Tobias Binder, Olaf Eisen, Mark W Jessell, Maria-Gema Llorens, Florian Steinbach, Daniel Steinhage, et al. (2016). "Converging flow and anisotropy cause large-scale folding in Greenland's ice sheet." In: *Nature communications* 7.1, pp. 1–6.

Bons, Paul D, Thomas Kleiner, M-G Llorens, David J Prior, Till Sachau, Ilka Weikusat, and Daniela Jansen (2018). "Greenland Ice Sheet: Higher nonlinearity of ice flow significantly reduces estimated basal motion." In: *Geophysical Research Letters* 45.13, pp. 6542–6548.

Brezzi, F. (1974). "On the existence, uniqueness and approximation of saddle-point problems arising from lagrangian multipliers." In: *Revue française d'automatique, informatique, recherche opérationnelle. Analyse numérique* 8.R2, 129–151. ISSN: 0397-9342. DOI: 10.1051/m2an/197408R201291. URL: http://www.esaim-m2an.org/10.1051/m2an/197408R201291.

Brisbourne, A. M., C. Martín, A. M. Smith, A. F. Baird, J. M. Kendall, and J. Kingslake (Jan. 2019). "Constraining Recent Ice Flow History at Korff Ice Rise, West Antarctica, Using Radar and Seismic Measurements of Ice Fabric." en. In: *Journal of Geophysical Research: Earth Surface* 124.1, pp. 175–194. ISSN: 21699003. DOI: 10.1029/2018JF004776. URL: http://doi.wiley.com/10.1029/2018JF004776 (visited on 08/16/2021).

Brisbourne, Alex M., Michael Kendall, Sofia-Katerina Kufner, Thomas S. Hudson, and Andrew M. Smith (July 2021). "Downhole distributed acoustic seismic profiling at Skytrain Ice Rise, West Antarctica." en. In: *The Cryosphere* 15.7, 3443–3458. ISSN: 1994-0424. DOI:

10.5194/tc-15-3443-2021. URL: https://tc.copernicus.org/articles/15/3443/2021/.

Brondex, Julien, Fabien Gillet-Chaulet, and Olivier Gagliardini (2019). "Sensitivity of centennial mass loss projections of the Amundsen basin to the friction law." en. In: *The Cryosphere* 13.1, pp. 177–195. ISSN: 1994-0424. DOI: 10.5194/tc-13-177-2019. (Visited on 08/16/2021).

Burgard, Clara, Nicolas C. Jourdain, Ronja Reese, Adrian Jenkins, and Pierre Mathiot (Dec. 2022). "An assessment of basal melt parameterisations for Antarctic ice shelves." en. In: *The Cryosphere* 16.12, 4931–4975. ISSN: 1994-0424. DOI: 10.5194/tc-16-4931-2022. URL: https://tc.copernicus.org/articles/16/4931/2022/.

Callens, D., K. Matsuoka, D. Steinhage, B. Smith, E. Witrant, and F. Pattyn (May 2014). "Transition of flow regime along a marine-terminating outlet glacier in East Antarctica." en. In: *The Cryosphere* 8.3, pp. 867–875. ISSN: 1994-0424. DOI: 10.5194/tc-8-867-2014. URL: https://tc.copernicus.org/articles/8/867/2014/ (visited on 11/21/2021).

Callens, Denis, Reinhard Drews, Emmanuel Witrant, Morgane Philippe, and Frank Pattyn (June 2016). "Temporally stable surface mass balance asymmetry across an ice rise derived from radar internal reflection horizons through inverse modeling." en. In: *Journal of Glaciology* 62.233, pp. 525–534. ISSN: 0022-1430, 1727-5652. DOI: 10.1017/jog.2016.41. URL: https://www.cambridge.org/core/product/identifier/S0022143016000411/type/journal_article (visited on 01/13/2022).

Cavitte, Marie G.P., Hugues Goosse, Sarah Wauthy, Thore Kausch, Jean-Louis Tison, Brice Van Liefferinge, Frank Pattyn, Jan T.M. Lenaerts, and Philippe Claeys (2022). "From ice core to ground-penetrating radar: representativeness of SMB at three ice rises along the Princess Ragnhild Coast, East Antarctica." en. In: *Journal of Glaciology* 68.272, 1221–1233. ISSN: 0022-1430, 1727-5652. DOI: 10.1017/jog.2022.39. URL: https://www.cambridge.org/core/product/identifier/S0022143022000399/type/journal_article.

Cook, A. J. and D. G. Vaughan (Feb. 2010). "Overview of areal changes of the ice shelves on the Antarctic Peninsula over the past 50 years." en. In: *The Cryosphere* 4.1, pp. 77–98. ISSN: 1994-0424. DOI: 10.5194/tc-4-77-2010. URL: https://tc.copernicus.org/articles/4/77/2010/ (visited on 08/16/2021).

Cornford, Stephen L. et al. (July 2020). "Results of the third Marine Ice Sheet Model Intercomparison Project (MISMIP+)." en. In: *The Cryosphere* 14.7, pp. 2283–2301. ISSN: 1994-0424. DOI: 10.5194/tc-14-2283-2020. URL: https://tc.copernicus.org/articles/14/2283/2020/ (visited on 08/16/2021).

De Rydt, J., P. R. Holland, P. Dutrieux, and A. Jenkins (Apr. 2014). "Geometric and oceanographic controls on melting beneath Pine Island Glacier." en. In: *Journal of Geophysical Research: Oceans* 119.4, 2420–2438. ISSN: 21699275. DOI: 10.1002/2013JC009513. URL: http://doi.wiley.com/10.1002/2013JC009513.

Depoorter, M. A., J. L. Bamber, J. A. Griggs, J. T. M. Lenaerts, S. R. M. Ligtenberg, M. R. van den Broeke, and G. Moholdt (Oct. 2013). "Calving fluxes and basal melt rates of Antarctic ice shelves." en. In: *Nature* 502.7469, pp. 89–92. ISSN: 0028-0836, 1476-4687. DOI: 10.1038/nature12567. URL: http://www.nature.com/articles/nature12567 (visited on 08/16/2021).

Deschamps, Pierre, Nicolas Durand, Edouard Bard, Bruno Hamelin, Gilbert Camoin, Alexander L. Thomas, Gideon M. Henderson, Jun'ichi Okuno, and Yusuke Yokoyama (Mar. 2012). "Ice-sheet collapse and sea-level rise at the Bølling warming 14,600 years ago." en. In: *Nature* 483.7391, pp. 559–564. ISSN: 0028-0836, 1476-4687. DOI: 10.1038/nature10902. URL: http://www.nature.com/articles/nature10902 (visited on 08/16/2021).

Doake, C. S. M., H. F. J. Corr, H. Rott, P. Skvarca, and N. W. Young (Feb. 1998). "Breakup and conditions for stability of the northern Larsen Ice Shelf, Antarctica." en. In: *Nature* 391.6669, pp. 778–780. ISSN: 0028-0836, 1476-4687. DOI: 10.1038/35832. URL: http://www.nature.com/articles/35832 (visited on 08/16/2021).

Drews, R., K. Matsuoka, C. Martín, D. Callens, N. Bergeot, and F. Pattyn (2015). "Evolution of Derwael Ice Rise in Dronning Maud Land, Antarctica, over the last millennia." en. In: *Journal of Geophysical Research: Earth Surface* 120.3, pp. 564–579. ISSN: 21699003. DOI: 10.1002/2014JF003246. (Visited on 08/16/2021).

Drews, Reinhard, Carlos Martín, Daniel Steinhage, and Olaf Eisen (2013). "Characterizing the glaciological conditions at Halvfarryggen ice dome, Dronning Maud Land, Antarctica." en. In: *Journal of Glaciology* 59.213, pp. 9–20. ISSN: 0022-1430, 1727-5652. DOI: 10.3189/2013JoG12J134.

Dupont, T. K. and R. B. Alley (2005). "Assessment of the importance of ice-shelf buttressing to ice-sheet flow." en. In: *Geophysical Research Letters* 32.4. ISSN: 00948276. DOI: 10.1029/2004GL022024. URL: http://doi.wiley.com/10.1029/2004GL022024 (visited on 08/16/2021).

Durand, G., O. Gagliardini, B. de Fleurian, T. Zwinger, and E. Le Meur (Aug. 2009). "Marine ice sheet dynamics: Hysteresis and neutral equilibrium." en. In: *Journal of Geophysical Research* 114.F3, F03009. ISSN: 0148-0227. DOI: 10.1029/2008JF001170. URL: http://doi.wiley.com/10.1029/2008JF001170 (visited on 08/16/2021).

Durand, Gaël, F Gillet-Chaulet, A Svensson, O Gagliardini, S Kipfstuhl, J Meyssonnier, F Parrenin, P Duval, and D Dahl-Jensen (2007). "Change in ice rheology during climate variations – implications for ice flow modelling and dating of the EPICA Dome C core." In: *Climate of the Past* 3.1, pp. 155–167.

Duval, Paul, MF Ashby, and I Anderman (1983). "Rate-controlling processes in the creep of polycrystalline ice." In: *The Journal of Physical Chemistry* 87.21, pp. 4066–4074.

Ershadi, M. Reza, Reinhard Drews, Carlos Martín, Olaf Eisen, Catherine Ritz, Hugh Corr, Julia Christmann, Ole Zeising, Angelika Humbert, and Robert Mulvaney (2022). "Polarimetric radar reveals the spatial distribution of ice fabric at domes and divides in

East Antarctica." en. In: *The Cryosphere* 16.5, 1719–1739. ISSN: 1994-0424. DOI: 10.5194/tc-16-1719-2022. URL: https://tc.copernicus.org/articles/16/1719/2022/.

Favier, L., O. Gagliardini, G. Durand, and T. Zwinger (Jan. 2012). "A three-dimensional full Stokes model of the grounding line dynamics: effect of a pinning point beneath the ice shelf." en. In: *The Cryosphere* 6.1, pp. 101–112. ISSN: 1994-0424. DOI: 10.5194/tc-6-101-2012. URL: https://tc.copernicus.org/articles/6/101/2012/ (visited on 08/16/2021).

Favier, Lionel and Frank Pattyn (June 2015). "Antarctic ice rise formation, evolution, and stability." en. In: *Geophysical Research Letters* 42.11, pp. 4456–4463. ISSN: 0094-8276, 1944-8007. DOI: 10.1002/2015GL064195. URL: https://onlinelibrary.wiley.com/doi/abs/10.1002/2015GL064195 (visited on 08/16/2021).

Favier, Lionel, Frank Pattyn, Sophie Berger, and Reinhard Drews (Nov. 2016). "Dynamic influence of pinning points on marine ice-sheet stability: a numerical study in Dronning Maud Land, East Antarctica." en. In: *The Cryosphere* 10.6, pp. 2623–2635. ISSN: 1994-0424. DOI: 10.5194/tc-10-2623-2016. URL: https://tc.copernicus.org/articles/10/2623/2016/ (visited on 12/09/2021).

Feldmann, J., T. Albrecht, C. Khroulev, F. Pattyn, and A. Levermann (2014). "Resolution-dependent performance of grounding line motion in a shallow model compared with a full-Stokes model according to the MISMIP3d intercomparison." en. In: *Journal of Glaciology* 60.220, pp. 353–360. ISSN: 0022-1430, 1727-5652. DOI: 10.3189/2014JoG13J093. URL: https://www.cambridge.org/core/product/identifier/S0022143000205406/type/journal_article.

Franke, Steven, Paul D Bons, Julien Westhoff, Ilka Weikusat, Tobias Binder, Kyra Streng, Daniel Steinhage, Veit Helm, Olaf Eisen, John D Paden, et al. (2022). "Holocene ice-stream shutdown and drainage basin reconfiguration in northeast Greenland." In: *Nature Geoscience*, pp. 1–7.

Fürst, J. J., G. Durand, F. Gillet-Chaulet, N. Merino, L. Tavard, J. Mouginot, N. Gourmelen, and O. Gagliardini (Aug. 2015). "Assimilation of Antarctic velocity observations provides evidence for uncharted pinning points." en. In: *The Cryosphere* 9.4, pp. 1427–1443. ISSN: 1994-0424. DOI: 10.5194/tc-9-1427-2015. URL: https://tc.copernicus.org/articles/9/1427/2015/ (visited on 08/16/2021).

Fürst, Johannes Jakob, Gaël Durand, Fabien Gillet-Chaulet, Laure Tavard, Melanie Rankl, Matthias Braun, and Olivier Gagliardini (May 2016). "The safety band of Antarctic ice shelves." en. In: *Nature Climate Change* 6.5, pp. 479–482. ISSN: 1758-678X, 1758-6798. DOI: 10.1038/nclimate2912. URL: http://www.nature.com/articles/nclimate2912 (visited on 08/16/2021).

Gagliardini, O., J. Brondex, F. Gillet-Chaulet, L. Tavard, V. Peyaud, and G. Durand (Feb. 2016). "Brief communication: Impact of mesh resolution for MISMIP and MISMIP3d experiments using Elmer/Ice." en. In: *The Cryosphere* 10.1, pp. 307–312. ISSN: 1994-0424. DOI: 10.5194/tc-10-307-2016. URL: https://tc.copernicus.org/articles/10/307/2016/ (visited on 02/08/2022).

Gagliardini, O., D. Cohen, P. Råback, and T. Zwinger (May 2007). "Finite-element modeling of subglacial cavities and related friction law." en. In: *Journal of Geophysical Research* 112.F2, F02027. ISSN: 0148-0227. DOI: 10.1029/2006JF000576. URL: http://doi.wiley.com/10.1029/2006JF000576 (visited on 08/16/2021).

Gagliardini, O., G. Durand, T. Zwinger, R. C. A. Hindmarsh, and E. Le Meur (2010). "Coupling of ice-shelf melting and buttressing is a key process in ice-sheets dynamics: ICE-SHELF MELTING AND BUTTRESSING." en. In: *Geophysical Research Letters* 37.14, n/a–n/a. ISSN: 00948276. DOI: 10.1029/2010GL043334. (Visited on 08/16/2021).

Gagliardini, O. and T. Zwinger (June 2008). "The ISMIP-HOM benchmark experiments performed using the Finite-Element code Elmer." en. In: *The Cryosphere* 2.1, pp. 67–76. ISSN: 1994-0424. DOI: 10.5194/tc-2-67-2008. URL: https://tc.copernicus.org/articles/2/67/2008/ (visited on 08/16/2021).

Gagliardini, O. et al. (2013). "Capabilities and performance of Elmer/Ice, a new-generation ice sheet model." en. In: *Geoscientific Model Development* 6.4, pp. 1299–1318. ISSN: 1991-9603. DOI: 10.5194/gmd-6-1299-2013. URL: https://gmd.copernicus.org/articles/6/1299/2013/ (visited on 08/16/2021).

Garbe, Julius, Torsten Albrecht, Anders Levermann, Jonathan F. Donges, and Ricarda Winkelmann (Sept. 2020). "The hysteresis of the Antarctic Ice Sheet." en. In: *Nature* 585.7826, pp. 538–544. ISSN: 0028-0836, 1476-4687. DOI: 10.1038/s41586-020-2727-5. URL: http://www.nature.com/articles/s41586-020-2727-5 (visited on 08/16/2021).

Gerber, Tamara Annina, David A Lilien, Nicholas Mossor Rathmann, Steven Franke, Tun Jan Young, Fernando Valero-Delgado, M Reza Ershadi, Reinhard Drews, Ole Zeising, Angelika Humbert, et al. (2023). "Crystal orientation fabric anisotropy causes directional hardening of the Northeast Greenland Ice Stream." In: *Nature Communications* 14.1, p. 2653.

Gillet-Chaulet, Fabie, Olivier Gagliardini, Jacques Meyssonnier, Maurine Montagnat, and Olivier Castelnau (2005). "A user-friendly anisotropic flow law for ice-sheet modeling." In: *Journal of glaciology* 51.172, pp. 3–14.

Gillet-Chaulet, Fabien, Olivier Gagliardini, Jacques Meyssonnier, Thomas Zwinger, and Juha Ruokolainen (2006). "Flow-induced anisotropy in polar ice and related ice-sheet flow modelling." In: *Journal of non-newtonian fluid mechanics* 134.1-3, pp. 33–43.

Gillet-Chaulet, Fabien, Richard C. A. Hindmarsh, Hugh F. J. Corr, Edward C. King, and Adrian Jenkins (Dec. 2011). "*In-situ* quantification of ice rheology and direct measurement of the Raymond Effect at Summit, Greenland using a phase-sensitive radar." en. In: *Geophysical Research Letters* 38.24, n/a–n/a. ISSN: 00948276. DOI: 10.1029/2011GL049843. URL: http://doi.wiley.com/10.1029/2011GL049843 (visited on 11/21/2021).

Gillet-Chaulet, Fabien and Richard CA Hindmarsh (2011). "Flow at ice-divide triple junctions: 1. Three-dimensional full-Stokes modeling." In: *Journal of Geophysical Research: Earth Surface* 116.F2.

Gladstone, Rupert M., Antony J. Payne, and Stephen L. Cornford (2012). "Resolution requirements for grounding-line modelling: sensitivity to basal drag and ice-shelf buttressing." en. In: *Annals of Glaciology* 53.60, pp. 97–105. ISSN: 0260-3055, 1727-5644. DOI: 10.3189/2012AoG60A148. URL: https://www.cambridge.org/core/product/identifier/S0260305500251793/type/journal_article (visited on 08/16/2021).

Gladstone, Rupert Michael, Roland Charles Warner, Benjamin Keith Galton-Fenzi, Olivier Gagliardini, Thomas Zwinger, and Ralf Greve (Jan. 2017). "Marine ice sheet model performance depends on basal sliding physics and sub-shelf melting." en. In: *The Cryosphere* 11.1, pp. 319–329. ISSN: 1994-0424. DOI: 10.5194/tc-11-319-2017. URL: https://tc.copernicus.org/articles/11/319/2017/ (visited on 08/16/2021).

Goel, Vikram, Kenichi Matsuoka, Cesar Deschamps Berger, Ian Lee, Jørgen Dall, and René Forsberg (Dec. 2020). "Characteristics of ice rises and ice rumples in Dronning Maud Land and Enderby Land, Antarctica." en. In: *Journal of Glaciology* 66.260, pp. 1064–1078. ISSN: 0022-1430, 1727-5652. DOI: 10.1017/jog.2020.77. URL: https://www.cambridge.org/core/product/identifier/S0022143020000775/type/journal_article (visited on 08/16/2021).

Goldberg, D., D. M. Holland, and C. Schoof (Dec. 2009). "Grounding line movement and ice shelf buttressing in marine ice sheets." en. In: *Journal of Geophysical Research* 114.F4, F04026. ISSN: 0148-0227. DOI: 10.1029/2008JF001227. URL: http://doi.wiley.com/10.1029/2008JF001227 (visited on 08/16/2021).

Graham, Felicity S., Mathieu Morlighem, Roland C. Warner, and Adam Treverrow (Mar. 2018). "Implementing an empirical scalar constitutive relation for ice with flow-induced polycrystalline anisotropy in large-scale ice sheet models." en. In: *The Cryosphere* 12.3, 1047–1067. ISSN: 1994-0424.

Grant, K. M. et al. (Dec. 2014). "Sea-level variability over five glacial cycles." en. In: *Nature Communications* 5.1, p. 5076. ISSN: 2041-1723. DOI: 10.1038/ncomms6076. URL: http://www.nature.com/articles/ncomms6076 (visited on 11/23/2021).

Greenwood, Sarah L., Lauren M. Simkins, Monica C. M. Winsborrow, and Lilja R. Bjarnadóttir (Jan. 2021). "Exceptions to bed-controlled ice sheet flow and retreat from glaciated continental margins worldwide." en. In: *Science Advances* 7.3, eabb6291. ISSN: 2375-2548. DOI: 10.1126/sciadv.abb6291. URL: https://advances.sciencemag.org/lookup/doi/10.1126/sciadv.abb6291 (visited on 08/16/2021).

Greve, Ralf and Heinz Blatter (2009). *Dynamics of ice sheets and glaciers*. Dordrecht: Springer. ISBN: 9783642034145 9783642034152.

Gudmundsson, G. H. (Apr. 2013). "Ice-shelf buttressing and the stability of marine ice sheets." en. In: *The Cryosphere* 7.2, pp. 647–655. ISSN: 1994-0424. DOI: 10.5194/tc-7-647-2013. URL: https://tc.copernicus.org/articles/7/647/2013/ (visited on 08/16/2021).

Gudmundsson, G. H., J. Krug, G. Durand, L. Favier, and O. Gagliardini (Dec. 2012). "The stability of grounding lines on retrograde

slopes." en. In: *The Cryosphere* 6.6, pp. 1497–1505. ISSN: 1994-0424. DOI: 10.5194/tc-6-1497-2012. URL: https://tc.copernicus.org/articles/6/1497/2012/ (visited on 11/21/2021).

Gudmundsson, G. Hilmar (May 2003). "Transmission of basal variability to a glacier surface." en. In: *Journal of Geophysical Research: Solid Earth* 108.B5. ISSN: 01480227. DOI: 10.1029/2002JB002107. URL: http://doi.wiley.com/10.1029/2002JB002107 (visited on 08/16/2021).

Haseloff, Marianne and Olga V. Sergienko (June 2018). "The effect of buttressing on grounding line dynamics." en. In: *Journal of Glaciology* 64.245, pp. 417–431. ISSN: 0022-1430, 1727-5652. DOI: 10.1017/jog.2018.30. URL: https://www.cambridge.org/core/product/identifier/S0022143018000308/type/journal_article (visited on 08/16/2021).

Helanow, Christian and Josefin Ahlkrona (Aug. 2018). "Stabilized equal low-order finite elements in ice sheet modeling – accuracy and robustness." en. In: *Computational Geosciences* 22.4, 951–974. ISSN: 1420-0597, 1573-1499. DOI: 10.1007/s10596-017-9713-5. URL: http://link.springer.com/10.1007/s10596-017-9713-5.

Hindmarsh, R. C. A. (Mar. 2004). "A numerical comparison of approximations to the Stokes equations used in ice sheet and glacier modeling: HIGHER-ORDER GLACIER MODELS." en. In: *Journal of Geophysical Research: Earth Surface* 109.F1. ISSN: 01480227. DOI: 10.1029/2003JF000065. URL: http://doi.wiley.com/10.1029/2003JF000065 (visited on 08/16/2021).

Hindmarsh, R. G. A. (1996). "Stochastic perturbation of divide position." en. In: *Annals of Glaciology* 23, pp. 94–104. ISSN: 0260-3055, 1727-5644. DOI: 10.1017/S0260305500013306. URL: https://www.cambridge.org/core/product/identifier/S0260305500013306/type/journal_article (visited on 08/16/2021).

Hindmarsh, Richard CA, Edward C King, Robert Mulvaney, Hugh FJ Corr, Gisela Hiess, and Fabien Gillet-Chaulet (2011). "Flow at ice-divide triple junctions: 2. Three-dimensional views of isochrone architecture from ice-penetrating radar surveys." In: *Journal of Geophysical Research: Earth Surface* 116.F2.

Holland, David M. and Adrian Jenkins (Aug. 1999). "Modeling Thermodynamic Ice–Ocean Interactions at the Base of an Ice Shelf." en. In: *Journal of Physical Oceanography* 29.8, 1787–1800. ISSN: 0022-3670, 1520-0485. DOI: 10.1175/1520-0485(1999)029⟨1787:MTIOIA⟩2.0.CO;2. URL: http://journals.ametsoc.org/doi/10.1175/1520-0485(1999)029⟨1787:MTIOIA⟩2.0.CO;2.

Holschuh, Nicholas, Byron R. Parizek, Richard B. Alley, and Sridhar Anandakrishnan (June 2017). "Decoding ice sheet behavior using englacial layer slopes." en. In: *Geophysical Research Letters* 44.11, 5561–5570. ISSN: 0094-8276, 1944-8007. DOI: 10.1002/2017GL073417. URL: https://agupubs.onlinelibrary.wiley.com/doi/10.1002/2017GL073417.

Iacopini, D., C.W. Passchier, D. Koehn, and R. Carosi (Feb. 2007). "Fabric attractors in general triclinic flow systems and their application to high strain shear zones: A dynamical system approach."

en. In: *Journal of Structural Geology* 29.2, 298–317. ISSN: 01918141. DOI: 10.1016/j.jsg.2006.10.002. URL: https://linkinghub.elsevier.com/retrieve/pii/S0191814106002379.

Jacobs, Stanley S., Adrian Jenkins, Claudia F. Giulivi, and Pierre Dutrieux (Aug. 2011). "Stronger ocean circulation and increased melting under Pine Island Glacier ice shelf." en. In: *Nature Geoscience* 4.8, pp. 519–523. ISSN: 1752-0894, 1752-0908. DOI: 10.1038/ngeo1188. URL: http://www.nature.com/articles/ngeo1188 (visited on 08/16/2021).

Jenkins, Adrian, Keith W. Nicholls, and Hugh F. J. Corr (Oct. 2010). "Observation and Parameterization of Ablation at the Base of Ronne Ice Shelf, Antarctica." en. In: *Journal of Physical Oceanography* 40.10, 2298–2312. ISSN: 1520-0485, 0022-3670. DOI: 10.1175/2010JPO4317.1. URL: http://journals.ametsoc.org/doi/10.1175/2010JPO4317.1.

Kennedy, Joseph H and Erin C Pettit (2015). "The response of fabric variations to simple shear and migration recrystallization." In: *Journal of Glaciology* 61.227, pp. 537–550.

Kingslake, J., R. P. Scherer, T. Albrecht, J. Coenen, R. D. Powell, R. Reese, N. D. Stansell, S. Tulaczyk, M. G. Wearing, and P. L. Whitehouse (June 2018). "Extensive retreat and re-advance of the West Antarctic Ice Sheet during the Holocene." en. In: *Nature* 558.7710, pp. 430–434. ISSN: 0028-0836, 1476-4687. DOI: 10.1038/s41586-018-0208-x. URL: http://www.nature.com/articles/s41586-018-0208-x (visited on 08/16/2021).

Kingslake, Jonathan, Carlos Martín, Robert J. Arthern, Hugh F. J. Corr, and Edward C. King (2016). "Ice-flow reorganization in West Antarctica 2.5 kyr ago dated using radar-derived englacial flow velocities." In: *Geophysical Research Letters* 43.17, pp. 9103–9112. DOI: https://doi.org/10.1002/2016GL070278. eprint: https://agupubs.onlinelibrary.wiley.com/doi/pdf/10.1002/2016GL070278. URL: https://agupubs.onlinelibrary.wiley.com/doi/abs/10.1002/2016GL070278.

Kluskiewicz, Dan, Edwin D. Waddington, Sridhar Anandakrishnan, Donald E. Voigt, Kenichi Matsuoka, and Michael P. McCARTHY (Aug. 2017). "Sonic methods for measuring crystal orientation fabric in ice, and results from the West Antarctic ice sheet (WAIS) Divide." en. In: *Journal of Glaciology* 63.240, 603–617. ISSN: 0022-1430, 1727-5652. DOI: 10.1017/jog.2017.20. URL: https://www.cambridge.org/core/product/identifier/S002214301700020X/type/journal_article.

Lenaerts, Jan T.M. et al. (2014). "High variability of climate and surface mass balance induced by Antarctic ice rises." en. In: *Journal of Glaciology* 60.224, pp. 1101–1110. ISSN: 0022-1430, 1727-5652. DOI: 10.3189/2014JoG14J040. URL: https://www.cambridge.org/core/product/identifier/S0022143000201627/type/journal_article (visited on 08/16/2021).

Lenton, Timothy M., Johan Rockström, Owen Gaffney, Stefan Rahmstorf, Katherine Richardson, Will Steffen, and Hans Joachim Schellnhuber (Nov. 2019). "Climate tipping points — too risky to bet against."

en. In: *Nature* 575.7784, 592–595. ISSN: 0028-0836, 1476-4687. DOI: 10.1038/d41586-019-03595-0. URL: https://www.nature.com/articles/d41586-019-03595-0.

Leysinger Vieli, G.J.-M.C., R.C.A. Hindmarsh, and M.J. Siegert (2007). "Three-dimensional flow influences on radar layer stratigraphy." en. In: *Annals of Glaciology* 46, 22–28. ISSN: 0260-3055, 1727-5644. DOI: 10.3189/172756407782871729. URL: https://www.cambridge.org/core/product/identifier/S026030550025386X/type/journal_article.

Lilien, David A., Nicholas M. Rathmann, Christine S. Hvidberg, and Dorthe Dahl-Jensen (2021). "Modeling Ice-Crystal Fabric as a Proxy for Ice-Stream Stability." en. In: *Journal of Geophysical Research: Earth Surface* 126.9. DOI: 10.1029/2021JF006306. URL: https://onlinelibrary.wiley.com/doi/10.1029/2021JF006306.

Llorens, Maria-Gema, Albert Griera, Paul D. Bons, Ilka Weikusat, David J. Prior, Enrique Gomez-Rivas, Tamara De Riese, Ivone Jimenez-Munt, Daniel García-Castellanos, and Ricardo A. Lebensohn (2022). "Can changes in deformation regimes be inferred from crystallographic preferred orientations in polar ice?" en. In: *The Cryosphere* 16.5, 2009–2024. ISSN: 1994-0424. DOI: 10.5194/tc-16-2009-2022. URL: https://tc.copernicus.org/articles/16/2009/2022/.

Löfgren, André, Josefin Ahlkrona, and Christian Helanow (Sept. 2022). "Increasing stable time-step sizes of the free-surface problem arising in ice-sheet simulations." en. In: *Journal of Computational Physics: X* 16, p. 100114. ISSN: 25900552. DOI: 10.1016/j.jcpx.2022.100114.

Ma, Ying, Olivier Gagliardini, Catherine Ritz, Fabien Gillet-Chaulet, Gaël Durand, and Maurine Montagnat (2010). "Enhancement factors for grounded ice and ice shelves inferred from an anisotropic ice-flow model." en. In: *Journal of Glaciology* 56.199, 805–812. ISSN: 0022-1430, 1727-5652. DOI: 10.3189/002214310794457209. URL: https://www.cambridge.org/core/product/identifier/S0022143000214068/type/journal_article.

Macayeal, D.R., R.A. Bindschadler, S. Shabtaie, S. Stephenson, and C.R. Bentley (1987). "Force, Mass, and Energy Budgets of the Crary Ice Rise Complex, Antarctica." en. In: *Journal of Glaciology* 33.114, pp. 218–230. ISSN: 0022-1430, 1727-5652. DOI: 10.1017/S0022143000008728. URL: https://www.cambridge.org/core/product/identifier/S0022143000008728/type/journal_article (visited on 08/16/2021).

Martín, C. and G. H. Gudmundsson (2012). "Effects of nonlinear rheology, temperature and anisotropy on the relationship between age and depth at ice divides." en. In: *The Cryosphere* 6.5, 1221–1229. ISSN: 1994-0424. DOI: 10.5194/tc-6-1221-2012. URL: https://tc.copernicus.org/articles/6/1221/2012/.

Martín, Carlos, G. Hilmar Gudmundsson, and Edward C. King (2014). "Modelling of Kealey Ice Rise, Antarctica, reveals stable ice-flow conditions in East Ellsworth Land over millennia." en. In: *Journal of Glaciology* 60.219, pp. 139–146. ISSN: 0022-1430, 1727-5652. DOI: 10.3189/2014JoG13J089. URL: https://www.cambridge.org/

core/product/identifier/S0022143000203286/type/journal_article (visited on 08/16/2021).

Martín, Carlos, Richard C. A. Hindmarsh, and Francisco J. Navarro (2006). "Dating ice flow change near the flow divide at Roosevelt Island, Antarctica, by using a thermomechanical model to predict radar stratigraphy." en. In: *Journal of Geophysical Research* 111.F1, F01011. ISSN: 0148-0227. DOI: 10.1029/2005JF000326. URL: http://doi.wiley.com/10.1029/2005JF000326 (visited on 08/16/2021).

— (Apr. 2009). "On the effects of divide migration, along-ridge flow, and basal sliding on isochrones near an ice divide." en. In: *Journal of Geophysical Research* 114.F2, F02006. ISSN: 0148-0227. DOI: 10.1029/2008JF001025. URL: http://doi.wiley.com/10.1029/2008JF001025 (visited on 08/16/2021).

Matsuoka, Kenichi et al. (Nov. 2015). "Antarctic ice rises and rumples: Their properties and significance for ice-sheet dynamics and evolution." en. In: *Earth-Science Reviews* 150, pp. 724–745. ISSN: 00128252. DOI: 10.1016/j.earscirev.2015.09.004. URL: https://linkinghub.elsevier.com/retrieve/pii/S0012825215300416 (visited on 08/16/2021).

McCormack, F. S., R. C. Warner, H. Seroussi, C. F. Dow, J. L. Roberts, and A. Treverrow (Mar. 2022). "Modeling the Deformation Regime of Thwaites Glacier, West Antarctica, Using a Simple Flow Relation for Ice Anisotropy (ESTAR)." en. In: *Journal of Geophysical Research: Earth Surface* 127.3, e2021JF006332. ISSN: 2169-9003, 2169-9011. DOI: 10.1029/2021JF006332. URL: https://agupubs.onlinelibrary.wiley.com/doi/10.1029/2021JF006332.

Millstein, Joanna D, Brent M Minchew, and Samuel S Pegler (2022). "Ice viscosity is more sensitive to stress than commonly assumed." In: *Communications Earth & Environment* 3.1, pp. 1–7.

Morland, L. W. and I. R. Johnson (1980). "Steady Motion of Ice Sheets." en. In: *Journal of Glaciology* 25.92, 229–246. ISSN: 0022-1430, 1727-5652. DOI: 10.3189/S0022143000010467.

Morlighem, Mathieu, Eric Rignot, Tobias Binder, Donald Blankenship, Reinhard Drews, Graeme Eagles, Olaf Eisen, Fausto Ferraccioli, René Forsberg, Peter Fretwell, et al. (2020). "Deep glacial troughs and stabilizing ridges unveiled beneath the margins of the Antarctic ice sheet." In: *Nature Geoscience* 13.2, pp. 132–137.

Naughten, Kaitlin A., Jan De Rydt, Sebastian H. R. Rosier, Adrian Jenkins, Paul R. Holland, and Jeff K. Ridley (Dec. 2021). "Two-timescale response of a large Antarctic ice shelf to climate change." en. In: *Nature Communications* 12.1, p. 1991. ISSN: 2041-1723. DOI: 10.1038/s41467-021-22259-0. URL: http://www.nature.com/articles/s41467-021-22259-0 (visited on 08/16/2021).

Passchier, C.W. (Jan. 1997). "The fabric attractor." en. In: *Journal of Structural Geology* 19.1, 113–127. ISSN: 01918141. DOI: 10.1016/S0191-8141(96)00077-6. URL: https://linkinghub.elsevier.com/retrieve/pii/S0191814196000776.

Pattyn, F. et al. (2008). "Benchmark experiments for higher-order and full-Stokes ice sheet models (ISMIP–HOM)." en. In: *The Cryosphere* 2.2, pp. 95–108. ISSN: 1994-0424. DOI: 10.5194/tc-2-95-2008.

URL: https://tc.copernicus.org/articles/2/95/2008/ (visited on 08/16/2021).

Pattyn, F. et al. (May 2012). "Results of the Marine Ice Sheet Model Intercomparison Project, MISMIP." en. In: *The Cryosphere* 6.3, pp. 573–588. ISSN: 1994-0424. DOI: 10.5194/tc-6-573-2012. URL: https://tc.copernicus.org/articles/6/573/2012/ (visited on 01/13/2022).

Pattyn, Frank et al. (2013). "Grounding-line migration in plan-view marine ice-sheet models: results of the ice2sea MISMIP3d intercomparison." en. In: *Journal of Glaciology* 59.215, pp. 410–422. ISSN: 0022-1430, 1727-5652. DOI: 10.3189/2013JoG12J129. URL: https://www.cambridge.org/core/product/identifier/S0022143000204425/type/journal_article (visited on 08/16/2021).

Pegler, Samuel S. (Oct. 2016). "The dynamics of confined extensional flows." en. In: *Journal of Fluid Mechanics* 804, 24–57. ISSN: 0022-1120, 1469-7645. DOI: 10.1017/jfm.2016.516. URL: https://www.cambridge.org/core/product/identifier/S0022112016005164/type/journal_article.

Pettit, Erin C., Throstur Thorsteinsson, H. Paul Jacobson, and Edwin D. Waddington (2007). "The role of crystal fabric in flow near an ice divide." en. In: *Journal of Glaciology* 53.181, 277–288. ISSN: 0022-1430, 1727-5652. DOI: 10.3189/172756507782202766.

Pettit, Erin C., Edwin D. Waddington, William D. Harrison, Throstur Thorsteinsson, Daniel Elsberg, John Morack, and Mark A. Zumberge (2011). "The crossover stress, anisotropy and the ice flow law at Siple Dome, West Antarctica." en. In: *Journal of Glaciology* 57.201, 39–52. DOI: 10.3189/002214311795306619.

Rathmann, Nicholas M., Christine S. Hvidberg, Aslak Grinsted, David A. Lilien, and Dorthe Dahl-Jensen (2021). "Effect of an orientation-dependent non-linear grain fluidity on bulk directional enhancement factors." en. In: *Journal of Glaciology* 67.263, 569–575. ISSN: 0022-1430, 1727-5652. DOI: 10.1017/jog.2020.117. URL: https://www.cambridge.org/core/product/identifier/S0022143020001173/type/journal_article.

Rathmann, Nicholas M. and David A. Lilien (2022). "Inferred basal friction and mass flux affected by crystal-orientation fabrics." en. In: *Journal of Glaciology* 68.268, 236–252. ISSN: 0022-1430, 1727-5652. DOI: 10.1017/jog.2021.88. URL: https://www.cambridge.org/core/product/identifier/S0022143021000885/type/journal_article.

Rathmann, Nicholas M., David A. Lilien, Aslak Grinsted, Tamara A. Gerber, Tun Jan Young, and Dorthe Dahl-Jensen (Jan. 2022). "On the Limitations of Using Polarimetric Radar Sounding to Infer the Crystal Orientation Fabric of Ice Masses." en. In: *Geophysical Research Letters* 49.1, e2021GL096244. ISSN: 0094-8276, 1944-8007. DOI: 10.1029/2021GL096244. URL: https://agupubs.onlinelibrary.wiley.com/doi/10.1029/2021GL096244.

Raymond, Charles F. (1983). "Deformation in the Vicinity of Ice Divides." en. In: *Journal of Glaciology* 29.103, pp. 357–373. ISSN: 0022-1430, 1727-5652. DOI: 10.1017/S0022143000030288. URL: https://www.cambridge.org/core/product/identifier/S0022143000030288/type/journal_article (visited on 08/16/2021).

Reese, R., G. H. Gudmundsson, A. Levermann, and R. Winkelmann (Jan. 2018). "The far reach of ice-shelf thinning in Antarctica." en. In: *Nature Climate Change* 8.1, pp. 53–57. ISSN: 1758-678X, 1758-6798. DOI: 10.1038/s41558-017-0020-x. URL: http://www.nature.com/articles/s41558-017-0020-x (visited on 08/16/2021).

Richards, Daniel H., Samuel S. Pegler, and Sandra Piazolo (2022). "Ice fabrics in two-dimensional flows: beyond pure and simple shear." en. In: *The Cryosphere* 16.10, 4571–4592. ISSN: 1994-0424. DOI: 10.5194/tc-16-4571-2022. URL: https://tc.copernicus.org/articles/16/4571/2022/.

Rignot, E., S. Jacobs, J. Mouginot, and B. Scheuchl (July 2013). "Ice-Shelf Melting Around Antarctica." en. In: *Science* 341.6143, pp. 266–270. ISSN: 0036-8075, 1095-9203. DOI: 10.1126/science.1235798. URL: https://www.sciencemag.org/lookup/doi/10.1126/science.1235798 (visited on 08/16/2021).

Rosier, Sebastian H. R., Ronja Reese, Jonathan F. Donges, Jan De Rydt, G. Hilmar Gudmundsson, and Ricarda Winkelmann (Mar. 2021). "The tipping points and early warning indicators for Pine Island Glacier, West Antarctica." en. In: *The Cryosphere* 15.3, pp. 1501–1516. ISSN: 1994-0424. DOI: 10.5194/tc-15-1501-2021. URL: https://tc.copernicus.org/articles/15/1501/2021/ (visited on 08/16/2021).

Rott, H., P. Skvarca, and T. Nagler (Feb. 1996). "Rapid Collapse of Northern Larsen Ice Shelf, Antarctica." en. In: *Science* 271.5250, pp. 788–792. ISSN: 0036-8075, 1095-9203. DOI: 10.1126/science.271.5250.788. URL: https://www.sciencemag.org/lookup/doi/10.1126/science.271.5250.788 (visited on 08/16/2021).

Rybak, Oleg and Philippe Huybrechts (2003). "A comparison of Eulerian and Lagrangian methods for dating in numerical ice-sheet models." en. In: *Annals of Glaciology* 37, 150–158. ISSN: 0260-3055, 1727-5644. DOI: 10.3189/172756403781815393. URL: https://www.cambridge.org/core/product/identifier/S0260305500266111/type/journal_article.

Schannwell, Clemens, Reinhard Drews, Todd A. Ehlers, Olaf Eisen, Christoph Mayer, and Fabien Gillet-Chaulet (Oct. 2019). "Kinematic response of ice-rise divides to changes in ocean and atmosphere forcing." en. In: *The Cryosphere* 13.10, pp. 2673–2691. ISSN: 1994-0424. DOI: 10.5194/tc-13-2673-2019. URL: https://tc.copernicus.org/articles/13/2673/2019/ (visited on 11/21/2021).

Schoof, Christian (2007). "Ice sheet grounding line dynamics: Steady states, stability, and hysteresis." en. In: *Journal of Geophysical Research* 112.F3, F03S28. ISSN: 0148-0227. DOI: 10.1029/2006JF000664. (Visited on 08/16/2021).

Seddik, H., R. Greve, T. Zwinger, and L. Placidi (2011). "A full Stokes ice flow model for the vicinity of Dome Fuji, Antarctica, with induced anisotropy and fabric evolution." In: *The Cryosphere* 5.2, pp. 495–508. DOI: 10.5194/tc-5-495-2011. URL: https://tc.copernicus.org/articles/5/495/2011/.

Sergienko, Olga V. and Duncan J. Wingham (2022). "Bed topography and marine ice-sheet stability." In: *Journal of Glaciology* 68.267, 124–138. DOI: 10.1017/jog.2021.79.

Seroussi, H. et al. (2019). "initMIP-Antarctica: an ice sheet model initialization experiment of ISMIP6." In: *The Cryosphere* 13.5, pp. 1441–1471. DOI: 10.5194/tc-13-1441-2019. URL: https://tc.copernicus.org/articles/13/1441/2019/.

Seroussi, Helene, Hachmi Ben Dhia, Mathieu Morlighem, Eric Larour, Eric Rignot, and Denis Aubry (2012). "Coupling ice flow models of varying orders of complexity with the Tiling method." en. In: *Journal of Glaciology* 58.210, 776–786. ISSN: 0022-1430, 1727-5652. DOI: 10.3189/2012JoG11J195. URL: https://www.cambridge.org/core/product/identifier/S0022143000207338/type/journal_article.

Seroussi, Hélène and Mathieu Morlighem (June 2018). *Representation of basal melting at the grounding line in ice flow models*. preprint. Ice sheets/Numerical Modelling. DOI: 10.5194/tc-2018-117. URL: https://tc.copernicus.org/preprints/tc-2018-117/tc-2018-117.pdf (visited on 08/16/2021).

Shapero, D. R., J. A. Badgeley, A. O. Hoffman, and I. R. Joughin (2021). "icepack: a new glacier flow modeling package in Python, version 1.0." In: *Geoscientific Model Development* 14.7, pp. 4593–4616. DOI: 10.5194/gmd-14-4593-2021. URL: https://gmd.copernicus.org/articles/14/4593/2021/.

Smith, A. (1986). "Ice rumples on Ronne ice shelf Antarctica." In.

Smith, Emma C., Alan F. Baird, J. Michael Kendall, Carlos Martín, Robert S. White, Alex M. Brisbourne, and Andrew M. Smith (2017). "Ice fabric in an Antarctic ice stream interpreted from seismic anisotropy." en. In: *Geophysical Research Letters* 44.8, 3710–3718. ISSN: 0094-8276, 1944-8007. DOI: 10.1002/2016GL072093. URL: https://onlinelibrary.wiley.com/doi/10.1002/2016GL072093.

Still, Holly and Christina Hulbe (June 2021). "Mechanics and dynamics of pinning points on the Shirase Coast, West Antarctica." en. In: *The Cryosphere* 15.6, pp. 2647–2665. ISSN: 1994-0424. DOI: 10.5194/tc-15-2647-2021. URL: https://tc.copernicus.org/articles/15/2647/2021/ (visited on 08/16/2021).

Sun, Sainan et al. (Dec. 2020). "Antarctic ice sheet response to sudden and sustained ice-shelf collapse (ABUMIP)." en. In: *Journal of Glaciology* 66.260, pp. 891–904. ISSN: 0022-1430, 1727-5652. DOI: 10.1017/jog.2020.67. URL: https://www.cambridge.org/core/product/identifier/S0022143020000672/type/journal_article (visited on 08/16/2021).

Thorsteinsson, Throstur, Edwin D. Waddington, and Raymond C. Fletcher (2003). "Spatial and temporal scales of anisotropic effects in ice-sheet flow." en. In: *Annals of Glaciology* 37, 40–48. ISSN: 0260-3055, 1727-5644. DOI: 10.3189/172756403781815429. URL: https://www.cambridge.org/core/product/identifier/S0260305500265944/type/journal_article.

Tinto, K. J. and R. E. Bell (Oct. 2011). "Progressive unpinning of Thwaites Glacier from newly identified offshore ridge: Constraints from aerogravity: THWAITES OFFSHORE RIDGE." en. In: *Geophysical Research Letters* 38.20, n/a–n/a. ISSN: 00948276. DOI: 10.1029/2011GL049026.

Višnjević, V., R. Drews, G. Moss, A.C.J.. Henry, and C. Wild (2023). "Mapping the composition of Antarctic Ice Shelves as a metric for their susceptibility to future climate change [in preparation]." In.

Wearing, Martin G. and Jonathan Kingslake (Aug. 2019). "Holocene Formation of Henry Ice Rise, West Antarctica, Inferred From Ice-Penetrating Radar." en. In: *Journal of Geophysical Research: Earth Surface* 124.8, pp. 2224–2240. ISSN: 2169-9003, 2169-9011. DOI: 10.1029/2018JF004988. URL: https://onlinelibrary.wiley.com/doi/abs/10.1029/2018JF004988 (visited on 08/16/2021).

Woodcock, N. H. (1977). "Specification of fabric shapes using an eigenvalue method." en. In: *Geological Society of America Bulletin* 88.9, p. 1231. ISSN: 0016-7606. DOI: 10.1130/0016-7606(1977)88⟨1231:SOFSUA⟩2.0.CO;2. URL: https://pubs.geoscienceworld.org/gsabulletin/article/88/9/1231-1236/202166.

Young, T. J., D. M. Schroeder, T. M. Jordan, P. Christoffersen, S. M. Tulaczyk, R. Culberg, and N. L. Bienert (2021a). "Inferring Ice Fabric From Birefringence Loss in Airborne Radargrams: Application to the Eastern Shear Margin of Thwaites Glacier, West Antarctica." en. In: *Journal of Geophysical Research: Earth Surface* 126.5, e2020JF006023. ISSN: 2169-9003, 2169-9011. DOI: 10.1029/2020JF006023. URL: https://agupubs.onlinelibrary.wiley.com/doi/10.1029/2020JF006023.

Young, Tun Jan, Carlos Martín, Poul Christoffersen, Dustin M Schroeder, Slawek M Tulaczyk, and Eliza J Dawson (2021b). "Rapid and accurate polarimetric radar measurements of ice crystal fabric orientation at the Western Antarctic Ice Sheet (WAIS) Divide ice core site." In: *The Cryosphere* 15.8, pp. 4117–4133.